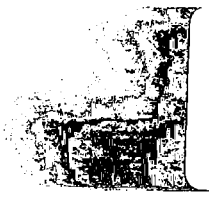

NASA Contractor Report 3699

A Preliminary Study of Solar Powered Aircraft and Associated Power Trains

David W. Hall, Charles D. Fortenbach,
Emanual V. Dimiceli, and Robert W. Parks

CONTRACT NAS1-16975
DECEMBER 1983

25th Anniversary
1958-1983

NASA

NASA Contractor Report 3699

A Preliminary Study of Solar Powered Aircraft and Associated Power Trains

David W. Hall, Charles D. Fortenbach,
Emanual V. Dimiceli, and Robert W. Parks
Lockheed Missiles and Space Company, Inc.
Sunnyvale, California

Prepared for
Langley Research Center
under Contract NAS1-16975

National Aeronautics
and Space Administration

Scientific and Technical
Information Branch

1983

TABLE OF CONTENTS

TABLE OF CONTENTS
(Continued)

LIST OF FIGURES

LIST OF FIGURES
(Continued)

LIST OF FIGURES
(Continued)

LIST OF FIGURES

(Continued)

LIST OF FIGURES

(Continued)

LIST OF TABLES

SUMMARY

This study has sought to determine the feasibility of regeneratively powered solar high altitude remotely piloted vehicles (RPV's) and to identify problem areas which must be overcome before these vehicles can be built. Previous internally funded work identified a variety of missions applicable to regeneratively powered high altitude powered platforms (HAPP's) and these are listed. Some are similar in makeup to the primary mission investigated in this report.

The U.S. Department of Agriculture has expressed a need for a high altitude long endurance suborbital platform which could carry a 250 lb_f (112.5 kg) payload with a daytime only power requirement of 300 watts. This platform would be capable of maintaining 20 Km (65 600 ft) over California's San Joaquin Valley (32° - 38°N latitude) for up to 12 months duration during which the payload would be monitoring crop conditions on an hourly basis. Several sections in this report deal with various aspects of this mission. Table 1 summarizes it and the others postulated in the Statement of Work (SOW).

Flight of a regeneratively powered solar HAPP at high altitude is a careful balance of two dozen or so variables, all of which must be considered together at the conceptual design stage. The power train may be analytically described in terms of component efficiencies and power-to-mass ratios and the resultant model used to evaluate the effects of changes in state-of-the-art (SOTA) on total power train mass and collector area. These two parameters may then be used to link power trains to the vehicles which carry them. Once this is done vehicles may be sized parametrically to fulfill given missions.

Of the many components of a solar HAPP, the chemical storage subsystem composed of electrolyzer, storage tanks and fuel cell, is the most crucial to vehicle performance. It is in this area that further research and development effort should be directed with specific application to regenerative solar HAPP RPV's of very long endurance.

TABLE 1 MISSIONS CONSIDERED IN THIS STUDY

MISSION	ALTITUDE	LATITUDE	MISSION DURATION	PAYLOAD MASS (kg)	CONSTANT PAYLOAD POWER (KW)	PURPOSE
PRIMARY	20	35°N to 38°N	12 months	113	0.3*	Monitor plant health and related agriculture phenomena in San Joaquin Valley, CA
SECONDARY: #1	20	20°S to 20°N	12 months	225	0.5	Monitor dynamics of troposphere/ stratosphere H_2O exchange
#2	20	38°N to 42°N	12 months	175	0.2	Monitor ocean disposal sites
#3	20	28°N to 38°N	12 months	225	0.4	Monitor Mississippi delta river/ocean interaction

*Daylight operation only

INTRODUCTION

Background

Keeping platforms aloft for long periods of time to observe happenings on the earth below has been a major justification of our space program. The desire to stay over the same spot for long periods was satisfied in concept, and in some applications, with geosynchronous satellites. One major disadvantage of satellites as high altitude observation platforms, though, is the cost of launching them into orbit, particularly geosynchronous orbit. Another is the enormous power required to loft satellites into their desired trajectories, although once there, power to maintain functions and orientation is relatively low. A third disadvantage, particularly applicable to geosynchronous satellites, is loss of resolution from orbital height. A fourth disadvantage, which applies only to non-geosynchronous satellites, is that, for the majority of every orbit, a satellite is in the wrong place to observe a fixed location on earth.

Might it be possible then to build a satellite to maintain constant station over a relatively small area of the earth's surface low enough that enormous power and complexity of maneuvers would not be necessary to loft it into its position? It is this wish which led to both government and private sector research into the possible uses of "suborbital spacecraft." Many reports have resulted from this research, several of which are listed in the bibliography, and several demonstrations resulted from further research and development (R&D), several of which will be discussed in this section.

The early 1970's saw a maturation of technologies necessary to build long endurance suborbital spacecraft. Among these were:

- Large lightweight composite structures;
- Solar photovoltaic collectors;
- Highly reliable micro-electronics;
- Efficient energy storage techniques;
- Operating and monitoring techniques of long endurance remotely piloted vehicles (RPV's) (a spacecraft is an RPV); and
- A design philosophy which has evolved out of several recently successful human-powered aircraft programs.

Also in the 1970's, both military and civilian government agencies began to postulate missions which acknowledged the prime importance of intelligence gathering, either over trouble spots in other parts of the world, or for monitoring tasks over the U.S. Another category of mission application

which surfaced was the use of long endurance high altitude RPV's as communications relays, either over the U.S. in emergencies, or over less developed areas of the world where satellite coverage would be limited and uneconomical.

Figure 1 presents some of these civilian and military missions as defined in conversations with potential user agencies. The civilian mission category marked with an asterisk is the one to be addressed in this report.

These various mission categories depend heavily on long lines of sight for both communication and detection, two of which are shown in Figure 2, visual and infrared detection distances to the horizon as functions of altitude. The second chart in this figure presents a profile of average wind speeds as a function of altitude. High altitude flights in the 1950's through 1970's showed that average wind speeds lessened to relatively modest levels in a range of altitudes from 55 000 to 80 000 feet. Observations also indicated that the air in this altitude band was relatively free of turbulence and, therefore, smooth enough to allow reduction of design load factors. Appendix A discusses the wind environment pertinent to this study in more detail. The next chart, Figure 3, presents the rms gust velocity environment based on observations made by Lockheed U-2 and SR-71 aircraft which will be the load criteria used later in this report to size solar HAPP RPV's.

Table 2 summarizes some of the observations which can be made to show the justifications for using high altitude powered platforms.

The 1970's were characterized by several demonstration programs of various forms of HAPP. The most ambitious was the High Altitude Super Pressurized Aerostat (HASPA) program carried out for the Navy by Martin Marietta. Launch difficulties prohibited high altitude flight and showed that the size required for very high altitude missions may create handling problems that may preclude the use of aerostats for these missions. NASA Dryden was active in HAPP demonstration programs with the Mini-Sniffer aircraft which regularly cruised at high altitudes for several hours showing that propellers and high lift airfoils work at extreme altitudes. These vehicles were limited in duration and ease of ground handling by their mono-propellant (hydrazine) fueled engines.

A military program in the early 1970's which produced operational experience on HAPP's was COMPASS COPE. The Boeing and Ryan RPV's which flew were quite large (wingspan of 27.4 m (90 ft)) by standards of the day and the vehicles were also limited in duration because of their power plants, in this case turbofans.

DARPA embarked upon a solar powered high altitude platform program in the mid-1970's with a contract to Astroflight with Lockheed as program manager. The DARPA work produced a pair of flight vehicles, SUNRISE I and II, which proved the feasibility of solar powered high altitude flight. NASA also began studying the high altitude applications of microwave power at Wallops and Langley Research Centers.

CIVILIAN MISSIONS

- Communications Relay
- In-Situ Measurement Aloft
- *Observe Surface Activity
- Astronomical Observation

COAST GUARD MISSIONS

- Search and Rescue
- Reconnaissance
- Traffic discrimination and direction
- Drug enforcement

MILITARY MISSIONS

- Intelligence gathering in relatively benign environments
- High altitude radiation sampling
- Communications relay
- Radio and radar emmission monitoring
- Large area surveillance
- Over-The-Horizon targeting

*This mission category is addressed in this study.

Figure 1. EXISTING CIVILIAN AND MILITARY MISSIONS WHICH COULD BE FULFILLED BY SOLAR HAPP RPV's

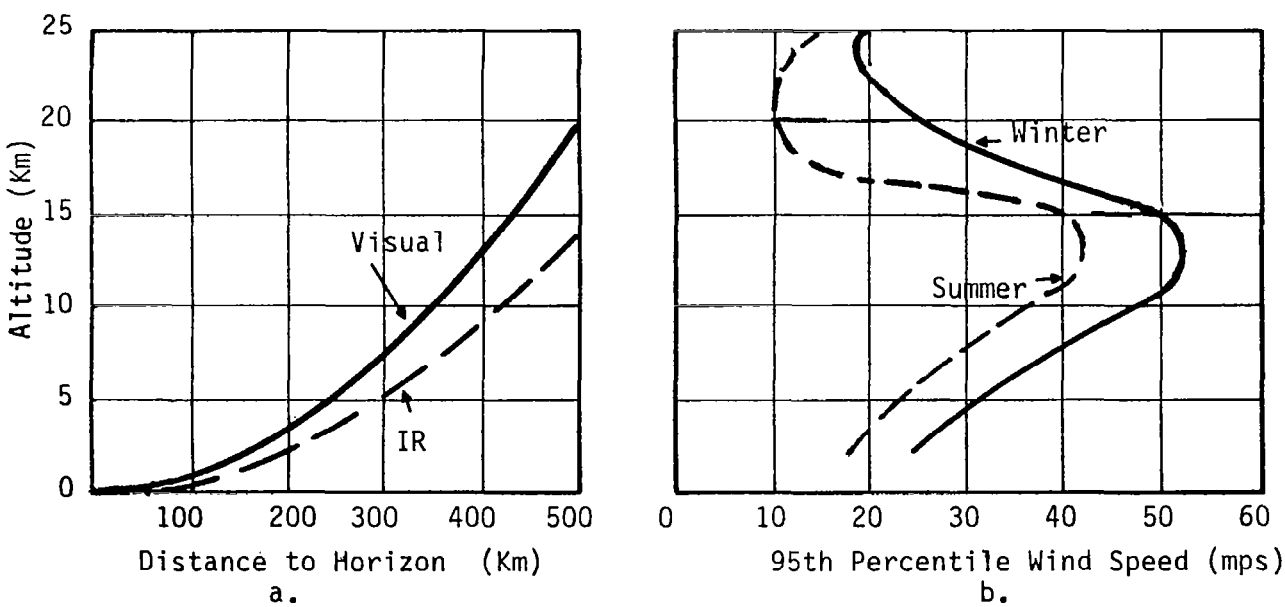

FIGURE 2. BENEFITS OF HIGH ALTITUDE FLIGHT
a. See a Long Way
b. Avoid Jet Stream and High Winds

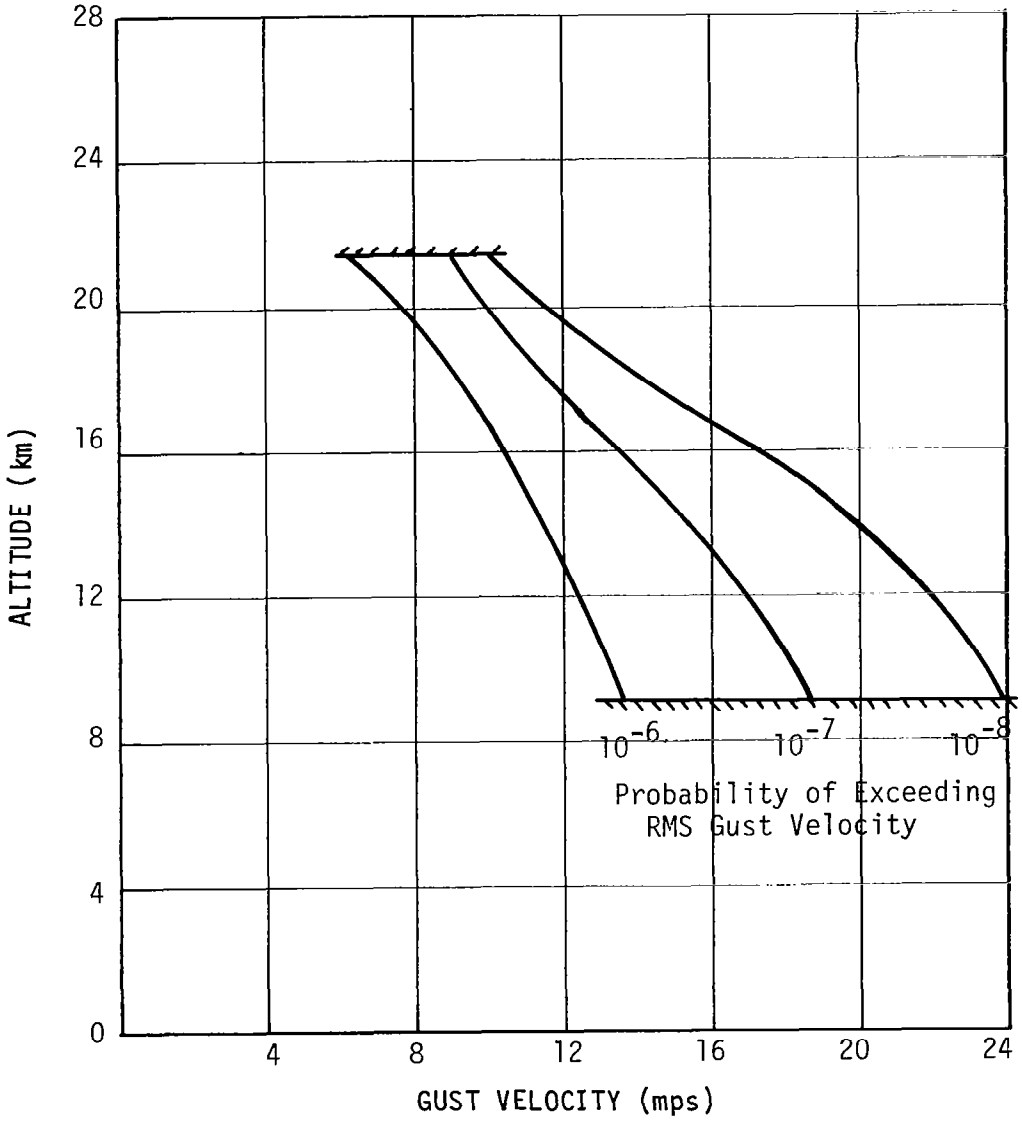

FIGURE 3 MEASURED GUST VELOCITY ENVIRONMENT (From Ref. 1) for 42.7 m (140 ft) to 12 195 m (40 000 ft) WAVELENGTHS

TABLE 2. WHY A HIGH ALTITUDE LONG ENDURANCE PLATFORM?

- COMMUNICATIONS RELAY MISSIONS REQUIRE LONG ENDURANCE:
  - For endurances much over 8 hours RPV's make sense
  - Flights should be as free from atmospheric distractions (such as winds, icing, clouds) as possible so high altitudes make sense
- SURVEILLANCE MISSIONS REQUIRE LONG LINES OF SIGHT AND THE ABILITY TO TRANSIT LONG DISTANCES:
  - High altitudes make sense
  - Low loiter speeds make sense for station-keeping and low power consumption
  - Long endurances make sense
- VERY LONG ENDURANCE AT HIGH ALTITUDES REQUIRES
  - Very light structures
  - Very low power (low drag at low speeds)
  - High cruise lift coefficients
  - Payloads integrated with vehicles
  - Satellite style operating procedures except for short periods

Last, but not least, the emergence of successful human-powered aircraft such as the Gossamer series and Chrysalis showed that large, very lightweight structures (wingspans of 30+ m (>100 ft)) could be built and flown at low speeds and Reynolds numbers.

The stage was set, then, for a program which combined modern technological advancements in several fields with definite mission needs to produce a solar powered long endurance high altitude powered platform RPV.

The Concept of Solar Powered Flight

Project SUNRISE demonstrated the feasibility of solar powered flight in 1975 and the ability of sunshine to lift person-sized payloads was demonstrated in 1981 by Solar Challenger. This report will endeavor to show that flight for long periods of time using a regenerative solar power train is feasible and could be demonstrated in this decade. Regenerative solar powered flight requires a careful balance over each day of energy collected and energy expended. This concept is an extension of conventional aircraft design considerations which include calculation of power required.

This power required is matched, at the steady state condition or conditions of interest, to power available. For conventional aircraft, power available is a function of the installed engine's performance at the speeds and altitudes specified in mission requirements. For a solar powered aircraft, power available is a function of solar flux and the factors which determine its intensity. For a regeneratively powered solar aircraft, power required is still applicable but the aircraft and its power train are sized by energy balance over the entire mission as opposed to power balance. The forces acting on a solar aircraft are shown in Figure 4.

Energy required includes the power required to provide propulsive thrust for the duration of the mission. It also includes power required for running on-board systems and payload. Energy required over the duration of a mission will be balanced by collected energy, or energy available. This equality must be satisfied every day during a mission and will be a function of altitude, latitude, and time of solar year as well as airspeed, aerodynamic efficiency and aircraft weight. Roughly two dozen parameters affect this energy balance. Table 3 presents these variables, Table 4 shows the degree to which several of these variables influence the design of a solar HAPP, and Table 5 relates each of the solar vehicle parameters to mission parameters.

It is the unique nature of solar powered aircraft stemming from the effects of diurnal, seasonal, and orientational variation of the solar flux which dictates the use of this energy balance approach to the design of workable solar HAPP RPV's. To quantify the impact of these effects on aircraft design a dedicated set of analytical tools has been assembled. These tools relate solar flux available to collector area and power train mass and then reconcile these power train quantities with vehicle sizing and performance parameters. The power train mass in a high-altitude, long-endurance solar RPV is a major fraction of total vehicle mass and, hence, plays a dominant role in sizing these vehicles. Scaling of a solar power train is, in turn, intimately related to power train component efficiencies and mass-to-power ratios. Therefore, overall vehicle design begins by using component characteristics and interactions to estimate power system mass and collector area. Basic aerodynamic and geometrical methods are then used to size a vehicle to carry the power train and payload.

The Purpose of This Investigation

This report will address power train and aerodynamic issues and variables such as those in Table 3 interwoven in such a way as to present a comprehensive methodology for determining the feasibility of regenerative solar powered aircraft. The first sections will deal with the solar power train. Middle sections will relate power train parameters to vehicle parameters. The final sections will address a specific mission, postulating a vehicle for it, and analyzing it in enough detail to draw conclusions about concept feasibility.

- LIFT ≡ MASS x G ⟷ CONSTANT FOR 24-HR. CYCLE ⟷ THRUST ≡ DRAG
- 24-HR. ENERGY REQ'D. TO MAINTAIN ALTITUDE & PAYLOAD ≡ ENERGY AVAILABLE

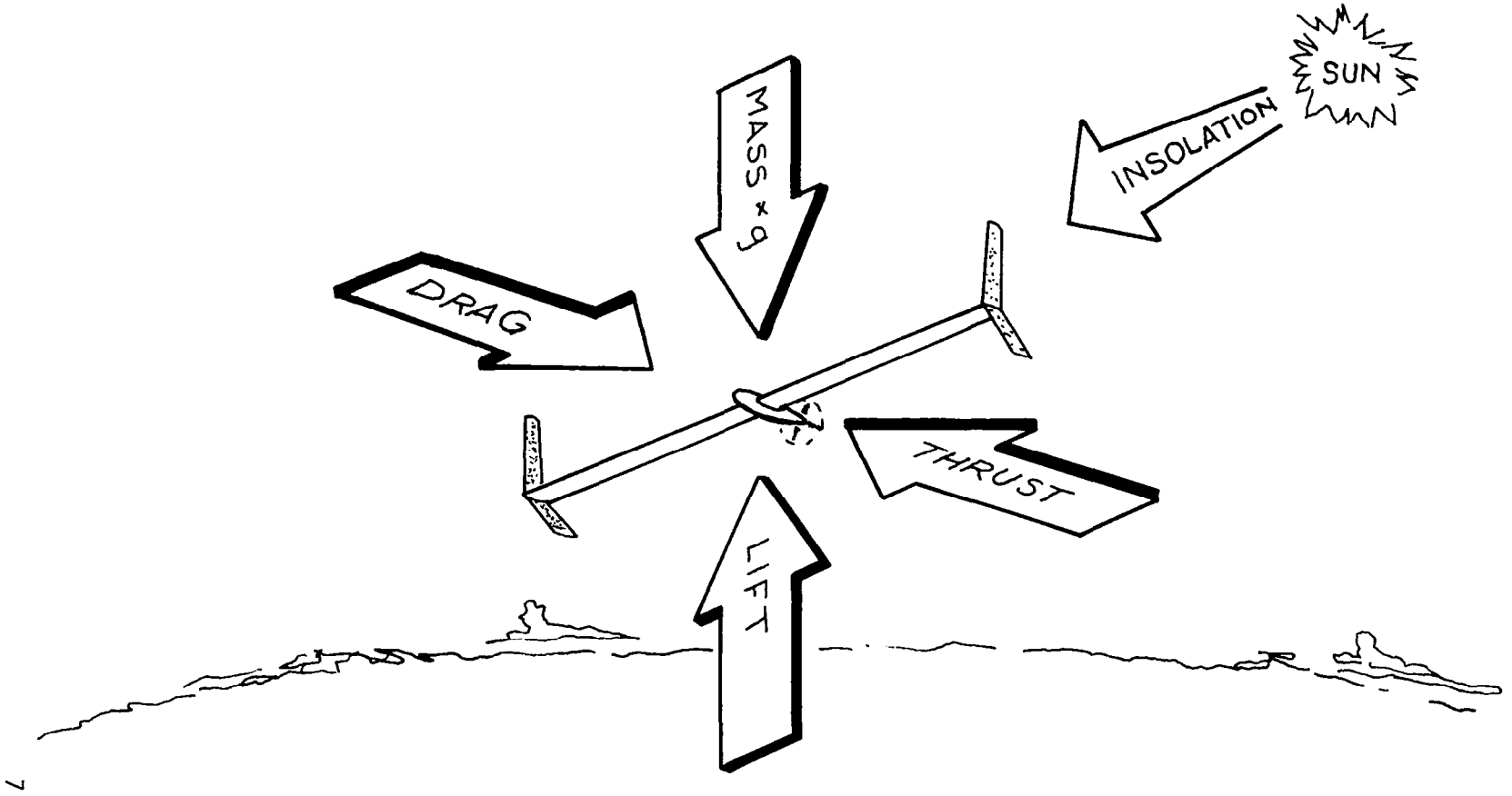

FIGURE 4 HAPP BALANCE PROBLEM

TABLE 3. VARIABLES AFFECTING HAPP PARAMETRICS

- MISSION
  - Speed
  - Payload Power
  - Payload Weight
  - Auxiliary Power
  - Endurance
  - Maneuvers
- ENVIRONMENTAL
  - Altitude
  - Latitude
  - Time of Day
  - Time of Year
  - Winds Aloft
- POWER TRAIN
  - Type
  - Component Efficiencies
  - Component Power Densities
  - Collector Position
  - Shaft Power Required
- AIRFRAME
  - Internal Volume
  - Surface Area
  - Structural Concept
  - Wing Area
  - Aspect Ratio
  - Sweep
- AERODYNAMICS
  - Lift
  - Drag
  - Stability

TABLE 4 MAJOR HAPP DESIGN DRIVERS

THRUST POWER REQUIRED: $$P_{REQ} = \left(\frac{2}{\rho S_{REF}}\right)^{.5} \left(C_{D_T}\right)^{1} \left(\frac{W}{C_L}\right)^{1.5}$$

ITEM	DEFINITION	RELATIVE EFFECT ON P_{REQ}	TO REDUCE P_{REQ}
W	Gross Weight	Strong	Decrease
C_L	Lift Coefficient	Strong	Increase
C_{D_T}	Drag Coefficient	Moderate	Decrease
S_{REF}	Wing Area	Weak	Increase
ρ	Air Density	Weak	Increase

THRUST POWER AVAILABLE: $$P_{AV} = \frac{\eta_{COLL}\eta_{ST}\eta_{BOTH}S_{COLL}\Delta E'_{SUN}}{\tau + \frac{\eta_{ST}\eta_{NIGHT}}{\eta_{DAY}\eta_{BOTH}}\beta\frac{\eta_{NIGHT}\tau}{\eta_{AUX}} + \frac{\eta_{ST}\eta_{NIGHT}}{\eta_{AUX}}}$$

ITEM	DEFINITION	RELATIVE EFFECT	TO INCREASE P_{AV}
$\Delta E'_{SUN}$	24 hr Integral of Flux Density	strong	increase
S_{COLL}	Collector Area	strong	increase
β	Payload Power/P_{AV}	moderate	decrease
τ	Night Hours/Day Hours	strong	decrease
η_{COLL}	Collection Subtrain Efficiency	strong	increase
η_{ST}	Storage " "	strong	increase
η_{NIGHT}	Night " "	strong	increase
η_{DAY}	Day " "	moderate	increase
η_{BOTH}	Both Night & Day Subtrain Efficiency	strong	increase
η_{AUX}	Auxiliary Subtrain Efficiency	moderate	increase

TABLE 5. HAPP VARIABLES AND THEIR EFFECTS

	Gross Mass (GM)	Wing Area (S_{REF})	Aspect Ratio	$\frac{GM}{S_{REF}}$	$\frac{PWR}{GM}$	C_L	L/D	COLL. AREA
Mission								
Speed	*	*	●	*	*	*	●	*
Payload Power Required	*	●					*	*
Payload Weight Required	*	●						*
Auxiliary Power	*	●					*	*
Endurance	*	●						*
Range								
Heading Flexibility	*	●						*
Environmental								
Altitude	●	●	*	*	*	●	●	*
Latitude	*	●						*
Time of Year	*	●						*
Winds Aloft	*	●		*	*	●	●	*
Power Train								
Type	*	●						*
Component Efficiencies	*	*						*
Component Mass/Power Ratios	*	●						*
Collector Position	*	*		●	●	●	●	*
Shaft Power Required	*	*						*
Vehicle								
Internal Volume								
Surface Area	*	*				●		*
Structural Concept	*		*				●	
Wing Area	*		●	●	●	*	*	●
Aspect Ratio	*	●		●	●		*	
Sweep	*		*				●	
Aerodynamics								
Lift	*	*				*	*	*
Drag	●	*	*				*	*
Pitching Moment Coefficient	●						●	

* Direct effect
● Indirect effect

Scope

The research effort described in this report is limited to an analytical study of the interactions of power train and aerodynamic variables affecting the parametric design of solar HAPP vehicles. The analysis was supported by the design of conceptual solar HAPP RPV's to provide representative dimensional and mass parameters.

The fundamental strategy of this investigation was to:

(1) Describe analytically the solar power train, its components, and their interactions;

(2) Describe analytically the pertinent aerodynamic parameters affecting solar vehicle design;

(3) Relate the two to analyze parametrically one or more candidate configurations;

(4) Draw conclusions and make recommendations about the technological levels required to make solar HAPP RPV's feasible.

SYMBOLS

Aerodynamic

A	cross-sectional area, meters^2 (feet^2)
AR	aspect ratio
b	wingspan, meters (feet)
C	coefficient
c	chord, meters (feet)
D	diameter, meters (feet)
D	vehicle drag force, newtons (pounds)
d	average or circular body diameter, meters (feet)
e	Oswald (airplane) efficiency factor
g	gravitational acceleration, meters/second^2 (feet/second^2)
h	endplate height, meters (feet) also altitude, meters (feet)
I	moment of inertia, kilogram - meters^2 (slug - feet^2)
i	counter for wing panels
j	counter for body panels
L	aircraft lift force, newtons (pounds); also thickness location parameter
l	moment arm, meters (feet)
l_B	body length, meters (feet)
M	Mach number
N	number
P	power, kilowatts (P)
q	dynamic pressure, newtons/meter^2 (pounds/feet^2)
R	lifting surface correction factor
R_N	Reynolds number
S	area, meters^2 (feet^2)
T	thrust, newtons (pounds)
t	thickness
u	induced drag factor
V	true airspeed, meters/second (feet/second)
W	total weight, newtons (pounds)
x, y, z	body fixed coordinate axes, meters (feet)

Λ	sweep angle, degrees
α	angle of attack, degrees
β	angle of sideslip, degrees
γ	flight path angle, degrees
δ	control deflection angle, degrees
λ	taper ratio
μ	dynamic viscosity coefficient, newton-seconds/meter^2 (pound-seconds/feet^2)
ρ	air density, kilograms/meter^3 (slugs/feet^3)

Subscripts:

AV	available
B	body
BASE	body base
BLADE	blade
BOOM	boom
CR	critical
C/4	quarter chord
D	drag
d_f	form drag
DIV	divergence
EQ	equivalent
EXP	exposed
FUS	fuselage
H	horizontal
I	induced
MAX	maximum
MIN	minimum
NAC	nacelles
L	lift
l	section lift
PROP	propeller
M	mach, also wing pitching moment
m	section pitching moment
REF	reference
REQ	required
ROOT	root
T	total
TIP	tip
V	vertical
W	wing
WET	wetted, usually surface area

A	elevation angle of the sun, radians, positive above local horizontal.
A_H	elevation angle of effective horizon, radians
C_a	atmospheric attenuation factor
C_e	thermal power per unit area radiated into space at the effective radiating radius of 10 km (32 800 ft) altitude
C_r	albedo coefficient
D	declination angle, degrees
d	days following the vernal equinox
$d\Delta$	dummy surface element used in determining F_e
I	extraterrestrial solar flux density, watts/meter^2 (horsepower/feet^2)
I_a	albedo radiation received by surface, watts/meter^2 (horsepower/feet^2)
I_c	total energy received (1352.8 watts per square meter) on a unit area perpendicular to the sun's rays at the mean earth-sun distance (ref. 3). The solar constant.
I_D	direct radiation received by a solar array, watts/meter^2 (horsepower/feet^2)
I_p	planet radiation received by surface, watts/meter^2 horsepower/feet^2)
$f(\lambda)$	solar cell response as a function of wavelength
F_e	geometrical view factor of the earth as seen from a HAPP used to compute planet reradiation received.
F_r	geometrical albedo view factor
F_R	relative cell response
h	altitude, meters (feet)
h_c	cloud layer altitude, meters (feet)
H	geopotential altitude, meters (feet); also hour angle, degrees
$I\ (h,A,\lambda)$	direct intensity as a function of altitude, elevation angle and wavelength
I_{AMO}	AMO direct solar intensity
L	latitude, degrees
n	number of days following 31 December
$\hat{n}$	unit vector normal to vehicle surface
$\hat{N}_1$	unit vector normal to surface $d\Delta$ at terminus of R
r	earth-sun distance, kilometers (miles)
r_a	earth's aphelion distance, kilometers (miles)

r_m	mean earth-sun distance, kilometers (miles)
r_p	earth's perihelion distance, kilometers (miles)
$\hat{r}$	vector from receiving panel to earth's surface
R	mean earth radius, meters (feet)
t	time from solar noon, hours
T	ambient absolute temperature, °K (°F)
Z	azimuth angle of the sun, radians, positive to the east with due south being 0
α	angle between ϕ and normal to surface at Q
α_E	angle between ρ and normal to surface at P
β	surface pitching angle, radians
γ	surface yawing angle, radians
δ	air pressure ratio
ϵ	earth's orbital eccentricity
η_ϕ	AMO solar efficiency
$\eta_{h,A}$	cell efficiency as a function of altitude and elevation angle
θ	air temperature ratio; also day angle
λ	wavelength, microns
λ_{ref}	wavelength for maximum cell response, microns
ρ	distance from point P to HAPP surface panel, meters (feet)
σ	air density ratio, also angle between earth-HAPP and earth-sun axis, radians
σ_E	angle between earth-sun axis and normal to Point P
ϕ	defining angle for point P
ψ	angle between array surface normal and sun vector, radians

POWER TRAIN

E	quantity of energy
F	tank safety factor
f	ratio of mass of tanks or containment vessel(s) to mass of storage media
G	Gibbs free energy
I	instantaneous solar flux
i	current density
M	total component mass or system mass
m	residual or tare mass
$\dot{m}$	mass flow rate (Kg/sec)
$\hat{m}_i$	molecular weight of substance i
p	pressure
P'_c	power per unit area of electrode in fuel cell and electrolyzer
P_{X_r}	instantaneous power out of component x_r
Q_{X_r}	instantaneous heat flux
$\dot{q}'$	heat transfer per unit time per unit area
R	gas constant
S_{COLL}	collector area
T	absolute temperature (° Kelvin)
t_{DAY}	length of time insolation is available for energy collection (day)
t_{NIGHT}	length of time insolation is not available for energy collection (night)
α	ratio of night time thrust power to day time thrust power $\left(\frac{P_{T_{NIGHT}}}{P_{T_{DAY}}}\right)$
α_S	solar absorptance
β_{DAY}	ratio of day time auxiliary and payload power to day time thrust power $\left(\frac{P_{AUX_{DAY}}}{P_{T_{DAY}}}\right)$
β_{NIGHT}	ratio of night time auxiliary and payload power to day time thrust power $\left(\frac{P_{AUX_{NIGHT}}}{P_{T_{DAY}}}\right)$
β_T	thermal coefficient of photo cell efficiency
δ	thickness

μ	mass-to-power ratio
η	efficiency
ϵ	ratio of energy storage media mass to energy content
ϵ_{IR}	infrared emittance
ρ	mass per unit volume
ρ'	mass per unit area
σ	tensile strength
τ	$\frac{t_{NIGHT}}{t_{DAY}}$
V	voltage or volume depending on context

Subscripts

X_r - Subscript to denote a particular value of a quantity or parameter. In general it refers to the rth component in subtrain X. It can also be assigned the other alpha designations listed below and has the indicated meaning.

ALPHA DESIGNATION FOR X_r	MEANING
A	albedo
AUX_{DAY}	as a subscript to P designates day time auxiliary and payload power
AUX_{NIGHT}	as a subscript to P designates night time auxiliary and payload power
BOTH	refers to subtrain used in both day and night as a whole
B_{DAY}	average value for subtrain B during the day
B_m	mth component of subtrain used in both day and night power trains
B_{NIGHT}	average value for subtrain B at night
CELL	refers to a single cell of either electrolyzer or fuel cell
COLL	refers to collection subtrain as a whole
$COLL_i$	ith component of collection subtrain
CONC	radiation concentrator
COND	electric power conditioner
DAY	refers to day time only subtrain as a whole
DAY_l	ℓth component of non-storage, non-collection day time only subtrain

ALPHA DESIGNATION FOR X_r	MEANING
DIST	electric power distribution
ECS	energy collection and storage subtrains
EFF	effective
ELEC	electrolyzer
END	endplates
EV	evaporator
FC	fuel cell
GEAR	rpm reduction gear
GEN	electric generator
HE	heat engine
HXR	heat exchanger
IR	infrared
MOTOR	electric motor
MPD	mechanical power distribution
NIGHT	refers to night time subtrain as a whole
$NIGHT_k$	kth component of night time only subtrain
o	ordinate intercept or constant value
PAY	payload
PER	periphery
PROD	products
PROP	with η or μ refers to propeller P; with δ, ρ refers to peripheral enclosure
PT	value of quantity for overall power train
PV	photovoltaic array
RAD	radiator
REACT	reactants
ST	refers to storage subtrain as a whole
ST_j	jth component of storage subtrain
T_{DAY}	as a subscript to P designates day time thrust power
T_{NIGHT}	as a subscript to P designates night time thrust power
TANK	tank
THRUST	thrust power or energy
Ø	zero
∞	free stream value

SUPERSCRIPT	MEANING
$\bar{\eta}$	average value of quantity in this case efficiency
$\hat{\eta}$	the value of quantity, in this case efficiency, at maximum or peak power
E'_{SUN}	value of quantity, in this case energy, per unit area or based upon area

Operators

$\prod_{r=1}^{R} \eta_{\chi_r}$ - notation for the product of R factors, in this case each factor is an instantaneous efficiency

$\sum_{r=1}^{R} Q_{\chi_r}$ - notation for sum of R terms, in this case each term is a heat flux

$\frac{dE}{dt}$ - notation for instantaneous rate of change of a quantity, in this case energy

ΔE - notation for the total change of a quantity, in this case energy

$\int_{t_{NIGHT}} Pdt$ - notation for the value of P integrated over time, t_{NIGHT}

POWER SUBSYSTEM SIZING METHODOLOGY

Overview

As presented in this study, the overall sizing of solar powered aircraft consists of the integration of sizing methodologies for:

- the aircraft power subsystem comprised of all components required to generate and deliver power for propulsion, flight control, auxiliaries and payload (A/PL); and
- the airframe subsystem comprised of structure, flight controls and fixed equipment for guidance, control and housekeeping functions.

For analysis purposes the terms "power train" and "power train configuration" are used to refer to the collection of components required in the power subsystem and the interrelationship of each component to others within the power subsystem, respectively.

The power subsystem sizing methodology used in this study of solar powered aircraft was developed to analyze and compare various solar power train configuration options. The analysis determines the collector area required, the mass and energy content of the required energy storage medium, and the mass and peak power out of each component in the configuration. This analysis can be performed over a broad range of thrust, auxiliary and payload power requirements and operating conditions (altitude, true airspeed, latitude and day of the year)[1]. The methodology involves essentially two major parts: (1) characterization of radiation and thermal environments and (2) characterization of the power train components and their relationship with the environment and with each other. In general terms, the radiation environment is expressed as the radiation from (1) direct solar radiation, (2) earth albedo and (3) terrestrial long wave radiation (LWR). In-situ levels of these radiation sources are determined as a function of the time of day, time of year, operating altitude and operating latitude. The thermal and aerodynamic environment is characterized by the standard atmosphere. Details of the modeling of these environments are provided in subsequent paragraphs.

The power train configuration is expressed in terms of:

- efficiency and mass-to-peak power ratio or mass-to-energy content for each component in the power train;
- collector orientation; and
- the relationship of the components to one another.

The characteristics of each component type considered in this study as well as the effects of collector orientation on power train size are discussed in subsequent paragraphs.

[1]In this context, auxiliaries refer to non-power train auxiliaries. Power train auxiliaries are accounted for in component efficiencies and mass-to-peak power ratios.

The general relationship of one component to another can be represented as a power train schematic having the general form of Figure 5. The general power train schematic of Figure 5 is drawn to highlight the qualitative similarities and differences of solar power trains. Whether solar radiation is used via thermal absorption, thermoelectric or photovoltaic energy conversion processes all solar power concepts require one or more components for solar energy collection (subtrain COLL). Furthermore, all long-endurance (greater than 8 to 16 hours) solar powered aircraft require a power system containing components devoted to energy storage (subtrain ST) for nighttime operation. Another common feature of power subsystems for solar powered aircraft is the need to distribute the energy collected and stored to propulsion, auxiliaries and payload.

High altitude operation using power levels commensurate with available solar energy requires flight at low true airspeeds. Therefore, to produce the required thrust at high efficiency, it is necessary that all solar aircraft employ a large, low-speed propeller for thrust power generation. This in turn leads to the need to produce shaft power matched to the propeller by the appropriate mechanical gearing. At a minimum, this set of components is common to both daytime and nighttime power subsystems (subtrain BOTH). The need for components used only for daytime and/or only for nighttime operation (subtrains DAY and NIGHT, respectively) is highly dependent upon power train configuration. Therefore, significant differences between power train configurations can be detected not only by the number of components in each of the required subtrains but also by comparing the need for and size of the nighttime (NIGHT) and daytime (DAY) only subtrains. An ideal configuration would contain no components that could be grouped into subtrains NIGHT and DAY.

Power train configurations can be quantitatively evaluated and compared with other configurations through the use of aggregate efficiencies (η_x) and aggregate mass-to-peak power ratios (μ_x) associated with each of the major subtrains (x = COLL, ST, NIGHT, DAY, or BOTH) depicted in Figure 5. The aggregate instantaneous efficiencies (η_x; x = COLL, ST, NIGHT, DAY, or BOTH) can be expressed in terms of the instantaneous efficiencies (η_{xr}; r = 1 to R) of each of the components (1,2,...R) in the specified (COLL, ST, NIGHT, DAY, or BOTH) subtrain as:

$$\eta_x = \prod_{r=1}^{R} \eta_{x_r} \qquad (1)$$

where R is the total number of components in the specified subtrain and $\prod$ denotes a product of all the efficiencies in the subtrain. Using similar notation, aggregate mass-to-peak power-out ratios (μ_x; x = COLL, ST, NIGHT, DAY or BOTH) can be expressed in terms of the peak power efficiencies ($\hat{\eta}_{x_r}$; r = 1 to R) and the mass-to-peak power ratios (μ_{x_r}; r = 1 to R) of of the components in the specified subtrain. This gives:

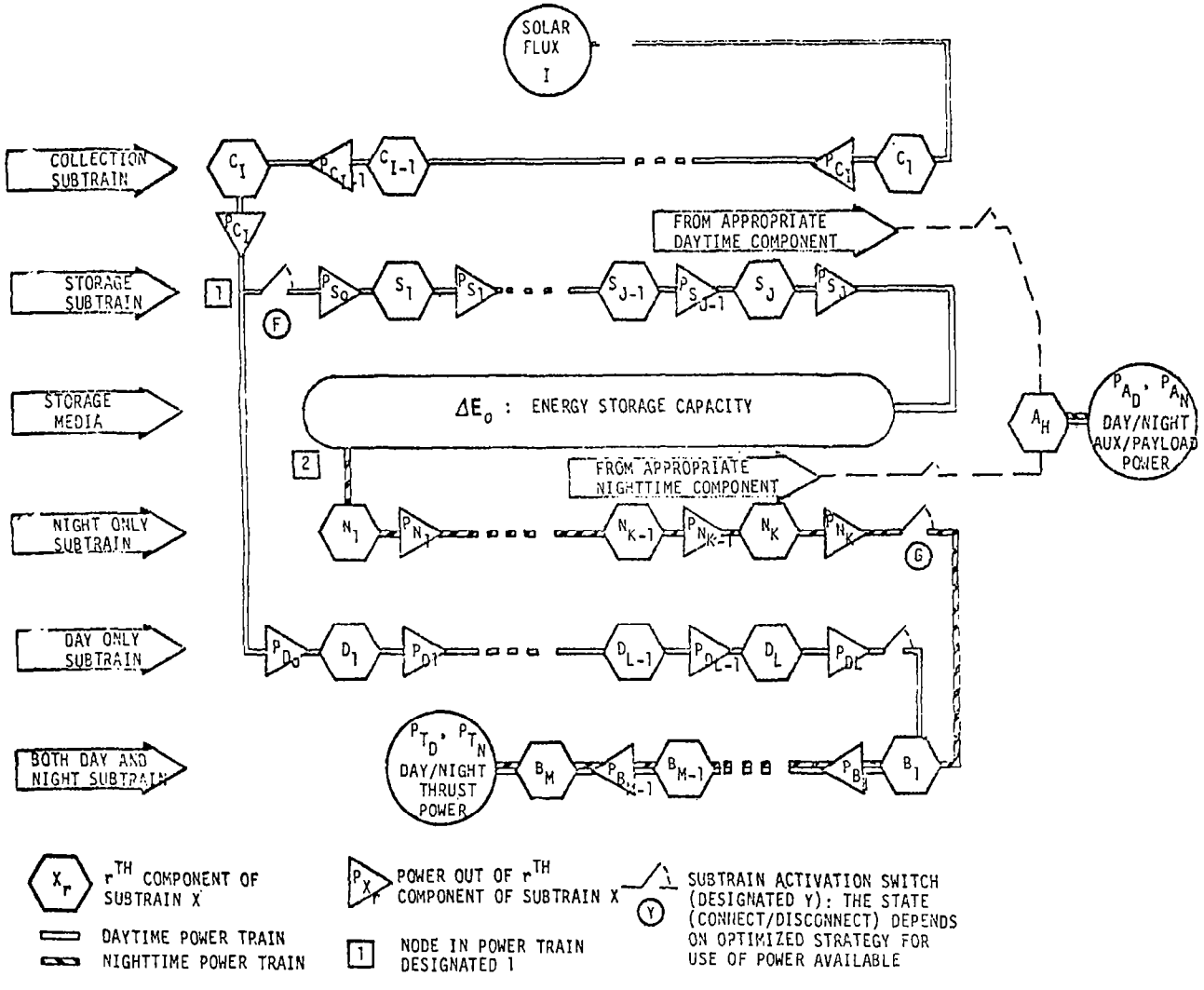

FIGURE 5 GENERALIZED SOLAR POWER TRAIN SCHEMATIC

$$\mu_x = \frac{M_x}{P_{x_R}} = \frac{\mu_{x_1} P_{x_1}}{P_{x_R}} + \frac{\mu_{x_2} P_{x_2}}{P_{x_R}} + \ldots + \mu_{x_R} \tag{2}$$

$$\mu_x = \frac{1}{\hat{\eta}_x} \sum_{r=1}^{R} \left(\pi_{q=1}^{r} \hat{\eta}_{x_q} \right) \mu_{x_r} \tag{3}$$

The primary objective of any solar power train sizing methodology is to determine the collector area required to meet a specified set of operating conditions and power requirements. The collector area can be determined from:

- the instantaneous solar flux (including albedo and any geometrical factors)
- the daytime thrust, payload and auxiliary power requirements
- the nighttime power requirements
- the instantaneous efficiencies of the power train components;
- the length of the day and night; and
- the principle of conservation of energy.

This method can be represented analytically by (1) using the aggregate efficiencies to express the power through selected nodes in the power train; (2) integrating those expressions over the time of day and night; and (3) equating the energy required at night to the energy put into storage during the day. If the $P_{T_{DAY}}$ and $P_{T_{NIGHT}}$ are the thrust power required for day and night, respectively; $P_{AUX_{DAY}}$ and $P_{AUX_{NIGHT}}$ are the A/PL power required for day and night, respectively; η_A is the aggregate efficiency of the components through which A/PL power must flow; and the power into the selected nodes is equated to the power out of the nodes, the following equations result:

$$\eta_{COLL} IS_{COLL} = \frac{1}{\eta_{ST}} + \frac{P_{T_{DAY}}}{\eta_{BOTH}\eta_{DAY}} + \frac{P_{AUX_{DAY}}}{\eta_{AUX}} \quad \text{(DAYTIME NODE 1)} \tag{4}$$

where $P_{C_I} = \eta_{COLL} IS_{COLL}$ and the power into storage, $P_{ST} = \frac{dE}{dt}$; and

$$-\frac{dE}{dt} = \frac{P_{T_{NIGHT}}}{\eta_{NIGHT}\eta_{BOTH}} + \frac{P_{AUX_{NIGHT}}}{\eta_{AUX}} \quad \text{(NIGHT TIME NODE 2)} \tag{5}$$

Rearranging and integrating over t_{DAY} and t_{NIGHT}, the energy into storage from node 1 is:

$$\Delta E_1 = \int_{t_{DAY}} dE = S_{COLL} \int_{t_{DAY}} \eta_{ST}\eta_{COLL} I \, dt - \int_{t_{DAY}} \frac{\eta_{ST} P_{T_{DAY}}}{\eta_{BOTH}\eta_{DAY}} \, dt - \int_{t_{DAY}} \frac{\eta_{ST} P_{AUX_{DAY}}}{\eta_{AUX}} \, dt \tag{6}$$

From node 2 the energy out of storage is:

$$\Delta E_2 = \int_{t_{NIGHT}} \frac{P_{T_{NIGHT}}}{\eta_{NIGHT}\eta_{BOTH}} \, dt + \int_{t_{NIGHT}} \frac{P_{AUX_{NIGHT}}}{\eta_{AUX}} \, dt \tag{7}$$

Equating the energy into storage, ΔE_1, and the energy out of storage, ΔE_2 ($\Delta E_2 = \Delta E_1 = \Delta E_0$), and rearranging, the collector area required for thrust, payload and auxiliaries can be expressed as:

$$S_{COLL} = \frac{\int_{t_{DAY}} \frac{\eta_{ST}}{\eta_{BOTH}\eta_{DAY}} P_{T_{DAY}} \, dt + \int_{t_{NIGHT}} \frac{P_{T_{NIGHT}}}{\eta_{NIGHT}\eta_{BOTH}} dt + \int_{t_{DAY}} \frac{\eta_{ST} P_{AUX_{DAY}}}{\eta_{AUX}} \, dt + \int_{t_{DAY}} \frac{P_{AUX_{NIGHT}}}{\eta_{AUX}} \, dt}{\int_{t_{DAY}} \eta_{ST}\eta_{COLL} I \, dt} \tag{8}$$

The computer method used in sizing the collector area involves performing a step-wise integration of this relationship such that efficiencies, solar flux and power equirements can all be any specified function of the time of the day and night. In the case where constant efficiencies and power requirements can be assumed, the above expression simplifies to:

$$S_{COLL} = \frac{\frac{P_{T_{DAY}} t_{DAY}}{\eta_{BOTH_{DAY}}\eta_{DAY}} + \frac{P_{T_{NIGHT}} t_{NIGHT}}{\eta_{NIGHT}\eta_{BOTH_{NIGHT}}\eta_{ST}} + \frac{P_{AUX_{DAY}} t_{DAY}}{\eta_{AUX_{DAY}}} + \frac{P_{AUX_{NIGHT}} t_{NIGHT}}{\eta_{AUX_{NIGHT}}\eta_{ST}}}{\eta_{COLL} \Delta E'_{SUN}} \tag{9}$$

where $\Delta E'_{SUN} = \int_{t_{DAY}} I\, dt$ and the subscripts on the efficiencies have been expanded to recognize that certain values (η_{BOTH} and η_{AUX}) may be different for nighttime and daytime operating conditions. This can also be expressed as:

$$S_{COLL} = \frac{P_{T_{DAY}} t_{DAY}}{\eta_{COLL}\eta_{BOTH_{DAY}} \Delta E'_{SUN}} \left\{ 1 + \beta_{DAY} \left(\frac{\eta_{BOTH_{DAY}} \eta_{DAY}}{\eta_{AUX_{DAY}}} \right) + \frac{\tau}{\eta_{ST}} \left[\alpha \left(\frac{\eta_{BOTH_{DAY}} \eta_{DAY}}{\eta_{BOTH_{NIGHT}} \eta_{NIGHT}} \right) + \beta_{NIGHT} \left(\frac{\eta_{BOTH_{DAY}} \eta_{DAY}}{\eta_{AUX_{NIGHT}}} \right) \right] \right\} \quad (10)$$

where: $\tau = \frac{t_{NIGHT}}{t_{day}}$, $\beta_{DAY} = \frac{P_{AUX_{DAY}}}{P_{T_{DAY}}}$, $\alpha = \frac{P_{T_{NIGHT}}}{P_{T_{DAY}}}$ and $\beta_{NIGHT} = \frac{P_{AUX_{NIGHT}}}{P_{T_{DAY}}}$

This form of the equation can be instructive in discussing the relative impact on collector size of various factors such as component efficiencies, day/night ratios, relative sizes of daytime and nighttime power requirements and variations of insolation with latitude, time of year and collector orientation.

As with any power train sizing methodology it is also necessary to estimate the mass of each component within the power train as well as the overall power train mass. This is accomplished using input values for (1) mass-to-peak power ratios, μ_{X_p}; (2) mass-to-energy-stored ratio, ϵ; (3) mass fraction of containment vessel for energy storage medium together with values of (1) peak power demand for each power train component, $\hat{P}_{X_p}$; (2) the collector area size, S_{COLL}; and (3) the energy storage requirement, ΔE_0, that were obtained in determining the collector area requirement. If (1) it is assumed that thrust and A/PL power requirements are constant during the day and night (but not necessarily equal); (2) an expanded notation for the aggregate mass-to-peak power ratio is adopted such that $\mu_{AUX_{DAY}}$ is the aggregate ratio for the components through which all power must flow in the daytime and $\mu_{AUX_{NIGHT}}$ is the aggregate mass-to-peak power ratio of nighttime-only components through which all power must flow; and (3) the A/PL power out of the nighttime-only subtrain is $P_{AUX_{NIGHT}}/\eta_o$, an expression for the power train mass, μ_{PT}, can be obtained as follows:

$$M_{PT} = \mu_{COLL}\hat{\eta}_{COLL}\hat{I}\,S_{COLL} + \mu_{ST}\hat{\eta}_{ST}\left(\hat{\eta}_{COLL}\hat{I}\,S_{COLL} - \frac{P_{T_{DAY}}}{\eta_{BOTH_{DAY}}\eta_{DAY}} - \frac{P_{AUX_{DAY}}}{\eta_{AUX_{DAY}}}\right)$$

$$+ \frac{\mu_{DAY}P_{T_{DAY}}}{\eta_{BOTH_{DAY}}} + \mu_{BOTH}P_{T_{DAY}} + \frac{\mu_{NIGHT}P_{T_{NIGHT}}}{\eta_{BOTH_{NIGHT}}} + \mu_{AUX_{DAY}}P_{AUX_{DAY}} + \mu_{AUX_{NIGHT}}\frac{P_{AUX_{NIGHT}}}{\eta_o}$$

$$+ (1+f)\,\epsilon\left(\frac{P_{T_{NIGHT}}t_{NIGHT}}{\eta_{NIGHT}\eta_{BOTH_{NIGHT}}} + \frac{P_{AUX_{NIGHT}}t_{NIGHT}}{\eta_{AUX_{NIGHT}}}\right) \qquad (11)$$

Grouping into coefficients of the various powers this can also be expressed as:

$$M_{PT} = \left(\mu_{COLL} + \mu_{ST}\hat{\eta}_{ST}\right)\hat{\eta}_{COLL}\,\hat{I}\,S_{COLL} + \left[\mu_{BOTH} + \frac{\mu_{DAY}}{\eta_{BOTH_{DAY}}} - \mu_{ST}\left(\eta\frac{\hat{\eta}_{ST}}{\eta_{BOTH_{DAY}}\eta_{DAY}}\right)\right]P_{T_{DAY}}$$

$$+ \left(\mu_{AUX_{DAY}} - \mu_{ST}\frac{\hat{\eta}_{ST}}{\eta_{AUX_{DAY}}}\right)P_{AUX_{DAY}} + \left(\frac{\mu_{NIGHT}}{\eta_{BOTH_{NIGHT}}} + \frac{(1+f)\,\epsilon\,t_{NIGHT}}{\eta_{NIGHT}\eta_{BOTH_{NIGHT}}}\right)P_{T_{NIGHT}}$$

$$+ \left(\frac{\mu_{AUX_{NIGHT}}}{\eta_o} + \frac{(1+f)\,\epsilon\,t_{NIGHT}}{\eta_{AUX_{NIGHT}}}\right)P_{AUX_{NIGHT}} \qquad (12)$$

Using the ratios, β_{NIGHT}, β_{day}, α and τ and equation (10) for S_{COLL} the power train mass-to-daytime-power ratio can be expressed as:

$$\frac{M_{PT}}{P_{T_{DAY}}} = \frac{t_{DAY}}{E'_{SUN}} \hat{I} \left[\frac{(\mu_{COLL} + \mu_{ST}\hat{\eta}_{ST})\eta_{COLL}}{COLL} \right] \left[\frac{1}{\eta_{BOTH_{NIGHT}}\eta_{DAY}} + \beta_{DAY} \left(\frac{1}{\eta_{AUX_{DAY}}} \right) \right]$$

$$+ \; t_{DAY} \tau \left[\alpha \left(\frac{1}{\eta_{BOTH_{NIGHT}}\eta_{NIGHT}} \right) + \beta_{NIGHT} \left(\frac{1}{\eta_{AUX_{NIGHT}}} \right) \right]$$

$$\left\{ \frac{I}{E'_{SUN}} \left[\frac{(\mu_{COLL} + \mu_{ST}\hat{\eta}_{ST})\hat{\eta}_{COLL}}{COLL\ ST} \right] + (1+f)\epsilon \right\} + \mu_{BOTH} + \frac{\mu_{DAY}}{\eta_{BOTH_{DAY}}}$$

$$+ \mu_{ST} \left(\frac{\hat{\eta}_{ST}}{\eta_{BOTH_{DAY}}\eta_{DAY}} \right) + \beta_{DAY} \left(\mu_{AUX_{DAY}} + \frac{\mu_{ST}\hat{\eta}_{ST}}{\eta_{AUX_{DAY}}} \right)$$

$$+ \left(\frac{\mu_{NIGHT}}{\eta_{BOTH_{NIGHT}}} \right) + \beta_{NIGHT} \left(\frac{\mu_{AUX_{NIGHT}}}{\eta_o} \right) \qquad (13)$$

These analytical expressions will help to interpret some power train sizing results and will be referred to in subsequent paragraphs. They will be particularly instructive in interpreting the effects of changes in component characteristics, seasonal variations of solar energy available and length of day.

Atmospheric Environment

The natural environment strongly influences the design of HAPP vehicles. Almost all surface weather elements can, at times, adversely affect the launch and recovery of RPV's. Climb-out and return-to-base let-down conditions such as strong turbulence (both clear-air and in-cloud turbulence), icing, strong shears, and the like can adversely affect missions. The ability to forecase these parameters allows for launch/recovery operations to be scheduled for periods of calm weather. For the bulk of most missions (i.e., loiter at altitudes of 16 km (52 480 ft, 90 mb) to 21 km (68 880 ft, 40 mb)) the principal controlling factor is winds aloft.[1] At these altitudes most other environmental factors can be ignored (assuming latitudes and seasons which allow for proper solar flux for solar cell operation).

Standard Atmosphere Model. In order to compute solar cell efficiency, the cell surface temperature must be known. The cell temperature is a function of air density and ambient temperature. Also, the total power required for a HAPP vehicle's thrust is a function of air density. To compute these quantities, a standard atmosphere model is necessary.

A simple and accurate methodology has been developed which, given altitude, will compute the ratios of air pressure, density, and temperature to their sea level values. The 1976 U.S. Standard Atmosphere (Ref. 2) equations have been incorporated into this methodology giving very accurate predictions of standard atmospheric quantities for altitudes up to and including 47 kilometers (154 160 ft).

Practically any air vehicle design computer code needs a standard atmosphere model. Every new code found in the literature invariably has its own unique method. The following set of equations are used in this study and have proven to be efficient, accurate and easy to incorporate into any computer code. The following equations are based on a geopotential altitude given by

$$H = \frac{Rh}{(R + h)} \quad , m \tag{14}$$

If the desired altitude is less than or equal to 11 000 m (36 080 ft), then the temperature lapse rate is given by

$$T = 288.15 - .0065\ H \quad , °K \tag{15}$$

and the density ratio,

$$\sigma = \left(\frac{288.15}{T}\right)^{-4.255876} \tag{16}$$

[1]Meteorological data in this section are frequently presented in millibars. Standard day sea-level pressure is 1012.6 mb.

If altitude is greater than 11 000 m (36 080 ft) but less than 20 000 m (65 600 ft), then

$$T = 216.65 \text{ , } ^\circ K \tag{17}$$

and

$$\sigma = 0.2970776 \, e^{(-(H-11000)/6341.62)} \tag{18}$$

If altitude is greater than 20 000 m (65 600 ft) but less than 32 000 m (104 960 ft), then

$$T = 216.65 + (H - 20000)/1000, ^\circ K \tag{19}$$

and

$$\sigma = 0.07186531 \left(\frac{216.69}{T}\right)^{35.16319} \tag{20}$$

If altitude is greater than 32 000 m (104 960 ft) but less than 47 000 m (154 160 ft), then

$$T = 228.65 + 2.8 (H - 32000)/1000, ^\circ K \tag{21}$$

and

$$\sigma = 0.01079592 \left(\frac{228.65}{T}\right)^{13.20114} \tag{22}$$

The temperature ratio is given by

$$\theta = \frac{T}{288.15} \tag{23}$$

and the pressure ratio by

$$\delta = \sigma \theta . \tag{24}$$

Meteorological Limits for HAPP Flight. As presented in Figure 2, winds aloft decrease at higher altitudes and reach a minimum somewhere in the vicinity of the cruise altitude. This condition will vary from day to day, but appears to be constant enough that flight can continue at constant altitude if desired for long periods of time. Table 6 presents statistical data supporting this conclusion.

The existence of clouds at an operating altitude of 20 km (65 600 ft) over California is unlikely, the highest clouds occuring at this latitude being cumulonimbus and varieties of cirrus. These clouds will reach a height of 15 km (49 200 ft). As California is in a marine environment rather than the continental environment of the mid-west, cloud heights will be lower than these upper limits. Therefore, HAPP flights could safely fall as low as 15 km (49 200 ft) without cloud shading problems. Appendix A presents additional information on winds aloft.

TABLE 6. WIND SPEEDS GREATER THAN THE DESIGN CONDITION

	Northern California				
	150 mb	100 mb	70 mb	50 mb	30 mb
January					
% > 27 mps	61.3	30.6	0.01	0.0	0.0
% > 22 mps	82.3	55.9	0.08	0.04	0.05
July					
% > 27 mps	24.2	0.0	0.0	0.0	0.0
% > 22 mps	38.7	0.0	0.0	0.0	0.0

	Southern California				
	150 mb	100 mb	70 mb	50 mb	30 mb
January					
% > 27 mps	66.7	43.5	0.03	0.02	0.04
% > 22 mps	73.1	64.5	0.14	0.06	0.06
July					
% > 27 mps	0.04	0.0	0.0	0.0	0.0
% > 22 mps	0.06	0.0	0.0	0.0	0.0

Icing can be expected to occur at air temperatures between -3C and -30C degrees with the upper limit due to frictional heating with the air; icing below -30C is rare. For a mid-latitude location this would put the upper altitude limit on icing at 6 km (19 680 ft) for a winter worst case situation. Icing at greater altitudes could occur in towering cumulus.

The most recent (1977) turbulence investigations at the chosen flight altitude of 20 km (65 600 ft) involved the use of relatively high speed aircraft in determining the occurrence, duration in flight distance, wavelength and magnitude of turbulence.[1] Over the California central valley region turbulence was found to be of short duration, on the order of 10 to 30 km (32 800 to 98 400 ft) distance of flight path and of an order of 0.1 to 0.55 g units with most occurrences around 0.2 g. The frequency of occurrence of turbulence above 18 km (59 040 ft) is on the order of 1.2 percent of time in flight for light turbulence (less than 0.35 g) with the expectance of moderate turbulence (greater than 0.35 g) 0.3 percent of the time. The lower limit of flight for increased turbulence is 17 km (55 760 ft), which is mostly associated with mountainous terrain; the frequency of occurrence decreases with increasing altitude. The period of greatest turbulence occurs in the winter months of December, January and February. For all investigations, the shortest wavelengths reported were 140 feet. Wavelengths shorter than those encountered will no doubt be of interest to HAPP flight (ref. 1).

[1] Figure 3 presented some of these data.

Solar Radiation Environment

Included in the analysis of solar aircraft power trains must be a characterization of the power source, solar radiation. The term solar radiation as used here refers not only to direct radiation, but also to diffuse, reflected and thermal radiation from earth (Figure 6). Radiation received by a HAPP is not constant, but varies with time of day, day of year, altitude, latitude, cloud level, and underlying terrain.

The problem areas that were addressed in developing this methodology were as follows:

- Variation in direct solar radiation intensity with day of year;
- Solar position in the sky including elevation and azimuth of the sun as functions of latitude, time and date;
- Sunrise and sunset at altitude which results in an effective horizon below local horizontal;
- Atmospheric attenuation which reduces direct solar intensity at low sun elevation angles and HAPP altitudes;
- Spectral content of direct, diffuse, reflected and thermal radiation;
- Surface albedo; and
- Long wavelength infrared radiation (LWIR) emitted by the earth.

Variation in Direct Solar Radiation Intensity. Total solar radiation output in the spectral range of 0.3 to 3 μ can vary ±1.5 percent (ref. 3). Solar cells normally are sensitive in the 0.3 to 1.5μ region; therefore, the total solar output has been assumed constant in this model. However, the intensity of solar radiation received by the earth varies significantly over the course of a year. This is due primarily to earth's elliptical orbit about the sun. On any day during the year earth-sun distance is given by

$$r = \frac{r_m(1 - \epsilon^2)}{(1 + \epsilon \cos\theta)} \tag{25}$$

where:

$$\epsilon = 1 - \frac{r_p}{a}$$

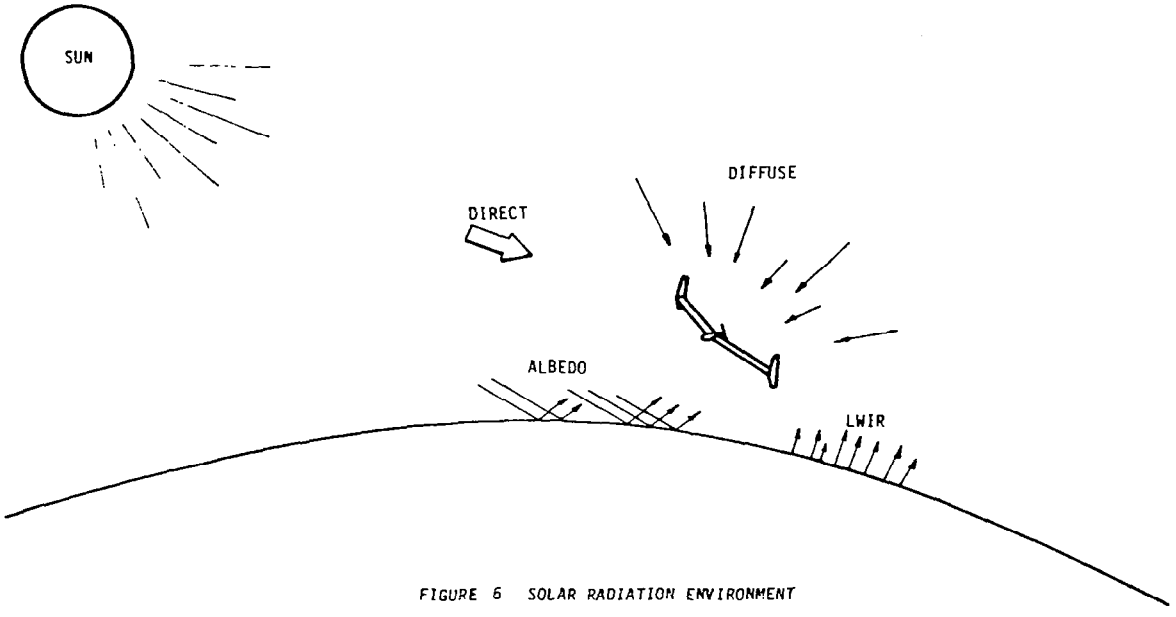

FIGURE 6 SOLAR RADIATION ENVIRONMENT

$$a = \tfrac{1}{2}(r_a + r_p)$$

and

$$\theta = \frac{2\pi(n - 4)}{365}$$

Direct intensity varies inversely with the square of the earth-sun distance, r, as follows:

$$I = \frac{I_c\, r_m^2}{r^2} \tag{26}$$

where I_c = total energy received (1352.8 watts per square meter) on a unit area perpendicular to the sun's rays at the mean earth-sun distance (ref 3).

Figure 7 shows the variation in the sun's direct intensity over a year.

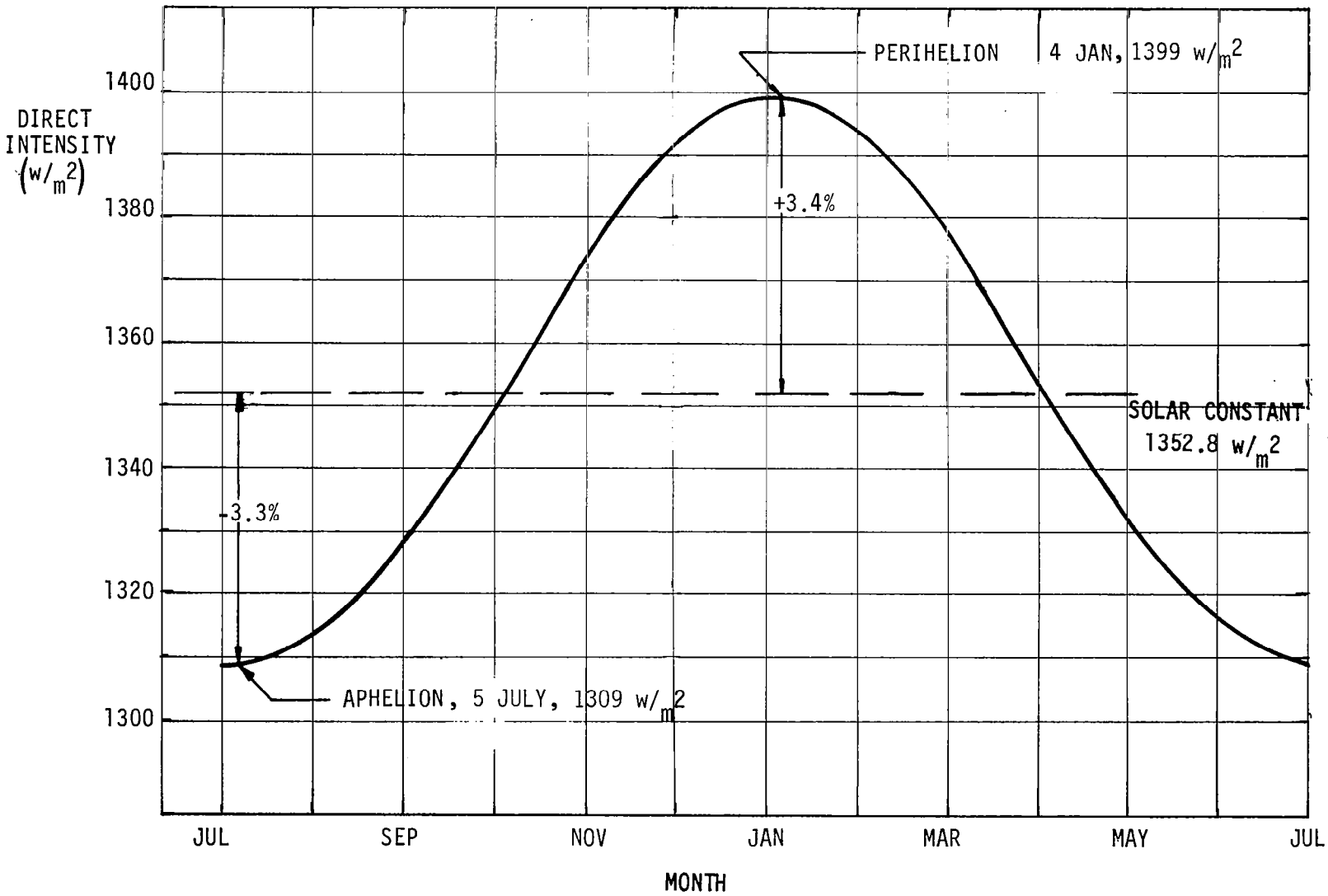

FIGURE 7 VARIATION IN SOLAR RADIATION DUE TO EARTH'S ELLIPTICAL ORBIT

Solar Position in the Sky. To account for the effects of atmospheric attenuation and collector orientation, it is necessary to know the position of the sun in the sky as a function of altitude, latitude, day of the year, and local solar time. The particular forms of the earth-sun geometry equations shown below have been drawn from reference 4.

The position of the sun in elevation and azimuth (Figure 8) can be determined by the following equations:

$$A = \arcsin \left(\cos D \cos H \cos L + \sin D \sin L\right) \tag{27}$$

$$Z = 2 \arctan \left(\frac{\text{Cos D sin H}}{\text{Cos L sin D - sin L cos D cos H - cos A}} \right) \tag{28}$$

where the declination angle, D, is given by,

$$D = 23.44 \sin \left(360 \frac{d}{365}\right), \text{ degrees} \tag{29}$$

The local solar time, t, may be expressed in terms of the quantity H, which represents 24 hours as 360 degrees of angle.

$$H = 15t, \text{ degrees} \tag{30}$$

The formulas as presented here are accurate to within half a degree based on observations.

In a view from above, the elevation and azimuth angles of the sun are plotted on a normal projection of a celestial hemisphere. The site in the center is located at 40° north latitude.

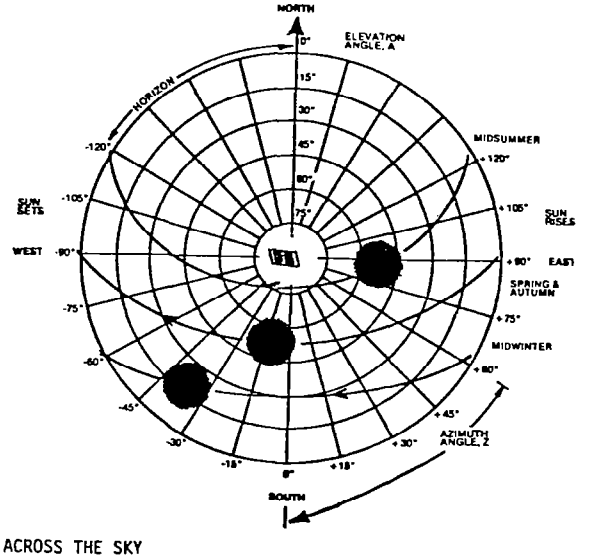

FIGURE 8. SEASONAL VARIATION OF SUN'S PATH ACROSS THE SKY

Source: (ref. 4)

Sunrise/Sunset at Altitude. The actual times of sunrise and sunset seen by a HAPP are earlier and later, respectively, than those predicted for a sea level observer, due to atmospheric refraction and to altitude.

Sunrise and sunset are defined by the appearance and disappearance of the upper limb (edge) of the sun as it crosses the horizon. In the present model the sun is represented as a point source. This assumption is adequate, since the total energy per unit area received over the interval of sunrise or sunset is equivalent for both the point source and the disk assumptions.

Refractive distortion has been neglected in this model since it adds only 6 to 7 minutes (about 1%) to total daylight time. However, effects of the altitude of the HAPP, including the possibility of a cloud layer at some intermediate altitude have been included. This effect amounts to lengthening total daylight time by roughly half an hour.[1]

Measured from the local horizontal, the elevation angle of the effective horizon is given by

$$A_H = \arcsin \frac{(R + h_c)}{(R + h)} - \pi/2 \tag{31}$$

Atmospheric Attenuation. The attenuation of solar radiation by the atmosphere is spectrally selective and varies in a complex manner with solar elevation angle and HAPP altitude. The direct-radiation intensity received by a solar array is given by,

$$I_D = C_a \, I \cos \psi \tag{32}$$

Results obtained from the LOWTRAN 4 (ref. 5) computer code were used as a basis for determining the attenuation coefficient, C_a, as a function of altitude and solar elevation angle. LOWTRAN 4, developed by the Air Force Geophysics lab, is designed to calculate atmospheric transmittance for a given atmospheric path at moderate spectral resolutions. The code contains an option to choose from six standard (geographical and seasonal) atmospheric models. Since the primary design condition is the winter solstice in California, the mid latitude, winter model atmosphere was chosen. The values shown in Figure 9 for the attenuation coefficient were obtained for the spectral region 0.25-4μ, which includes about 99% of total solar radiation. Figure 10 shows the effect on direct intensity due to changes in altitude for the 21st of December at 38°N.

[1] In winter at mid latitudes.

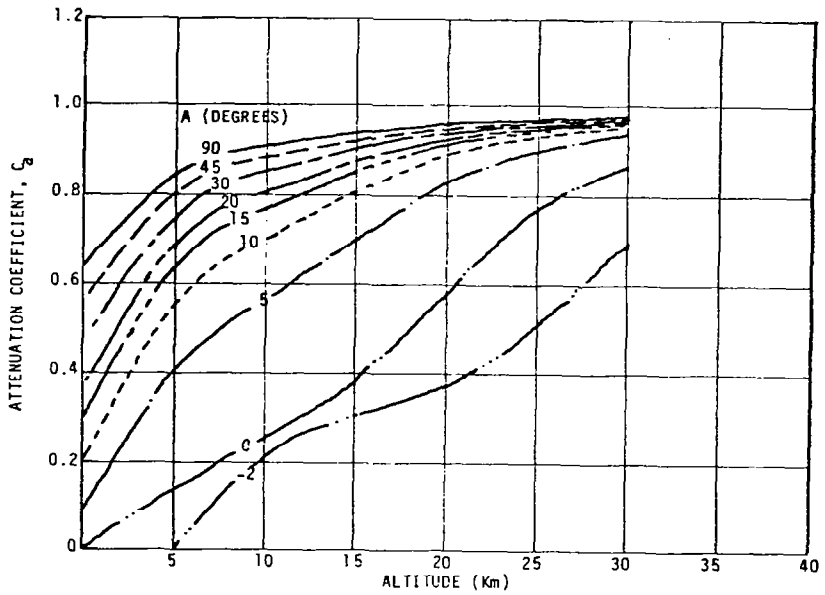

FIGURE 9 ATMOSPHERIC ATTENUATION COEFFICIENT (INTEGRATED AVERAGE 0.25 TO 4.0 μ)

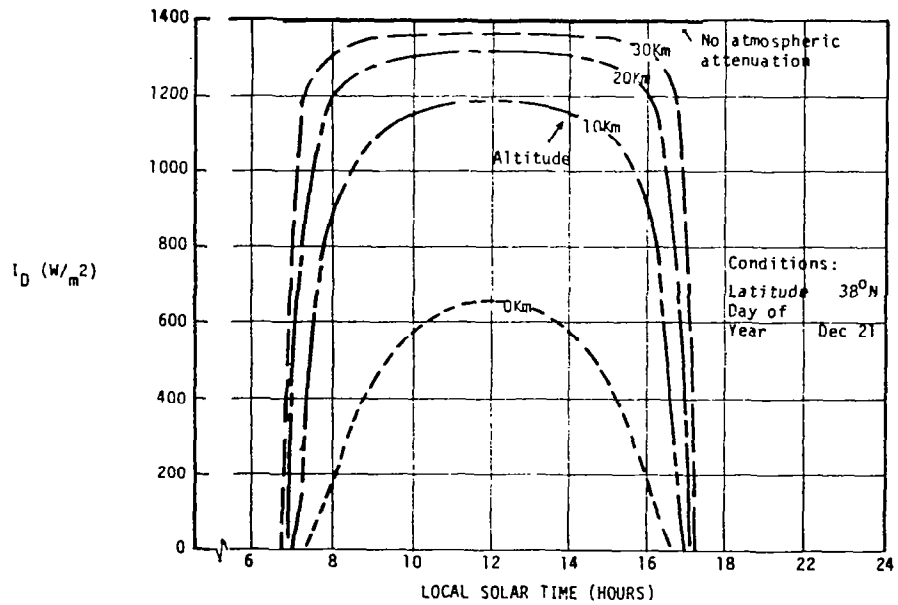

FIGURE 10 PREDICTED VARIATION OF DIRECT INTENSITY OF SOLAR FLUX WITH ALTITUDE

Spectral Characteristics. The spectral content of solar radiation received by a HAPP must be considered in a solar radiation model due to its impact on solar array efficiency.

The direct solar spectrum above the atmosphere (air mass zero, denoted AM0) may be approximated by the radiation emitted by a black body at 5750 °K as Figure 11 indicates.

Upwelling reflected radiation from the earth received by a HAPP on the average has the spectral content of direct radiation at the surface with the sun overhead (air mass one, demoted AM1). Figure 11 shows the AM1 spectrum is deficient in the blue region and a greater percentage of the total energy received is in the longer wavelength region where the sensitivity of the majority of solar cell types is highest.

Thermal reradiation from the earth peaks around 10μ as indicated Figure 11.

Diffuse radiation at the surface of the earth can be significant. However, the intensity of diffuse radiation at typical HAPP operating altitudes is very small (ref. 6). Therefore, no diffuse radiation effects are included in the model.

Figure 12 compares an AM0 solar spectrum to what a HAPP solar panel is exposed to in winter at mid latitudes (i.e., 20 km altitude, 30° and 10° sun elevation above local horizontal). The magnitude of the effect of this spectral shift from AM0 on solar cell efficiency is shown in the following analysis.

Solar cell energy conversion efficiency, η , at any altitude and solar elevation angle may be defined as:

$$\eta_{h,\,A} = \frac{\int_0^\infty f(\lambda) I(h,\,A,\,\lambda)\,d\lambda}{\int_0^\infty I,\,(h,\,A,\,\lambda)\,d\lambda} \tag{33}$$

If AM0 efficiency is

$$\eta_\phi = \frac{\int_0^\infty f(\lambda)\;\; I_{AM0}\,(\lambda)\,d\lambda}{\int_0^\infty I_{AM0}\,(\lambda)\,d\lambda} \tag{34}$$

where:

$I_{AM0}\,(\lambda)$ = AM0 intensity per unit wavelength as a function of wavelength, λ (ref. 3)

the ratio of efficiency at a particular altitude and elevation angle to the AM0 efficiency is given by

$$\frac{\eta_{h,A}}{\eta_\phi} = \frac{\int_0^\infty f\,(\lambda)\; I\,(h,\,A,\,\lambda)\,d\lambda}{\int_0^\infty f\,(\lambda)\; I_{AM0}(\lambda)\;\; d\lambda} \times \frac{\int_0^\infty I_{AM0}\,(\lambda)\;\; d\lambda}{\int_0^\infty I\,(h,\,A,\,\lambda)\,d\lambda} \tag{35}$$

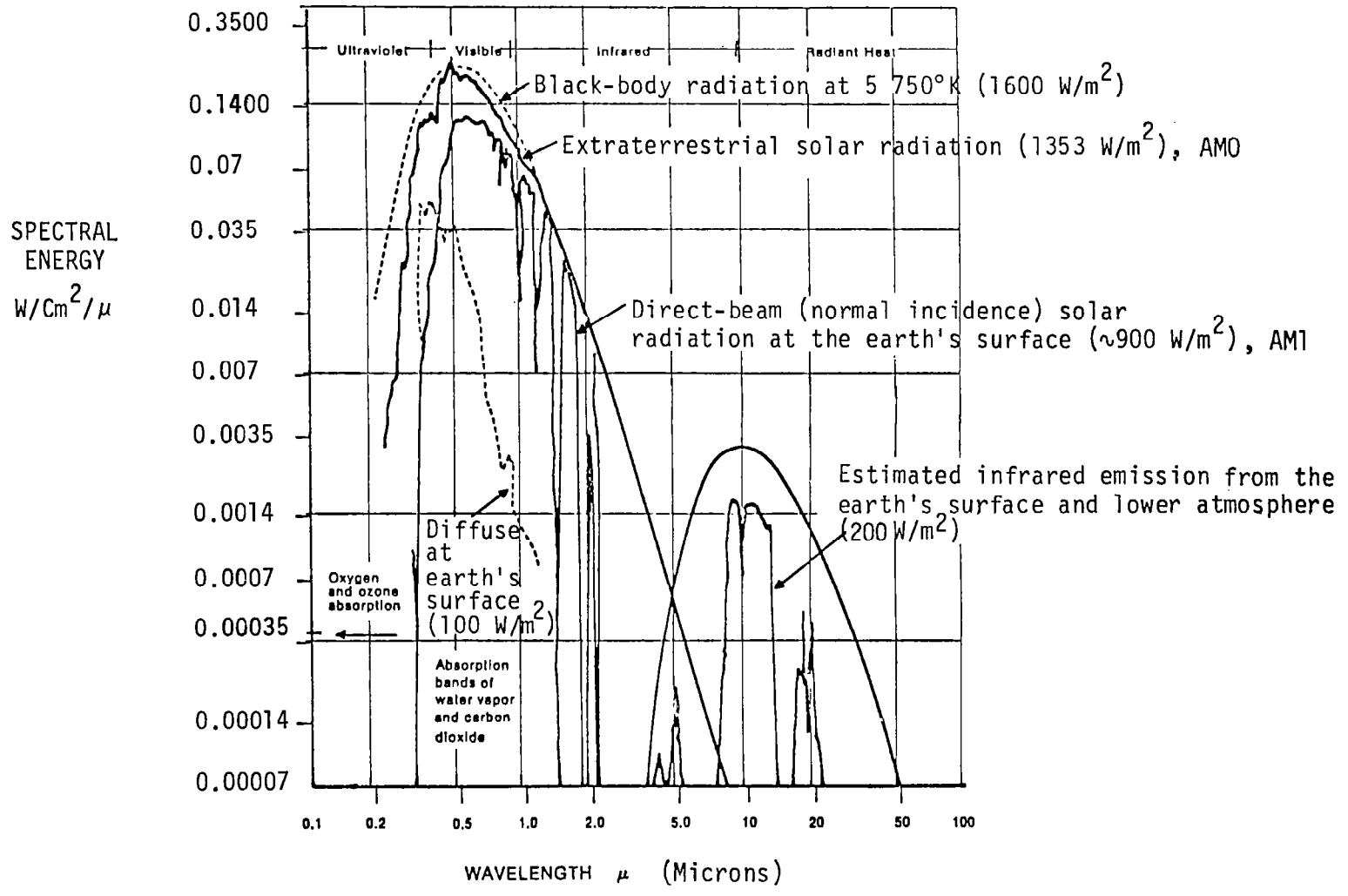

FIGURE 11. THE SOLAR SPECTRUM, Source: (ref. 4)

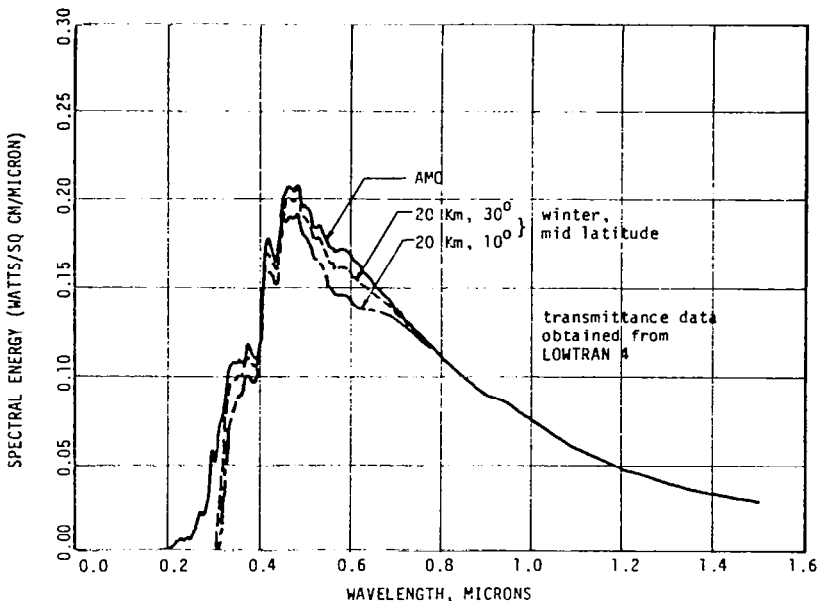

FIGURE 12 SPECTRAL SHIFTS DUE TO ATMOSPHERIC ATTENUATION (< 1.5 MICRONS)

Since the quantity of interest is the ratio of efficiencies, the response function f (λ) can be replaced in equation 35 by a relative response function

$$f(\lambda) = F_R(\lambda) \cdot f_{\lambda\,REF} \tag{36}$$

where: $f_{\lambda\,REF}$ = cell response at the wavelength for maximum response.

A typical silicon solar cell shown in reference 33 is insensitive to wavelengths below about 0.25μ and above about 1.2μ and is most sensitive around 0.8μ. Solar cell response has been approximated by the following piecewise linear function,

$$F_R(\lambda) = \begin{cases} 1.82\lambda - 0.46, & 0.25 < \lambda \leq 0.8\mu \\ -2.5\lambda + 3, & 0.8 < \lambda < 1.2\mu \\ 0, & \lambda \leq 0.25\,\mu \text{ and } \lambda \geq 1.2\,\mu \end{cases} \tag{37}$$

From equations 33 through 37 and using data shown in Figure 12, the estimated improvement in efficiency at 20 km and 30° solar elevation angle is about 2.5%, increasing to 3.9% at 10°. For example, if cell efficiency is 14% (AMO) then the typical HAPP average operating cell efficiency would be between 14.35% and 14.54%.

The effective solar cell efficiency change is small and favorable and has, therefore, been neglected in this solar radiation model.

Albedo. The ratio of reflected radiation from the surface of the earth, from clouds, and scattered by the atmosphere, to the direct solar radiation is termed albedo and is considered in this model. For high values of albedo the intensity of radiation falling on a HAPP can be increased as much as 80%. This increase in intensity may increase the solar cell output for certain array orientations but it will also raise the cell operating temperature reducing efficiency.

To model the variation of albedo with altitude, sun position, terrain, and vehicle orientation the method described in ref. 7 has been employed. This method was originally developed for predicting albedo effects on an earth satellite; nevertheless, it should give adequate results for a HAPP operating within the atmosphere well above the cloud altitudes.

The albedo energy incident upon a HAPP may be expressed by:

$$I_a = C_r \, I \, F_r \tag{38}$$

Table 7, reprinted from ref. 3, describes the spectral characteristics and angular distribution of reflected energy from various surfaces. An estimate of total reflectance variation is also given. Clearly from this table the albedo coefficient, C_r, can vary from 5% on a clear day over vegetation to as high as 80 to 84% over clouds and snow.

Referring to Figure 13 the albedo view factor, F_r, is defined as:

$$F_r = \int_{\phi L}^{\phi u} \int_{\theta L}^{\theta u} \frac{R^2}{\pi \rho^2} \, (\sin \phi \cos \sigma_E \cos \alpha_E \cos \alpha) \, d\theta \, d\phi \tag{39}$$

The variation of F_r with HAPP altitude and surface orientation is shown in Figure 14.

As an example, if the HAPP were flying at 20 km and 38°N latitude on the winter solstice at noon the solar elevation would be about 28.5°. For vertical panels looking toward the sun (i.e., view angle +90°) from Figure 14 the albedo view factor is about 0.26. With I at the winter solstice about 1400 W/m^2 from equation 38 the albedo radiation intensity would be 127 W/m^2 for an albedo coefficient, C_r, of 35%.

Planet Radiation. Long wave infrared radiation emitted by the earth is a significant factor in determining solar cell operating temperature and is considered in this methodology. As a first approximation, the earth radiates uniformly in all directions all the time.

Radiation a HAPP receives decreases in an inverse square manner with altitude and the solid angle subtended by the earth as seen from a HAPP decreases as altitude increases.

Reflecting Surface	Magnitude and Other Spectral Characteristics	Angular Distribution of Reflectance	Total Reflectance
Soils and Rocks	Increases to 1 μm Decreases above 2 μm.	Backscattering and forward scattering. Sand has large forward scattering. Loam has small forward scattering.	5 to 45 percent. Moisture decreases reflectance by 5 to 20 percent. Smooth surfaces have higher reflectance. Diurnal variation. Maximum reflectance for small Sun angles.
Vegetation	Small below 0.5 μm. A small maximum bump at 0.5 to 0.55 μm. Chlorophyll absorption at 0.68 μm. Sharp increase at 0.7 μm. Decrease above 2 μm. Depends on growing season.	Backscattering. Small forward scattering.	5 to 25 percent. Diurnal effects. Maximum reflectance for small angles. Marked annual variation.
Water Basins	Maximum at 0.5 to 0.7 μm. Depends on turbidity and waves.	Large back and forward scattering.	5 to 20 percent. Diurnal variation. Maximum for small Sun angles depends on turbidity and waves.
Snow and Ice	Decreases slightly with increasing wavelength. Large variability depends on purity, wetness, and physical condition.	Diffuse component plus mirror component. Mirror component increases with increasing angle of incidence.	Variable 25 to 80 percent. 84 percent in Antarctic. 74 percent in Ross Sea ice. 30 to 40 percent in White Sea ice.
Clouds	Constant from 0.2 μm to about 0.8 μm. Decreases with wavelength above 0.8 μm, showing water vapor absorption bands.	Pronounced forward scattering with small backscattering. Minimum for scattering angles of 80° to 120°. Fogbow* for scattering angle of 143°.	10 to 80 percent Varies with cloud type, cloud thickness, and type of underlying surface.

*A nebulous arc or circle of white or yellowish light sometimes seen in a fogbank.

TABLE 7 . SUMMARY OF REFLECTANCE DATA FOR EARTH SURFACE FEATURES AND CLOUDS REPRINTED FROM (REF. 3)

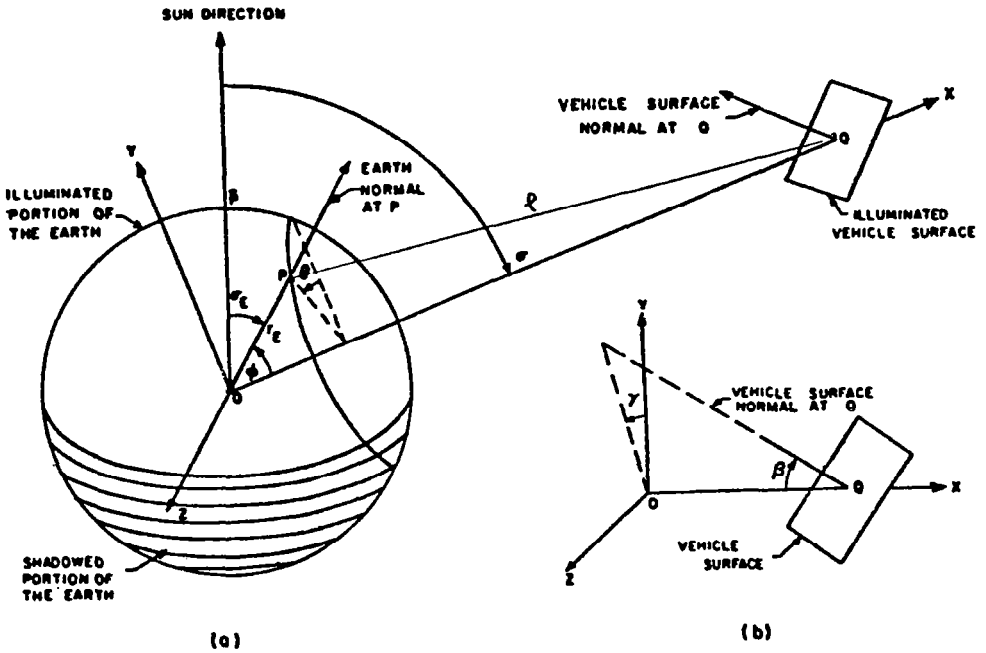

Figure 13. Earth-Sun Platform Geometry

Source: (ref. 7)

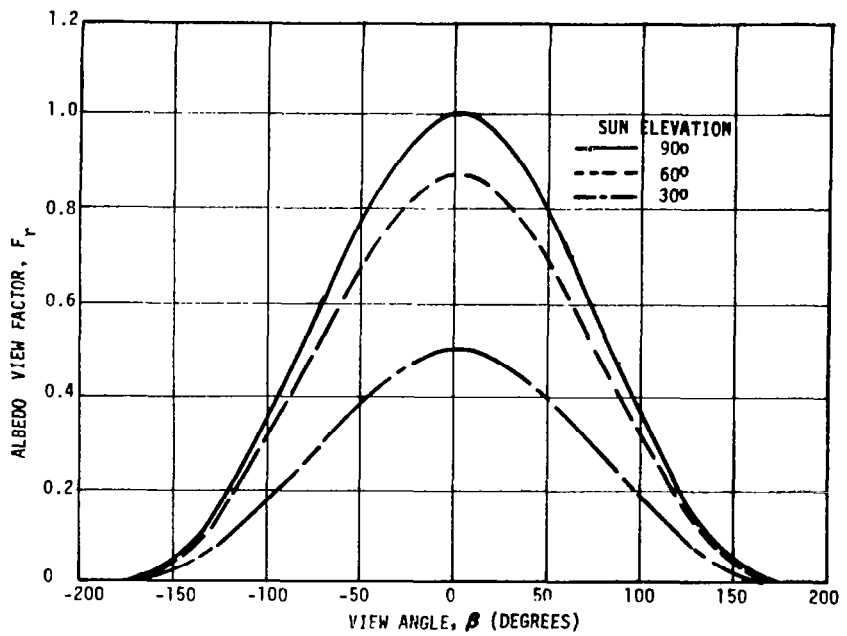

FIGURE 14. ALBEDO VIEW FACTOR

Planet radiation intensity, I_p, incident upon the surface of a HAPP, is expressed in reference 8 and with some modification here as:

$$I_p = C_e F_e \tag{40}$$

The thermal power coefficient, C_e, is affected by time of day, season and, to some extent, underlying terrain. However, for this purpose, C_e is assumed (California, mid winter, ref. 9) to be constant at about 200 W/m^2 at the effective earth radiating radius [about 10 km (32 800 ft) above the surface or an effective earth radius of 6 377 km (3 961 470 ft), ref. 10].

The planet radiation view factor, F_e is defined as:

$$F_e = \iint \frac{(\hat{r} \cdot \hat{n})(-\hat{r} \cdot \hat{N})}{r^4} \, d\Delta \tag{41}$$

Vector orientations and relationships are defined in Figure 15.

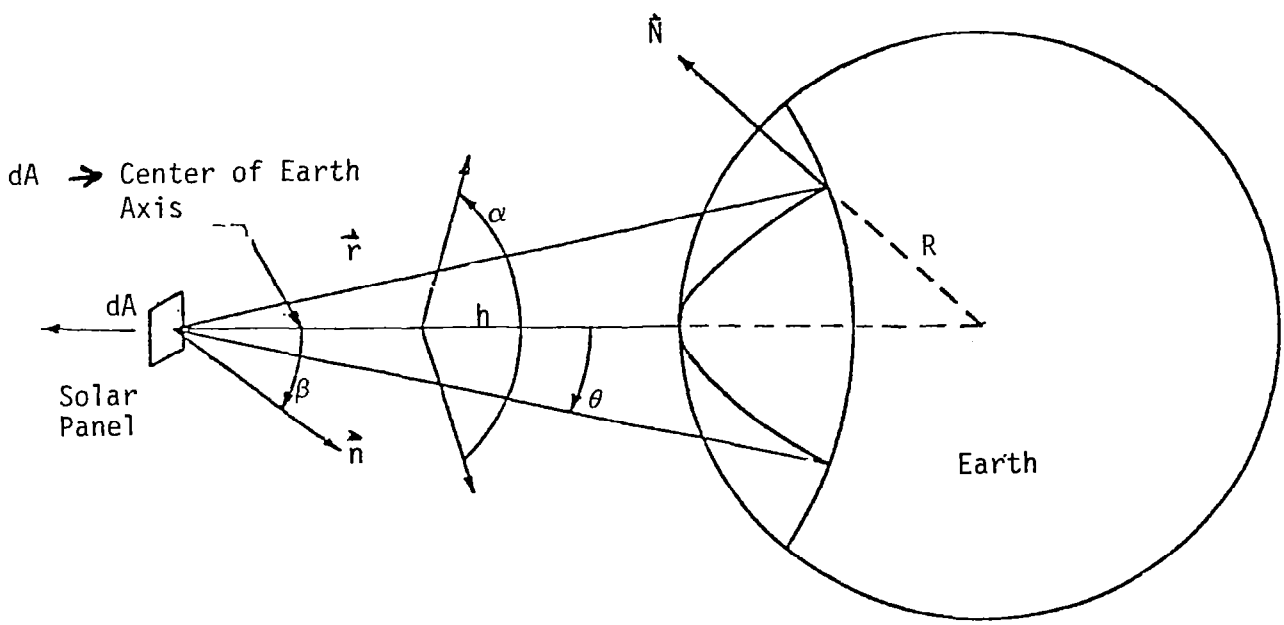

FIGURE 15. EARTH RADIATION AS SEEN FROM HAPP REFERENCE PLANE

This integration is performed over the portion of the earth's surface visible to the vehicle surface. Closed form expressions for F_e at various values of view angle β are given below:

View Angle, β	Illumination Integral, F_e
0 to $\pi/2 - \theta$	$\sin^2\theta \cos\beta$
$\pi/2 - \theta$ to $\pi/2 + \theta$	$\frac{1}{\pi}\left[\alpha \cos\beta \sin^2\theta - \sin\beta \sin\alpha \sin\theta \cos\theta + \tan^{-1}(-\cos\beta \tan\alpha)\right]$
90°	$\frac{1}{\pi}\left[-\sin\theta \cos\theta + \theta\right]$
$\pi/2 + \theta$ to π	0

where:

$$\Theta = \sin^{-1}\left[\frac{1}{1 + \frac{h}{R}}\right]$$

$$\alpha = \cos^{-1}(\cot\beta \cot\theta)$$

$$0 \leq \alpha \leq \pi$$

Figure 16 shows F_e at various view angles for altitudes of 15 and 50 km (49 200 and 164 000 ft, respectively).

Again, take as an example a HAPP flying at 20 km (65 600 ft) and 38°N at the winter solstice. The illumination integral, F_e for vertical panels (i.e., view angle ±90°) is about 0.45 from Figure 16. With C_e at 200 W/m^2, equation 40 gives the planet radiation intensity as 90 W/m^2 on both sides of the solar panel. This radiation, it must be remembered, is long wavelength infrared.

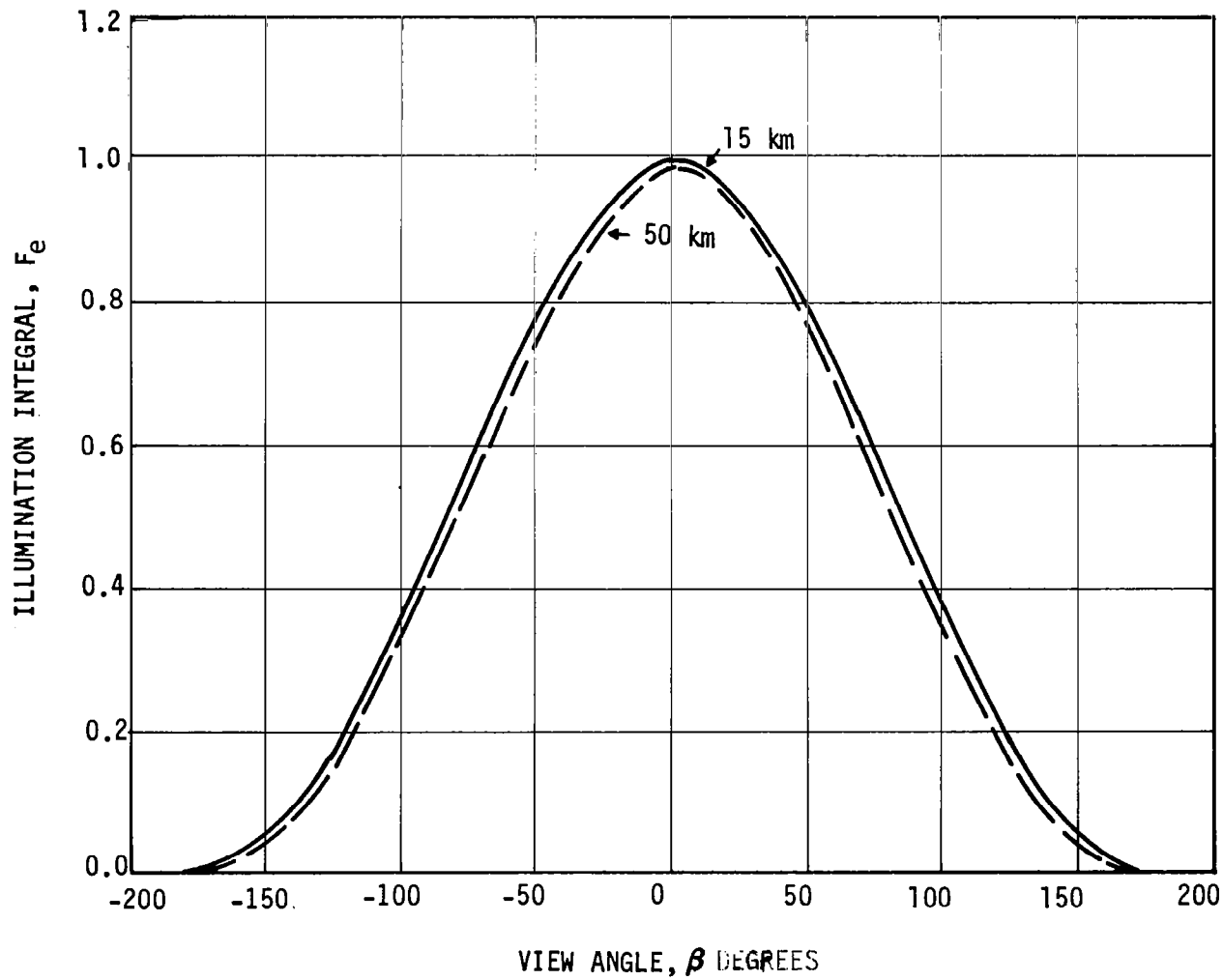

FIGURE 16 ILLUMINATION INTEGRAL VERSUS VIEW ANGLE

In summary, this solar radiation methodology addresses all of the important aspects of the solar radiation environment: direct, albedo, and planet radiation. It is of sufficient accuracy to allow its use for the conceptual design of the solar aircraft power trains presented in this report. A representative comparison of the various components of solar radiation is shown in Figure 17. The 60 degree solar zenith angle (corresponding to a 30° elevation angle) shown is near the design condition value at noon for 38°N on the winter solstice (21 December).

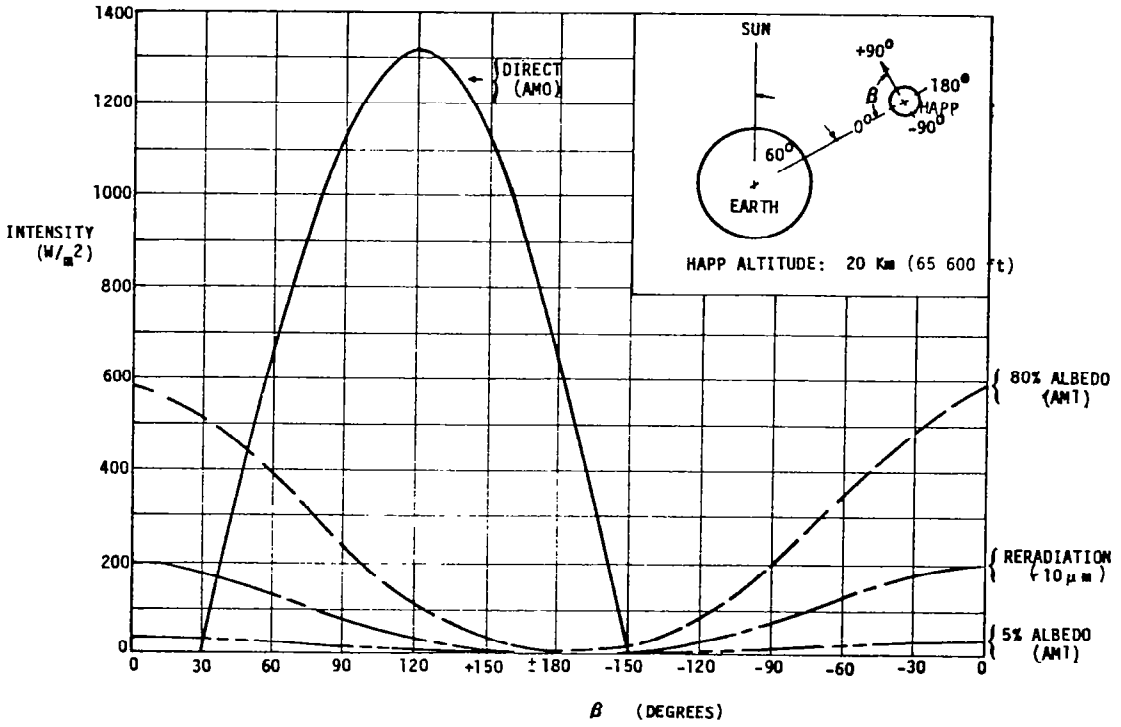

FIGURE 17. COMPARISON OF RADIATION INTENSITIES

Candidate Power Train Configurations

The complete power train sizing methodology previously defined can be used to identify the most promising solar powertrain configurations and determine whether state-of-the-art (SOTA) components could be used today to build a solar HAPP. In addition, proper utilization of this methodology will allow assessment of:

- the impact of collector orientation on power train size;
- the impact of component redundancy on power train size;
- the impact of power distribution requirements on power train size; and
- the effects of mission requirements on the power train.

Finally, this methodology will allow identification of those power train technologies which have the greatest impact on power train size and are, therefore, prime candidates for further research and development.

A variety of propulsion schemes exist to permit high altitude flight for long periods of time. These schemes fall into two categories, regenerative and nonregenerative systems, and can be listed by generic type within these two categories as in Table 8 . This report will address only those power trains using solar energy as a source of long endurance power. Figure 18 presents schematics for two solar power trains which will be analyzed here.

TABLE 8. ALTERNATIVE TECHNOLOGIES AVAILABLE FOR HIGH ALTITUDE LONG ENDURANCE RPVS

GIVEN: A NEED TO REMAIN ON STATION 1 MONTH OR MORE AND CARRY A MODEST PAYLOAD AT HIGH ALTITUDE

PROPULSION SYSTEM ALTERNATIVES:	
• NON-REGENERATIVE	
- RECIPROCATING	LOW SFC, LOW POWER TO WEIGHT, HEAVY POWERTRAIN SYSTEM WEIGHT FOR LONG MISSIONS
- TURBOFAN/TURBOJET/TURBOPROP	HIGH SFC, HIGH POWER TO WEIGHT, HEAVY POWERTRAIN SYSTEM WEIGHT FOR LONG MISSIONS
• REGENERATIVE	
- ISOTOPIC	VERY HEAVY, VERY EXPENSIVE, UNAVAILABILITY OF FUELS IN SUFFICIENT QUANTITIES, SOME RADIATION DANGER
- RF BEAMED ENERGY	SIMPLE VEHICLE POWERTRAIN, COMPLICATED GROUND STATION, LOGISTICS, TRACKING & STATIONKEEPING CONSTRAINTS
- SOLAR THERMAL	ADEQUATE EFFICIENCIES, COMPLICATED COLLECTION & TRACKING SUBSYSTEMS, VERY HEAVY, NEED FOR ON-BOARD POWER STORAGE
- SOLAR PHOTOVOLTAIC	LOW SYSTEM EFFICIENCIES, NEED FOR ON-BOARD POWER STORAGE, ADEQUATE SPACE TECHNOLOGY AVAILABLE
VEHICLE ALTERNATIVES:	
• LIGHTER THAN AIR	VERY LARGE EVEN FOR MODEST PAYLOADS AT SPEEDS TO STATIONKEEP AT ALTITUDE, CLIMB AND DESCENT PRESSURIZATION, LAUNCH AND RECOVERY
• HEAVIER THAN AIR	VERY LARGE EVEN FOR MODEST PAYLOADS, GOSSAMER TECHNOLOGY NEEDED, CARE NEEDED DURING LAUNCH AND RECOVERY

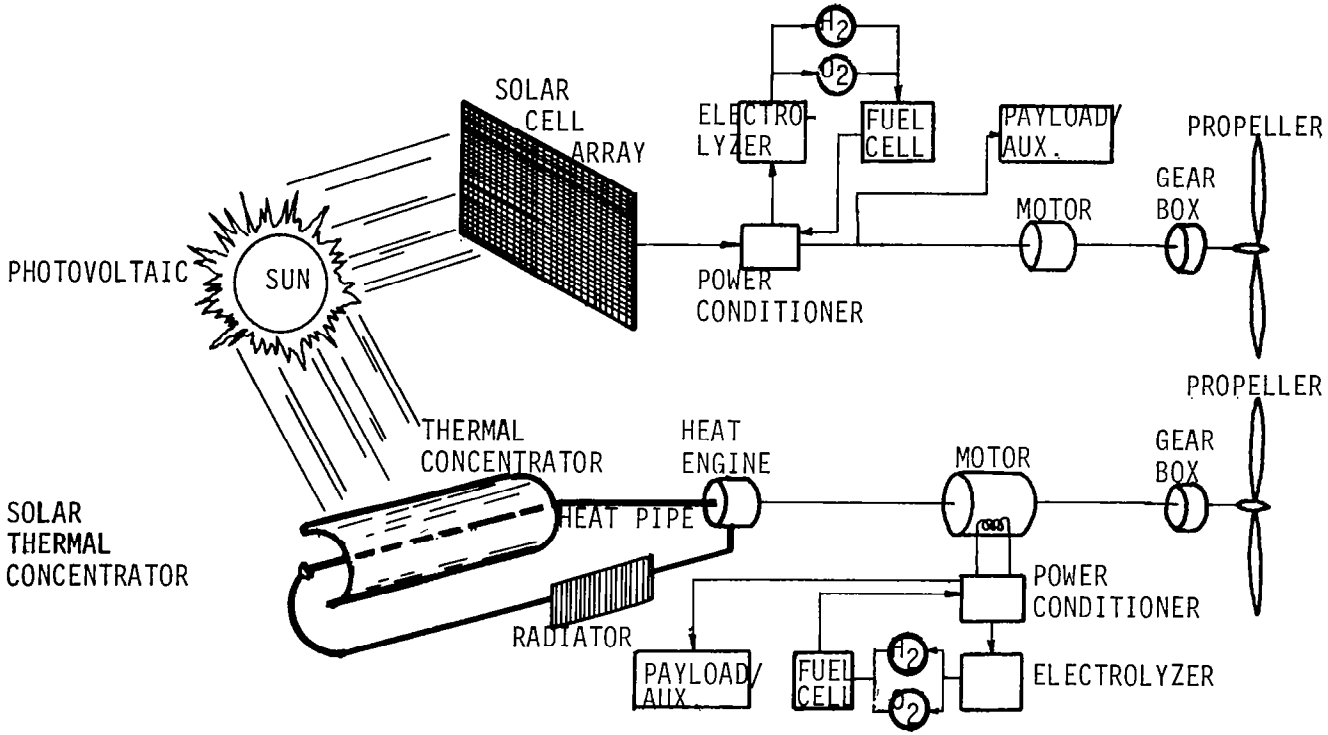

FIGURE 18. SOLAR POWER TRAIN ALTERNATIVES FOR HAPPS

The primary candidate power train configurations for a solar powered aircraft are either based upon photovoltaic collectors or thermal collectors. Because of the amount of energy needed in storage the only viable energy storage scheme identified to date is one based upon the reaction, $H_2 + \frac{1}{2}O_2 \rightarrow H_2O$ and the use of an electrolyzer and a fuel cell. The powertrain configurations discussed in the subsequent paragraphs will, therefore, have common energy storage schemes but different methods of energy collection.

Solar Thermal Power Train Configurations. There are two solar thermal powertrain configurations that are candidates for use in solar powered aircraft. One system directly uses the daytime heat engine shaft power for thrust; the other makes indirect use of the heat engine shaft power through a generator which drives the propeller through an electric motor. These powertrain configurations are represented in Figures 19 and 20. The components in each subtrain of these configurations as well as the aggregate efficiencies of each subtrain are summarized in Table 9.

Solar Photovoltaic Power Train Configuration. Solar photovoltaic power trains differ only in the type of photocell used. The power train configuration for photovoltaic collectors is represented by the configuration depicted in Figure 21 and the aggregate efficiencies $H_2 + \frac{1}{2}O_2 \rightarrow H_2O$ in Table 9 The characteristics of various photo cells will be discussed in a following section.

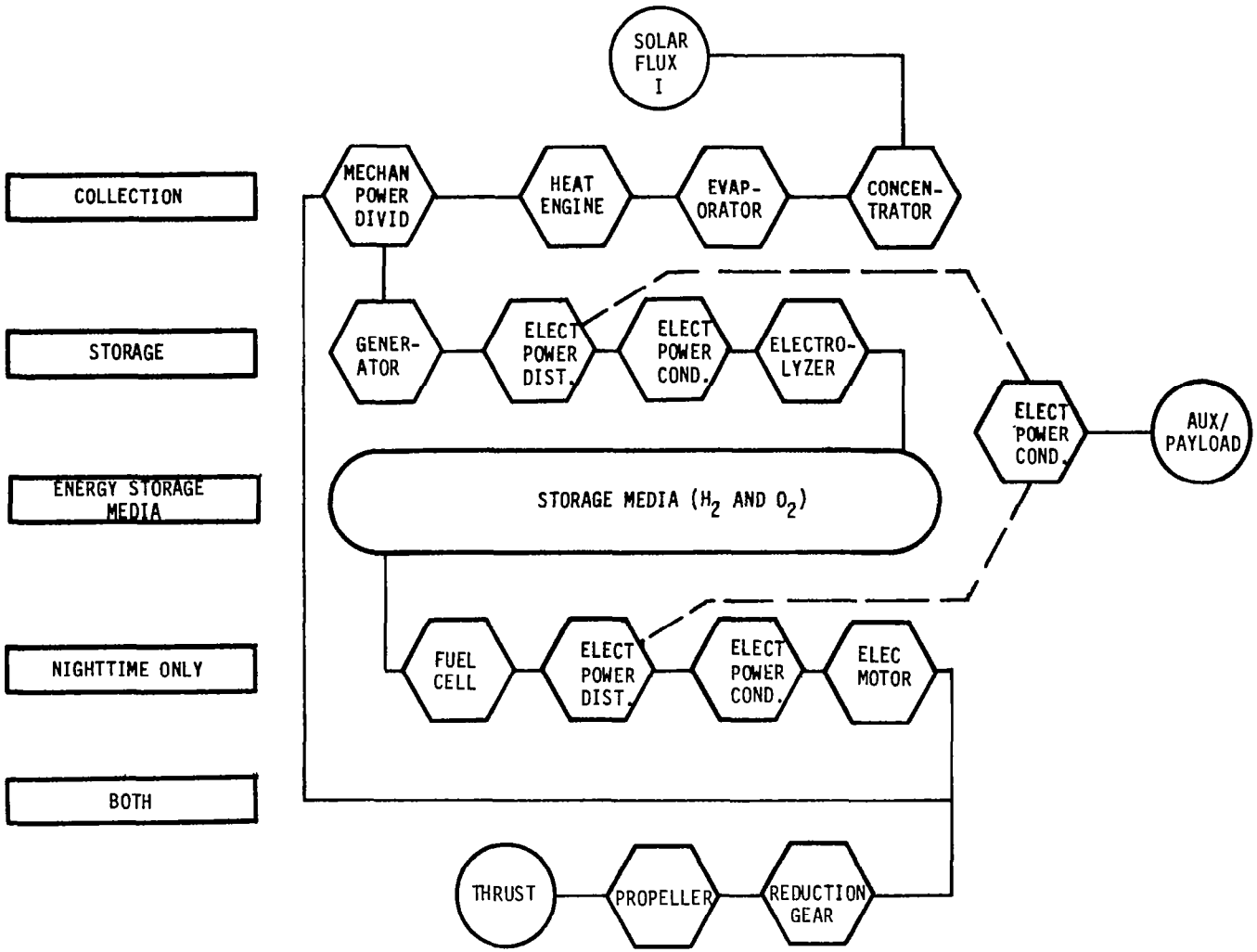

FIGURE 19. DIRECT DRIVE SOLAR THERMAL POWER TRAIN CONFIGURATION

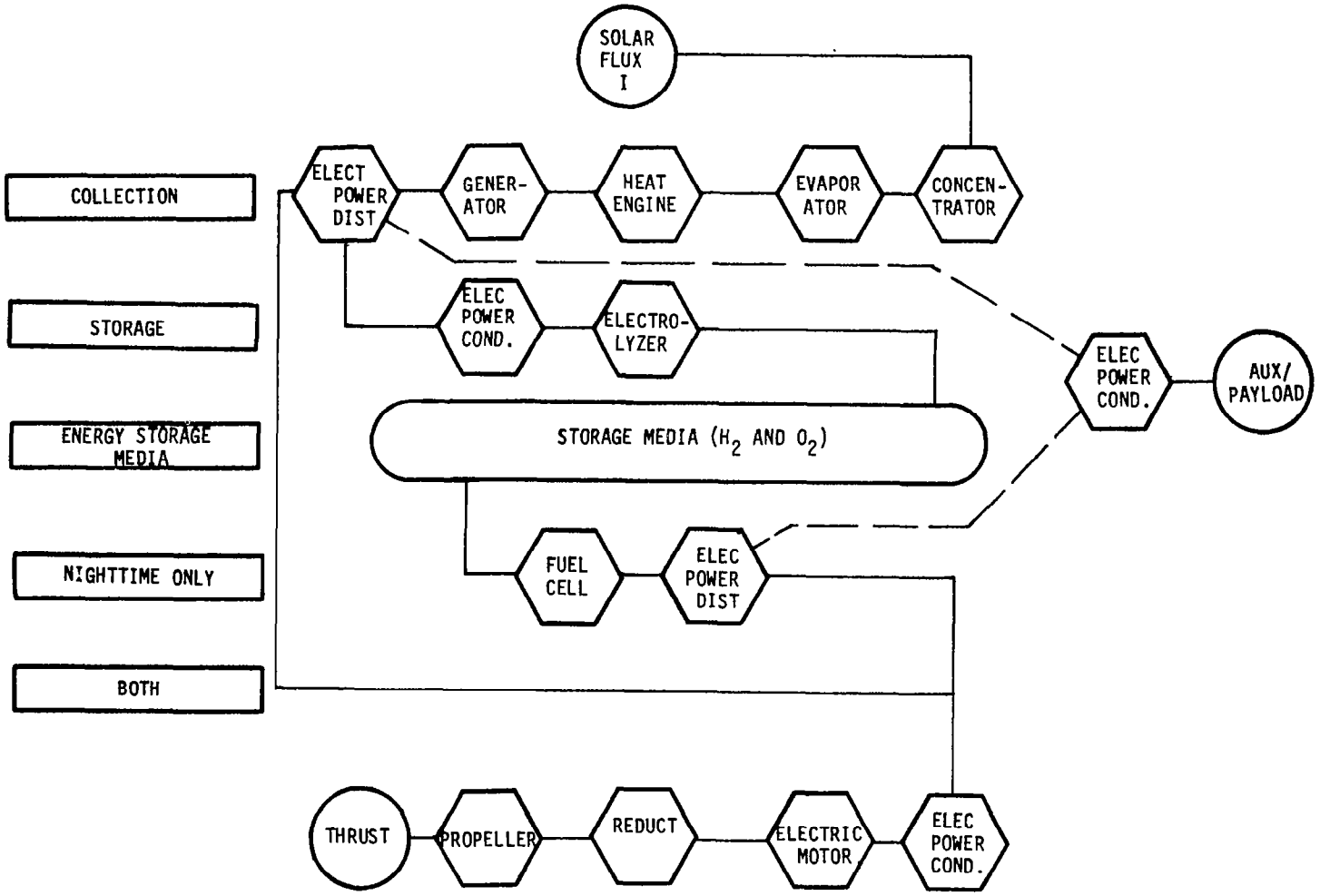

FIGURE 20. INDIRECT DRIVE SOLAR THERMAL POWER TRAIN CONFIGURATION

TABLE 9. SUMMARY OF AGGREGATE EFFICIENCIES

	DIRECT DRIVE SOLAR THERMAL	INDIRECT DRIVE SOLAR THERMAL	PHOTOVOLTAIC
COLLECTION (η_{COLL})	$\eta_{CONC}\eta_{EV}\eta_{HE}\eta_{MPD}$	$\eta_{CONC}\eta_{EV}\eta_{HE}\eta_{GEN}\eta_{EPD}$	$\eta_{COLL}\eta_{EPD}$
STORAGE (η_{ST})	$\eta_{GEN}\eta_{EPD}\eta_{PC}\eta_{ELEC}$	$\eta_{PC}\eta_{ELEC}$	$\eta_{PC}\eta_{ELEC}$
NIGHTTIME ONLY (η_{NIGHT})	$\eta_{FC}\eta_{EPD}\eta_{PC}\eta_{MOTOR}$	$\eta_{FC}\eta_{EPD}$	$\eta_{FC}\eta_{EPD}$
BOTH DAY AND NIGHT (η_{BOTH})	$\eta_{GEAR}\eta_{PROP}$	$\eta_{PC}\eta_{MOTOR}\eta_{GEAR}\eta_{PROP}$	$\eta_{PC}\eta_{MOTOR}\eta_{GEAR}\eta_{PROP}$

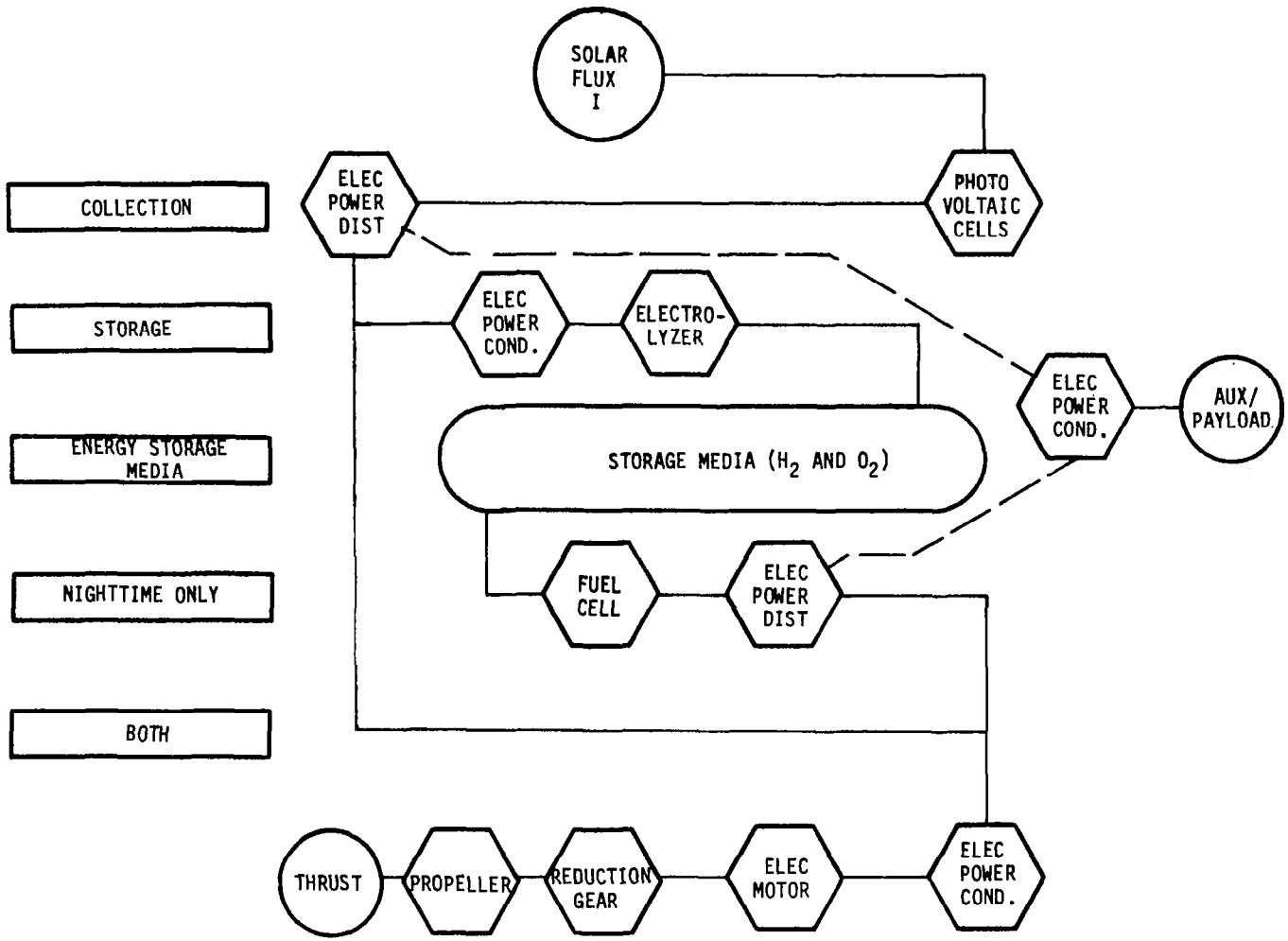

FIGURE 21. SOLAR PHOTOVOLTAIC POWER TRAIN CONFIGURATION

Component Characterization

The next level of detail of the power train model is the characterization of components within a particular configuration. A set of generalized component parameters (mass-to-peak power ratio and a corresponding efficiency) which correspond to present or projected capabilities can be selected to characterize each component. However, this must be done with due consideration of the relationships between the generalized parameters and component-specific parameters, as well as a relationship between mass properties and efficiency of each component. These relationships can be obtained from the first-order size, mass, and performance scaling laws peculiar to each component. These relationships allow the use of component-specific parameters in assessing component technology development and identifying any associated scaling nonlinearities.

The mass property of a photovoltaic cell component, for example, is best characterized by a mass-per-unit area. The efficiency of the cell is not only a function of the type of cell and the spectral content and intensity of the solar radiation but also of the cell temperature, which must be determined by radiative and convective heat transfer analysis. Furthermore, while one particular cell material may provide a higher efficiency than another, the material used may require a more massive cell. Consideration of these factors allows important collector tradeoffs to be performed.

Analysis of fuel cell or electrolyzer components can also be done using component-specific parameters. In this case a mass-per-unit electrode area and power-per-unit electrode area are appropriate. These parameters, together with the thermodynamics of the reactants and properties of the electrolyte, provide an interrelationship between fuel cell (or electrolyzer) mass and efficiency. These efficiencies also determine heat transfer requirements and affect system mass through the sizing of heat exchangers.

The propeller is an important component in HAPP vehicles and, because of the demand for high propulsive efficiency, it requires special attention and analysis. This analysis is composed of both a minimum-induced-loss propeller design method, which gives propeller efficiency and blade geometry, and a radially-graded-momentum-theory analysis method which provides a propeller performance map. The methods should allow the specification of parameters appropriate to efficient high-altitude propeller design.

Solar Energy Collection Devices. The two solar energy collection schemes considered in this study are solar thermal and solar photovoltaic. A principal difference between the two schemes is that solar thermal is a broad spectrum black-body response and photovoltaics is a relatively narrow-band quantum response. The advantage of the broad spectrum response of thermal absorption is, however, offset by the fact that the thermal-to-mechanical energy conversion efficiency is limited by the second law of thermodynamics. Photovoltaics, on the other hand, produce an electrical current and voltage which is a form of energy readily compatible with both the production of shaft power (electric motors) and the storage of energy (electrolyzers). The major factors affecting both the mass and collector area of these two schemes are discussed in the following paragraphs.

Solar Thermal Energy Collectors. In order to achieve high thermal-to-mechanical energy collection efficiencies it is necessary to achieve high operating temperatures. This in turn requires concentration of the available solar radiation. To do this a primary reflector of significant surface curvature is required. It is also necessary that the reflector have and maintain a precisely determined shape so that the concentrated radiation will strike the secondary surface at which the energy is transferred to a working fluid. Furthermore, it is necessary to incorporate in the collector design a highly accurate method of pointing the concentrator in order to maintain the flux at the secondary surface as the sun traverses the sky. Another feature of thermal energy collection is the fact that the area requirement obtained by calculations refers to the aperture of the curved surface and not the curved surface itself. In practice, the reflector-to-aperture area ratio can be as high as 3.14. Another factor which contributes to the mass of thermal systems is the high operating pressure within the system. Therefore, while thermal collectors offer higher collection efficiencies, this can only be achieved with significant weight penalties.

Efficiencies given in Table 10 were obtained from heat transfer calculations and thermodynamic models representing the various cycles. Mass estimates were derived from assumptions indicated in footnotes to the table. In general, the requirement for high efficiency dictates high radiation concentration, high temperatures and high pressures, all of which significantly increase the mass-to-power out ratios of the components in a solar thermal power train. Furthermore, because of the pointing requirements and collector depth dictated by the requirement to concentrate radiation, collectors must be mounted in pods rather than in or on the wings. The placement of collectors in pods reduces configurational flexibility. It also restricts the ability to make a beneficial correlation between lifting surfaces and collector surfaces and to minimize parasitic drag of the solar energy collectors.

TABLE 10. CHARACTERISTICS OF THERMAL SOLAR ENERGY COLLECTORS

COMPONENT	SOTA(1) Mass/Area (kg/m^2)	ADV(2) Mass/Area (kg/m^2)	SOTA Efficiency (%)	ADV Efficiency (%)	SOTA Mass/ Power Out (kg/kW)	ADV Mass/ Power Out (kg/kW)
Heat Pipe/Evaporator	---	---	---	---	3.2	2.2
Heat Exchangers (regenerators and radiators)					2.0	2.0
Heat Engine (3)			---	---		
T_{PEAK} = 700°k T_{MIN} = 300k						
Brayton Cycle (open)	---	---	25	30	2.0	2.0
Stirling Cycle	---	---	35	40	4.6	4.6
Rankine (single fluid)	---	---	32	36	5.5	4.0
Rankine (binary fluid)	---	---	28	33	5.0	3.5
Fresnel Concentrator	5.4	5.4	60-63(4)	65 - 70(4)	---	---
Reflector	12.0	4.6				
	($\frac{W}{\delta}$ = 15; f = .1)(5)	($\frac{W}{\delta}$ = 20;f=.05)(5)	60	66	---	---

(1) State of the art.
(2) Advanced concepts.
(3) Includes regenerators and radiators, as needed.
(4) Increases with power needs/availability.
(5) $\frac{W}{\delta}$ is the ratio of characteristic dimension of concentrator aperture mass (W) to thickness of concentrator surface (δ); f is the ratio of actual concentrator mass to the mass of concentrator if it were solid structure.

This review of particular power train components points to the need to reconcile the interrelationship between the efficiency and mass properties of each component. This reconciliation is particularly important because higher efficiency often means more mass for a given power output. If proper care is taken in this regard, meaningful tradeoffs between the efficiency and mass of a particular component in a configuration can be accomplished on the basis of total power system impact. The model presented here provides mass, peak power, and, where appropriate, area and volume data for each component included in a particular configuration. These data, in turn, can be used to identify individual component contributions to total power train mass and can be used in the required aircraft weight and balance analysis.

Photovoltaic Collectors. To maximize the photovoltaic energy conversion efficiency it is necessary to minimize the temperature of the cell and optimize the cell design and configuration with respect to the cell's electrical loads. Furthermore, photovoltaics offer good prospects for making maximum possible use of the array surfaces for lift generation. While concentrators have been used with photovoltaics, the weight penalty and loss of efficiency associated with heating make such a scheme unsuitable for solar powered flight.

The primary photocells of interest to solar powered flight are made of gallium arsenide (GaAs) and silicon (Si). Gallium Arsenide has the advantage of higher efficiencies at standard conditions (25°C and AMO) but has the disadvantage of having a fairly complex multi-layered structure which is expensive to manufacture and weighs significantly more per unit area than silicon cells. While the efficiency of GaAs degrades more slowly with increasing temperature than does silicon, there is less to be gained in the development of cell designs which minimize cell temperature.

The major advantage of silicon cells over any other candidate photocell is that they have been in design and production for many years. Producibility in the large quantities needed for solar powered flight is well in hand. In addition, refinements in cell design have allowed the manufacture of very thin (2 mil) silicon cells without penalties to efficiency. Use of gridded back cells which create a degree of cell transparency also offers the potential to significantly reduce cell temperature and, hence, increase cell operating efficiency.

Characterization of photo cells in this study is accomplished by specifying (1) the 25°C, AMO cell efficiency consistent with cell design and application, (2) the temperature coefficient for efficiency (%/°K), (3) the solar absorptance and infra-red emittance, and (4) the mass per unit area of the cell, interconnects, covershields and substrate. The first three photocell characteristics are used in a heat transfer analysis described in Appendix D to determine cell operating temperature and efficiency as a function of the time of day. An example of the result of such an analysis is given in Figure 22. The last item is used in conjunction with the determination of collector area to determine the mass of the photovoltaic array. The near and far term state-of-the-art values for these characteristics of GaAs and Si photocells are summarized in Table 11.

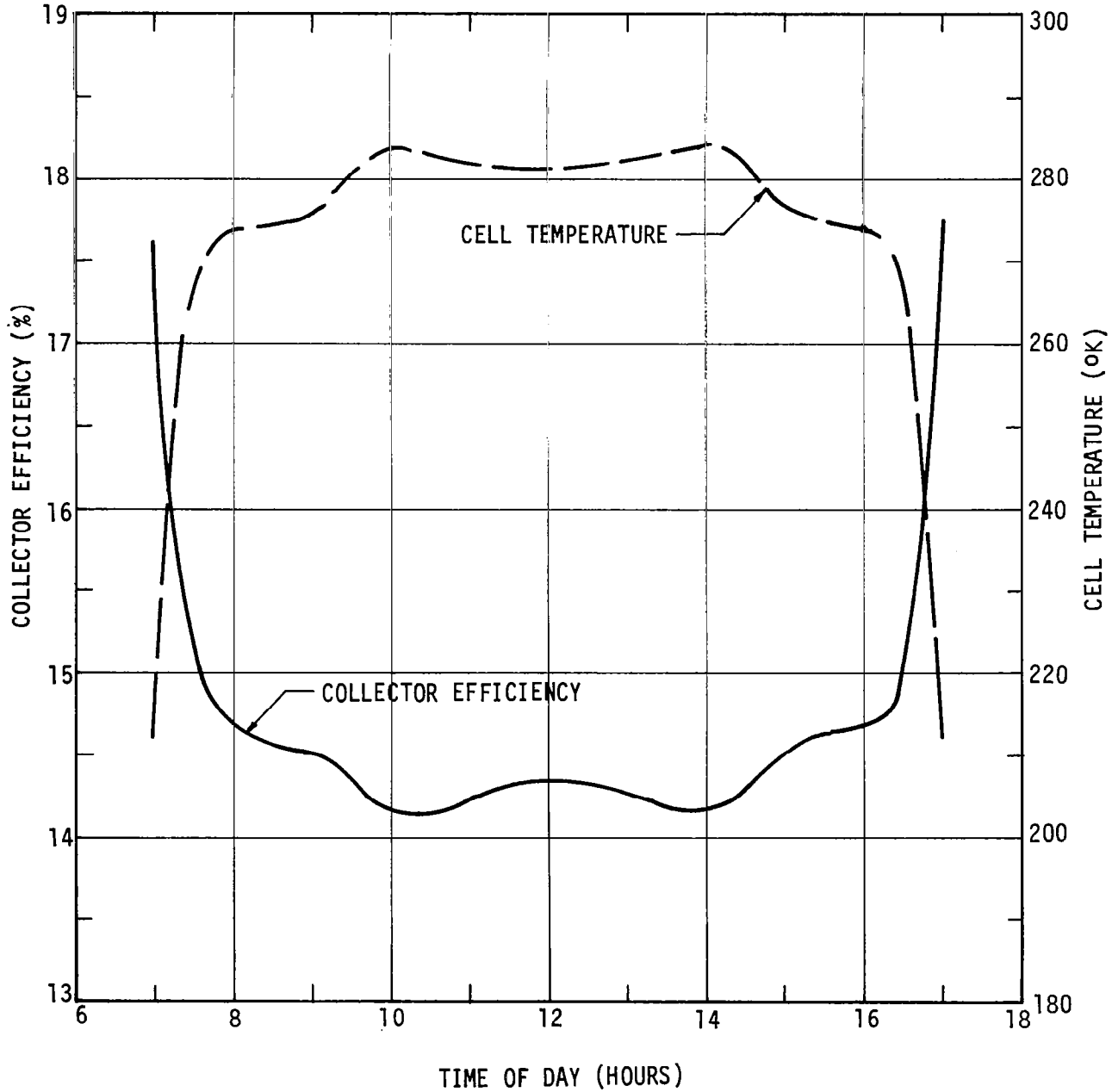

FIGURE 22. CELL TEMPERATURE AND EFFICENCY AS FUNCTIONS OF TIME OF DAY

Power Conditioning. One major requirement in a solar power train is to keep all of the individual components operating as near as possible to their individual peak efficiency points while operating over a wide range of power input, power output and solar environment. The operating characteristics of the fuel cell, motor-controller and a variable pitch propeller can adequately cover most of the critical output conditions with little loss of efficiency. The most critical matching problem is to couple the solar cell array into its daytime loads of the electrolyzer and the motor. The problem is illustrated in Figure 23. Solar cell array output characteristic for a horizontal array on December 21 at 38 deg. North latitude is shown for three different times of the day. The primary difference in the curves is the increasing peak output current as the sun rises to its zenith. A secondary effect is the decrease in the array peak voltage as the cell temperature increases with increasing solar flux. The peak output power (also the peak efficiency) point is shown on each of the three curves.

Also shown on the chart is a typical electrolyzer load curve which has been matched into the peak cell output at noon. The intersection of the load curve with the solar cell curves indicates the actual operating points for each of the three illumination conditions. It can be seen that the array is forced to operate significantly off the peak efficiency point on the lower two curves. For the assumed match of the collector and the electrolyzer, another large mismatch will occur in the summer when the sun elevation and the flux vary over a larger range.

TABLE 11. CHARACTERISTICS OF PHOTOVOLTAIC SOLAR ENERGY COLLECTORS

	η_ϕ (%)	β_T (Δ%/Δ°K)	α_S	ϵ_{IR}	ρ' kg/m^2
Si					
1985-1990(1)	14.5	.05	.70	.83	.414
1991-2000(2)	14.5	.05	.60	.83	.414
GaAs					
1991-2000	16.0	.03	.70	.83	.52

(1) 2 mil Si cells

(2) 2 mil Si cells with gridded-back design

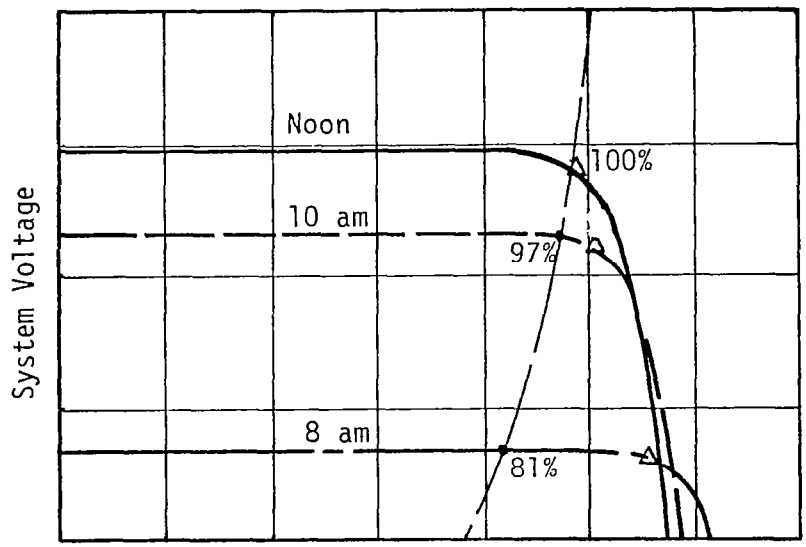

FIGURE 23 . SOLAR CELL-ELECTROLYZER MATCHING FOR HORIZONTAL CELLS

There are two methods to deal with this matching problem. The first is to carefully select the system operating point to minimize losses. This will provide maximum efficiency at the selected point only, with decreasing efficiency away from this point. This might not be particularly bad if the selected design point were for a northern latitude during the winter. There would be larger losses in the summer, but this would be more than compensated for by the increased incident flux. The second method is to actively match supply and load using a peak power tracker or power conditioner. This device would allow continuous operation at the cell peak power point; however, there would be a constant loss due to the inefficiency of the power conditioner itself.

A power conditioner is included in this methodology for simplicity. (The operating point for a system without a conditioner must be determined by iteration). In practice, a detailed analytical model of a proposed HAPP design should be exercised in a typical operational scenario to determine if the fixed loss of the power conditioner is superior to the variable loss, higher peak efficiency, lighter weight and potentially higher reliability of a direct connection.

A survey of power conditioners for use in space based solar power systems indicated that a state-of-the-art conditioner has an efficiency of about 92% and (for a HAPP operating environment) a mass of 0.5 Kg (1.103 lbs) per peak Kw.

This discussion has centered on matching the solar array to an electrolyzer. A similar problem exists for matching the array to a motor during daytime. This problem is not as critical as electrolyzer matching since much lower power levels are involved, and the motor load point can be adjusted somewhat by its controller and by varying propeller pitch. These controls alone should be sufficient to efficiently match the motor to the solar array during the day and to the fuel cell at night.

Energy Storage. Because of the need for powered flight during at least part of the night, every solar powered aircraft must have a power train capable of delivering power to some form of energy storage medium and extracting power from that energy storage medium. At most latitudes of interest for solar powered vehicles, winter nights can be twice as long as days. In this situation, more than two thirds of the energy collected in the day must be put into storage for night use. This fraction of energy collected can be much larger unless the energy can be delivered and extracted at high efficiencies and the energy medium can retain the energy stored for long times (up to 24 hours) without significant storage losses. Storage losses to be minimized or avoided include losses due to heat transfer, friction, leakage or parasitic chemical reactions.

After examination of many energy storage schemes such as flywheels and various forms of thermal and chemical energy storage, the only scheme identified to date with all the necessary attributes is the electrochemical process which uses an electrolyzer to put energy into a storage medium and a fuel cell to extract power from the storage medium. The idealized maximum energy that can be obtained in an electrochemical reaction is the Gibbs free energy of the reaction. The reaction with the highest Gibbs free energy per unit mass is the reaction

$$H_2 + \tfrac{1}{2}O_2 \rightarrow H_2O \qquad (42)$$

Other candidates are presented for comparison in Table 12.

TABLE 12. THEORETICAL PERFORMANCE OF CANDIDATE FUEL CELL REACTANTS

REACTANTS	ENERGY DENSITY* (kw-hr/kg)	MASS/ENERGY* (kg/kw-hr)	THEORETICAL* VOLTAGE (VOLTS)
H_2 and Cl_2 (AQUEOUS)	1.02 (NO H_2O INCLUDED)	.979	1.35
H_2 and Cl_2 (GASEOUS)	7.43	1.346	.99
H_2 and Br_2 (AQUEOUS)	.355 (NO H_2O INCLUDED)	2.817	1.06
H_2 and NO_2	1.18	.846	1.03
H_2 and O_2	3.69	.27	1.23

*At standard conditions (273K, 1 atmosphere)

To model the mass of an energy storage scheme in detail, it was divided into: (1) energy storage media (H_2 and O_2), (2) media containment (tanks), (3) electrolyzer (electrodes, enclosure and auxiliaries), (4) fuel cell (electrodes, enclosure and auxiliaries), and (5) heat exchanger. The mass of energy storage media or reactants is characterized by its Gibbs free energy per unit mass, the efficiency of the fuel cell, and the energy requirements of the fuel cell for nighttime operation,

$$\Delta E_o = \overline{P}_{FC} t_{NIGHT}, \text{ such that} \tag{43}$$

$$M_R = \frac{\Delta E_o}{\varepsilon \overline{\eta}_{FC}} = \frac{\overline{P}_{FC} t_{NIGHT}}{\varepsilon \overline{\eta}_{FC}} \tag{44}$$

The reactants must be stored in gaseous form because a change of state would require prohibitive levels of auxiliary power.

The mass of containment tanks is expressed as a fraction, f, of the mass of the storage media. Therefore, the mass of reactants and tanks, $M_{REACT + TANK}$, is given as

$$M_{REACT + TANK} = (1+f) \frac{\overline{P}_{FC} t_{NIGHT}}{\varepsilon \overline{\eta}_{FC}} \tag{45}$$

The value of f can be obtained for spherical tanks from the equation,

$$f = \frac{M_{TANK}}{M_{REACT}} = \frac{3}{2} \frac{R_{TANK}}{m_{PROD}} \frac{\rho_{TANK}}{\sigma_{TANK}} F, \tag{46}$$

which is derived in Appendix C.

For a safety factor of 2, Kevlar tanks give

$$f = (1.854 \times 10^{-3}/°K)\ T \tag{47}$$

With 15% attachments, this becomes $f = (2.13 \times 10^{-3}/°K)\ T$ (48)

and for $T = 323°K$, this gives $f = \frac{M_{TANK}}{M_{REACT}} = 0.69$ (49)

Mass of the electrolyzer or fuel cell is obtained from the following:

$$M_{ELEC,\ FC} = \underbrace{(N_{CELL}A_{CELL}\rho'_{CELL})}_{\text{Electrode Cells}}{}_{ELEC,FC} + \underbrace{(N_{CELL}S_{CELL}S_{PER}P_{PER}G_F A_{CELL}^{1/2} + 2\rho_{END}\delta_{END}A_{CELL})}_{\text{Electrode Enclosure}}{}_{ELEC,FC} + \underbrace{(a_1 \hat{\dot{M}}_{REACT} + m_o)}_{\text{Auxiliaries}}{}_{ELEC,\ FC} \quad (50)$$

where

A = cell planform area in square meters

a_1 = mass of auxiliaries per peak reactant mass flow rate

G_F = geometrical factor corresponding to cell geometry $\left(G_F = \frac{\text{Circumference}}{\sqrt{A_{CELL}}}\right)$

When the data on mass properties of fuel cell and electrolyzer accessories, shown in Table 13, is plotted versus mass flow rate of reactants as in Figure 24, a representative value for a_1 can be obtained. In this case, the data indicates a representative value of 4.3 $Kg/_{(Kg/Hr)}$.

The mass of the electrolyzer and fuel cell can also be expressed in terms of the peak power density per cell, $\hat{P}'_{CELL} = V_{CELL}i$, and efficiency of either the electrolyzer or fuel cell (η_{ELEC} or η_{FC}). This is the preferred representation because the efficiency can also be expressed as a function of the power density of a cell, such that system mass can be minimized with respect to cell peak power density. This representation can be obtained from equation (50) by expressing the peak power, $P_{ELEC,\ FC}$, in terms of the total area of the unit.

$$\hat{P}_{EL} = \hat{\eta}_{EFF}N_{CELL}A_{CELL}\hat{V}_{CELL}\hat{i}_{CELL} = \hat{\eta}_{EFF}N_oA_{CELL}\hat{P}'_{CELL} = \varepsilon\hat{\dot{m}}R_{ELEC} \quad (51)$$

where $\hat{\eta}_{EFF}$ = efficiency at peak power

$\hat{V}_{CELL}$ = cell voltage at peak power

$\hat{i}_{CELL}$ = cell current density at peak power

A similar expression for the peak power out of a fuel cell gives

$$\hat{P}_{FC} = N_{CELL}A_{CELL}\hat{V}_{CELL}\hat{i}_{CELL} = N_{CELL}A_{CELL}P'_C = \frac{\varepsilon\hat{\dot{m}}R_{FC}}{\eta_{FC}} \quad (52)$$

TABLE 13. DATA ON MASS PROPERTIES OF FUEL CELL AND ELECTROLYZER ACCESSORIES

Accessory Mass (Kg)	Power Out of Fuel Cell (kw)	Power Into Electrolyzer (kw)	Efficiency	$\dot{m}_R$ (kg/Hr)	Type	Mfg/Source
27.7		18	.765	3.7	Electrolyzer	ref. 26
49.0		33.3	.773	7.0	Electrolyzer	ref. 32
123.3		133.3	.76	27.3	Electrolyzer	ref. 32
30.9	30		.733	11.0	Fuel Cell	
27.2	10		.80	3.4	Fuel Cell	
71.6	40		.78	13.8	Fuel Cell	

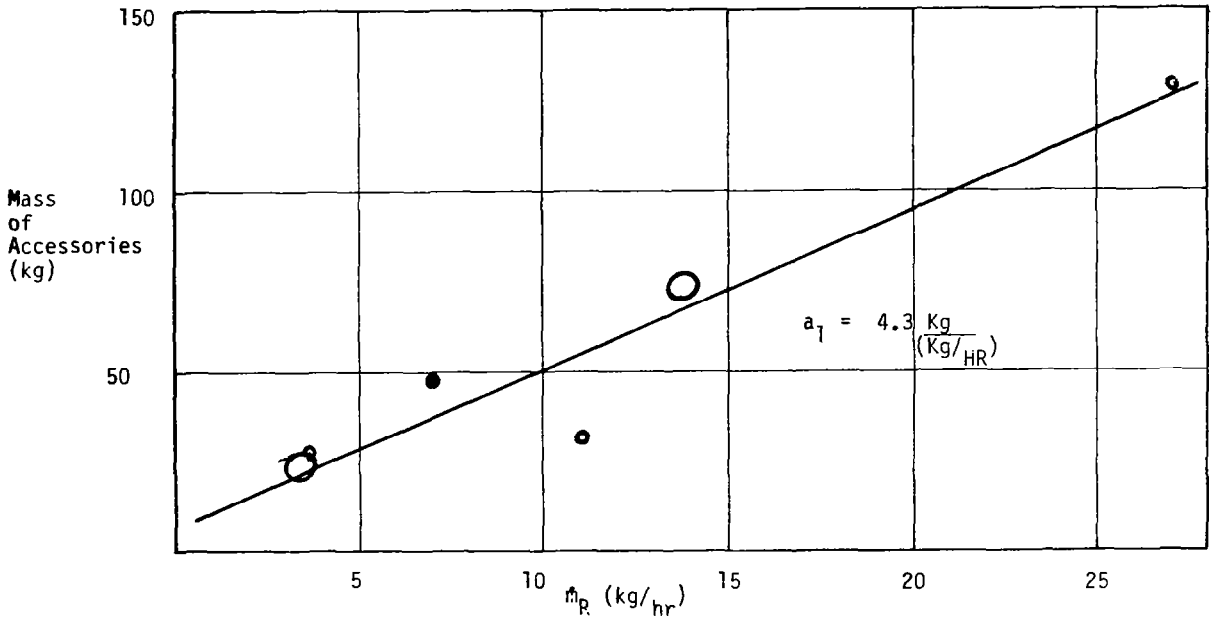

FIGURE 24. DETERMINATION OF GENERALIZED MASS PROPERTIES CONSTANTS FOR FUEL AND ELECTROLYZER ACCESSORIES

Using the appropriate peak power expression in equation (51), the mass of the electrolyzer can be expressed as:

$$M_{ELEC} = \frac{\hat{P}_{ELEC}}{\hat{\eta}_{ELEC}} \left(\frac{\rho'_{CELL}}{\hat{P}'_C} + \frac{\delta_{CELL}\delta_P\rho_P G_F}{A_{CELL}^{1/2}\hat{P}'_{CELL}} + \frac{\hat{n}\, a_1}{\varepsilon} \right)_{ELEC} + m_{o_{ELEC}} + (2\rho_{END}\delta_{END}A_{CELL})_{ELEC}; \quad (53)$$

$$M_{ELEC} = \frac{\hat{P}_{ELEC}}{\hat{\eta}_{ELEC}} \left(\mu_{ELEC} + \hat{\eta}_{ELEC}\, \mu_{ELEC_o} \right) + m_{ELEC};$$

or

$$M_{ELEC} = \hat{P}_{ELEC}\, \mu_{ELEC_{EFF}} + m_{ELEC} \quad (54)$$

where

$$\mu_{ELEC_{EFF}} = \frac{\mu_{ELEC_1}}{\hat{\eta}_{ELEC}} + \mu_{ELEC_o}$$

$$\mu_{ELEC_1} = \frac{1}{\hat{P}'_{C_{ELEC}}} \left(\rho'_{CELL} + \frac{\delta_{CELL}\delta_P\rho_P G_F}{A_{CELL}^{1/2}} \right)_{ELEC} = \left(\frac{\rho'_{C_{EFF}}}{\hat{P}_{CELL}} \right)_{CELL} \quad (55)$$

$$\mu_{ELEC_o} = \left(\frac{a_1}{\varepsilon} \right)_{ELEC} \quad \text{and}$$

$$m_{ELEC} = (2\rho_{END}\delta_{CELL}A_{CELL})_{ELEC} + m_{o_{ELEC}}$$

Similiary the mass of the fuel cell can be expressed from equation (52) as:

$$M_{FC} = \hat{P}_{FC} \left(\frac{P'_C}{\hat{P}'_C} + \frac{\delta_{CELL}\delta_P\rho_P G_F}{A_{CELL}^{1/2}\hat{P}'_{CELL}} + \frac{a_1}{\hat{\eta}\,\varepsilon} \right)_{FC} + (2\rho_{END}\,\delta_{END}\,A_{CELL})_{FC} + m_{o_{FC}}; \quad (56)$$

$$M_{FC} = \hat{P}_{FC} \left(\mu_{FC_1} + \frac{\mu_{FC_o}}{\eta_{FC}} \right) + m_{FC};$$

or

$$M_{FC} = \hat{P}_{FC}\, \mu_{FC_{EFF}} + m_{FC} \tag{57}$$

where

$$\mu_{ELEC_{EFF}} = \mu_{FC_1} + \frac{\mu_{FC_o}}{\eta_{FC}}$$

$$\mu_{FC_1} = \frac{1}{\hat{P}'_{C_{FC}}} \left(\rho'_{CELL} + \frac{\delta_{CELL}\delta_P P^{G_F}}{A_{CELL}^{\frac{1}{2}}} \right)_{FC} = \left(\frac{\rho'_{C_{EFF}}}{\hat{P}'_C} \right)_{FC} \tag{58}$$

$$\mu_{FC_o} = \left(\frac{3}{\varepsilon} \right)_{FC}$$

$$m_{FC} = (2\rho_{END}\, \delta_{END}\, \eta_{CELL})_{FC} + m_{o_{FC}}$$

Equations (54) and (57) are the simplest forms for convenient use in actual sizing, but (53) and (56) are useful in determining the optimum operating conditions, i.e., P'_C and η.

Using data which is contained in Table 14 on both electrolyzer and fuel cell power sections, the effective mass per unit area of electrode in equations (55) and (58) has been plotted in Figure 25 as a function of electrode area. The only set of data that corresponds to simply a scaling of the size of the power section is that corresponding to the light-weight alkaline fuel cell. The line drawn through this data set shows the general form,

$$P'_{C_{EFF}} = P'_{CELL} + \frac{(CONSTANT)}{A_{CELL}^{\frac{1}{2}}},$$

which is predicted by equations (55) and (58).

TABLE 14. FUEL CELL AND ELECTROLYZER POWER SECTION MASS DATA

	NO. CELLS	CELL AREA (m^2)	TOTAL AREA (m^2)	MASS (Kg)	MASS/ AREA (Kg/m^2)	MFG	SOURCE	NOTE:
FUEL CELLS	34	.0232	.79	10.4	13.2	UTC	ref. 28	(Light-weight fuel cell power plant) FCR-3045
	96	.186	17.86	156.0	8.75	UTC	ref. 30	
	128	.047	6.04	69.4	11.5	UTC	ref. 30	
	120	.047	5.64	100.4	17.8	UTC	ref. 27 and 28	"BASELINE"
	120	.047	5.64	75.2	13.3	UTC		"ADVANCED"
	137	.082	10.38	94.6	9.1	GE/SPE		"STATE-OF-THE-ART"
	132	.082	10.82	84.2	7.8	GE/SPE		"ADVANCED"
ELECTROLYZER	50	.0929	4.64	84.3	18.2	LIFE SCIENCES	ref. 26	
	60	.0929	5.57	107.0	19.2	LIFE SCIENCES	ref. 30	
	207	.0929	19.23	345.0	18.0	LIFE SCIENCES	ref. 30	
	59	.042	2.47	40.2	16.3	GE/SPE		"STATE-OF-THE-ART"
	64	.043	2.73	33.9	12.4	GE/SPE		"ADVANCED"

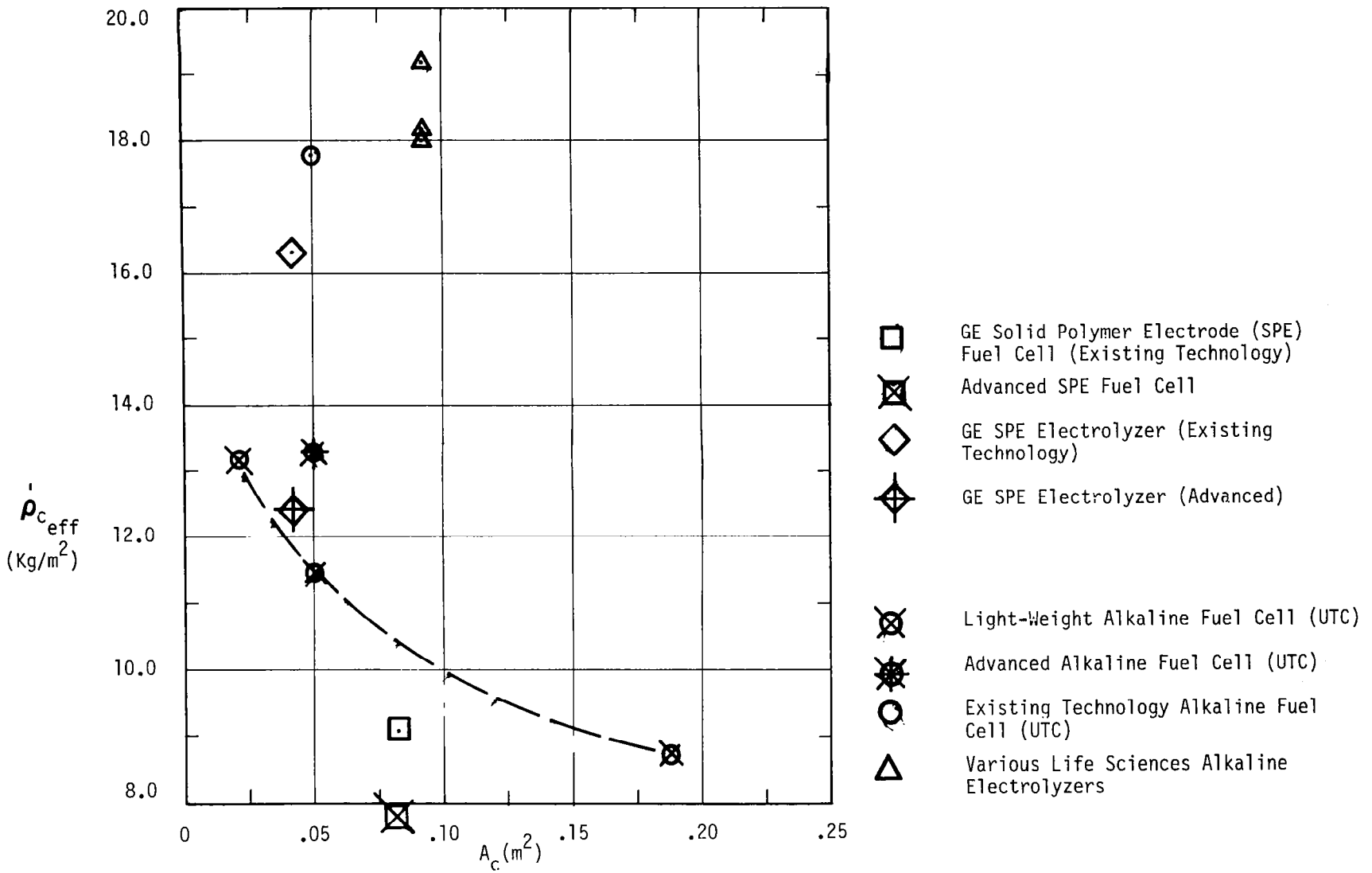

FIGURE 25 FUEL CELL AND ELECTROLYZER POWER SECTION MASS DATA

The heat exchanger (HXR) needed for the fuel cell and electrolyzer is sized based upon peak heat rejection requirements. Since the electrolyzer has the higher peak power operating condition and the less favorable heat transfer conditions; that is, it must reject heat in daylight hours, it usually determines peak heat rejection requirements. If it is assumed that the heat exchanger is a flat plate radiator oriented such that at most it is exposed to albedo, q_{IR}, and infrared earth radiation, then the heat transfer per unit area can be approximated by:

$$q''_{HXR} = \bar{h}_{CELL} (T_{REACT} - T_{\infty}) + T_{REACT}^4 - (q''_A + q''_{IR}) \quad (59)$$

where T_{REACT} is radiator average temperature and T_{∞} is free stream temperature. For an albedo of .8 and a downward pointing surface, $q''_A = 560 W/m^2$ and $q''_{IR} = 200\ W/m^2$. A graph of q''_{HXR} as a function of radiator average temperature is provided in Figure 26. If the radiator has a mass per unit area of ρ'_{HXR} and the peak power radiated is approximated by $\frac{P_{ELEC}}{\eta \hat{}_{ELEC}} - P_{ELEC}$, then the mass of the radiator, M_{HXR}, is

$$M_{HXR} = \frac{\rho'_{HXR}}{q_{HXR}} = \frac{(1-\eta_{ELEC})}{\eta_{ELEC}} \hat{\rho}_{ELEC} = \mu_{HXR} \frac{(1-\eta_{ELEC})}{\eta_{ELEC}} \hat{\rho}_{ELEC} \quad (60)$$

where $\mu_{HXR} = \frac{\rho'_{HXR}}{q_{HXR}}$

A typical value for ρ'_{HXR} is $5.5\ Kg/m^2$.

Using the expressions developed in preceding paragraphs, the mass of the energy storage system can be summarized as follows:

$$M_{ST} = M_{REACT} + M_{TANK} + M_{ELEC} + M_{FC} + M_{HXR} \quad (61)$$

$$M_{ST} = \frac{(1+f)}{\varepsilon} \frac{\bar{P}_{FC}\, t_{NIGHT}}{\eta_{ELEC}} + \hat{P}_{ELEC}\, \mu_{ELEC} + \frac{\mu_{HXR}(1-\eta_{ELEC})}{\hat{\eta}} + M_{ELEC}$$

$$+ \hat{P}_{FC}\mu_{FC} + M_{FC} \quad (62)$$

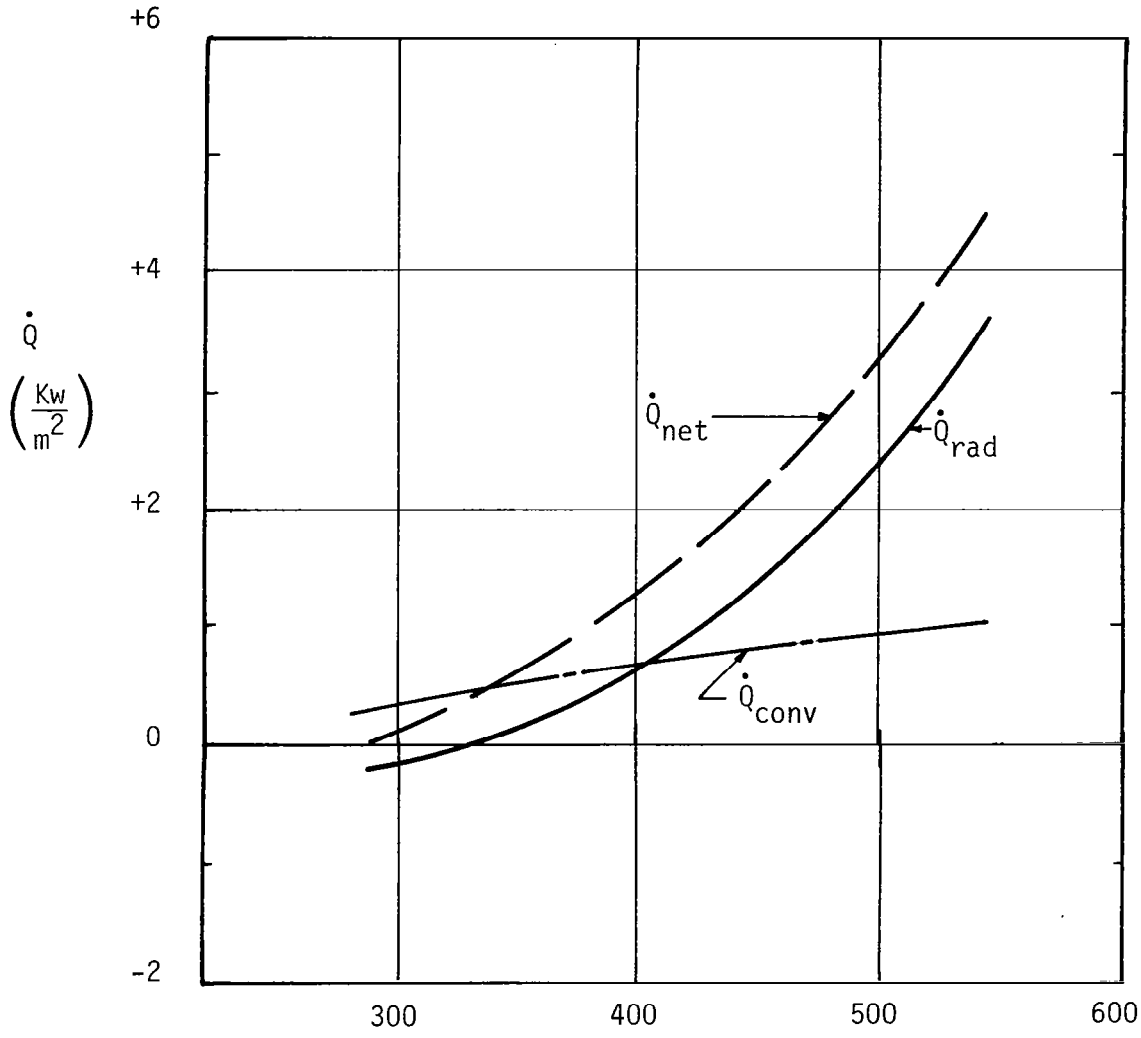

EARTH-POINTING

α_s = .75 ALBEDO = 560 w/m^2

ε_{IR} = .85 LWIR = 200 w/m^2

V = 27 m/s

STREAM-WISE LENGTH = 10 ft

ALTITUDE = 20 km

FIGURE 26 BASELINE HEAT TRANSFER CONDITIONS

$$\text{or} \quad M_{ST} = \frac{(1+f)\,\bar{P}_{FC}\,t_{NIGHT}}{\varepsilon\bar{\eta}_{FC}} + \hat{P}_{FC}\,\mu_{FC_1} + \frac{\mu_{FC_o}}{\hat{\eta}_{FC}} + M_{FC}$$

$$+ P_{ELEC}\,\frac{\mu_{ELEC_1}}{\eta_{ELEC}} + \mu_{ELEC_o} + \mu_{HXR}\,\frac{(1-\eta_{ELEC})}{\hat{\eta}} + M_{ELEC} \qquad (63)$$

From chemical kinetics (see Appendix B for derivation) the voltage efficiency of the electrolyzer can be expressed as

$$\frac{1}{\eta_{ELEC}} = 1 + e_1 + e_2 \ln(i) + e_3 i + \frac{V_c}{V_o} \qquad (64)$$

or in terms of the power density, $P'_{C_{ELEC}} = V_{ci} = \frac{V_o i}{\eta_{ELEC}}$

$$\frac{1}{\eta_{ELEC}} = 1 + e'_1 + e_2 \ln\left(P'_{C_{ELEC}}\,\eta_{ELEC}\right) + e_3\,\eta_{ELEC}\,P'_{C_{ELEC}} \qquad (65)$$

Using a representation of electrolyzer efficiency as shown in (65), the effects of the variation of solar flux available during the day on electrolyzer mass flow rate and efficiency can be determined as in Figure 27.

The peaks either side of noon are due to the effects of solar cell temperature on the cell efficiency which, in turn, affects the power available for electrolysis.

Similarly, the efficiency of the fuel cell can be expressed as

$$\eta_{FC} = 1 - f_1 - f_2 \ln(i) - f_3 i \qquad (66)$$

or in terms of

$$P'_{C_{FC}} = V_{CELL}\,i = \eta_{FC}\,V_o\,i \qquad (67)$$

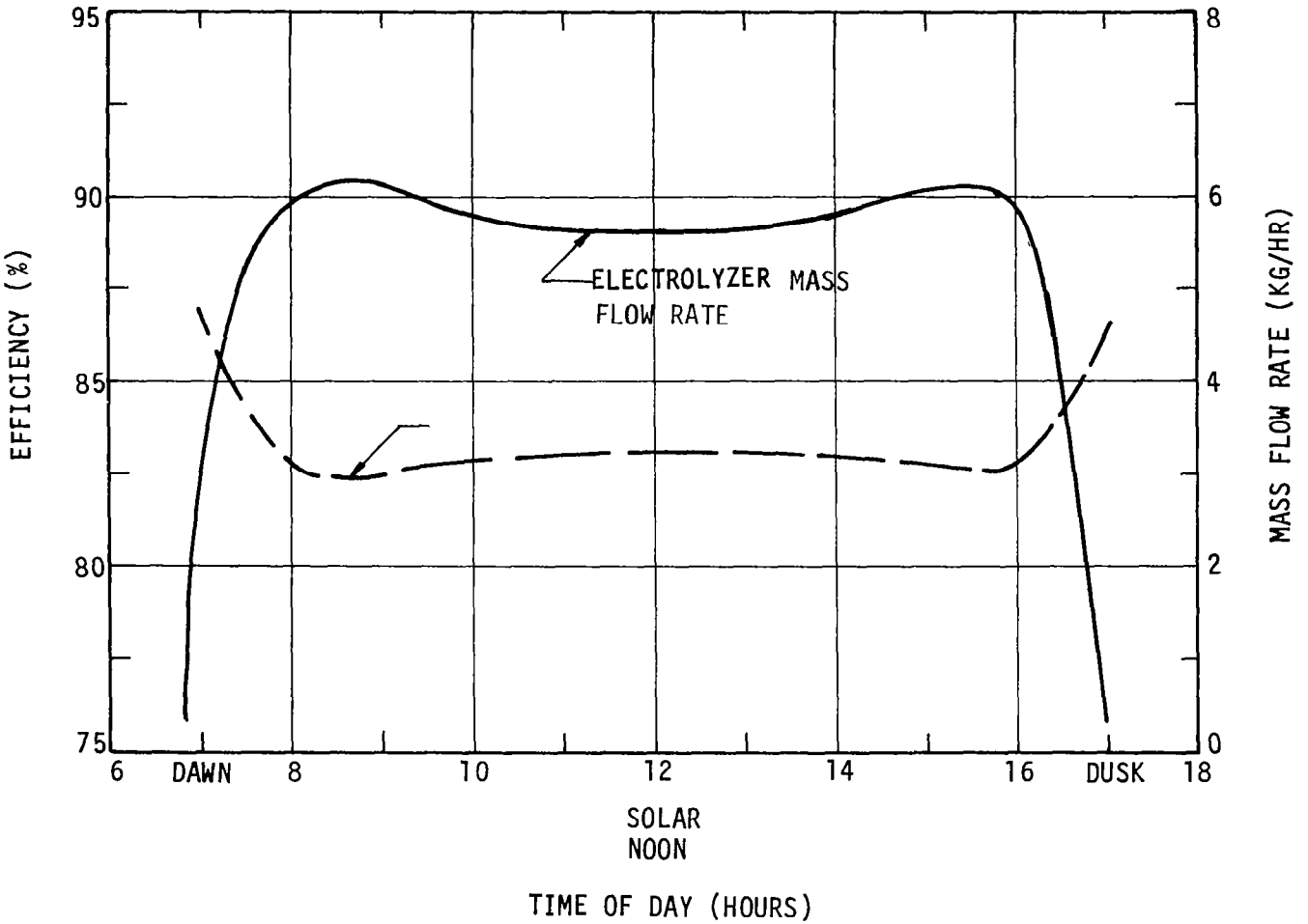

FIGURE 27 ELECTROLYZER EFFICIENCY AND MASS FLOW RATE AS A FUNCTION OF TIME OF DAY

$$\eta_{FC} = 1 - f_1 - f_2 \ln\left(\frac{P'_{C\,FC}}{\eta_{FC}}\right) - f_3\left(\frac{P'_{C\,FC}}{\eta_{FC}}\right) \qquad (68)$$

The values of e_i and f_i can be evaluated from graphs of voltage versus current density for a particular cell design.

To illustrate the optimization possible with the parameters of the energy storage scheme discussed in this section, the following simplifying assumptions will be made:

(a) The power available from the energy collection scheme is constant $S_{COLL} I_{SUN} \eta_{COLL}$ and equal to the power supplied to the electrolyzer, $\frac{P_{ELEC}}{\eta_{ELEC}}$.

(b) The nighttime power demand on the fuel cell is constant.

(c) No power conditioner is needed to match loads.

(d) The efficiency can be simplified to

$$\eta_{FC} = f_1' - f_3 \frac{P'_{C\,FC}}{\eta_{FC}} \qquad \text{and} \qquad (69)$$

$$\frac{1}{\eta_{ELEC}} = C_1 + \eta_{ELEC} P'_{C_{ELEC}} \qquad (70)$$

With these assumptions, the average power and peak powers are equal and so are the corresponding efficiencies. Without distinguishing between average and peak values, equation (63) becomes

$$M_{ST} = \frac{(1+f)P_{FC}t_{NIGHT}}{\varepsilon\eta_{FC}} + P_{FC}\ \mu_{FC_1} + \frac{\mu_{FC_o}}{\eta_{FC}} + M_{FC} + \tag{71}$$

$$P_{ELEC}\left(\frac{\mu_{ELEC_1}}{\eta_{ELEC}}\right) + \mu_{ELEC_o} + \mu_{HXR}\ \frac{(1-\eta_{ELEC})}{\eta_{ELEC}} + M_{ELEC} \tag{72}$$

Adding the mass of the collector this becomes

$$M_{ST+COLL} = P_{FC}\ \frac{1}{\eta_{FC}}\ \frac{(1+f)}{\varepsilon}\ t_{NIGHT} + \mu_{FC_o} + \mu_{FC_1} + M_{FC} +$$

$$P_{ELEC}\left(\frac{1}{\eta_{ELEC}}\right)\left(\mu_{ELEC_1}\right) + \mu_{HXR} + \mu_{ELEC_o} - \mu_{HXR} + M_{ELEC} +$$

$$\rho'_{COLL}S_{COLL} \tag{73}$$

From conservation of energy

$$P_{ELEC}t_{DAY} = \frac{P_{FC}\ t_{NIGHT}}{\eta_{FC}} \tag{74}$$

and power continuity

$$\frac{P_{ELEC}}{\eta_{ELEC}} = S_{COLL}\ I_{SUN}\eta_{COLL} \tag{75}$$

This then gives the relationship

$$S_{COLL} = \frac{P_{FC}\ t_{NIGHT}}{\eta_{COLL}\eta_{ELEC}\eta_{FC}\ t_{DAY}I_{SUN}} \tag{76}$$

such that

$$M_{ST + COLL} = P_{FC} \left[\frac{1}{\eta_{FC}} \left[\frac{(1+f)\, t_{NIGHT}}{\varepsilon} + \mu_{FC_o} \right] + \frac{\rho'_{COLL}\, t_{NIGHT}}{\eta_{ELEC}\, \eta_{COLL}\, t_{DAY}\, I_{SUN}} \right.$$

$$\left. + \frac{t_{NIGHT}}{t_{DAY}} \frac{1}{\eta_{ELEC_1}} \left[\mu_{ELEC_1} + \mu_{HXR} \right] + \left[\mu_{ELEC_o} - \mu_{HXR} \right] + \mu_{FC_1} \right]$$

$$+ M_{FL} + M_{ELEC} \qquad (77)$$

$$M_{ST + COLL} = \left(\frac{P_{FC}}{\eta_{FC}} \right) \mu_{EFF} + \mu_{FC_1} + M_o \qquad (78)$$

where

$$\mu_{EFF} = \frac{(1+f)\, t_{NIGHT}}{\varepsilon} + \mu_{FC_o} + \frac{\rho'_{COLL}\, t_{NIGHT}}{\eta_{ELEC} \eta_{COLL}\, t_{DAY}\, I_{SUN}} + \frac{t_{NIGHT}}{t_{DAY}} \frac{(\mu_{ELEC} + \mu_{HXR})}{\eta_{ELEC}}$$

$$+ \left[\mu_{ELEC_o} - \mu_{HXR} \right]$$

and $M_o = M_{FC} + M_{ELEC}$

The value of η_{FC} which gives minimum $M_{ST + COLL}$ can be found by differentiating with respect to η_{FC} such that

$$\frac{\delta M_{ST + COLL}}{\delta \eta_{FC}} = -\left(\frac{P_{FC}}{\eta_{FC}^2} \right) \mu_{EFF} + \mu_{FC_1} + \frac{P_{FC}}{\eta_{FC}} \frac{\delta \mu_{FC_1}}{\delta \eta_{FC}} = 0 \qquad (79)$$

Evaluation of $\frac{\delta \mu_{FC_1}}{\delta \eta_{FC}}$ can be obtained from (58) as

$$\frac{\delta \mu_{FC_1}}{\delta \eta_{FC}} = - \left(\frac{\rho'_{CELL_{EFF}}}{(P'_C)^2} \right)_{FC} \frac{\delta P'_C}{\delta \eta_{FC}} = - \frac{\mu_{FC_1}}{P'_C} \left(\frac{\delta P_{CELL}}{\delta \eta_{FC}} \right) \tag{80}$$

Using the assumption that

$$\eta_{FC} = f_1 + f_2 \left(\frac{P'_C}{\eta} \right)_{FC} \quad \text{and rearranging this becomes} \tag{81}$$

$$P'_C = \frac{f_1}{f_3} \eta_{FC} - \frac{1}{f_3} \eta_{FC}^2 = \frac{\eta_{FC}}{f^3} (f_1 - \eta_{FC}) \tag{82}$$

so that

$$\frac{\delta P'_C}{\delta \eta_{FC}} = \frac{f_1}{f_3} - \frac{2}{f_3} \eta_{FC} = \left(\frac{1}{f_3} \right) f_1 - 2\eta_{FC} \tag{83}$$

Substituting (58) and (80) into (79) and rearranging, (79) becomes

$$\eta_{FC}^3 - 2f_1\eta_{FC}^2 + f_1^2 - 3f_3 \frac{\rho'_{C_{EFF}}}{\mu_{EFF}} \eta_{FC}$$

$$+ 2f_1 f_3 \left(\frac{\rho'_{C_{EFF}}}{\mu_{EFF}} \right) FC = 0 \tag{84}$$

or

$$\eta_{FC} = y_1 + \frac{2f_1}{3} \tag{85}$$

where y_1 is a real root of

$$y^3 - 1/3\ f_1^2 + \left(\frac{9f_3\ \rho'_{CELL_{EFF}}}{\mu_{EFF}}\right)_{fc} y + 2/27\ f_1^3 + \left(\frac{9f_3\ \rho'_{CELL_{EFF}}}{\mu_{EFF}}\right)_{fc} = 0 \tag{86}$$

such that $0 \leq \eta_{FC} \leq 1$. The variation of power train mass with fuel cell efficiency is depicted in Figure 28. Similarly the variation in power train mass with electrolyzer efficiency is depicted in Figure 29. Note that minimum overall power train mass is achieved at other than the minimum fuel cell or minimum electrolyzer mass. Furthermore the mass optimum operating points of the fuel cell depend on the mass properties of all components between the collector and the fuel cell and the mass optimum operating point of the electrolyzer depends on all the components between it and the collector.

Motor/Controller, Gearbox. The major output of the power train is thrust power required to fly the aircraft. The final stages of the power train must accept the power from electrical cells and then transform this power into the required thrust. As before, minimum weight and maximum efficiency are prime requirements; however, these elements will tend to be a relatively small fraction of the total power train weight. Since thrust generation elements are at the end of the power train, a small increase in efficiency here will be "leveraged" into a significant reduction in the size and weight of the remainder of the system. Where possible, size and mass of thrust generation elements must be optimized with respect to minimizing total system mass.

With near-term technology, the most efficient way to convert electric power to thrust power at the very low flight speeds of solar HAPPS is by means of an electric motor driving a propeller. The low flight dynamic pressure requires that the propeller have a low thrust loading for high efficiency. This, in turn, leads to a large diameter, slow turning design. The motor can either be designed to match the propeller directly, or it may be matched through a gearbox. For this reason, the motor and gearbox must be considered as a unit, and not as individual devices when performing the optimization.

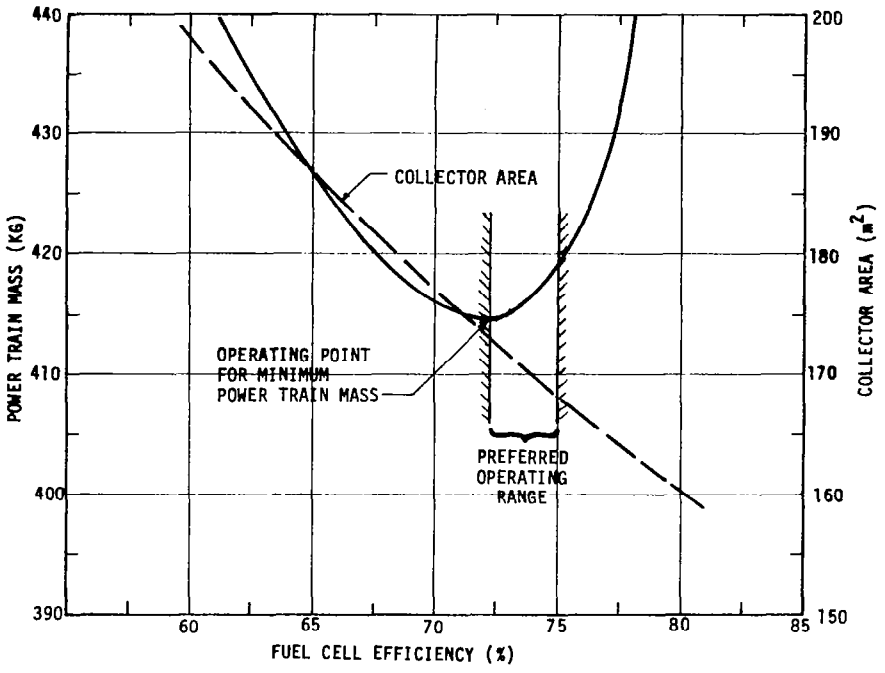

FIGURE 28. COLLECTOR AREA AND POWER TRAIN MASS VERSUS FUEL CELL EFFICIENCY

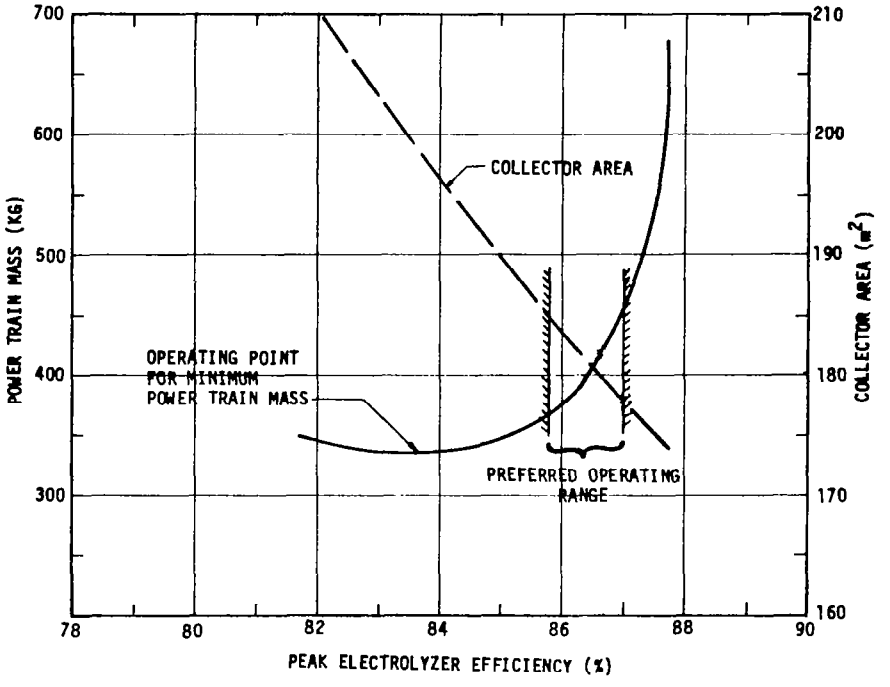

FIGURE 29. COLLECTOR AREA AND POWER TRAIN MASS VERSUS ELECTROLYZER EFFICIENCY

Given the requirements of very high efficiency and of availability in the required size range, brushless DC motors with rare earth magnets appear to be the best choice at this time. The data used in this study was provided by Sunstrand Corp., and was based on the motor used in the Air Force XBQM-106 electric RPV program. Additional preliminary designs were performed to determine the effect of motor shaft speed on weight and efficiency of the system. These results are shown in Figure 30. The shape of the efficiency curve is due to the combined characteristics of the motor and of the controller. Controller losses are mostly switching losses and increase with increasing switching frequency, and thus with increasing motor shaft speed. The motor, however, tends to have maximum efficiency and minimum weight at high shaft speeds. Since all of the feasible motors would require some gearing to match the propeller, a high speed motor was selected for its lower weight.

One problem peculiar to electrically powered airplanes is the determination of peak power required. For a conventionally powered high altitude aircraft, installed power is generally set by the high altitude cruise power requirement. Engine peak power will significantly increase at lower altitudes, thus providing more than adequate take-off and climb performance. An electric propulsion system, however, must be designed to a peak power which is independent of altitude. This is combined with a lower propeller efficiency due to off-design operation at the high air density and very low climb speeds typical of a solar HAPP. Pending a detailed analysis of the off-design characteristics of the motor and prop, combined with the vehicle low altitude climb performance, the motor design power level has been arbitrarily set at twice peak cruise power.

Given the peak-to-cruise power ratio, the motor was scaled from the Sundstrand designs. For a nominal 10Kw (13.17 HP) thrust output, a motor output power of 11.23Kw (15.14 HP) is required. With the peak power factor included this gives a maximum continuous design power of 22.4Kw (30 HP). This gives a scaled mass of 18Kg (39.7 lbs) and a nominal efficiency of 90% at a shaft speed of 10000 rpm. Controller efficiency and maximum speed are strongly dependent on power semiconductor design and should show considerable improvement within the next decade.

The gearbox is based on a Sundstrand preliminary design for a 7.46KW (10 HP) output. The Sundstrand gearbox was scaled for the required peak power, lifetime and reduction ratio. The resulting gearbox, which can be used as an example, has a reduction ratio of 67:1, is sized for a cruise thrust power of 10Kw (13.17 HP), weighs 10Kg (22.05 lbs) and has an efficiency of 97%. It was assumed that the gearbox would scale linearly with shaft power output. It should be noted that there are several evolving technologies that could provide the required reduction ratios with improved efficiency and reduced weight.

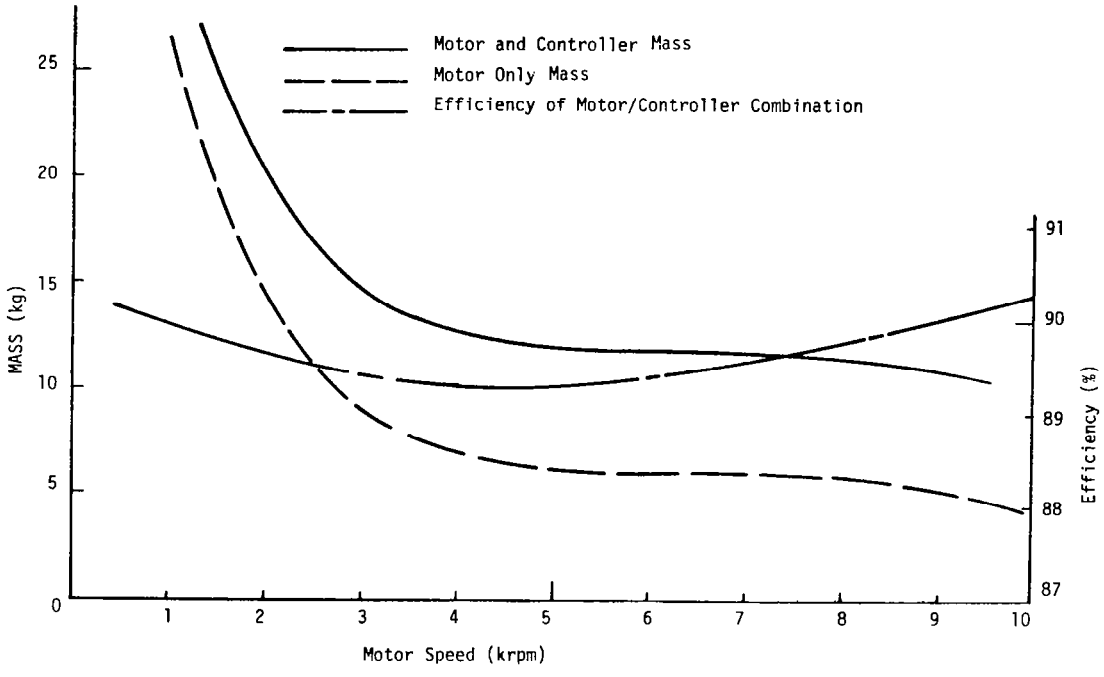

FIGURE 30. MASS AND EFFICIENCY SUMMARY FOR MOTOR AND CONTROLLER

Propeller. The propeller is the final element in the power train. A low efficiency propeller can cause a large increase in power train mass. Propeller efficiency is closely linked with its diameter and thus its own mass. This allows a mass versus efficiency trade to be made over a relatively wide range when minimizing total power train mass.

Propeller performance is calculated by the minimum induced loss method described in reference 13. This method requires inputs of the diameter, shaft speed, number of blades, air density, design true air speed and either the desired thrust output or the shaft power input. The desired blade section lift coefficient and lift-to-drag ratio must also be supplied. The output is blade twist, chord distribution and efficiency. Propeller performance was calculated and optimized off-line and the results used as inputs to the main power train methodology.

The propeller design method was subjected to several external constraits. First, tip relative mach number was limited to a value of 0.9. This was only a consideration for the smaller and faster turning propellers. Second, blade chord 0.30 of the radius out from the hub was constrainted to be not less than 0.08 of propeller radius. This limit is similar to an aspect ratio limit on a wing. The value chosen is representative of recent human powered aircraft (HPA) propellers. Finally, the design blade lift coefficient was selected to be 0.6. This value allows enough blade stall margin to absorb takeoff and climb power levels.

The high cruise altitude and slow speed of a solar HAPP will result in very low Reynolds numbers for the propeller blades. The propeller presented here has cruise Reynolds numbers in the range of 100000 to 170000 over most of the blade. This is a region where airfoil performance degrades rapidly as R_N is reduced. Based on the data in Reference 14, a blade section L/D of 50:1 was used.

Low Reynolds numbers tend to discourage the use of several small propellers, or the use of more than 2 blades. For example, when replacing a two-bladed propeller with a three-blade design with all other factors held constant, the blade chord and Reynolds number will both be reduced by 33%. Total blade area will remain nearly constant. This would reduce L/D to about 35 and the efficiency by several percent. If the same limit on chord-to-diameter ratio is imposed on both propellers, diameter or shaft speed must be reduced on the three-blade design which will also tend to hurt efficiency. A single two-bladed propeller has, therefore, been used in all calculations in this study.

Weight estimation is based on a method from Reference (15). The equation has been converted to metric variables and is:

$$M_{PROP} = .793\ N^{.391}\ (D \times P)^{.782} \qquad (87)$$

The constant was adjusted to give good results when referenced to recent HPA propellers and previous HAPP designs.

The propeller baseline to be presented later was selected for a thrust power output of 10Kw (13.2 HP) at 20Km (65 600 ft) altitude and 27mps (52.5 Kts) cruise speed. For a given shaft speed, diameter was varied until either blade chord-to-diameter limit or tip mach number limit was reached. In all cases, maximum efficiency occurred at these limits. The results are shown in Figure 31. It can be seen that there is an optimum diameter for peak efficiency and that propeller weight increases rapidly with increasing diameter. The optimum propeller was selected by minimizing the total power train system mass as shown in Figure 32. The result is shown in Figure 33 and is slightly smaller and lighter than the most efficient propeller.

The resulting propeller diameter of 12 meters (39 feet) is quite large by normal standards. When compared to the vehicle wingspan, a diameter-to-wingspan ratio of about 1:9 is obtained. This is smaller than the typical values of 1:5 found on conventional single propeller aircraft. The use of multiple propellers will reduce the diameter of each propeller, but the total disc area will remain approximately constant. Twin propellers would each have a diameter of about 8.5 meters (28 ft).

A three-bladed propeller will tend to run with significantly less vibration than a two-blade design; however, there will be a reduction in efficiency due to lower Reynolds numbers. A more detailed analysis should be performed to determine exact efficiency loss and if the greater smoothness of the three-bladed propeller is worth the extra losses.

A single controller-motor-gearbox-propeller system is obviously undesirable for reliability reasons. However, the use of two systems may result in excessive assymetric thrust if either system fails. This redundancy will result in some increase in motor and controller weights. Propeller and gearbox weights will be nearly constant. Lower Reynolds numbers will result in an efficiency loss. One possible solution would be to use two separate motor and controller units to drive one large propeller through a combining gearbox. The single motor and propeller used as the baseline represent the highest possible efficiency and minimum weight; however, penalties for redundant systems might be small enough to be acceptable.

Finally, there is relatively little chance of improving propeller efficiency. The major improvements possible are to increase blade aspect ratio, decrease weight and improve airfoil lift-to-drag ratio. At best, an increase to about 96% efficiency might be possible.

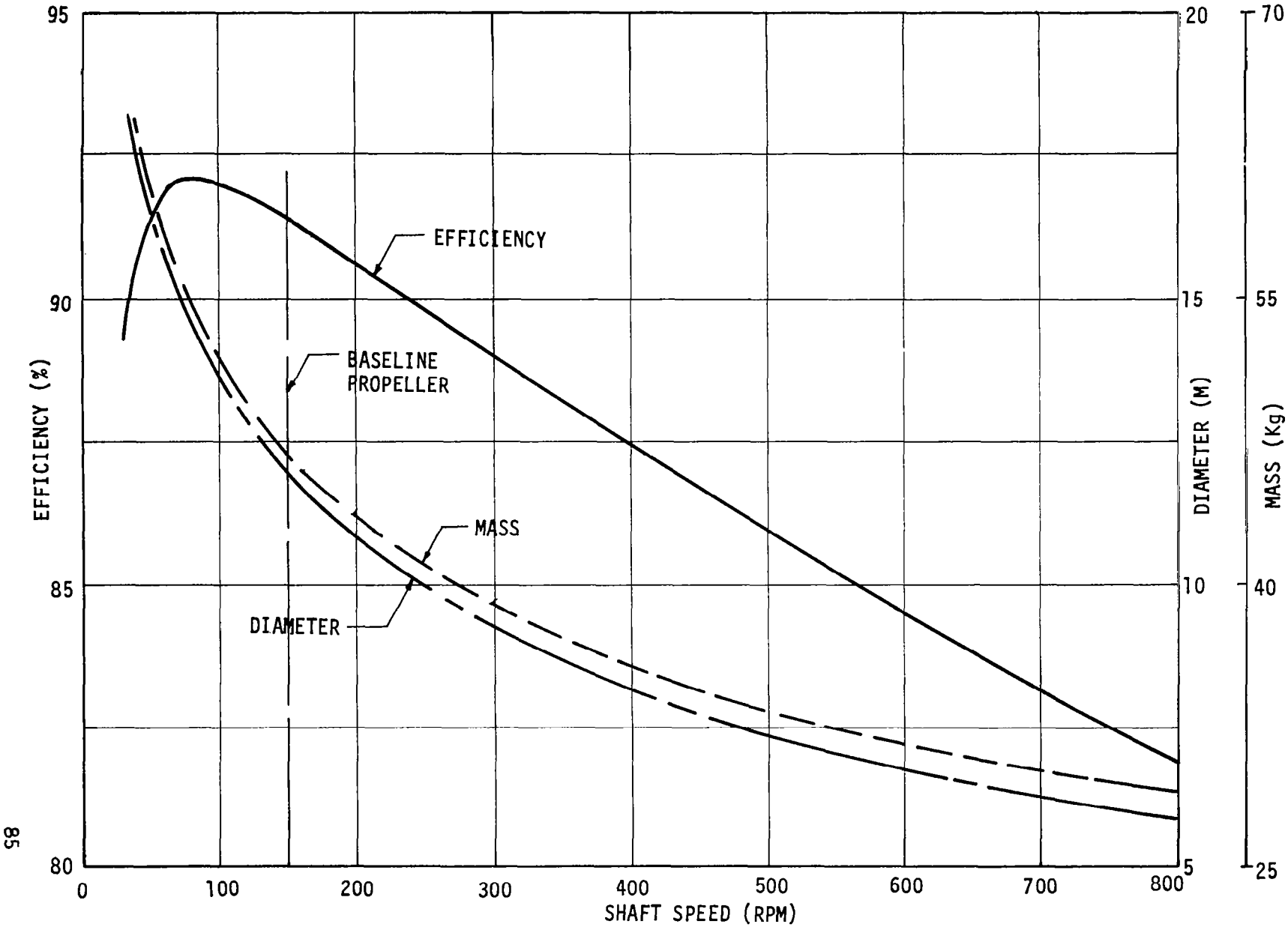

FIGURE 31. PROPELLER DESIGN FOR 10 Kw (13.2 HP) THRUST POWER

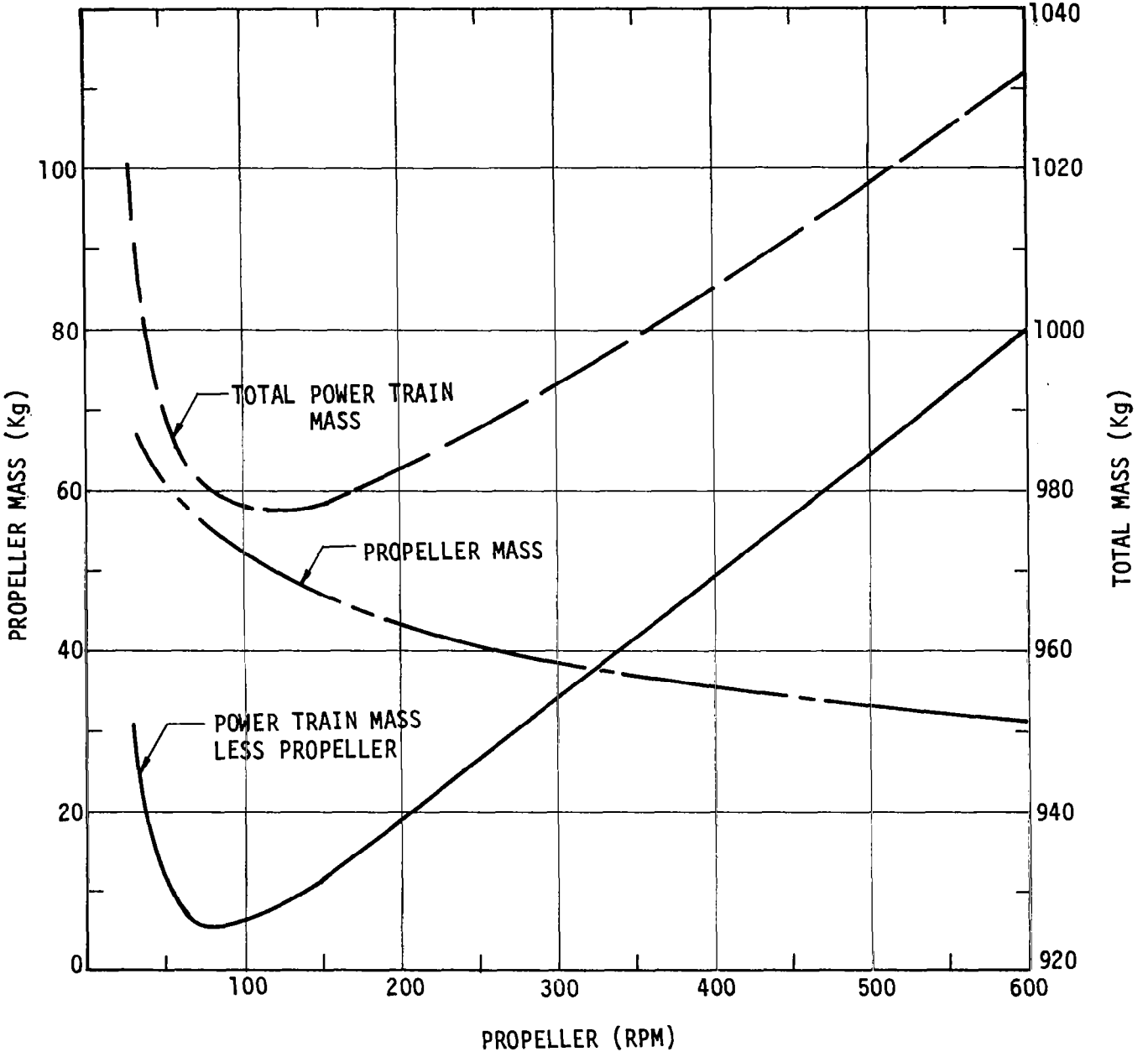

FIGURE 32. PROPELLER MASS OPTIMIZATION

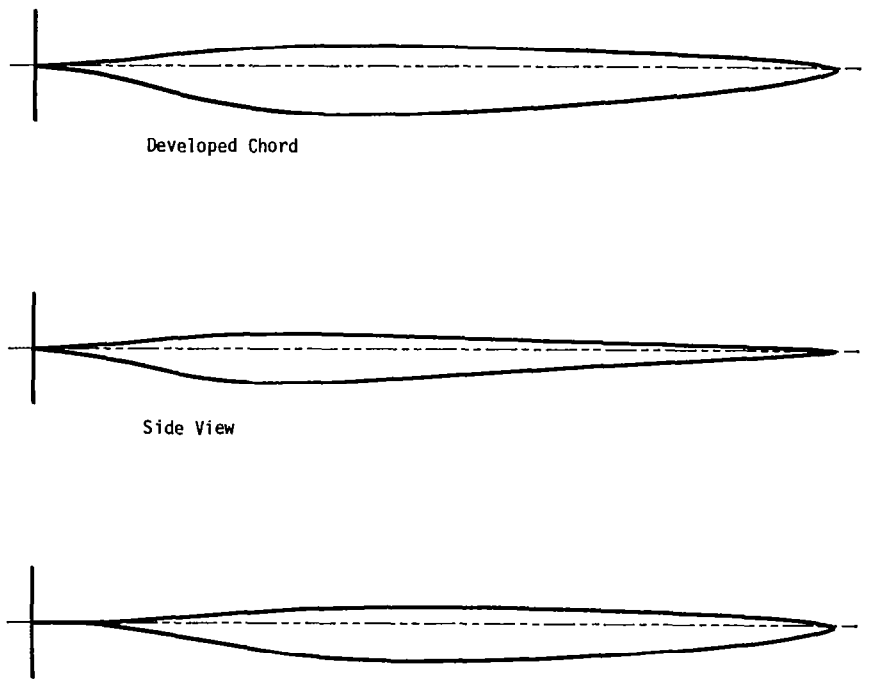

FIGURE 33. BASELINE PROPELLER DESIGN

VEHICLE DESIGN METHODOLOGY

Overview

As discussed in earlier sections, there are many variables which must be considered in the design of a long endurance regeneratively powered aircraft which take it out of the category of conventional vehicles. A list of these variables was presented in Table 3 and all must be examined together during any parametric sizing task to assure that complex interactions are taken into account.

The method presented here which was just discussed as a series of parts takes all pertinent variables identified in this study into consideration and analyzes their interactions by iterating between power train and vehicle sizing equations. It starts with a qualitative judgment of the critical factors in the desired mission. Then environmental information for the mission areas is examined to determine environmental worst cases where sunlight is at a minimum angle or of a minimum duration. The method then works as follows:

- Basic mission parameters are specified such as altitude to be maintained, worst case latitude, worst case time of year, initial collector orientation, minimum allowable speeds, on-board power required for mission payload.
- Solar flux is determined per square unit of collector area and this is integrated over a day to provide specific energy into the collector.
- Non-thrust power levels and durations are specified.
- Power train component efficiencies and specific power relationships are specified.
- Starting points for iterations are chosen (usually gross mass, thrust power available, collector area, aspect ratio, or lift coefficient).

The result of these calculations is a matrix of vehicles which meet, to one degree or another, mission sizing conditions. These vehicles are described in terms of basic physical and aerodynamic parameters which lend themselves to comparison. Typical examples used are wing loading, power-to-weight ratio, lift-to-drag ratio, collector packing factor if horizontal collectors are used, ratio of vertical panels to span if variable geometry vertical collectors are used, and lift coefficient.

Parametric Analysis Methods

In order to identify domains of HAPP's which potentially fulfill mission requirements, the data generated by combining power train and vehicle sizing methodologies must be presented in such a way that all pertinent variables are taken into account. Two parameters against which data may be plotted are aircraft power-to-weight ratio and wing loading. These characteristics are not unique to solar HAPP's and are commonly used in conceptual design. Many of the parameters used here are peculiar to solar HAPP's. Starting with parameters applicable to all aircraft (see Figure 34) and adding constraints peculiar to solar HAPP's may assist the reader in gaining a feel for why these vehicles are, indeed, unique. Figure 35 will be the basic working plot to be used in this analysis. Note that the center plot, although sizable in the range of solar HAPP's incorporated in it, is only a small point in the lower left hand corner of Figure 34.

Early work in this study showed that variable geometry aircraft offered the most promise for missions at moderate to high latitudes. The detailed reasoning that led to a decision to consider variable geometry will be explained in the configuration characteristics section. Consideration of vehicles which vary geometry from daytime to nighttime leads to the necessity to decide which set of power-to-weight ratio/wing loading numbers to use to describe each aircraft. The design point is typically the winter solstice which is characterized by up to 16 hours of darkness at the latitudes considered here. For this reason, nighttime values of power-to-weight ratio and wing loading were chosen as starting parameters. Other parameters applicable to variable geometry solar HAPP's are daytime lift coefficient, daytime aspect ratio, nighttime aspect ratio, and vertical panel height-to-daytime wingspan ratio (h/b). These variables are all interconnected through h/b. Using a simplified model to illustrate, consider a HAPP with rectangular wing planform such that geometric chord is constant in both daytime and nighttime configurations. Then:

$$b_{NIGHT} = b_{DAY} + 2h \tag{88}$$

$$b_{NIGHT} = b_{DAY} \left(1 + 2 \frac{h}{b}\right) \tag{89}$$

Dividing by wing chord yields:

$$\frac{b_{NIGHT}}{\bar{c}} = \frac{b_{DAY}}{\bar{c}} \left(1 + 2 \frac{h}{b}\right) \tag{90}$$

$$AR_{NIGHT} = AR_{DAY} \left(1 + 2 \frac{h}{b}\right) \tag{91}$$

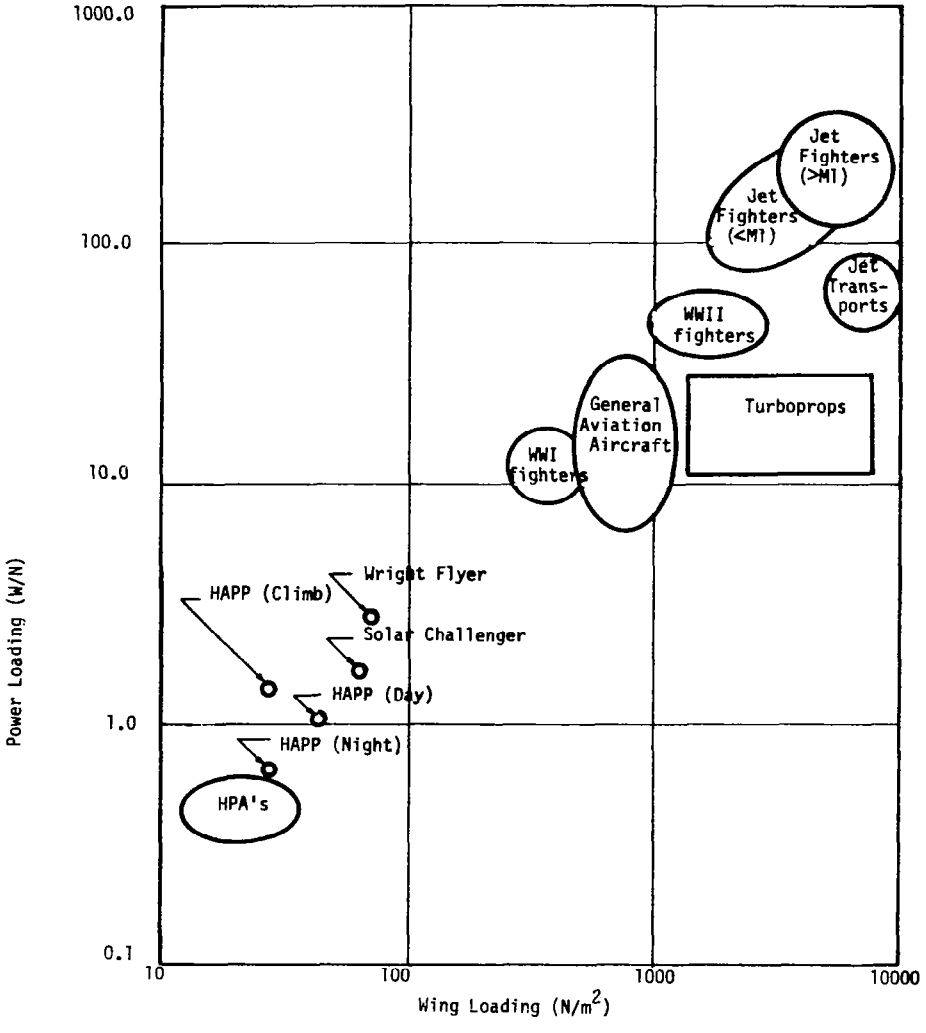

FIGURE 34 HISTORICAL RANGES OF POWER LOADING AND WING LOADING

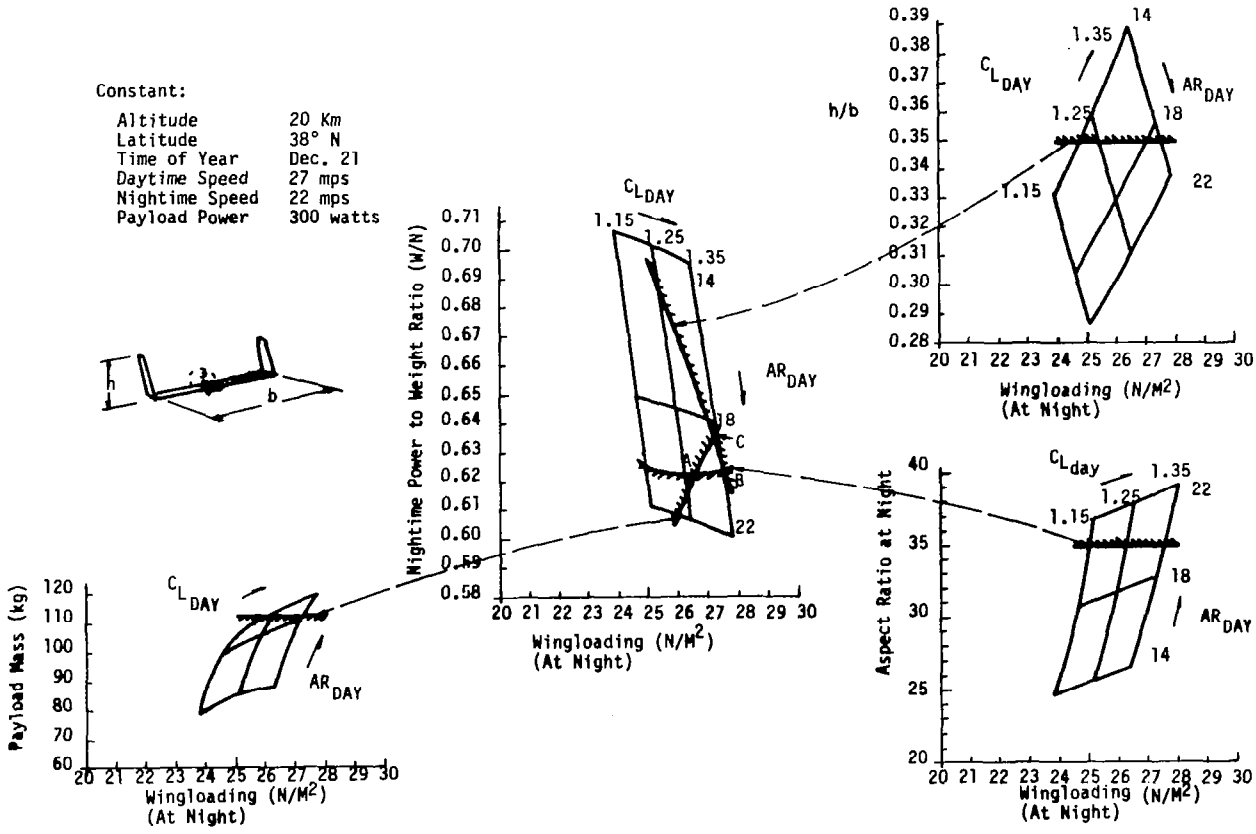

FIGURE 35 PARAMETRIC SIZING METHODOLOGY RESULTS SHOWING DATA PRESENTATION METHOD USED

Of these variables, all but AR_{DAY} have artificial limits applied to them. Sizing studies done to date have shown solar HAPP's to be quite large aircraft characterized by very high aspect ratio wings. Limiting aspect ratio is typically that at which structural weight increases overpower aerodynamic efficiency gains. This limit has been around 35 in previous studies and is the limit applied here to nighttime aspect ratio.

If nighttime aspect ratio is limited and $\frac{h}{b}$ is allowed to get too high, then daytime aspect ratio will be lower than may be desirable for low daytime drag coefficients. In determining a practical upper limit to $\frac{h}{b}$, other factors must be taken into consideration. If $\frac{h}{b}$ is too high and daytime aspect ratio is too low, a significant portion of vehicle mass will be above the aircraft in the daytime configuration raising the vertical center of gravity location. This will affect both static and dynamic stability. Endplate effect on total drag coefficient from raised wingtips continues to increase with increasing $\frac{h}{b}$ to a point. Beyond that point little further benefit may be derived from increases in $\frac{h}{b}$. This limit has been around 0.35 for configurations considered in previous internally funded studies. Since roughly the same total drag coefficient can be obtained from combinations of high daytime aspect ratio (low $\frac{h}{b}$) and low daytime aspect ratio (high $\frac{h}{b}$), the preference will be toward high daytime apsect ratio (low $\frac{h}{b}$) to minimize vertical c.g. displacement. Limits imposed on nighttime aspect ratio and $\frac{h}{b}$ will keep daytime aspect ratio in the 10 to 25 range and it will be monitored during this parametric investigation to assure that daytime/nighttime geometric relationships appear workable.

Also coupled to aspect ratio changes with time of day and $\frac{h}{b}$ is lift coefficient. Since more wing area is available at night than in the daytime, daytime lift coefficient will be higher than that at night. High lift coefficients should be attainable with properly chosen airfoils as will be discussed in the airfoil characteristics section. For purposes of this parametric investigation, daytime lift coefficient will be monitored with an artificial upper limit of 1.35 imposed if necessary.

To summarize, the procedure described in the previous section is followed to provide a matrix of parametric aircraft which are all similar in that

- Cruise altitude
- Most sensitive latitude for solar energy collection

- Most sensitive time of year for solar energy collection
- Minimum daytime and nighttime speeds for station keeping in 95th percentile winds and
- Payload power required

are held constant while daytime lift coefficient and daytime aspect ratio are varied. Plots will be prepared comparing nighttime aspect ratio with nighttime wing loading for monitored values of daytime lift coefficient and daytime aspect ratio. Constraint lines to be applied will be found by analyzing the sensitivities to wing loading of the parameters to be limited. In this series of plots these will be nighttime aspect ratio and h/b. If payload mass is limited to a certain value, this may be handled the same way and its constraint line applied to the parametric plot. Figure 35 center presents an example of this parametric analysis method applied to a solar HAPP vehicle. Plots to determine constraint lines are shown around the periphery. The triangular region of interest in the center defines a domain of workable HAPP's, all of which meet desired mission and aerodynamic criteria, but only one aircraft in this domain is the best vehicle. Consider the vertices first. Point A is a good choice if payload is limited to a specified value and lift coefficient is to be minimized. Point B is the point at which payload is maximized. Point C is the point at which nighttime aspect ratio is minimized.

For the given primary mission with a specified payload, point C will yield the smallest workable aircraft for each gross mass value examined. Similar plots can be put together for other values of gross mass, the same constraints applied and other points similar to point C found. If these points are examined with regard to some other aircraft parameter to be maximized (payload fraction, for instance) or minimized (installed power-to-weight ratio which will be a strong cost driver), then an optimum gross mass may be found with regard to these particular parameters.

Point B is another point of interest if the designer's goal is to provide a maximum payload capability for vehicle size. This analysis would start with the preparation of plots such as Figure 35 for a range of gross masses, the data to be discussed here ranging from 550 Kg to 1100 Kg. Constraints are applied and the points B are picked off. A few quick calculations will yield the payload corresponding to each point B which can be plotted against gross mass to yield a curve as in Figure 36. The tangent to this curve which passes through the origin defines the maximum payload per unit vehicle weight and there is a vehicle gross mass and payload associated with this point. If other factors are unimportant, such as cost or power train size, then this vehicle will be the most efficient payload lifter at this altitude, latitude, and time of year.

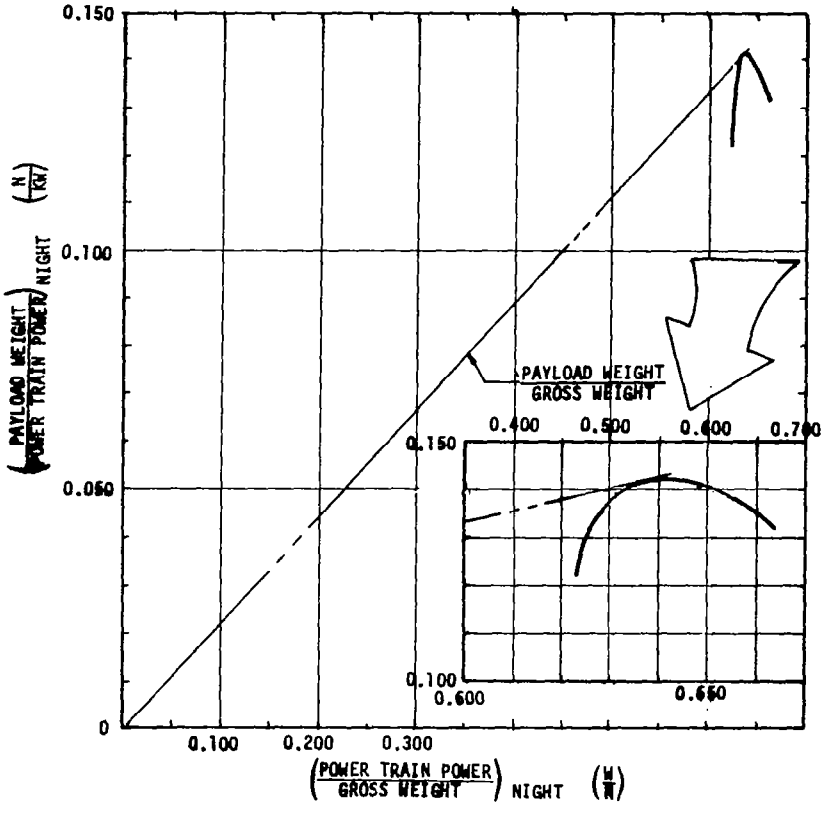

FIGURE 36 DETERMINATION OF MAXIMUM PAYLOAD WEIGHT PER UNIT INSTALLED POWER

If, however, the maximum payload fraction can be traded off against installed power-to-weight ratio to find the lowest powered vehicle for lifting maximum payloads, then a plot like Figure 37 bottom may be prepared. The vehicle chosen would be defined by the bucket in this curve. It would also be the most economical payload lifter.

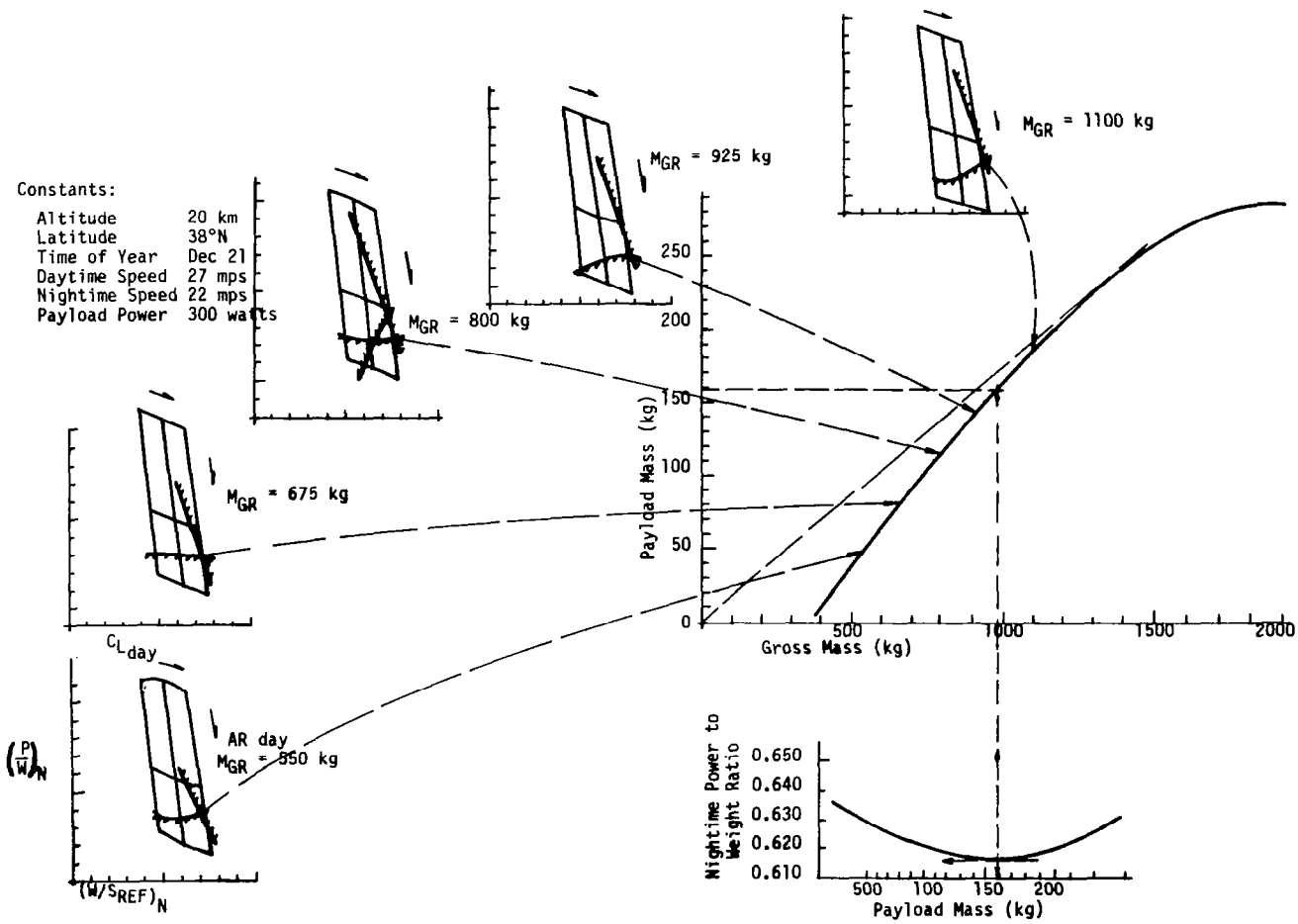

FIGURE 37 DETERMINATION OF MAXIMUM PAYLOAD DESIGN POINT

Aerodynamic Characterization

A generalized methodology for predicting the lift, drag and pitching moment characteristics of a HAPP will be presented in this section. In the case of lift coefficient and pitching moment coefficient prediction, open literature has been consulted to determine what may be achievable within HAPP design constraints.[1]

The drag coefficient, C_{D_T}, has been modelled in as general a manner as possible to allow the analysis of drastically different configurations. The C_{D_T} may be written as:

$$C_{D_T} = C_{D_{MIN}} + C_{D_L} \tag{92}$$

In this methodology it has been convenient to separate the drag coefficient into three components as Figure 38 indicates.

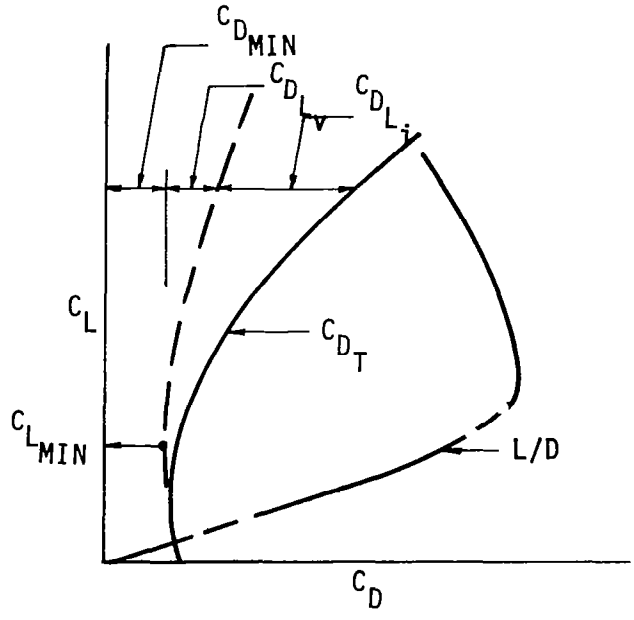

FIGURE 38 TYPICAL DRAG POLAR

1 Throughout this discussion the finite wing characteristics, C_L, C_D, and C_M are assumed to be equivalent to the section characteristics, C_l, C_d, and C_m, since in most cases the wings analyzed are of very high aspect ratio.

Equation 92 can be rewritten as:

$$C_{D_T} = C_{D_{min}} + C_{D_{L_v}} + C_{D_{L_i}} \tag{93}$$

where:

$C_{D_{L_v}}$ = viscous drag due to angle of attack (i.e., increased skin friction and separation)

$C_{D_{L_i}}$ = inviscid or induced drag due to lift

General analytic methods have been set up to predict values for $C_{D_{min}}$ and $C_{D_{L_i}}$, while again data from open literature has been used to estimate $C_{D_{L_v}}$ vs. C_L behavior.

Minimum Drag. Standard industry prediction methods applicable to conventional aircraft have been adapted for use in determining the minimum drag coefficient of a HAPP. Each candidate configuration is analyzed as a collection of wing panels (including any vertical panel surfaces), streamlined bodies, and miscellaneous items such as wires and bracing posts.

The min drag coefficient, $C_{D_{min}}$ of any HAPP wing panel (vertical, horizontal or otherwise) can, according to reference 15, be expressed as:

$$\left(C_{D_{min}}\right)_W = C_{f_T}\left[1 + L\left(\frac{t}{c}\right) + 100\left(\frac{t}{c}\right)^4\right] R \frac{S_{WET}}{S_{REF}} \tag{94}$$

where:

L = airfoil thickness location parameter; L = 1.2 for max thickness located at or aft of 30% chord, L = 2.0 for max thickness forward of the 30% chord point

R = Lifting surface correction factor; R = 1.07 for Mach numbers less than 0.25 and sweep of the max thickness line less than 10^o

C_{f_T} = flat plate normal transition turbulent skin friction coefficient

$$C_{f_T} = \frac{.427}{\left\{\log_{10} R_N - .407\right\}^{2.64}}$$

R_N = Reynolds number based on the mean chord length of the wing section

$$R_N = \frac{\rho V \bar{c}}{\mu}$$

Experimentally determined values of $\left(C_{D_{min}}\right)_W$ at Reynolds numbers between 0.25 and 1.3 million for several high lift airfoil sections are compared in Figure 39 to $\left(C_{D_{min}}\right)_W$ values predicted by equation 94. It appears from the figure that the method of equation 94 that has been used to predict the minimum drag coefficient of wing panels is very conservative. However, it should be noted that the data points shown are for smooth, rigid wind tunnel models. Any surface imperfections that might appear in a real HAPP design would tend to increase $\left(C_{D_{min}}\right)_W$ considerably.

The minimum drag coefficient of any smooth slender body on a HAPP is expressed by reference 15 as:

$$\left(C_{D_{min}}\right)_B = \left(C_{D_f}\right)_B + C_{D_B} \tag{95}$$

The skin friction term is given by:

$$\left(C_{D_f}\right)_B = C_{f_T}\left\{\frac{1 + 60}{\left(\frac{l_B}{d}\right)^3} + 0.0025\left(\frac{l_B}{d}\right)\right\}\frac{\left(S_{WET}\right)_B}{S_{REF}} \tag{96}$$

where:

$\frac{l_B}{d}$ = body fineness ratio, shown below. An equivalent diameter, d_{Eq}, sometimes is needed for non-circular bodies.

$$d_{Eq} = \sqrt{\frac{\left(S_{WET}\right)_B}{0.7854}}$$

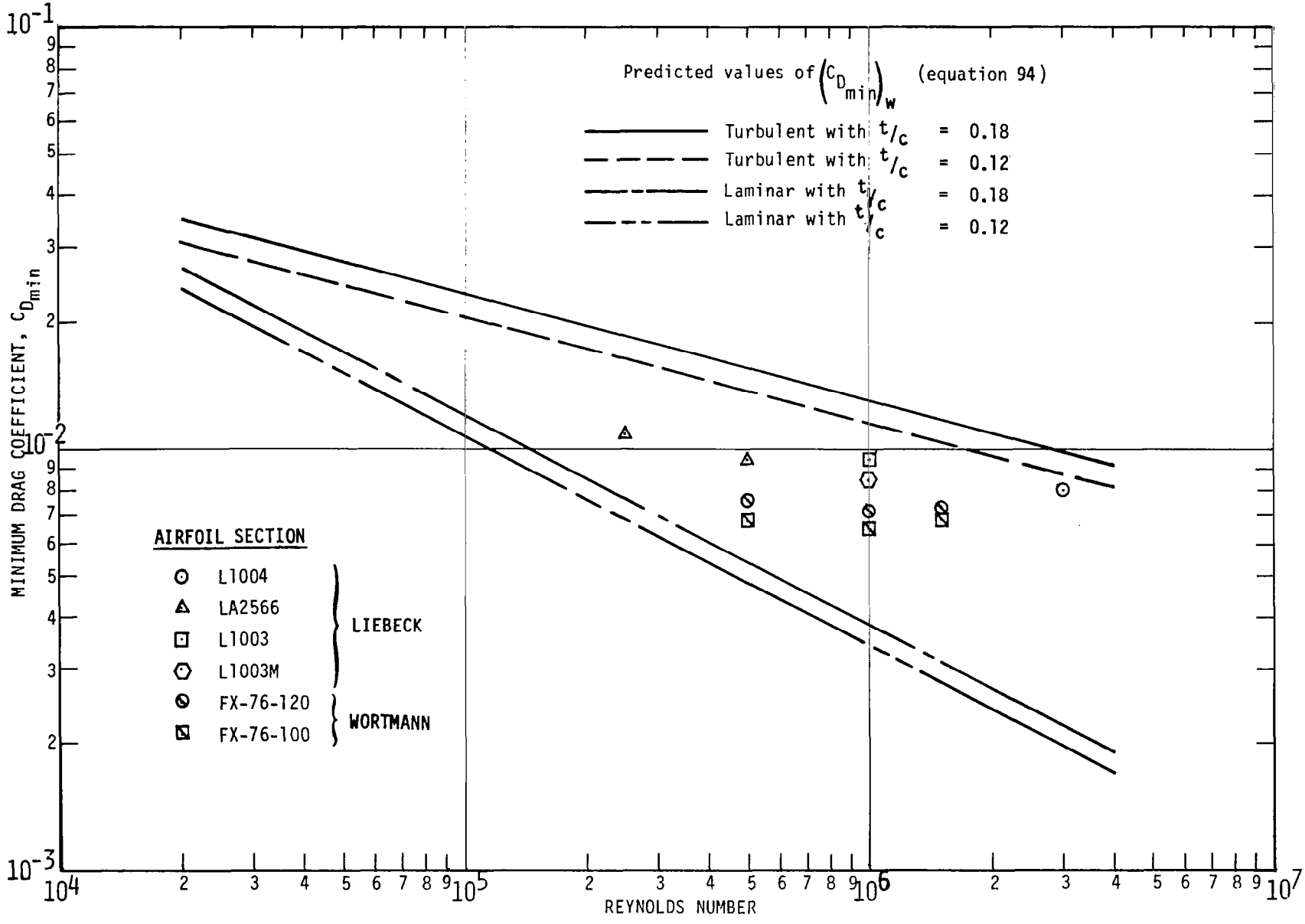

FIGURE 39 WING PANEL MINIMUM DRAG COEFFICIENT

C_{f_T} = turbulent skin friction coefficient based on body length

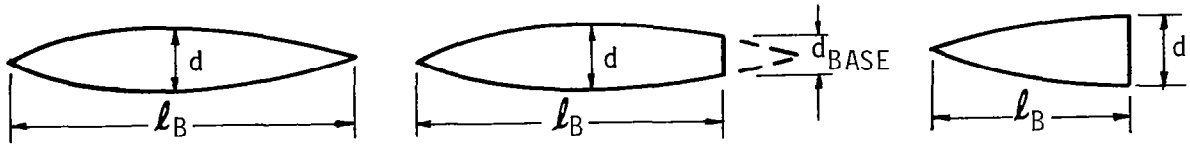

CLOSED BODY BODY HAVING A BLUNT BASE FOREBODY

Reference 15 gives the base pressure coefficient as

$$C_{D_B} = \frac{\left(\frac{d_{BASE}}{d}\right)^3 \left\{\frac{S_B}{S_{REF}}\right\}}{\left(C_{D_f}\right)_B} \tag{97}$$

It is difficult to make an accurate estimate of wire drag in the initial concept phase due to the uncertainty in bracing schemes, loads, etc. It can be assumed, therefore, that if the particular configuration under analysis is wire braced, the total $C_{D_{min}}$ is increased by 3%.

The drag contribution of miscellaneous items and interference is accounted for by increasing $C_{D_{min}}$ an additional 4%.

The total vehicle $C_{D_{min}}$ can now be expressed as:

$$C_{D_{min}} = \sum_{i=1}^{n} \left(C_{D_{min}}\right)_W + \sum_{j=1}^{n} \left(C_{D_{min}}\right)_B + 0.07 C_{D_{min}} \tag{98}$$

where:

i = number of wing panels

j = number of bodies

Drag Due to Lift. The drag due to lift term, C_{D_L}, of equation 92 can be separated into viscous and inviscid components,

$$C_{D_L} = C_{D_{L_i}} + C_{D_{L_v}} \tag{99}$$

The inviscid drag term is classically referred to as the induced drag. This drag term is a result of vortices shedding from a finite wing which induce a downwash at and behind the wing. The effect of this downwash is to rotate the lift vector to produce a drag force.

Reference 16 expresses the induced drag for straight tapered wings, assuming no twist as

$$C_{D_{L_i}} = \frac{C_L^2}{\pi AR u} \tag{100}$$

where:

u = induced drag factor given by,

$$u = 1 - \left\{0.0016 + 0.00996\ (\lambda - 0.25)^2\right\}\ (AR - 2.5)$$

$$\text{for} \begin{cases} 0.4 < \lambda < 1 \\ 4 < AR < 35 \end{cases}$$

To account for sweep effects equation 100 is modified, according to reference 17, as

$$C_{D_{L_i}} = \frac{C_L^2}{\pi AR u} \left[\frac{1}{\cos\ (\Lambda_{c/4} - 5^o)}\right] \tag{101}$$

Wing tip panels, variously called winglets or endplates effectively increase the aspect ratio of the wing, thus reducing $C_{D_{L_i}}$. Reference 17 defines this effective aspect ratio as

$$AR_{EFF} = AR\left(1 + 1.9\frac{h}{b}\right) \tag{102}$$

The viscous drag term of equation 99 is caused by separation and increased skin friction at angles of attack other than that for $C_{D_{min}}$. It is assumed that in the preliminary design phase the wing incidence angle with respect to any streamlined bodies would be adjusted to reduce $C_{D_{L_v}}$ of the bodies at the design cruise angle of attack. Therefore, the method for predicting $C_{D_{L_v}}$ considers only the main wing as a contributor. The experimental $C_{D_{L_v}}$ vs. C_L behavior of any candidate airfoil section (e.g., Figure 40) can be included as a curve fit in the model.

Airfoil Characteristics. The design requirements imposed on HAPP wing airfoil sections may be difficult to satisfy. The main wing must cruise at very high values of C_L and maintain a low C_D while operating in a low Reynolds number flow. Values of pitching moment coefficient must be kept low (sometimes even positive for a flying wing configuration) for structural and stability reasons. The airfoil's performance must be tolerant of imperfections in contour brought about by very lightweight construction. Also provision for placement of solar cell arrays on some wing sections must be made, including attention to maintaining cooling flow over the surface.

The HAPP design methodology presented in this report does not include an airfoil synthesis technique. Clearly, if a HAPP design were to proceed beyond an initial concept phase, sophisticated airfoil design procedures should be used to optimize an airfoil that would fulfill the requirements.

The general principles of low speed single element airfoil design are discussed in detail in References 18 to 22. In recent years there has been significant progress in designing high-lift, low drag airfoils as Figure 41 indicates. For instance, the "Stratford Recovery" airfoils described in Reference 18 have good performance (i.e., high lift, low drag) at Reynolds numbers of a million and below, low pitching moment coefficients and large thickness ratios, which are good from a structural standpoint.

The lift curves, drag polars and pitching moment curves shown in Figure 41 are representative of available data that has been used to establish bounds on an achievable design C_L, and to estimate C_{D_T} and $C_{M_{C/4}}$ versus C_L behavior for HAPP wing airfoil sections.

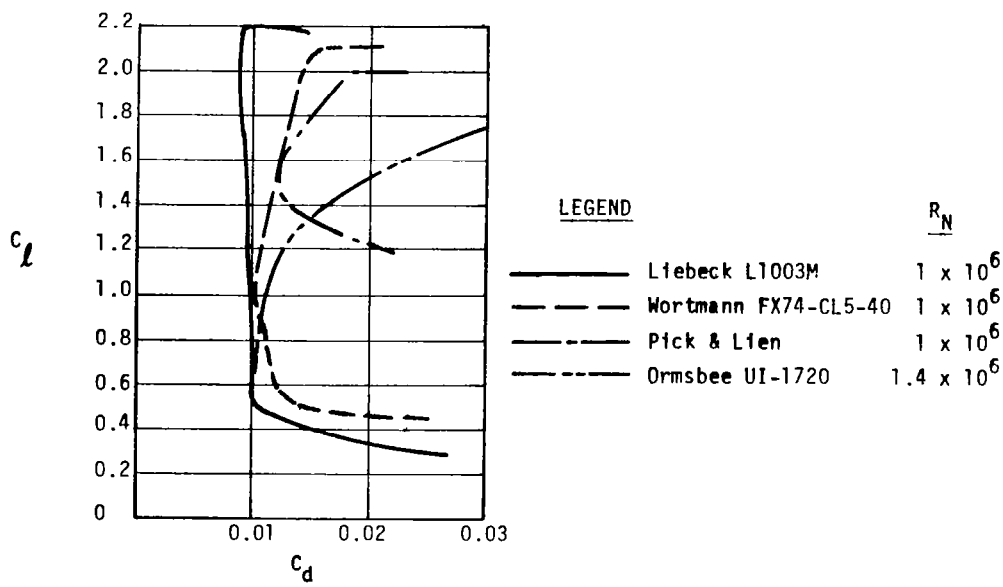

FIGURE 40 EXPERIMENTALLY DETERMINED LIFT VERSUS DRAG POLARS FOR SEVERAL HIGH-LIFT AIRFOILS

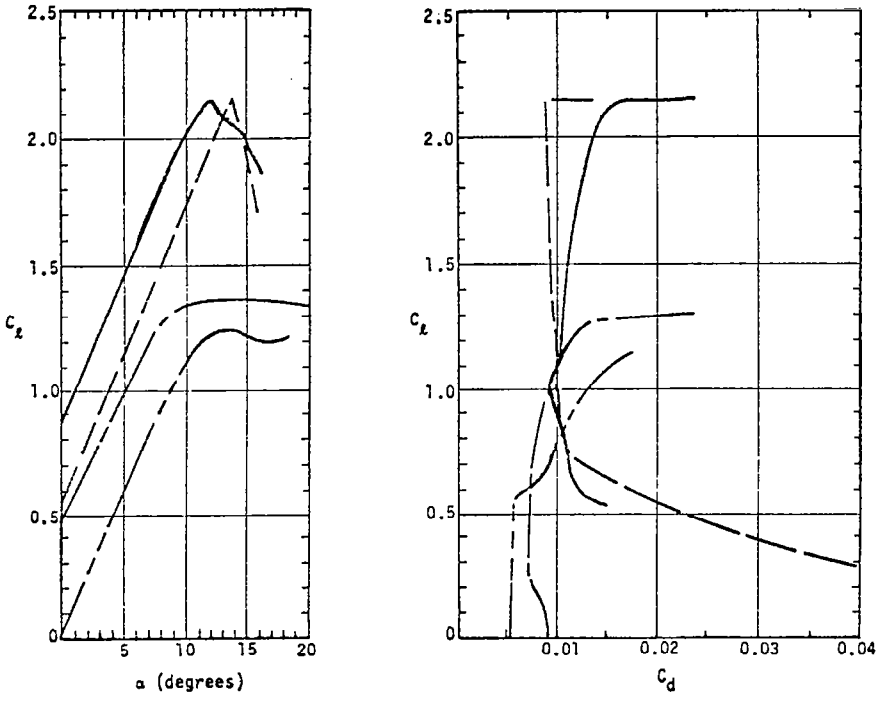

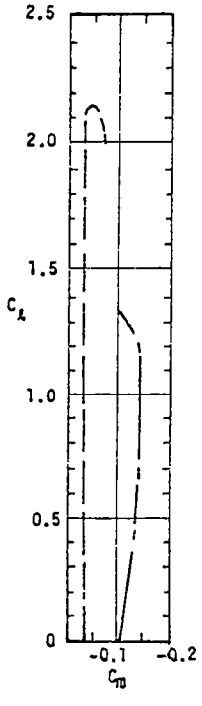

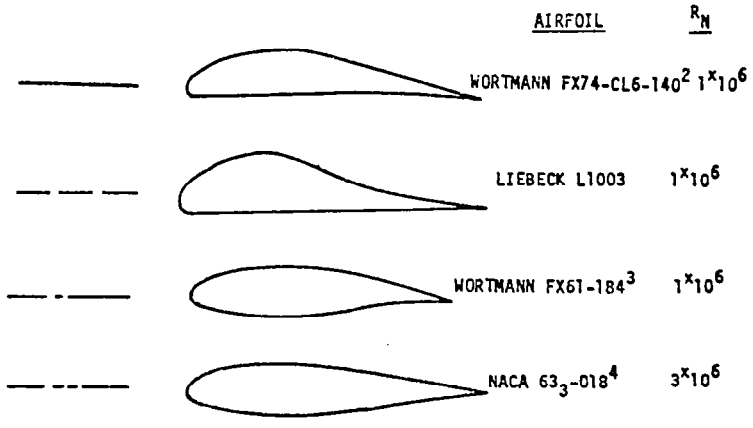

(Reference 23)

FIGURE 41 AIRFOIL CHARACTERISTICS FOR FOUR LOW SPEED AIRFOILS

Structure Mass Estimation

Structural mass of a solar HAPP is second only to the power train in contribution to total mass. For conceptual design purposes a simple and accurate mass estimation method is desirable. However, the very light wing and very large size of a HAPP are outside the range of standard statistical weight estimation methods. For this reason, a simple estimation technique has been developed analytically. This method was then calibrated to match the structure mass of a previous, more detailed HAPP design.

The first problem encountered is in determination of the required velocity-load factor (V-n) operating envelope. The main requirement is to obtain an acceptably low failure rate in normal flight operations. As will be shown in a later section, geometric maneuvering constraints will limit the maximum additional g loads in turns to less than 0.02 g. This will obviously have minimal effect on the structure design. Limited power output of a solar HAPP will limit speed and dynamic pressure to a relatively narrow range. The only remaining design loads will be due to turbulence.

The actual high altitude cruise environment appears to be relatively favorable in terms of turbulence levels. However, the existing data base (Ref. 1) does not contain any information for shorter gust wavelengths of concern for HAPP design. In any case, it is expected that low altitude turbulence likely to be encountered during climb and descent will prove to be the design limit case.

A HAPP is also unique in its response to turbulence. The design climb airspeed is less than common gust velocities and the aircraft could actually be much larger than a typical gust wavelength. It would be quite conceivable to encounter an up gust at each wing tip while a down gust occurs in the center. In this case, the resulting bending load might be reduced by unsteady aerodynamic effects and by induced flow near the wing. The long flight duration of a solar HAPP should also allow climb and descent operations to occur only in favorable geographic areas and during periods of relatively low wind and turbulence.

From all of the above it appears that some additional research is required before truly meaningful loads requirements can be developed. For purposes of this report, an ultimate load of 3 g's has been used. This is certainly within the range used by other large (but much faster) aircraft and also greater than used on the Gossamer series of human powered aircraft (Ref. 29).

It has been assumed that the structure will be externally wire braced. The low flight speed will tend to minimize wire drag in relation to total drag, while wires will allow structure weight reductions on the order of 30%. The optimum quantity and location of the wires must still be determined, and is very dependent upon the final configuration. The optimum amount of wire will increase with increases in the ultimate load factor and decrease with an increase in cruise dynamic pressure.

Wire bracing will also result in a significant increase in the stiffness of the structure when compared to a similar vehicle with the same ultimate load factor but no external bracing. This should significantly reduce any weight penalty associated with aeroelastic constraints.

Previous reports (Ref. 24) on solar powered aircraft have claimed that wire bracing was unfeasible due to the partial shading of solar cells by the wires. This problem is magnified because the output current of an entire series string of solar cells is forced to the current level of the weakest cell. For the baseline HAPP in this report, it is expected that the wire diameters will be no more than 1.5 mm (1/16 inch) in diameter. If a typical cell is 4 cm (1.6 inches) across then energy loss based on relative areas and due to shading is 3.7%. When the cells are connected into arrays, it is common to begin by wiring 3 cells into a parallel module which is then combined with other modules into a series string. If the module is arranged on the wing so that only one of the three cells would be shaded at any given time then the loss would be only 1.25%. The use of larger cells and/or more cells in a parallel string would further reduce losses. Even though the 1.25% loss would occur for an entire cell block, the magnitude of the loss is small enough that wire bracing is still desirable.

Another major characteristic of a wire-braced structure is that ultimate load and limit load are essentially the same. The wing spar in an externally braced wing is primarily in compression. The ultimate failure mode in a lightweight structure such as a solar HAPP will be due to compressive instability, either column buckling or local crippling. In an aircraft wing, either of these failures will occur suddenly when some critical load is reached. The region of gradual yielding that normally occurs between limit load and ultimate load will not exist. For this reason, design loads have been expressed in terms of ultimate load and not limit load. It should also be realized that a solar HAPP will be an unmanned vehicle. This means that the normal safety margins used in manned aircraft can be somewhat relaxed.

Structural Concept. The solar HAPP concept requires very light wing loadings to be feasible with near-term state-of-the-art. It is currently not possible to make an efficient monocoque wing structure at the required weight. The only viable option is to design a spar of adequate strength and then add ribs and a thin film covering to form an airfoil. This is the approach, combined with wire bracing that was responsible for the success of several recent human powered aircraft.

The major spar load is compression to balance tension in the bracing wires. The spar must also carry bending loads due to wing lift between wire attachment points. Finally, in some configurations it must carry bending and/or compression due to the drag distribution along the wing. In a lightweight wing the spar must also supply a large fraction of the torsional rigidity. Of all these loads, the dominant one is the compression load. For this report, spar weight has been considered to scale only as a function of compression load. This scaling equation was then

referenced to a detailed spar design produced for an earlier HAPP. Since this design included all of the above mentioned loads, it is believed that the resulting weight model is reasonably accurate.

There are several feasible design concepts for the spar. All of the recent wire-braced, human-powered aircraft have used relatively small diameter thin walled tubes, either of carbon fiber or aluminum. In some cases, the spar was 2 inches (5,08 cm) in diameter while the wing overall thickness was about 13 inches (30,48 cm). Small spar size is directly contradictory to normal aircraft practice where the thickest possible spar is desired. The explanation for this is twofold: First, in a compression buckling load, the spar is just as likely to buckle in the fore and aft direction as in the vertical direction. This results in a circular tube for a spar. Second, the tubes in the HPA's were all made close to the wall thickness-to-diameter ratio where failure by local crippling will occur before the column buckling of the entire spar. Thus the tube diameters selected essentially represented the minimum weight spar for each configuration assuming that a monocoque tube was used. Small size, low loads and simplicity requirements of the HPA's precluded the use of more complex structure.

The larger size of solar HAPPs will allow a somewhat more elaborate spar to be made. The options are either a more sophisticated tube structure (composite sandwich wall or semi-monocoque) or else a space frame truss which is itself made of thin-wall tubes. These designs will essentially allow the construction of a spar that is comparable to thin wall tube, but with a "wall thickness-to-diameter" ratio much smaller than the normal thin wall tube. There will, however, be some mass added for the purpose of stabilizing the "tube" against local crippling. This mass will increase as the spar cross-section dimensions are increased, so it is expected that, for a given concept, there will be some cross-section dimension that will result in minimizing total spar weight.

No attempt has been made to analytically compare the various spar concepts. Previous concepts examined before this study have all used a tubular truss. This concept is illustrated in Figure 42. This weight analysis is based on such a truss design. No attempt was made to optimize the previous truss with regard to cross-sectional area; however, since only 25% of the total mass was in the span wise caps and the diagonal members were generally limited by local buckling, it appears that a smaller cross-section would reduce total spar weight. The use of this truss as the baseline for weight estimates is considered to be conservative at this time.

The major outcome of this discussion is that the spar for an externally braced, lightly loaded wing will have an optimum thickness which will probably be less than the maximum thickness allowed by the airfoil. If the optimum is slightly greater than the wing thickness, then the weight penalty involved should be small. This means that the spar weight will only be a function of the wingspan, the gross weight and the ultimate

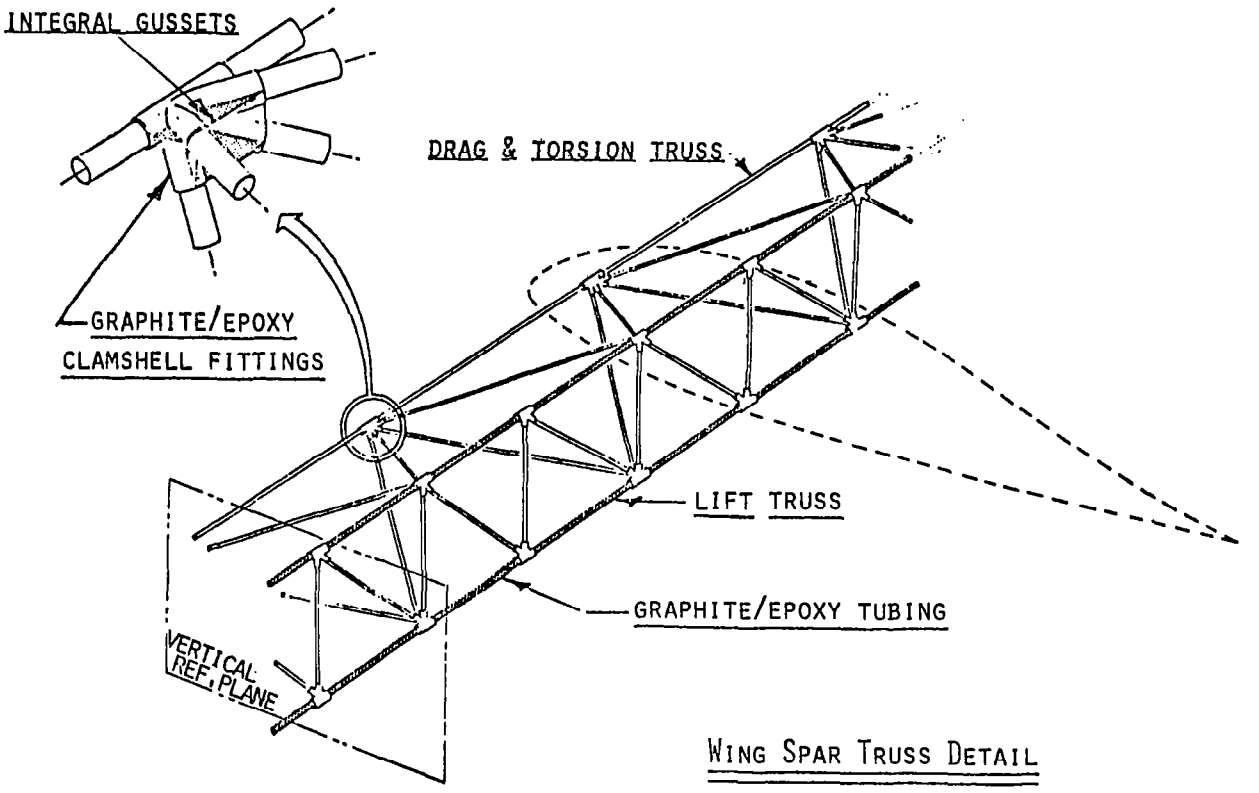

FIGURE 42 PRELIMINARY STRUCTURAL DESIGN UTILIZING ADVANCED COMPOSITES

load factor. The usual factor in a weight equation of spar thickness-to-span ratio (which will sometimes show up as an absolute thickness, thickness-to-chord ratio, aspect ratio or similar term) is not important.

Mass Estimation. The structure mass estimation given here was developed for a flying wing type aircraft. Weight terms can be developed for fuselages and tail surfaces by similar methods if required.

The most critical element of wing structure is the spar. Since compressive loads are dominant, the scaling equation will be derived from the standard Euler column equation:

$$P_{cr} = \frac{\pi^2 EI}{L^2} \tag{103}$$

where E is the modulus of elasticity, I is the section area moment of inertia for the cross-section, L is the length of the column and P_{cr} is the load at which buckling occurs. Since the only design concern is the weights of different sizes of geometrically similar structures and E can be considered constant for all structures

$$P_{cr} \propto \frac{I}{L^2} \tag{104}$$

For any given aircraft structure, peak bending loads in the wing will tend to be proportional to gross weight and design load factor. Since a constant load factor independent of vehicle has been assumed here, design loads must be proportional to gross mass or:

$$P_{cr} \propto M_{GROSS} \tag{105}$$

The other term remaining in the buckling equation is the section moment of inertia, I. For similar geometric sections, I will scale as the fourth power of the linear dimension (h) or:

$$I \propto h^4 \tag{106}$$

This assumes that the section is made of a homogeneous material; however, a composite sandwich structure can be transformed into an "equivalent" homogenous structure by standard techniques. Similarly, the tubular truss can be considered to be a tubular structure with lightening holes.

The above relation should be approximately true in these cases. Finally, mass of the structure will be proportional to volume or:

$$\text{Mass} \propto \text{Volume} \propto h^2 L \tag{107}$$

The first relationship needed is the effect on spar mass when gross mass is varied for a fixed wingspan. In this case the column length, L, is constant so equation 104 reduces to:

$$P_{cr} \propto I \tag{108}$$

and equation 104 reduces to:

$$M_{SPAR} \propto h^2 \tag{109}$$

Combining equations 109, 110, 112, and 113 gives:

$$M_{SPAR}{}^2 \propto h^4 \propto I \propto P_{cr} \propto M_{GROSS} \tag{110}$$

which reduces to:

$$M_{SPAR} \propto \sqrt{M_{GROSS}} \tag{111}$$

The other case of concern is varying the wingspan at constant gross mass. In this case, equation 104 reduces to:

$$I \propto L^2 \tag{112}$$

Combining equations 106 and 107 gives:

$$h^4 \propto I \propto L^2 \tag{113}$$

which can be reduced to:

$$h^2 \propto L \tag{114}$$

This can be combined with equation 107 and reduced to:

$$M_{SPAR} \propto L^2 \tag{115}$$

Therefore, the final form of the spar mass equation is:

$$M_{SPAR} \propto L^2 \quad M_{GROSS} \tag{116}$$

Using the truss data from a previous internally funded HAPP design the final truss weight is:

$$M_{SPAR} = 0.000275\ b^2 \quad M_{GROSS} \tag{117}$$

where the span is in meters and mass is in kilograms.

Other primary structure mass is in bracing wire, although this term is small compared with the truss weight. Since the wires are only loaded in tension, they will scale linearly with both span and gross mass. Referencing the HAPP detail design from previous work as before:

$$M_{WIRE} = \frac{M_{GROSS}\ b}{10,000} \tag{118}$$

Now that the primary structure is in place, it can be wrapped with a minimum weight airfoil shape. Again, utilizing recent HPA technology, this will consist of lightweight ribs made from foamed plastic webs with carbon or Kevlar caps and reinforcement. Alternately, the very large size of a HAPP wing could make a built-up truss-style rib feasible. An attractive material for this would be carbon fiber and plastic foam sandwich material currently used for sailboat battens. This material has approximately twice the stiffness-to-weight ratio of aircraft spruce. Since the purpose of ribs is to maintain airfoil section to some required accuracy, and the major inaccuracy will be sagging of the covering between the ribs, the use of a rib spacing which is a constant fraction of the chord will produce a constant percentage distortion of the airfoil. For recent HPA's rib spacing has been about 0.4 to 0.5 times the chord. Assuming that the mass of the rib is proportional to the surface area enclosed by the rib itself (the rib web area), then the mass is proportional to the chord length squared. The number of ribs will increase with the wingspan, but will decrease with the wing chord as mentioned above. This gives mass scaling for the ribs as follows:

$$M_{RIBS} = 0.015 \ S_{REF} \quad (119)$$

The wing covering is assumed to be some type of plastic film such as Mylar or Teflon FEP. A 0.3 mil thickness has proved adequate on HPAs and Solar Challenger. The HAPP will, however, require a much longer lifetime with little or no maintenance. For this reason, 1 mil covering has been assumed. These plastics are attached to the structure and then shrunk using hot air guns. They are also available in versions where the material will shrink much more on one axis than the other. This can be utilized to minimize sagging between ribs. Weight of the covering is, of course, proportional to wing surface area so that

$$M_{COVERING} = 0.106 \ S_{REF} \quad (120)$$

Finally, some structure is required to hold a reasonably accurate leading edge shape and to support the trailing edge. The best candidate material for the leading edge is very low density plastic foam. The foam could be cut from blocks to the shape of the leading edge and to whatever thickness is required. The leading edge sections on Gossamer Albatross were approximately 1/4 inch thick section of 0.01 Kg/m^3 (1 lbs per cu ft) polystyrene foam. For the much larger size HAPP vehicle these sections have been assumed to be 2.54 cm (1 inch) thick and to cover approximately 40% of total wing wetted area. These sections should not be excessively stiff as this will cause a discontinuity in the airfoil at the aft edge of the sheeting. The leading edge must be allowed to deform to maintain a smooth airfoil section. An extremely lightweight trailing edge structure is difficult to design. HPA's have used tensioned wire trailing edges, which while very light, are quite difficult to implement. A conventional rigid structure is placed in both bending and compression by covering tension, and is thus prone to buckling. A mass term for the trailing edge that is greater than just the mass of the wire, has been included as a measure of conservatism.

$$M_{LE} = 0.081 \ S_{REF} \quad (121)$$

$$M_{TE} = 0.019 \ S_{REF} \quad (122)$$

The previous solar HAPP wing design that these numbers were based on was an 82 meter (269 foot) span, aspect ratio 20 wing with no span loading other than the wing weight itself. The ultimate load factor was 3.13. The total vehicle gross mass was 1000 KG (2205 lbs). It is expected that wing weight could be reduced in the current design by spanloading as much of the power train weight as possible. In this regard current mass estimation techniques could be considered conservative.

It must be emphasized that an aircraft structure of the size and weight proposed has not been built. The success of the smaller human powered aircraft and the limited detail design that has been done to date give reasonable confidence that it can be done. The method presented here yields structure mass-to-gross mass fractions that are reasonably in line with other aircraft practice. The final test, however, will be in the design, construction and flight test of such a structure.

Other Non-Power Train Masses. There are several other items that must be accounted for in the HAPP mass buildup. These are of relatively small magnitude, but should be included for completeness. The aircraft will have some additional weight for take off and landing provisions as well as ground handling. As covered elsewhere, these weights can and should be minimized in the HAPP design. They are estimated as a constant fraction of gross mass or:

$$M_{LANDING\ GEAR} = 0.00725\ M_{GROSS} \tag{123}$$

The aircraft will require a rather sophisticated avionics suite to handle all control, navigation and communication functions. This will consist of at least one computer, command and navigation receivers, transponders, attitude instruments and some sort of autoland system. It is beyond the scope of this report to determine the requirements and mass of this system exactly. The rapid advance of miniature electronics technology will also tend to give a significant reduction in this mass in the next decade. Finally, some tradeoff must be made between designing special lightweight HAPP avionics or using lower cost off-the-shelf equipment. The avionics mass has therefore been estimated as:

$$M_{AVIONICS} = 40\ KG \tag{124}$$

This mass is consistent with the avionics mass used by other HAPP designs as well as the Lockheed Aquila mini-RPV.

Finally, the mass of the servos required to move flight controls must be estimated. These have been a constant fraction of the gross weight. It is expected that the servos will be electrically powered and utilize high speed samarium cobalt motors of similar technology to the main propulsion motors. This mass is:

$$M_{SERVOS} = 0.015\ M_{GROSS} \tag{125}$$

Effect of Flight Profile on Vehicle Size

The sizing methodology discussed so far assumes flight at a constant altitude. It is possible to design a solar HAPP to do this, but flight at constant altitude may not provide the smallest aircraft for any given mission and certainly won't provide the simplest. Deviating from constant altitude will complicate mission planning and may complicate payload performance. Other flight profiles which might be possible are:

- No on-board chemical storage of energy for nightime flight. This would require storage of energy in the form of altitude.
- Partial on-board storage of energy (1) that would store sufficient energy for eight hours of flight at constant altitude so that constant altitude could be maintained at the summer solstice.
- Partial on-board storage of energy (2) that would store enough energy to maintain constant altitude flight at some altitude where collection of eight hours of energy could be used for power the remainder of the night.
- Partial on-board storage of energy (3) that would store enough energy for partial power descent at night.

These are not all the flight profile alternatives possible, but these four should bound the problem and allow some conclusions to be drawn about what type of flight profile would provide the smallest vehicle.

Assumptions. In order to simplify calculations, some assumptions can be made about power train and vehicle performance. All components in the power train will be assumed to have perfect efficiency. Horizontal cells will be assumed in order to directly link collector area to wing area. Constant dynamic pressure (q) flight will be assumed. Two days will be examined: launch day on December 21st and the day after as the profile stabilizes. Climbs will be at best rate-of-climb speed and descents at power-off-minimum rate-of-sink speed. Thrust power required will be at best endurance speed or at a lift coefficient of 1.35, whichever is attainable for a given altitude. Drag coefficient will be constant. Figure 43 presents the curves used for these calculations and Figure 44 presents each of these flight profiles. Table 15 summarizes the vehicles required for each flight profile which are elaborated upon below.

No On-Board Chemical Energy Storage. Since the energy storage components of the power trains discussed in previous sections have accounted for most of the power train subsystem mass, it follows that doing away with energy storage in a chemical form will not only make a solar HAPP simpler but will also make it lighter. Since this is an RPV, its end of glide altitude should be kept as high as possible in order to avoid adverse reactions from an air traffic control (ATC) system which is set up to handle

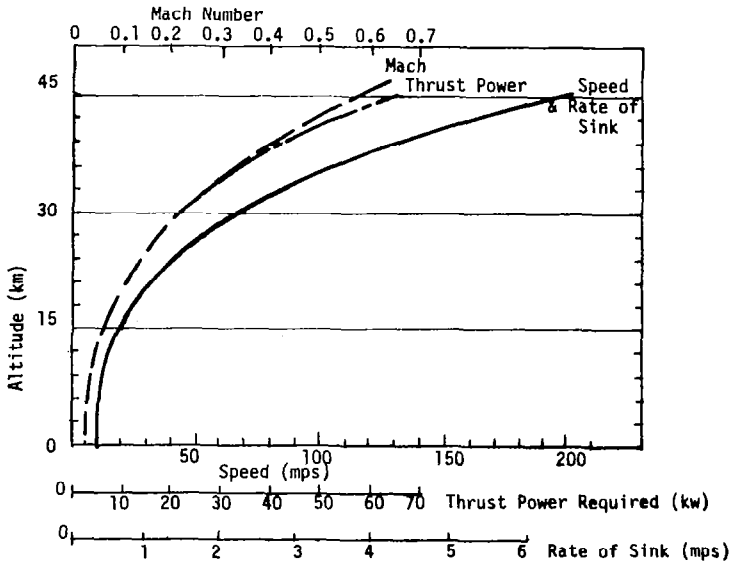

FIGURE 43 RELATIONSHIP OF CONSTANT DYNAMIC PRESSURE TO PERFORMANCE PARAMETERS WITH INCREASING ALTITUDE

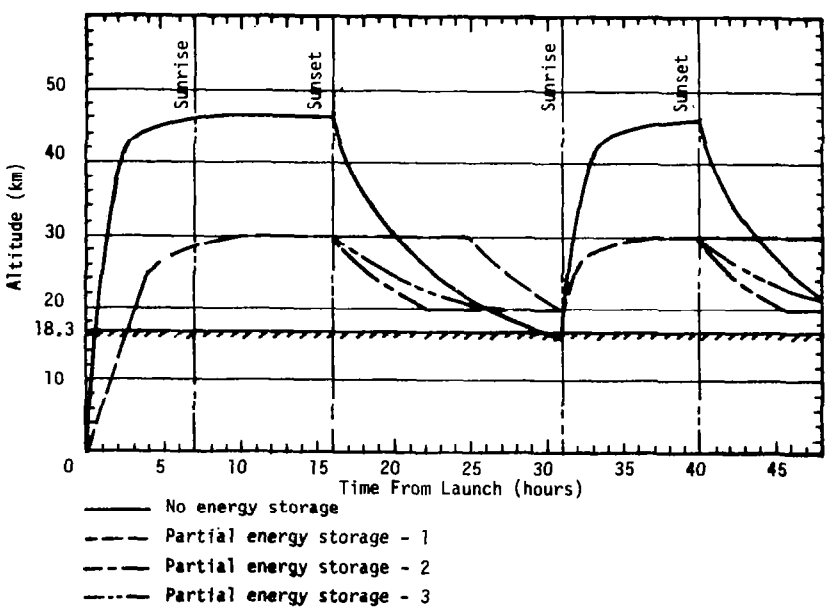

FIGURE 44 FOUR POSSIBLE FLIGHT PROFILES FOR A SOLAR HAPP RPV

TABLE 15. VEHICLES REQUIRED FOR EACH FLIGHT PROFILE WITH PERFECT COMPONENT EFFICIENCIES

	ALTITUDE									
	NO STORAGE		POB #1[1]		POB #2		POB #3		CONSTANT ALTITUDE	
	METRIC	ENGLISH	METRIC	ENGLISH	METRIC	ENGLISH	METRIC	ENGLISH	METRIC	ENGLISH
Sunrise Altitude	18 Km	59 040ft	20	65 600	20	65 600	20	65 600	20	65 600
Max Altitude Attained	46 Km	150 880ft	20	98 400	30	98 400	30	98 400	20	65 600
Climb Power Required	91 Kw	122 HP	23	31	23	31	23	31	--	--
Storage Energy Required	--	--	184 Kwh	248 HP Hr	80 Kwh	105 HP Hr	344 Kwh	464 HP Hr	160 Kwh	640 HP Hr
Collector Area Required	523 m^2	4860ft^2	331	3556	318	3419	309	3324	216	2319
Wing Required	747 m^2	8038ft^2	472	5080	454	4885	441	4748	308	3313
Wingspan[2]	162 m	530ft	129	472	126	414	124	408	104	341

[1]POB = partial onboard storage scheme

[2]assumes a constant aspect ratio at night of 35

aircraft with pilots on-board. The regulated upper limit of their jurisdiction is 60 000 ft (18.3 Km) and that should be considered as a lower limit for HAPP flight to avoid bureaucratic bickering.

Partial On-Board Storage (1). Starting with a desired minimum altitude of 20 Km (65 600 ft) at sunrise the second day and for the preceding eight hours of darkness, the power off minimum rate of sink curve will extrapolate backwards to a required maximum altitude the first day of 30 Km (98 400 ft). Climb to 30 Km will be required the second and subsequent days with maintenance of that altitude until sunset.

Partial On-Board Storage (2). Desired altitude to be maintained at sunrise is 20 Km (65 600 ft). Power-off descent from sunset to 20 Km will take 6 hours from an altitude of 20 Km (98 400 ft) and 20 Km (65 600 ft) will be maintained for the remaining 9 hours.

Partial On-Board Storage (3). Starting with 30 Km (98 400 ft) at sunset (23 Kw climb power requirement), reduce power to 10 Kw (13.2 HP) and descend on partial power to 20 Km (65 600 ft).

Full On-Board Energy Storage to Maintain 20 Km (65 600 ft) For 24 Hours. Power requirement will be 10 Kw (13.2 HP) for the first eight hours plus 10 each for the next two eight hour segments.

Flight Profile to Be Used In This Study. There are other flight profiles besides these four which could be investigated and should be in future work. From the standpoint of power train complexity the simplest method of storing energy for nightime use is potential. This method requires constantly changing altitude which may not be appropriate for some missions. It also does not yield the smallest airplane if wingspan is a suitable indication of size. If wingspan is plotted against some indicator of energy storage capacity such as total energy collected, then the result is Figure 45 which shows the trend with energy storage methods and shows the vehicle capable of maintaining a constant altitude to be smallest. This constant cruise altitude is, in reality, a carefully chosen balance between energy required and energy available, an equilibrium altitude. This equilibrium altitude approach was the basis of early internally funded work and is therefore, of historical interest. (See Appendix E for a theoretical treatment of this interesting concept.)

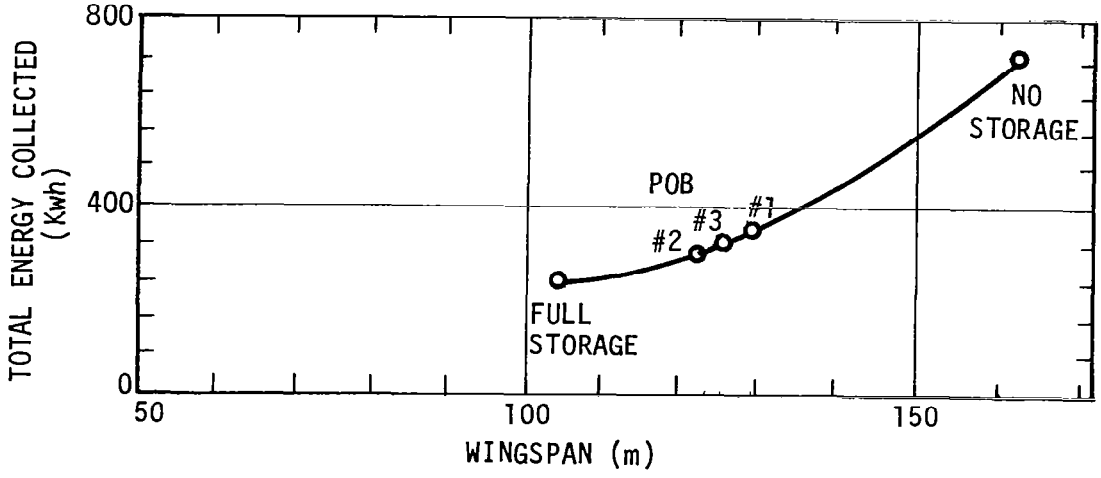

FIGURE 45 EFFECT OF FLIGHT PROFILE ON VEHICLE SIZE

Candidate Configurations

As highlighted at the bottom of Table 2 high altitude long endurance flight requires very efficient platforms both aerodynamically and structurally in order to minimize power required as expressed in Table 4. Solar HAPPs will also require large surface areas for energy collection.

The preceding discussions of methodologies used in the conceptual design of solar HAPP RPVs touched on desirable basic configuration characteristics of each subsystem. These are summarized below:

- Power train
  - As many components as possible running all the time so that the HAPP isn't carrying non-functioning components for sizable portions of the day
  - Collectors as small as possible implying careful placement and tracking capability
  - Large, low-speed propeller(s) carefully placed to minimize trim changes;
- Aerodynamics
  - Wings which generate as high a lift coefficient as possible at as low a section profile drag coefficent as possible
  - Little or no aerodynamic pitching moment to trim out
  - As low a boundary layer drag as possible implying effort to maintain laminar flow
  - Low drag due to surface area implying collector surfaces which generate lift
  - Maximum wing efficiency;
- Structures
  - Lightweight composite materials with space-style construction techniques
  - External bracing where the weight saving is more beneficial than the drag increase
  - Simplicity wherever possible;
- On-Board systems
  - As few on-board systems as possible which are parasitic in nature.

With these expectations in mind, a wide variety of configurations may be hypothesized which fulfill them. Previous internally funded work examined many configurations which fulfilled these expectations to one degree or another and these may be grouped chronologically as in Figures 46 and 47 with appropriate comments here as to why each was considered.

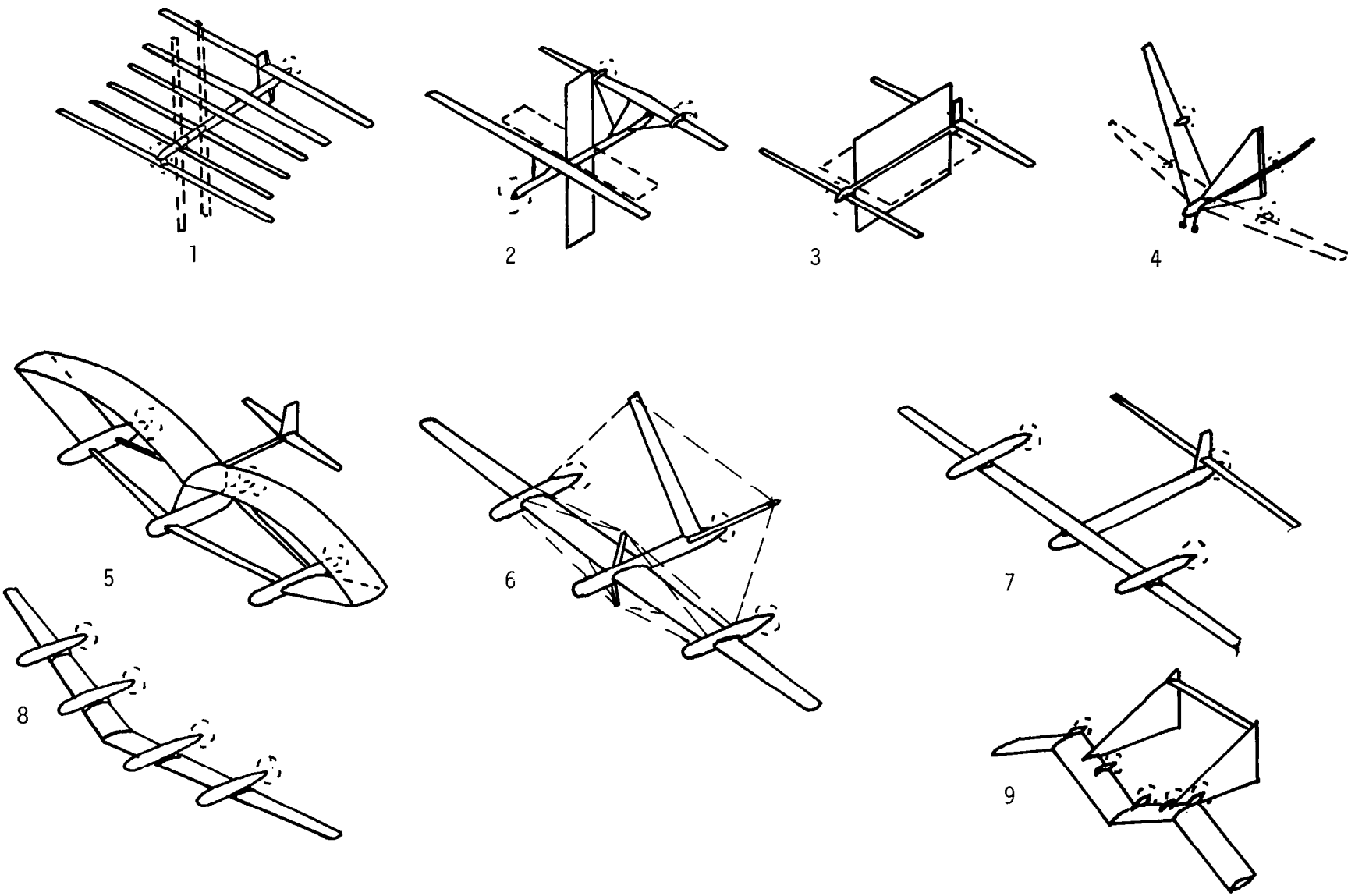

FIGURE 46. CONFIGURATION EVOLUTION 1977 - 1979

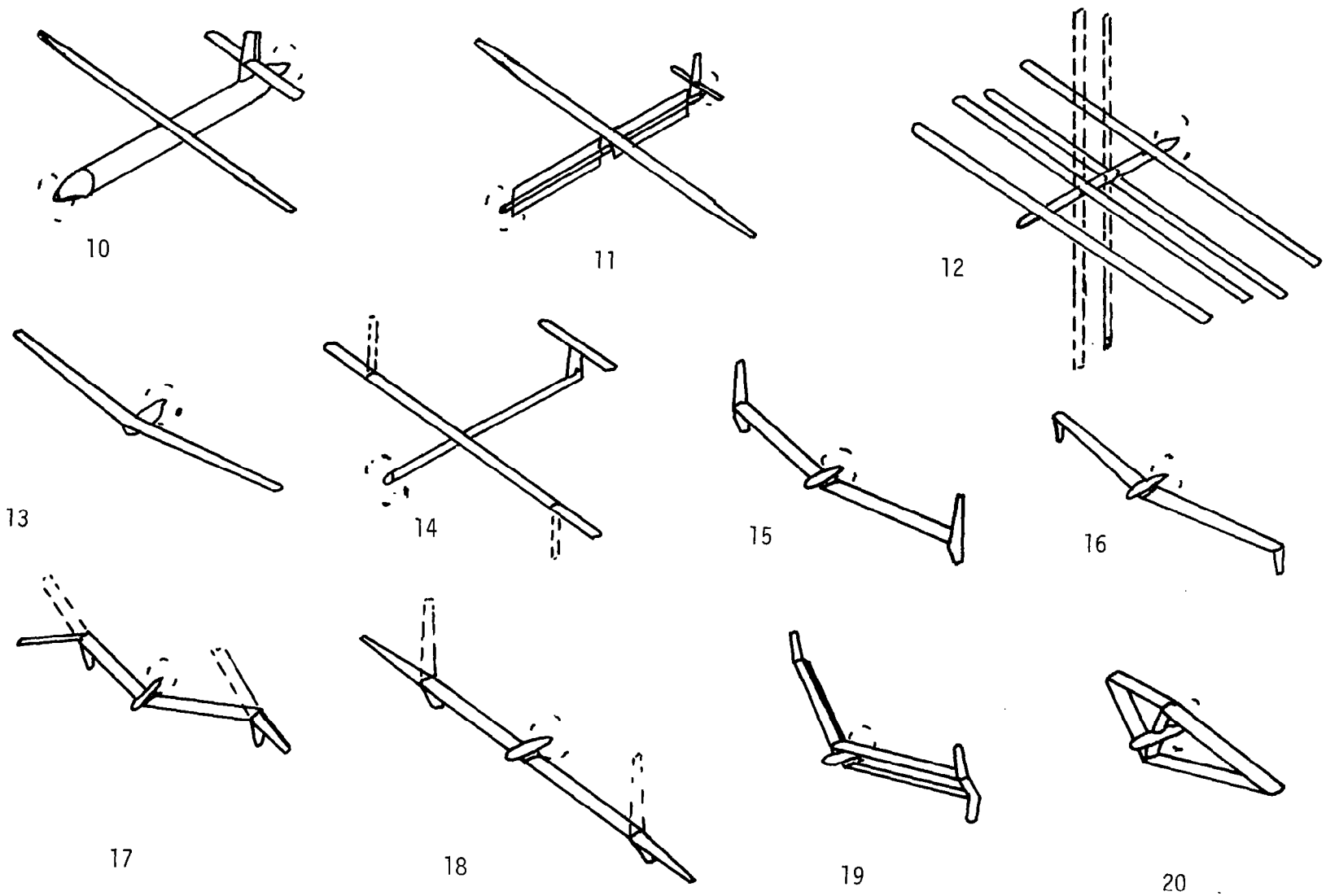

FIGURE 47. CONFIGURATION EVOLUTION 1980 - 1981

Early mission scenarios considered operation at high latitudes in the winter to be essential and, therefore, tracking photovoltaic cells or thermal concentrators were deemed mandatory with as much lifting surface provided as possible. Configurations 1 through 9 illustrate attempts to provide large tracking areas which doubled as lifting surfaces all or part of each day. Configurations 5, 6, 7, and 8 attempted to do the same with podded thermal concentrators. The progression shows an increasing consideration of aerodynamic cleanliness, simplicity and an awareness of shadowing effects on collectors. Configuration 10 was the final thermal concentrator configuration and had been selected as a baseline for that approach to solar energy collection. For reasons discussed elsewhere in this report the thermal approach was dropped and Configuration 10 was modified to Configuration 11 by the addition of photovoltaic collectors. Trim drag led to a return to making rotating collectors part of the lifting surfaces and this was compared to a simple fixed geometry Configuration 13. Analyses showed the benefit of vertical surfaces over fixed horizontal ones and a definite progression from Configuration 14 to Configuration 18 can be seen to once again stress simplicity of design. Configurations 19 and 20 were attempts to improve on the variable geometry Configuration 18 by adding combinations of vertical, angled and horizontal fixed geometry photovoltaic panels, but shading proved to be a problem.

Configuration 13 was originally selected for the primary mission examined, the justification being that horizontal panels should be adequate at latitudes to 38°N in the winter. The vehicles became increasingly large with increasing payload and decreased in size only marginally with addition of fixed vertical surfaces (Configurations 15 and 16). Vehicles, in fact, only became workably sized with addition of variable geometry outer vertical panels rotating to horizontal at sunset (Configuration 18). For meeting the collection requirements in winter at 38°N, fixed vertical panels were then added and the wing swept slightly for stability (Figure 48). Trailing horizontal/vertical fins were added on short booms at the intersections of the fixed and variable geometry portions of the wing as a result of static stability analyses to assure proper trim at all flight conditions. This final configuration is shown in Figure 49 and this is the configuration parametrically analyzed in this report.

TABLE GEOMETRY SOLAR HAPP CONFIGURATION.

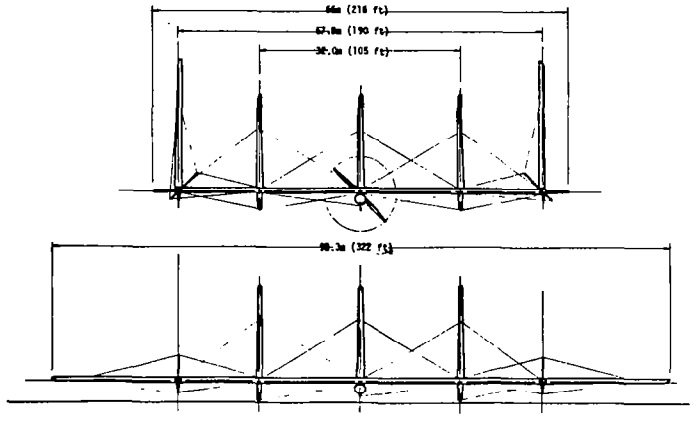

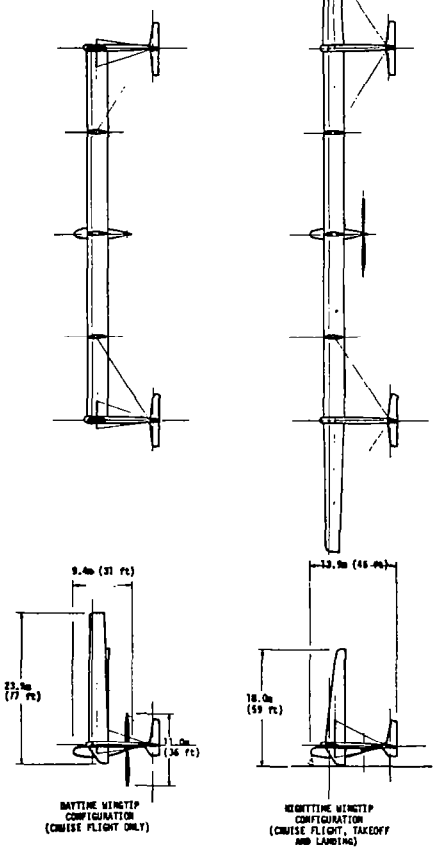

QTY REQD	CODE IDENT	PART OR IDENTIFYING NO	NOMENCLATURE OR DESCRIPTION	MATERIAL DESCRIPTION OR NOTE	MATERIAL SPECIFICATION	ZONE	ITEM NO

PARTS LIST

INTERPRET DWG PER	UNLESS OTHERWISE SPECIFIED DIM ARE IN INCHES. TOLERANCES ON: FRACTIONS = ± 1/16 DECIMALS: .X = ± .1 .XX = ± .03 .XXX = ± .010 ANGLES = ± 2 DEG	DATE D. W. HALL	LOCKHEED MISSILES & SPACE COMPANY, INC. SUNNYVALE, CALIFORNIA
		DWN FEBRUARY ', 1983	
		APVD	
		APVD	FIGURE 49 BASELINE SOLAR PHOTOVOLTAIC HIGH ALTITUDE POWERED PLATFORM
		ENGRG	
		CHKR	
		APVD	SIZE D / CODE IDENT / DRAWING NO PD-01-024 / REV
NEXT ASSY / USED ON	CONTR	APVD	
APPLICATION	CCA/CI/FD		SCALE 1 mm = 400 mm / SHEET 1 of 1

DISCUSSION OF RESULTS

Comparison of Candidate Power Trains

Using the configuration and component characteristics discussed in a previous section, the total power train mass and collector area for the thermal and photovoltaic systems can be compared. Referring to Table 16 thermal System I corresponds to a power train using a Stirling cycle heat engine and an advanced Beryllium mirror design. Thermal System II is the same except that it uses an advanced concept Rankine cycle heat engine. The photovoltaic system used for comparison assumes a conservative 12% efficient cell with a mass per unit area of 0.7 Kg/m^2 (0.14 lbs/sq. ft). Because the energy storage scheme and nighttime power trains are identical, comparison is confined to those components which collect energy and generate shaft power. As can be seen from Table 16, the thermal systems do yield collector areas that are 52 to 58% of the area needed for the baseline photovoltaic system. Use of advanced design cells, however, could reduce the photovoltaic area by nearly 67% thus making the advanced heat engine concepts only 80 to 90% of the area associated with advanced photovoltaics. Masses of the thermal systems, however, are greater than twice that of even the state-of-the-art photovoltaic power train. Because of the weight of thermal systems and the constraints of placement and pointing of thermal collectors on aircraft, the thermal concepts have been discarded in favor of a photovoltaic power train.

Capabilities of SOTA Components and Recommended Goals

Sensitivity of collector area and power train mass to the efficiencies of the propeller, gear box and electric motor are indicated in Figures 50 and 51, respectively. Improvements in the indicated state-of-the art efficiencies will at most change the area or mass by only a few percent. Furthermore, these components altogether comprise about 15% of total power train mass. Therefore, improvements in their mass-to-power ratios will also have a small effect on overall system mass. Improvements in these components, while welcome, will not significantly impact the size of a solar powered aircraft.

Sensitivity of the power train mass and collector area to improvements in collection efficiency are depicted in Figures 52 and 53. Improvement in the efficiency of the collector has a marked impact on the collector area. The collector area could be reduced as much as 30-40% as improvements are realized over the next decade. The impact on power train mass is less pronounced but nevertheless could result in a 15% reduction. Improvements in efficiency can be expected due to either the development of photovoltaic materials like GaAs or the redesign of Si cells such that their operating temperature is greatly reduced. The development of gridded-back silicon cells will contribute significantly to the latter possibility. This technology should be pursued because its impact on solar aircraft design is more easily realized than the development of GaAs in production quantities.

TABLE 16. COMPARISON OF THERMAL AND PHOTOVOLTAIC SYSTEMS

	THRUST POWER (kW)	COLLECTOR AREA (m^2)	TOTAL POWER TRAIN MASS (kg)	PERCENT OF MASS COLLECTOR	PERCENT OF MASS HEAT ENGINE	COLLECTOR[d] LENGTH (m)
THERMAL SYSTEM I[a]						
HEAT ENGINE EFFICIENCY: 40%	8 (40kW heat engine)	93	1139	37.6	16.2	30.5
HEAT ENGINE MASS TO POWER RATIO 46 kW/kg	40 [200kw heat engine(s)]	482	5904	37.6	16.2	69.4
MASS PER UNIT AREA OF COLLECTOR: 4.6 kg/m^2						
THERMAL SYSTEM II[b]						
HEAT ENGINE EFFICIENCY: 36%	8 (40 kW heat engine)	105	1163	41.5	12.0	32.4
HEAT ENGINE MASS TO POWER OUT RATIO: 3.5 kW/kg	40 [200kW heat engine(s)]	543	6033	41.5	12.0	73.7
MASS PER UNIT AREA OF COLLECTOR: 4.6 kg/m^2						
STATE OF THE ART[c]						
PHOTOVOLTAIC SYSTEM	8 (10 kW electric motor)	180	536	23.5	3.7 (electric motor)	42.4
SOLAR CELL EFFICIENCY: 12%						
MASS PER UNIT AREA OF COLLECTOR: .7 kg/m^2	40 (50kW electric motor)	904	2688	23.5	3.7 (electric motor)	95.1

(a) ADVANCED STIRLING CYCLE
(b) ADVANCED RANKINE (SINGLE FLUID)
(c) SOTA PHOTOVOLTAIC SYSTEM
(d) BASED ON COLLECTOR WITH LENGTH-TO-WIDTH RATIO OF 10. (FOR THERMAL SYSTEM, THIS LENGTH CAN BE INDICATIVE OF FUSELAGE LENGTH OR THE TOTAL LENGTH OF PODS WHICH MAY BE DISTRIBUTED ALONG WINGS.)

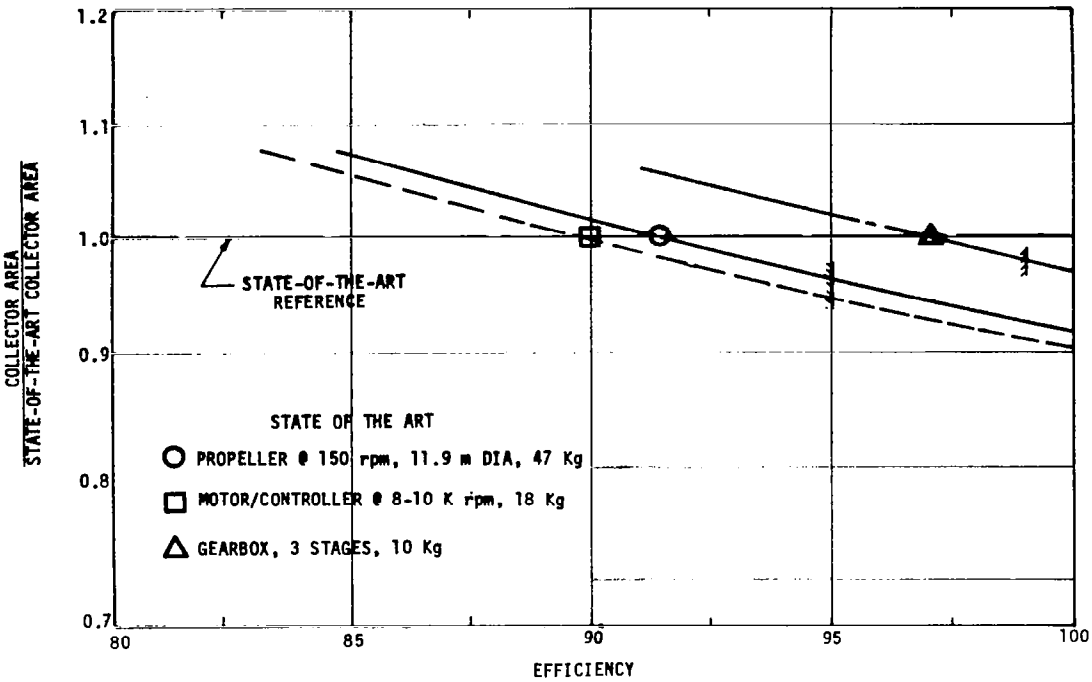

FIGURE 50 SENSITIVITY OF SOLAR ARRAY AREA TO COMPONENT EFFICIENCY VARIATIONS

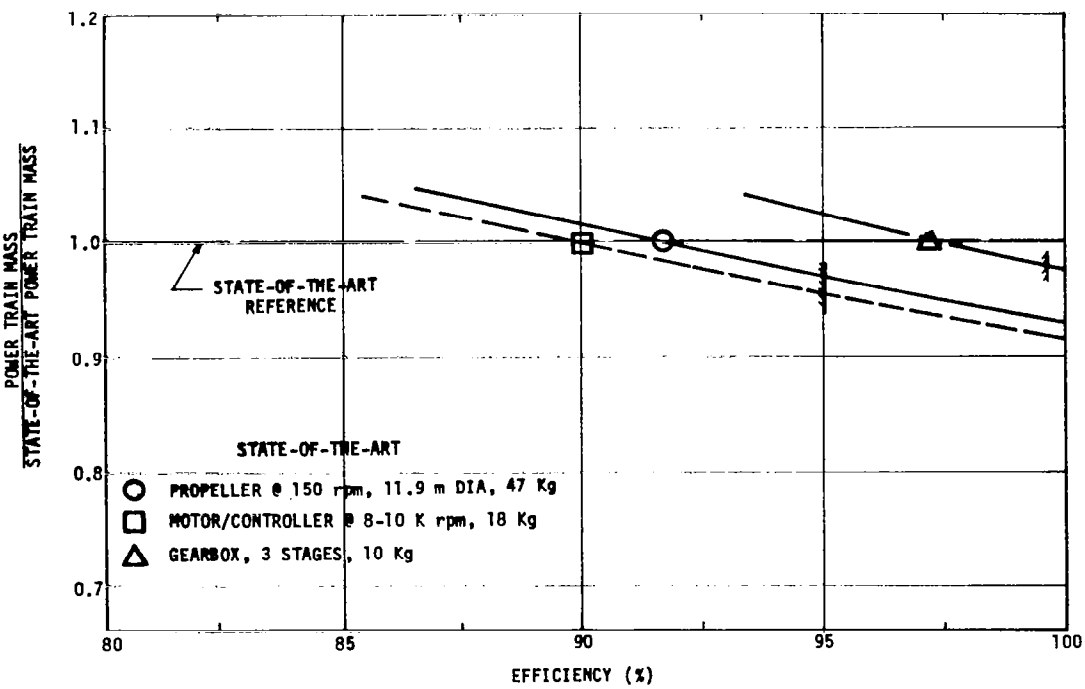

FIGURE 51 SENSITIVITY OF OVERALL POWER TRAIN MASS TO COMPONENT EFFICIENCY VARIATIONS

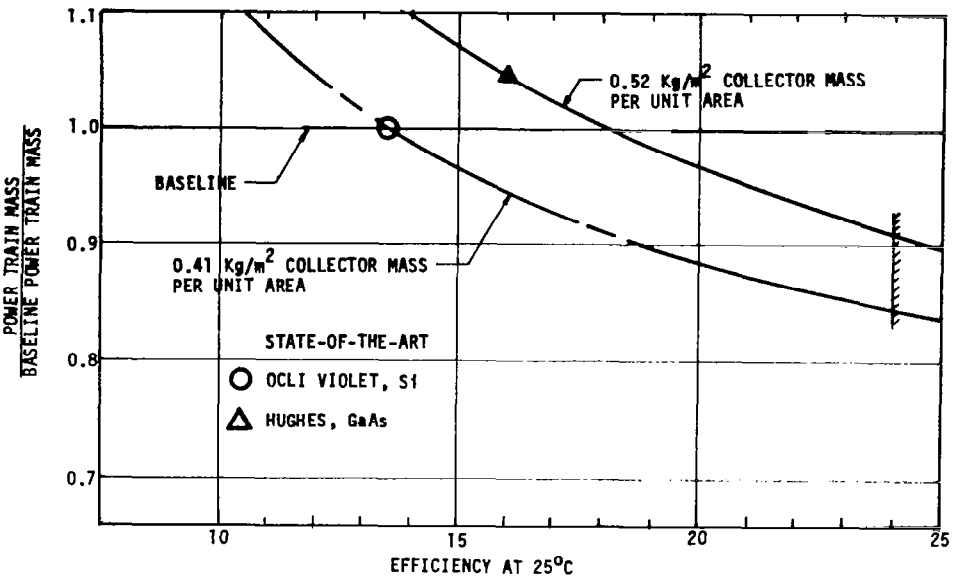

FIGURE 52 SENSITIVITY OF OVERALL POWER TRAIN MASS TO SOLAR CELL EFFICIENCY VARIATIONS

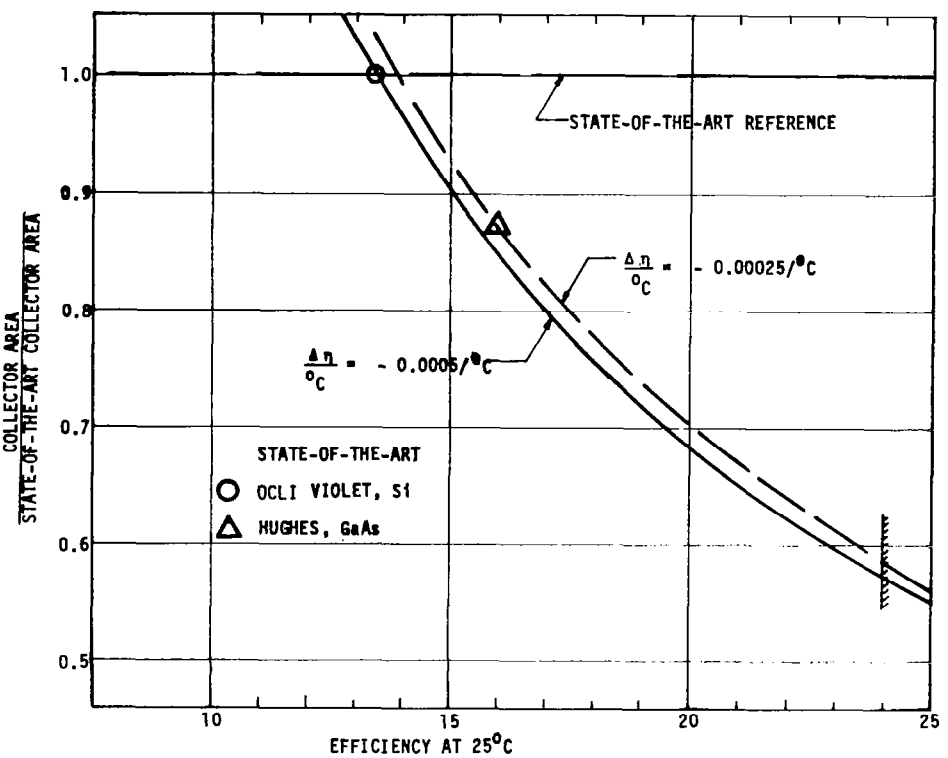

FIGURE 53 VARIATIONS OF SOLAR ARRAY AREA TO SOLAR CELL EFFICIENCY

The fuel cell, electrolyzer and reactant comprise nearly 2/3 of the power train mass. The efficiency at which the fuel cell and electrolyzer are to operate involves a minimization of power train mass as discussed previously. The details of the optimization depend upon the voltage-current and mass property characteristics of these devices. The voltage-current characteristics can only be helped by developing new electrodes which yield lower activation losses. Electrodes made with Paladium offer some hope in this area. The voltage-current characteristics can also be improved by better module designs which minimize ohmic losses. The major area of improvement in the fuel cell and electrolyzer would be to lower their respective mass-to-power ratios. Work in this area is underway under the auspices of NASA-Lewis Research Center and should be encouraged in the context of solar powered aircraft.

Vehicle Sizing Results

Determination of Baseline Aircraft for Primary Mission. The parametric methods discussed earlier were used to size a solar HAPP RPV for the primary mission. The configuration used was a modification of number 18 in Figure 47 and its final form was shown in Figure 49.

The primary mission was examined to ascertain the most demanding day. Since this mission called for up to one year on station at 20 Km (65 600 ft) between 32^{o}N and 38^{o}N, the most demanding day would be the shortest with the lowest sun angle. This is December 21st at 38^{o}N at 20 Km (65 600 ft) and is the design point chosen to size this aircraft.

Using the power train and vehicle sizing methodologies discussed in this report, a set of candidate vehicles could be determined for the design point for each of several gross masses. These candidate sets are similar in presentation format to Figure 35 which is, in fact, one workable set of solar HAPP RPVs for the primary mission. Gross mass was varied from 550 Kg (1213 lb_f) to 1100 Kg (2426 lb_f) and similar plots generated. This wide range in gross masses was used to assess trends in several vehicle sizing parameters, the results of which will be discussed here.

Smallest Vehicle for Primary Mission. As pointed out in an earlier section, the upper vertex of the triangular cross-hatched section in Figure 35 is the smallest workable aircraft. These vertex/gross mass combinations are summarized in Figure 36. Two points are of interest in Figure 36 which is a plot of payload-to-gross weight ratio against power-to-gross weight ratio for that range of vehicles carrying a 112.5 Kg (250 lb_f) payload at the design point. The first point of interest is the maximum on the curve which is the vehicle with maximum payload fraction. The second point of interest is the tangent point of the curve to a line from the origin. The slope of this tangent line is

$$\left(\frac{W_{PAY}}{W}\right) \div \left(\frac{P_{PT_{NIGHT}}}{W}\right) = \left(\frac{W_{PAY}}{P_{PT_{NIGHT}}}\right)_{MAX} \qquad (126)$$

The tangent point identifies the aircraft with the maximum payload per unit power train power. This vehicle will be the one identified hereafter as the baseline solar HAPP for the primary mission. Its extrapolated characteristics are given in Table 17.

Largest Payload for Primary Mission. Referring again to Figure 35, another point of interest is the right-hand vertex of the triangle formed by the constraint lines. Applying the method presented in Figure 37 defines a set of HAPP's, all of which are carrying the maximum payloads for their gross masses. The data in Figure 37 addresses vehicles sized for the primary mission and identifies the minimum power-to-weight ratio per unit payload at a payload of 155 Kg (342 lb_f) corresponding to a vehicle gross mass of 1025 Kg (2260 lb_f).

TABLE 17. PHYSICAL CHARACTERISTICS OF BASELINE SOLAR HAPP RPV

SIZING CRITERIA	DAYTIME	NIGHTTIME
CRUISE ALTITUDE	20 Km	20 Km
CRUISE LATITUDE	38°N	38°N
DAY OF YEAR	DEC 21	DEC 21
PAYLOAD POWER	300 w (0.4 HP)	300 w (0.4 HP)
CRUISE SPEED	27 mps (52.5 Kts)	22 mps (42.8 Kts)
PARAMETRIC VALUES		
POWER TO WEIGHT RATIO	1.069 W/N (0.006 HP/lb_f)	0.6375 W/N (0.004 HP/lb_f)
WING LOADING	43.4 N/m^2 (0.907 psf)	27.2 N/m^2 (0.569 psf)
ASPECT RATIO	18.6	33.7
VERTICAL PANEL TO SPAN RATIO	0.35	--
PAYLOAD MASS	112.5 Kg (250 lb_f)	112.5 Kg (250 lb_f)
LIFT COEFFICIENT	1.34	1.26
WINGSPAN	57.8 m (189.6 ft)	98.3 m (322.4 ft)
THRUST POWER	8.35 Kw (11.2 HP)	4.98 Kw (6.68 HP)
TAPER RATIO	1.0	0.7
MEAN GEOMETRIC CHORD	3.11 m (10.22 ft)	2.674 m (8.772 ft)
GROSS MASS	797 Kg (1757.4 lb_f)	797 Kg (1757.4 lb_f)
POWER TRAIN MASS	414 Kg (912.9 lb_f)	414 Kg (912.9 lb_f)
STRUCTURAL MASS	270 Kg (595.4 lb_f)	270 Kg (595.4 lb_f)
WING AREA	180 m^2/1937 ft^2)	287 m^2 (3088 ft^2)
ROOT CHORD	3.11 m (10.22 ft)	3.11 m (10.22 ft)
TIP CHORD	3.11 m (10.22 ft)	2.18 m (7.15 ft)
HORIZONTAL TAIL VOLUME	0.3	0.3
VERTICAL TAIL VOLUME	0.02	0.01

A second point in Figure 37 is of interest. It corresponds to the mission payload mass of 112.5 Kg (250 lb_f) and identifies a vehicle of about 790 Kg (1742 lb_f) gross mass and a nightime of power-to-weight ratio of 0.6235 W/N for a nighttime power train thrust power of 4.83 Kw (6.47 HP). Note that this is very close to the point identified in the previous subsection and the difference may be strictly in interpolation of points in the two methods.

Impact of Mission Requirements on Vehicle Size. The mission parameters to be varied here are altitude, latitude, day of year, cruise speed, payload mass, payload power, duty cycle and combinations of these to size vehicles for each of the secondary missions.

As altitude increases, air density decreases and speed must increase to maintain constant lift. Power required increases with the cube of speed (linearly with V at constant dynamic pressure), and vehicle size increases roughly with power train mass and required collector area which both increase with power required. Figure 54 presents the change in aircraft size, as indicated by gross mass and wing span, with changes in altitude above and below the design point.

Latitude. As latitude increases at constant altitude and time of year, sun elevation changes and this angular change in relation to vertical solar cells changes power required. This change is reflected in vehicle gross mass and collector area required which is in turn, reflected in wing span. Figure 55 presents the effect of changes in aircraft size with changes in latitude.

Day of Year. As design day-of-year changes at constant altitude and latitude, sun position changes in both azimuth and elevation relative to vertical solar cells. This change is reflected in power train mass and required collector area which affect vehicle gross mass and wing span, respectively. Results of variations in design day of year are reflected in Figure 56.

Payload Mass. Reducing payload mass from 112.5 Kg (250 lb_f) to 45.4 Kg (100 lb_f) for a vehicle sized for the primary mission design point produces the series of plots shown in Figure 57. The characteristics of this vehicle are given in Table 17 comparing it with the baseline vehicle. Note that, although gross mass has been reduced 31% to 550 Kg (1212.8 lb_f) from 797 Kg (1757.4 lb_f), physical size of the aircraft as indicated by wingspan reduces only 15% from 98.3 m (322.4 ft) to 83.9 m (275.2 ft) at night.

Payload Power and Duty Cycle. Aside from the effect increased payload mass has on vehicle size, both payload power level required and payload duty cycle will affect power train mass and required collector area because of changing energy storage requirements with each of these. Figures 58 and 59 summarize the effects of changing payload power and duty cycle on required collector area and power train mass, each ratioed to the baseline condition.

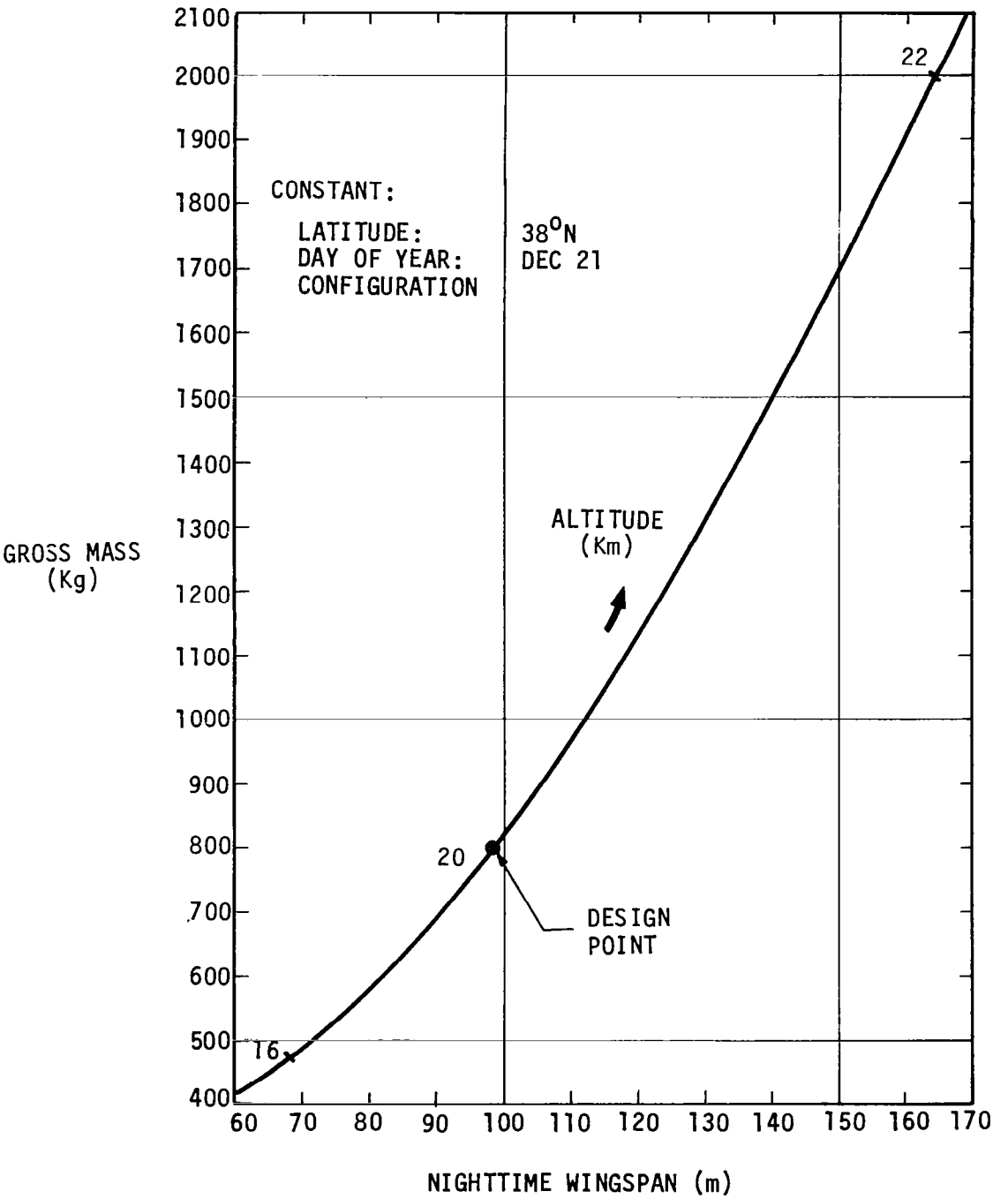

FIGURE 54 EFFECT OF CHANGES IN ALTITUDE ON AIRCRAFT SIZE FOR THE BASELINE CONFIGURATION

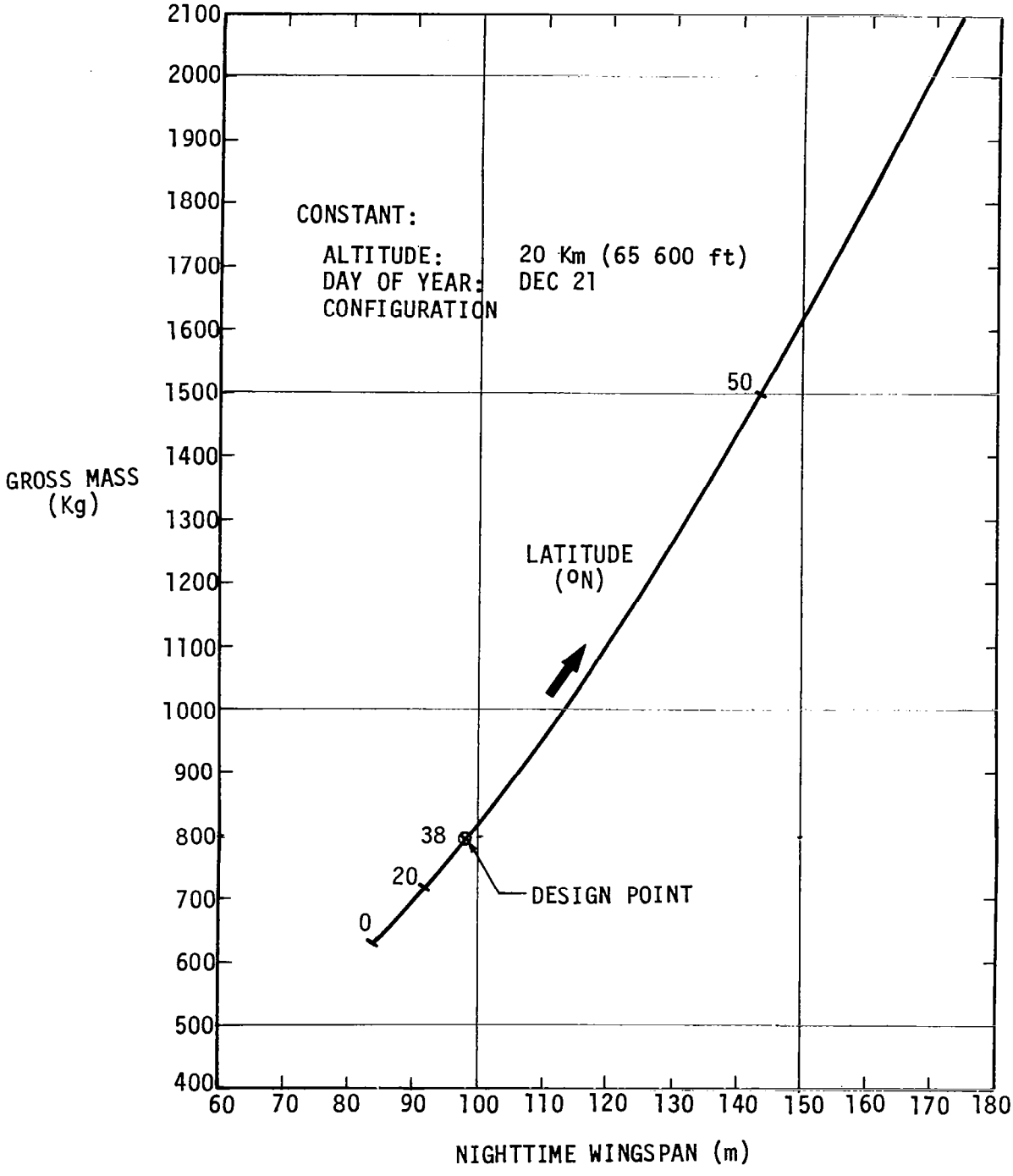

FIGURE 55 EFFECT OF CHANGES IN LATITUDE ON AIRCRAFT SIZE FOR THE BASELINE CONFIGURATION

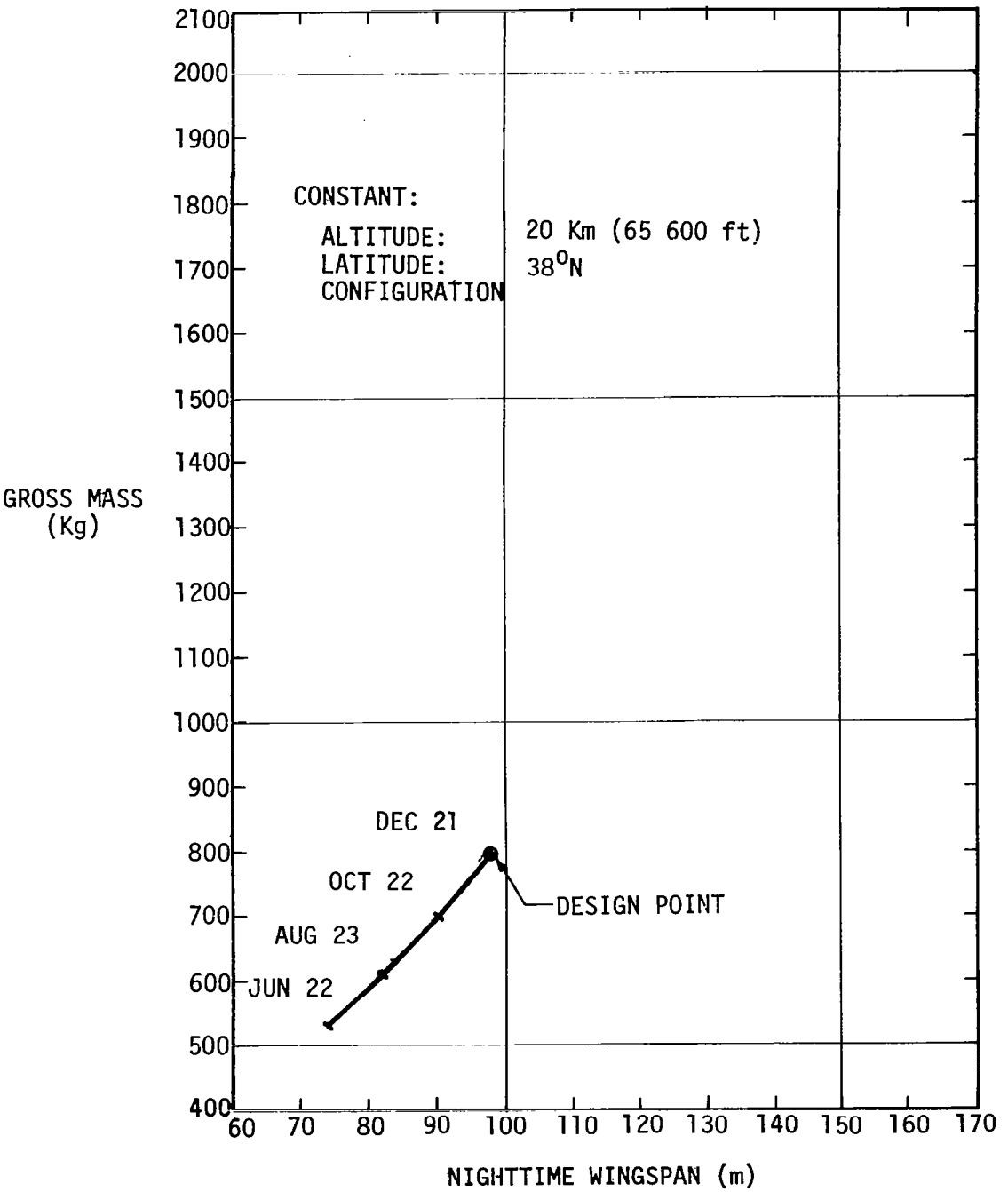

FIGURE 56 EFFECT OF CHANGES IN DAY OF YEAR ON AIRCRAFT SIZE FOR THE BASELINE CONFIGURATION

CONSTANT:

ALTITUDE:	20Km
LATITUDE:	38°N
DAY OF YEAR:	DEC 21
DAYTIME SPEED	27 mps
NIGHTTIME SPEED:	22 mps
PAYLOAD POWER:	300 watts

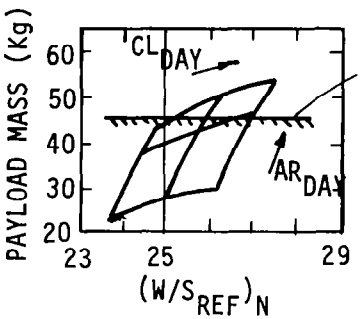

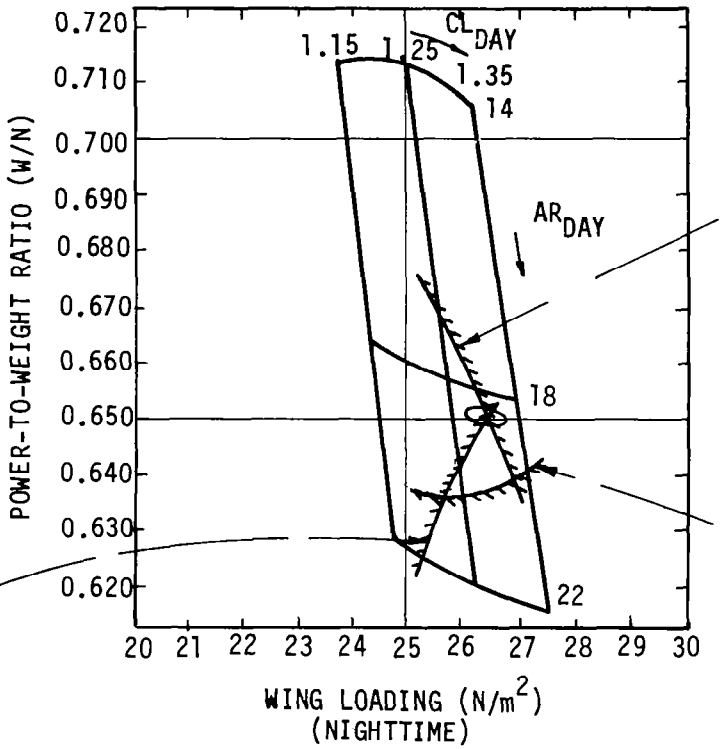

VERTICAL PANEL HEIGHT TO WINGSPAN CONSTRAINT:

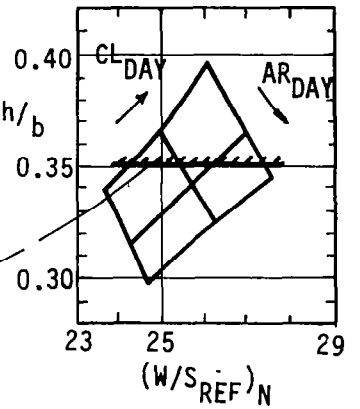

MAXIMUM ALLOWABLE ASPECT RATIO CONSTRAINT:

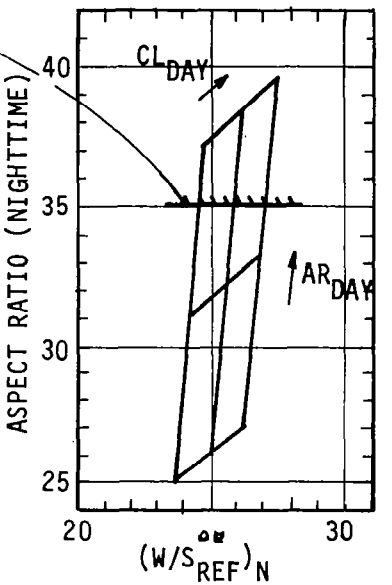

FIGURE 57 PARAMETRIC DETERMINATION OF SOLAR HAPP RPVs FOR PRIMARY MISSION WITH REDUCED PAYLOAD MASS

TABLE 18. EFFECT OF PAYLOAD ON BASELINE VEHICLE SIZE

SIZING CRITERIA	NIGHTTIME BASELINE	NIGHTTIME REDUCED PAYLOAD
CRUISE ALTITUDE	20 Km (60 980 ft)	20 Km (60 980 ft)
CRUISE LATITUDE	38°N	38°N
DAY OF YEAR	DEC 21	DEC 21
PAYLOAD POWER		
CRUISE SPEED	22 mps (42.8 Kts)	22 mps (42.8 Kts)
PARAMETRIC VALUES		
POWER TO WEIGHT RATIO	0.6375 W/N (0.004 HP/lb_f)	0.650 W/N (0.004 HP/lb_f)
WING LOADING	27.2 N/m^2 (0.569 psf)	26.5 N/m^2 (0.554 psf)
ASPECT RATIO	33.7	33.9
VERTICAL PANEL TO SPAN RATIO		
PAYLOAD MASS	112.5 Kg (250 lb_f)	45.4 Kg (100 lb_f)
LIFT COEFFICIENT	1.26	1.23
WINGSPAN	98.3 m (322.4 ft)	82.6 m (270.9 ft)
THRUST POWER	4.98 Kw (6.68 HP	3.50 Kw (4.69 HP)
TAPER RATIO	0.7	0.7
GROSS MASS	797 Kg (1757.4 lb_f)	550 Kg (1213 lb_f)
POWER TRAIN MASS	414 Kg (912.9 lb_f)	313 Kg (690.2 lb_f)
STRUCTURAL MASS	270 Kg (595.4 lb_f)	191 Kg (421.2 lb_f)
WING AREA	287 m^2 (3088 ft^2)	203 m^2 (2184 ft^2)

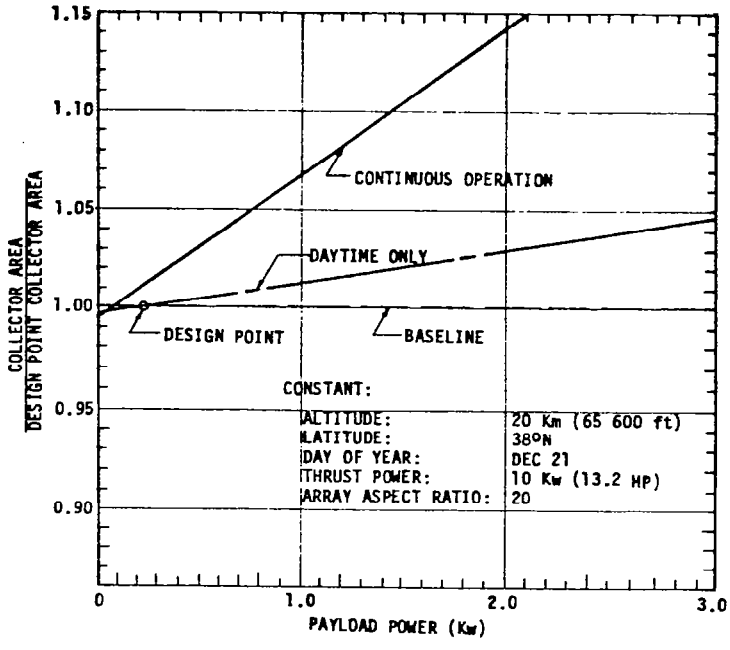

FIGURE 58 SENSITIVITY OF COLLECTOR AREA TO PAYLOAD POWER AND DUTY CYCLE

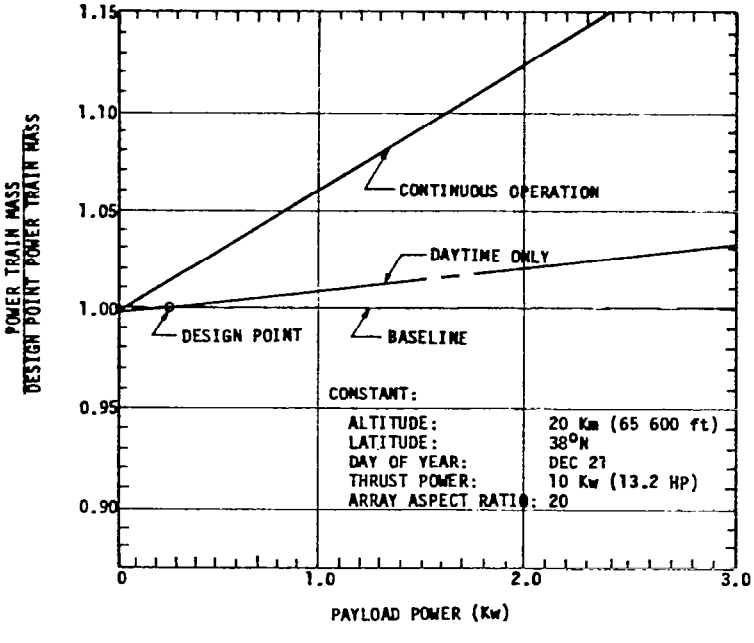

FIGURE 59 SENSITIVITY OF POWER TRAIN MASS TO PAYLOAD POWER AND DUTY CYCLE

Impact of Collector Orientation on Vehicle Size. Initial vehicle sizing attempts were made assuming horizontal collectors might be adequate for the low to moderate latitudes specified in the mission requirements section. This turned out to yield quite large aircraft with quite sizable power train masses and collector areas. The power train sizing methodology was then used to assess the impact of collector orientation in both azimuth and elevation on power train mass and collector area required. The collector array orientations analyzed were:

- Horizontal (reference);
- An array which is always normal to the sun by tracking it during the day;
- A vertical array which tracks the sun in azimuth only, simulating an airborne array which tracks the sun by varying flight path during the day; and
- A vertical array which tracks the sun in azimuth only but differs from the previous one in having collectors on both sides of the vertical panels.

The differences between the last two cases should be briefly elaborated upon. Vehicle sizing studies done in previous internally funded work indicated that overall size could be reduced by limiting collectors to one side of vertical surfaces only and accepting some restriction in daytime flight path flexibility. For this reason, all non-horizontal collectors examined here will have collectors on one side only. The efficacy of this decision will be borne out by the data presented in Figures 60 through 65 which show the effect of collector orientation on both collector area and power train mass for several latitudes. To construct these curves, a power train was sized with each type of collector for several design days of a solar year. Power train mass was ratioed to the equivalent power train mass of a power train with horizontal collectors, and collector area was ratioed to that of an equivalent power trian with horizontal collectors. Trends vary in intensity with time of year, but relative positions of each collector scheme stay the same. Of particular interest is the near-coincidence of the vertical tracking-in-azimuth only with cells on one side only with normal tracking curve around the winter solstice. This minute differential around the HAPP design point is the justification for choosing a power train with vertical solar cells on one side of vertical fins only and capable of tracking the sun in azimuth only by using flight path variations if necessary.

h-V Diagram. The altitude-velocity (h-V) diagram for the solar HAPP is shown in Figure 66. Since the aircraft is designed primarily for high altitude very long endurance cruise, it has relatively little capability at lower altitudes. This curve was produced using assumptions of constant propeller efficiency, motor power equal to twice peak cruise power and a non-parabolic drag polar with constant coefficients. A maximum C_L of 1.8 was assumed.

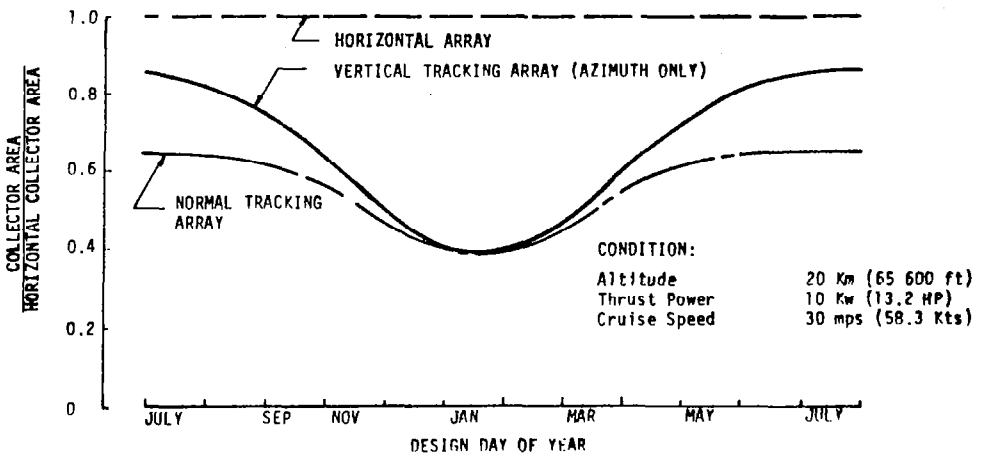

FIGURE 60 SENSITIVITY OF COLLECTOR AREA TO ORIENTATION AT 38°N LATITUDE

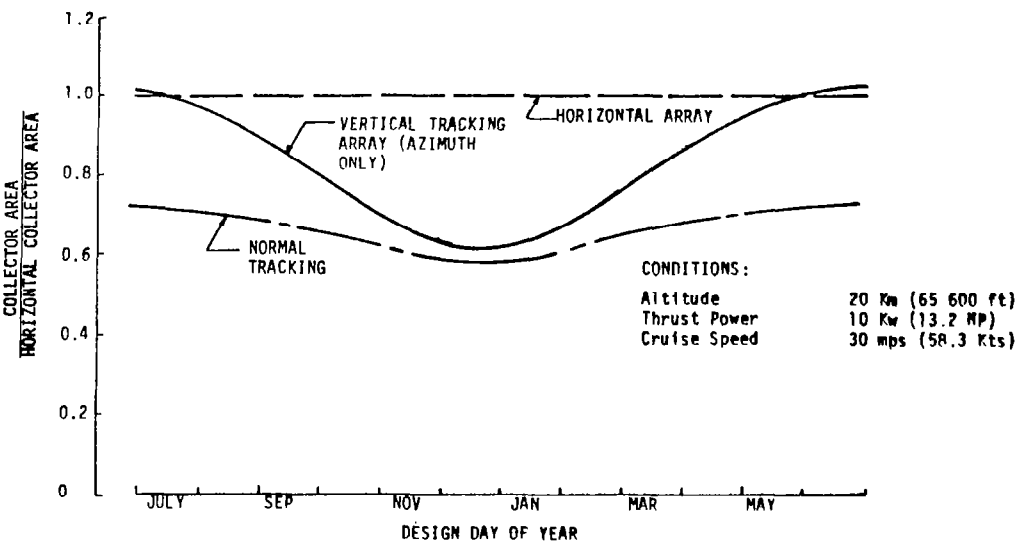

FIGURE 61 SENSITIVITY OF COLLECTOR AREA TO ORIENTATION AT 20°N LATITUDE

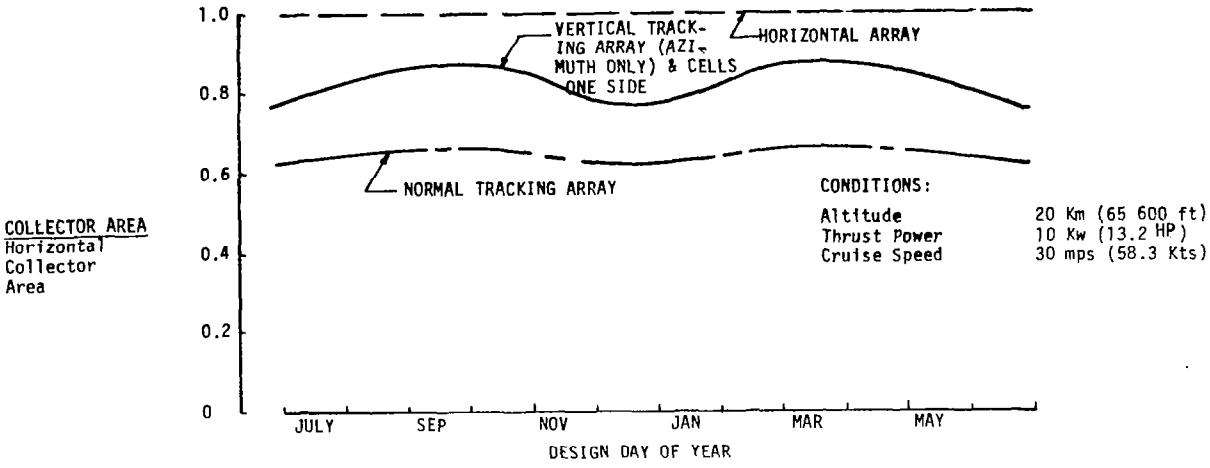

FIGURE 62 SENSITIVITY OF COLLECTOR AREA TO ORIENTATION AT 0° LATITUDE

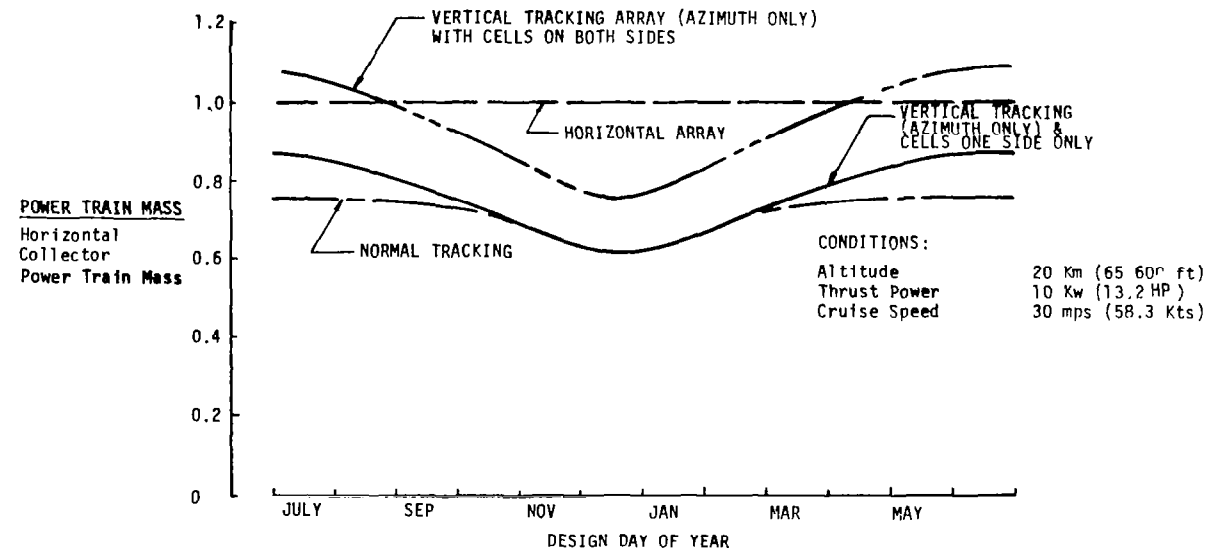

FIGURE 63 SENSITIVITY OF POWER TRAIN MASS TO COLLECTOR ORIENTATION AT 38°N LATITUDE

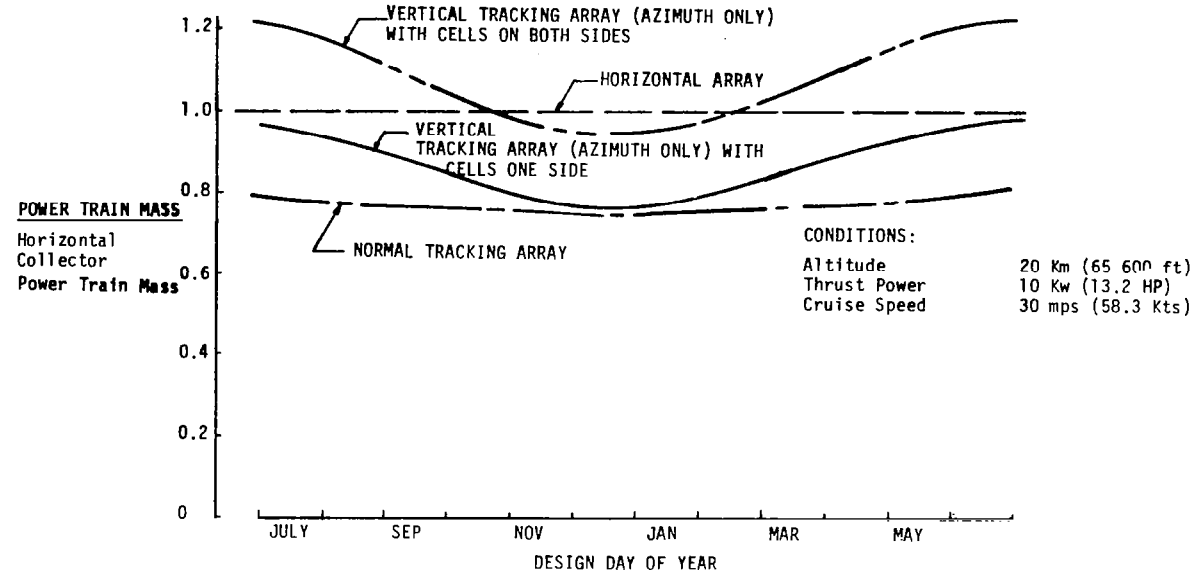

FIGURE 64 SENSITIVITY OF POWER TRAIN MASS TO COLLECTOR ORIENTATION AT 20°N LATITUDE

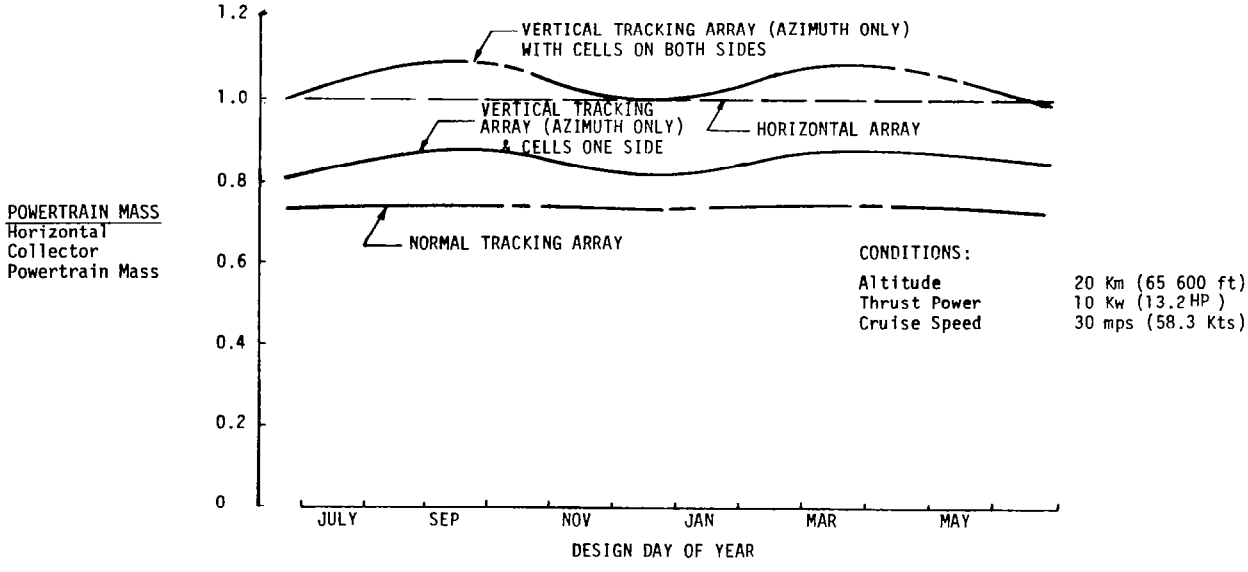

FIGURE 65 SENSITIVITY OF POWER TRAIN MASS TO COLLECTOR ORIENTATION AT 0° LATITUDE

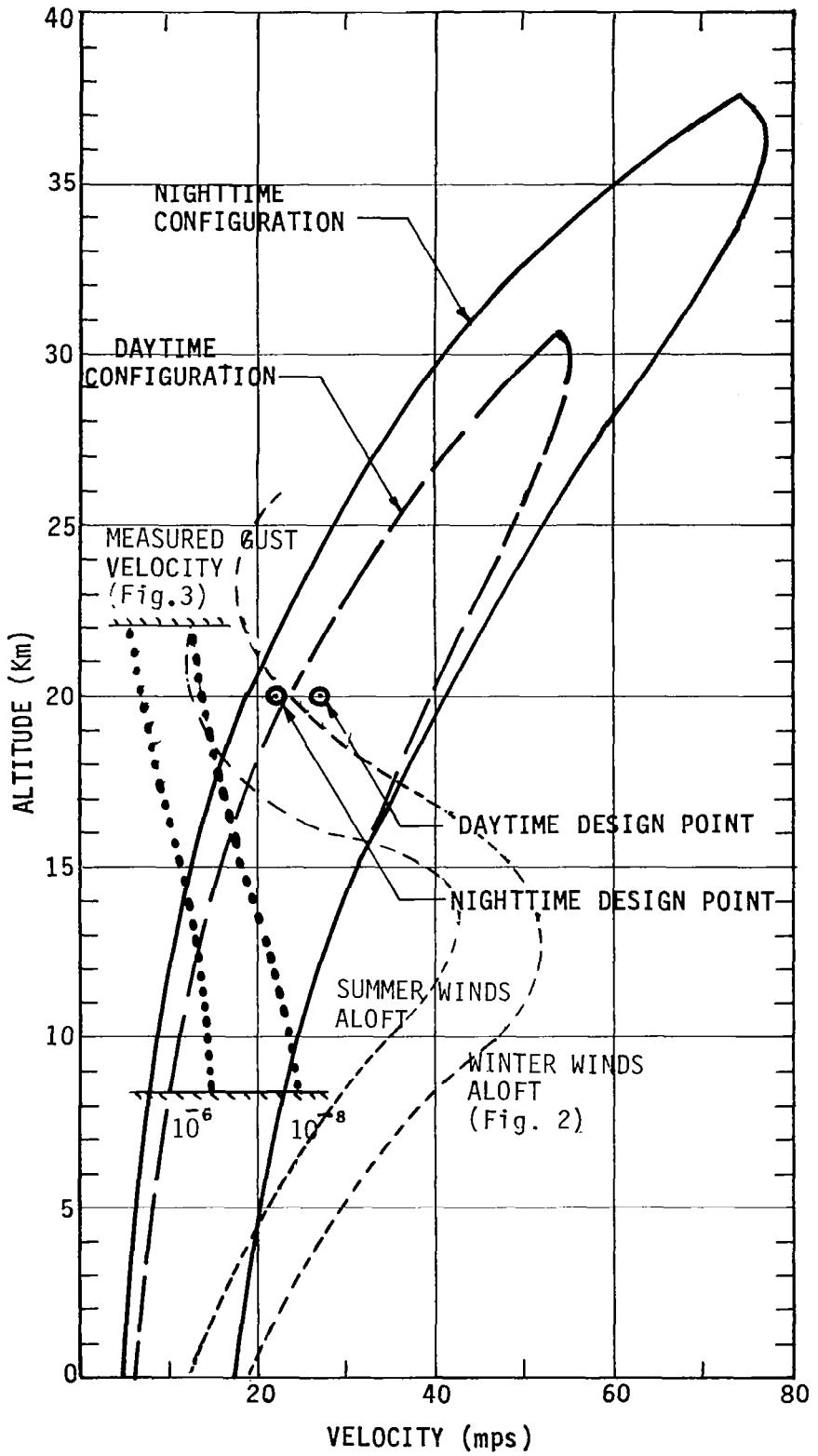

FIGURE 66 ALTITUDE-VELOCITY PROFILE FOR BASELINE SOLAR HAPP RPV

A load factor versus airspeed diagram for the HAPP has been generated (Figure 67). The gust lines shown on this figure are derived from OSTIV sailplane requirements extrapolated to HAPP operating altitudes. From the figure it appears that limit load factors of +2.0 and -0.5 should withstand moderate (3.2 mps) gusts and any maneuvers.

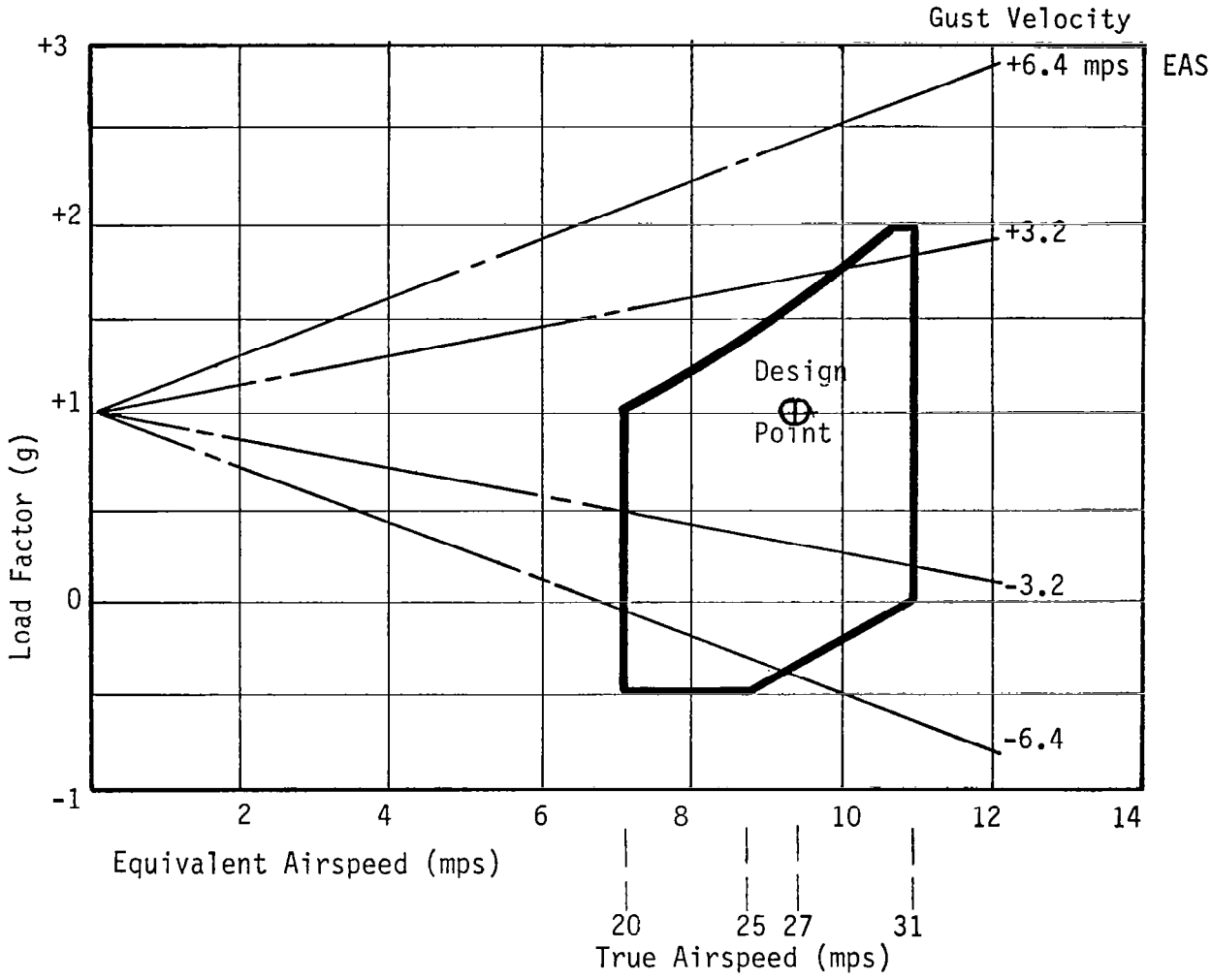

FIGURE 67. LOAD DIAGRAM FOR THE BASELINE SOLAR HAPP

Equilibrium Solar Flight Energy Envelope. A solar powered HAPP RPV has various flight envelopes associated with its performance. The previous section discussed conventional altitude-airspeed and load factor envelopes (h-V and V-n diagrams which are applicable to any airborne vehicle. Unique to solar powered vehicles, though, and particularly to regeneratively powered solar vehicles, is an envelope which takes into account the solar position of the HAPP as well as its altitude. This plot is three-dimensional and is put together holding vehicle configuration and equivalent airspeed constant at the primary mission values.(The fourth dimension,longitude,is ignored here).

This plot is used to describe the ability of a solar HAPP to maintain equilibrium flight at altitude, latitude, time of year combinations significantly different from the point for which it was designed because of the availability of excess solar energy. The vehicle sizing methodology described in previous sections is used with the baseline vehicle size, mass, and equivalent airspeed fixed at design point values. Combinations of altitude, latitude and time of year are systematically varied to determine if sufficient solar energy is available to maintain equilibrium flight for 24 hours. The zero-crossings are then plotted as in Figure 68. The lower portion of this curve stops at 18.3 Km (60 000 ft.) which is a regulated lower flight limit. Please note that, although this envelope is shown plotted inside a cube with finite edges, it is really part of a continuum along both time and latitude axes.

From a practical standpoint, the existence of this capability gives mission planners the flexibility to vary HAPP altitude and latitude certain times of the year to obtain information in different parts of the world. Figure 69 presents planar slices of the total envelope to show variations in altitude possible certain times of the year at 38°N, variations in latitude possible certain times of the year at 20 Km (65 600 ft.), and combinations of altitude and latitude possible at the summer solstice on June 21st.

Of particular interest is the capability of this vehicle to fly at the North Pole in June at high altitudes. Flight is possible, in fact, throughout the Northern Hemisphere and would be limited only by wind conditions.[1] The left side of this figure shows that flight at 38°N is possible throughout the year with higher altitudes possible most of the year. If it is desired to hold 20 Km (65 600 ft) altitude, then this can be done throughout the year in the latitude band of interest in the primary mission (32 to 38°N). Flight at 20 Km (65 600 ft) at lower latitudes is not possible part of the year because of high sun angles. It is possible at the equator, though, in the summer due to large values of solar flux encountered.

---

1 Not factored into this is wind speed variation with latitude and time of year.

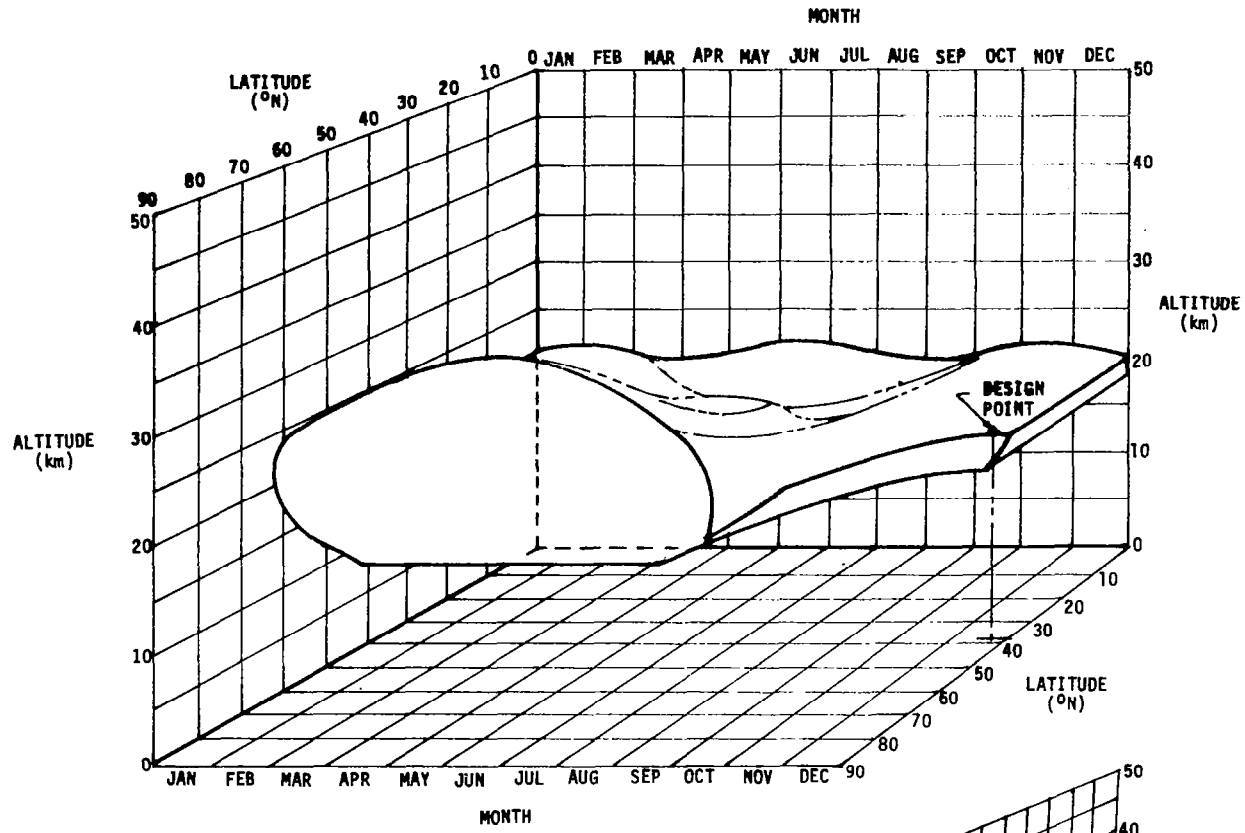

FIGURE 68 THE EQUILIBRIUM FLIGHT ENERGY ENVELOPE FOR A SOLAR HAPP RPV DESIGNED FOR THE PRIMARY MISSION

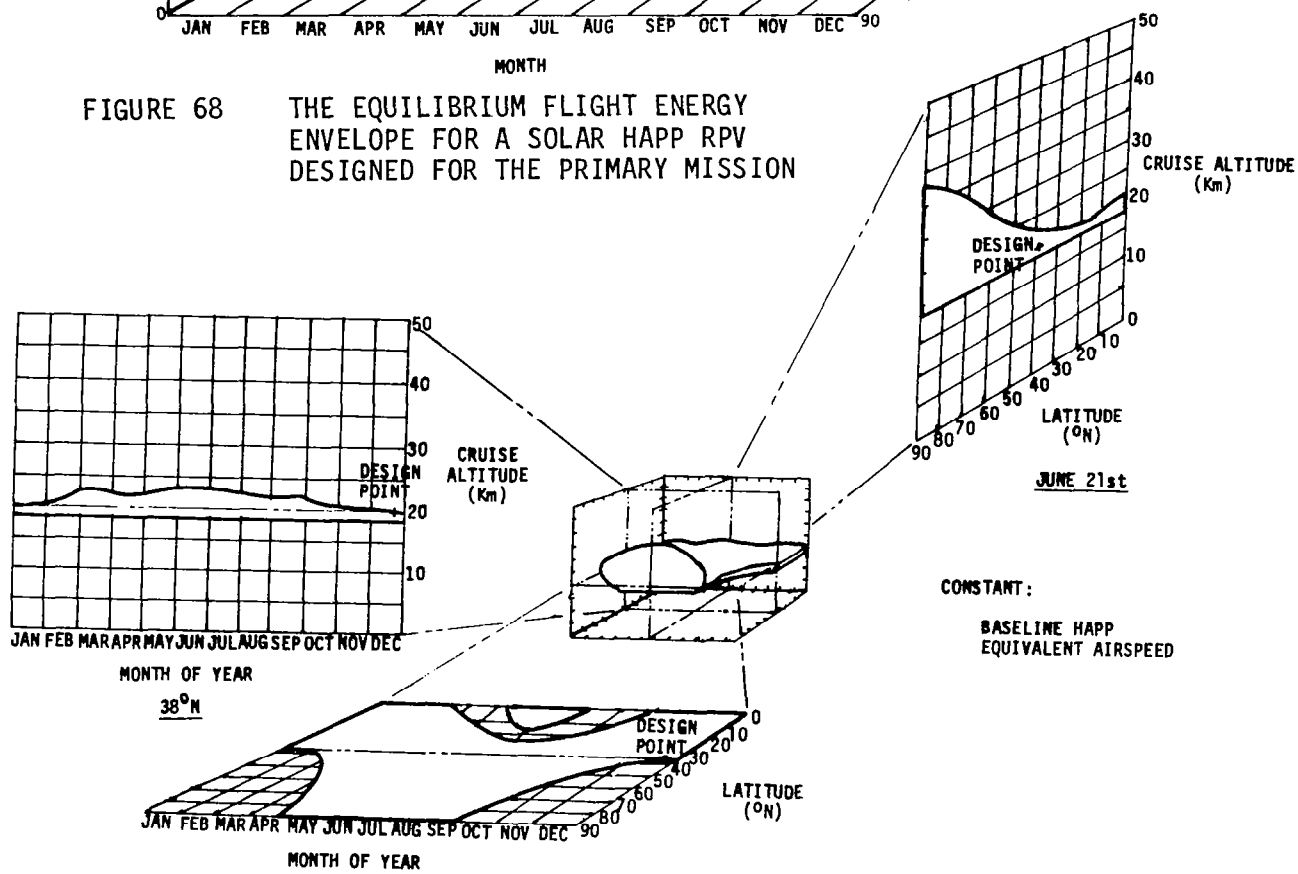

FIGURE 69 PLANAR CROSS-SECTIONS OF EQUILIBRIUM FLIGHT ENERGY ENVELOPE

Stability and Control Considerations. The static stability requirement for a solar HAPP must be carefully determined to minimize gross weight. A high level of aerodynamic stability will involve a trim drag penalty, while artificially provided stability will require heavier actuators and control surfaces and more auxilliary power. With extremely limited available power, it is likely that neutral stability may be optimum.

The dynamics of the aircraft will be quite unusual. High altitude characteristics will tend to approach a conventional lightweight airplane. At low altitude, the response will become dominated by apparent mass of the surrounding air instead of the actual mass of the vehicle. Even the 145 KG of air inside the wing will have a significant effect on vehicle moments of inertia. Slow speed and large size will produce very high levels of damping. The usual phugoid and short term pitch oscillations will probably turn into four overdamped subsidence modes. The ability of even a small yaw rate to give tip velocities equal to cruise airspeed will give limited maneuverability and possibly control reversals. A significant effort will be required to develop and verify analytical modelling tools and to develop autopilot control laws.

Large and flexible structure and slow flight speeds will result in strong coupling of structural modes to vehicle flight dynamics. Stiffness resulting from a wire-braced structure could result in a significant weight savings when aeroelastic effects are considered.

Balancing a HAPP is not expected to be a significant problem. A very large fraction of total mass is concentrated in the fuel cell, electrolyzer, tanks and payload. Since these items are very small compared to the total vehicle, they may be essentially located as required to satisfy both static and dynamic balance requirements. The nature of mission payloads for the primary and secondary missions is also not likely to require trimming a large center-of-gravity (cg) range.

Most of the normal constraints used to determine elevator and stabilizer size will not apply to a HAPP. A fly-by-wire control system will eliminate any stick-free stability requirement. Essentially, no cg range will be required since payload is not disposable and no fuel is consumed. Nosewheel liftoff is not a problem with the use of a dolly-and-towed-launch concept. The inherent maneuverability limits of a large slow aircraft reduce pitch rate requirements. It is likely that the tail will be sized to provide approximately neutral stability and adequate control forces.

The chosen configuration of the control surfaces provides several advantages. The cruciform tail design eliminates any torsion-bending oscillation mode in thin tailbooms. The surfaces can be allowed to rotate freely in roll and be controlled by ailerons to eliminate any pure torsion mode in the tail booms. This would also provide sun-tracking in elevation

for additional photovoltaic cells. Elimination of these aeroelastic modes will allow a large reduction in tail mass. Location of the stabilizers at the wingtip hinge will provide span loading, as well as greatly increasing damping of wingtips in the daytime position. A large degree of active control of this mode would be possible. Independent control of elevators allows twisting the entire wing for roll control. This would eliminate all control surfaces on the wing, minimizing the structure weight while increasing the area available for solar cells if necessary.

Maneuverability. At its normal cruise altitude, a HAPP will have no unusual maneuverability problems. At low altitude, large size, low density and low true air speed will produce maneuverability characterisitcs quite different from conventional aircraft. Apparent mass effects will be quite significant, and some research must be done to verify the associated prediction methods for use on this type of aircraft. Yaw rates will be limited by the reduction in dynamic pressure on the inside wingtip in a turn. For example, at 6 mps (11.7 Kts) and a span of 110 m (360.8 ft), a yaw rate of 0.11 radians per second (6.26 deg/sec) would result in zero airspeed (and zero lift) at the inner wingtip. In practice, trimming out this lift differential across the wing to obtain an equilibrium turn will limit the minimum turn radius to about 5 times the wingspan (based on recent human powered aircraft experience). This will still give a dynamic pressure ratio across the wing span of 0.67:1.0. Even at this minimum radius, the required bank angle will only be 3.7 degrees!

These constraints will require careful consideration when developing the control system and operational methods for a HAPP.

Climb Performance. The unique nature of a solar HAPP power train will also have an effect on the vehicle's climb performance. Maximum power available will only be a function of the motor's design power limit and of the propeller characteristics. Very long flight duration also tends to eliminate a mission-dependent climb requirement. (A 4 hour climb to cruise altitude is insignificant in a 3 month mission.) The only real requirement is that the vehicle be able to climb safely and consistently from launch elevation to cruise altitude. It would be desirable to minimize exposure to winds and turbulence at lower altitudes.

For this report, the motor, gearbox and propeller have been sized to operate at a continuous climb power of twice the maximum cruise power level. As will be seen, this provides a nearly constant climb rate of 1.5 mps (295 fpm) and a typical climb to operating altitude takes just under 4 hours. This power level is also consistent with launch and climb to altitude using only the onboard energy storage system. The vehicle may then be launched at night in a relative calm period, climb to altitude in darkness and be ready to begin collecting energy at first light.

The simplest climb performance calculation is that for cruise altitude. Assuming that the motor and propeller have both been designed to produce twice the peak cruise power required, and that there is only a minor change in efficiency at this power level (motor efficiency could actually improve slightly), the rate of climb will be equal in magnitude to the power-off rate of sink. For the estimated daytime conditions of 24:1 L/D and 27 mps (52.5 Kts) this would give 1.13 mps (222 fpm) rate of climb and a 2.4 degree climb angle. For the proposed variable geometry configuration with wingtips down, comparable values would be 30:1 at 22 mps (42.8 Kts) for a power-off rate of sink of 0.73 mps (144 fpm). Total specific power available would still be approximately 2.25 mps (7.4 fps) for a net rate of climb of 1.52 mps (300 fpm) and a 3.9 degree climb angle.

Exact sea level performance of the proposed motor and propeller combination has not been calculated at this time because no analysis has been done of the off-design point matching of the components. The biggest factor is the increase in air density by a factor of 13.8 which results in a decrease in minimum-power-required speed to only 6 mps (11.7 Kts). This change in airspeed must be compensated for by a change in propeller pitch setting or a reduction in shaft speed. Either change could be expected to reduce system efficiency.

Assuming that the proper design will allow sea level operation of the system at 75% of its normal high altitude efficiency, the initial climb performance can be estimated. As before, the motor and propeller can deliver twice daytime configuration power required at 20 Km altitude (65 600 ft) or three times the nighttime value. The decrease in airspeed at sea level results in another factor of 3.7 for a total ratio of power available to power required of approximately 11-to-1. This is reduced to 8-to-1 by the assumed efficiency losses. Since the specific power required at sea level for L/D=30:1 and 6 mps (11.7 Kts) airspeed is 0.2 mps (0.67 fps) this would give a rate of climb of 1.4 mps (276 fpm). While this rate of climb appears to be rather modest, low airspeed results in a 13 degree climb angle. If low altitude system efficiency is different from the above estimate, climb performance will also change. Even with a 50% reduction from cruise efficiency the climb performance should still be acceptable.

Assuming that power required and system efficiency both vary smoothly between sea level and cruise altitude, then it appears that the rate of climb with wingtips down will be a nearly constant 1.5 mps (295 fpm). This gives a 3.7 hour total time to climb using about three times the electrical power required for normal nighttime cruise power. Allowing for anticipated fuel cell efficiency loss at the higher power level, the total energy requirement for climb should be comparable to that required for a 12 to 13 hour nighttime cruise. It is therefore feasible to perform the entire climb to cruise altitude using the aircraft's normal energy storage capability.

Takeoff and landing. A typical HAPP will probably perform very few takeoffs and landings in its lifetime. If the airframe has the typical 30 000 flight hour design life of an airliner, then with 6 month missions, only 7 takeoff and landing cycles are required. The extreme weight sensitivity of a solar powered aircraft makes the addition of heavy landing gear most undesirable. The result of these concepts means that a HAPP launch can and should depend as much as possible on ground based equipment. Takeoffs are also complicated by the ground clearance required by 10 meter (32.8 ft) diameter propellers required for good cruise performance.

Weight penalty can be minimized by launching from a wheeled dolly. The aircraft could either rise from the dolly as soon as flying speed is reached, or the wheels could be dropped upon command before leaving the airfield boundary. Since a HAPP would have a sea level stall speed of only 5 mps (9.7 Kts) either very light-weight wheels (foamed plastic for example) or skids could be used.

The ground clearance problem can be solved by use of a ground-based tow vehicle or winch to tow the HAPP to an altitude of a hundred or so meters (which is out of most low level turbulence). After towline release, the motors could be started and a normal climb commenced. The props could be stopped and locked in a horizontal position for landing.

The main airfield requirement will be to allow adequate room for a HAPP to climb or descend over any nearby obstacles. The low flight speed will also require that all operations occur directly into whatever wind exists. Actual runway required is very small. Assuming a very low braking deceleration of 0.1 g gives a stopping distance about 18 meters (60 ft). The major requirement will be to allow for deviation from the planned touchdown point due to turbulence. The light weight of a HAPP should make operations from a grass airfield quite acceptable.

A major requirement for a HAPP is some sort of glide path control. The estimated 30:1 L/D results in a glide path angle of 1.9 degrees. This would tend to produce potentially large touchdown position errors. Spoilers or drag brakes could be used; however, installation weight could be significant. In this regard, the use of drogue parachutes could be considered. Slow airspeed would allow the use of a thin plastic film material. An adequate parachute could weigh as little as a kilogram.

The ideas presented here are all aimed at minimizing the takeoff and landing weight penalty that must be carried for the entire mission. The cost for this weight reduction is some complication of takeoff and landing operations. In view of the low frequency of these operations, some complexity is probably justified. An inherent assumption involved here is that the aircraft will be capable of relatively conventional climb and descent through the lower atmosphere. As has been seen, adequate power is available; however, a significant increase in primary structure weight may

be required to withstand low altitude turbulence. An increase in low altitude maximum speed may also be required to overcome winds. These problems may required the development of more complex launch and recovery schemes.

CONCLUDING REMARKS

When the concept of regeneratively powered solar high altitude long endurance flight is examined in a total system context, some conclusions can be reached. These will be discussed here and then followed by recommendations pertinent to each subject area.

Missions

Previous studies have shown that many civilian and military missions exist which could be done by solar HAPP RPV's. Most are in the intelligence gathering and communications relay categories, and all military missions would rely on operation in non-hostile environments. Mission planning must take into account prevailing atmospheric conditions in order to keep flight speeds as low as possible in altitude bands of interest. Payloads must be as light as possible and carefully integrated into the power train electrical and cooling subsystems to keep overall vehicle size as small as possible.

Future work in the mission area should involve specifically determining specific civilian and military missions which could be done by a vehicle such as the one postulated in this study. Payload parameters as well as operational altitudes, latitudes, and times of year should be stipulated and efforts made to conceptually design vehicles for these missions.

Solar Radiation and Atmospheric Properties

Forms of solar radiation other than direct solar flux must be treated as insignificant for energy gathering purposes since diffuse radiation and albedo both vary too much to be counted upon. The heat energy dissipation portion of a solar power train, however, must be designed to handle the highest levels of both. Winds do not appear to be a problem through the year in the region of primary interest in this study (latitudes 32^{o}N to 38^{o}N over California); however, this is not true elsewhere in the world and HAPP's may well have to be designed to operate only over certain portions of the globe. Very little unclassified high altitude turbulence data is available for arriving at suitable gust design loads. This is perhaps the most fruitful area for future investigation in the atmospheric properties category, and gathering this information is an excellent candidate mission for a near-term low speed, high altitude RPV.

Energy collection and Storage Components

The energy collection subsystem which looks most promising for future development is photovoltaics. The type of photovoltaic collector currently offering the most promise is silicon gridded-back cells and future research and development effort should be directed toward developing this technology for airborne applications, if possible. Energy collection systems which track the sun in both azimuth and elevation will be the smallest, but the aerodynamic and mechanical penalties paid may offset these efficiency gains. In fact, analyses performed during this contract indicate that vertical collectors tracking the sun in azimuth by flight path control are as efficient as fully tracking collectors around the most critical days of the solar year. At other times, fully tracking collectors are noticeably better, but enough additional energy exists over the day to more than make up the difference.

The most promising energy storage devices appear to be electrolyzer/fuel cell combinations using hydrogen and oxygen as chemical reactants. Since this portion of the power train is the most massive, it is a very fruitful area for future research and development effort, particularly if long endurance airborne applications can be considered.

In order to minimize total power train mass and collector area, collectors, electrolyzer, storage tanks and fuel cell must be considered together. Loads on these components should also be matched to avoid using power conditioning wherever possible. Another area which should be investigated is off-design point operation. If a power train is designed to collect sufficient energy to power a vehicle at the worst time of year, usually around the winter solstice, then how is excess energy dissipated at the summer solstice? The answer to this question is beyond the scope of this study but should be addressed nevertheless.

Thrust Generation Components

Electric motor and gearbox technologies are well in hand and not much efficiency can be gained from further research and development. However, reliability of these components which will be rotating for long periods of time should be addressed to assess the impact on efficiency and power-to-mass ratio. Propellers will be very large and turn at low speeds with consequent low Reynolds number flows. Some attention should be paid to designing large, lightweight propellers. Motor, controller, gearbox and propeller must also be analyzed together to match component impedances for the lowest overall power train mass.

To summarize, every component in a regenerative solar power train should be designed to minimize overall power train mass and collector area.

Airframe Related Issues

Detailed modelling of large lightweight airborne structures was beyond the scope of this study but should definitely be investigated with several preliminary designs constructed and analyzed. Conclusions and scaling laws should then be put together and these used to test the efficacy of the large HAPP structures suggested in this and other recent works. Large anti-symmetric configurations appear quite flexible with regard to flight path constraints and should be investigated to determine if their highly unorthodox characteristics contribute to improved mission performance. With regard to flight path constraints at certain times of year, specific mission requirements should be used to determine the effect of prevailing winds on forward flight speed with sun azimuth angle taken into account. Vehicle dynamics should be considered to determine if structural flexibility could be used to improve dynamic stability and control problems.

Last, but not least, further work should be done to define actual launch, recovery, guidance and control scenarios which are applicable to the size and performance class of vehicle postulated in this study.

To summarize, a regeneratively powered long endurance HAPP RPV appears feasible for operation in the late 1980s or 1990s based on the work performed in this study. This conclusion does not imply, however, that a fully capable (one year plus duration at any altitude/latitude combination) is feasible with the current state-of-the-art. Much research and development must be performed before this will be possible. The most fruitful areas have been mentioned in the preceding paragraphs.

APPENDIX A

METEOROLOGICAL DATA APPLICABLE TO PRIMARY MISSION

A large base of meteorological data exists and has been accessed during this study to provide data on winds aloft throughout the year in the mission areas of concern. These data are stored at grid points covering most of the northern hemisphere. The grid separation is approximately 360 km (194.2 nmi) between grid points. Figure A-1 shows the coverage of this grid.

For each day of the months of January and July 1969, 1970, and 1971, Figure A-2 presents the wind speed (in meters per second). These data are extracted from two grid points - the grid point nearest Northern California (39.05N - 122.27W) and the other grid point nearest Southern California (32.3N - 115.5W). These data are given for 100 mb (twice per day), and 50 mb, and 30 mb (once per day) pressure levels.

Presented in Figure A-2 are histograms for each level for January and July at two California locations. If mission success is defined as scalar wind speed less than or equal to 30 mps (58.2 Kts) 98 percent of the time, it is seen that for the winter cases, only the highest pressure levels (50 mb and 30 mb) have wind speed distributions that meet this criterion. For the summer months for California locations the winds are much lighter with even the 100 mb level having winds less than 30 mps (58.2 Kts).

If mission success is defined as daytime winds equal to or less than 27 mps (52.5 Kts) and nighttime winds less than or equal to 22 mps (42.8 Kts), then from Table 6 it can be seen that for both California locations in January, success if only possible above 70 mb and in July all levels above 100 mb are favorable levels.

In order to provide a feel for the wind regimes at 150 mb and 50 mb, Figure A-3 also presents the wind fields for 15 Jan 1969 and 15 Jul 1969. The arrow points in the direction the wind is blowing and the tail-barbs give the wind speed, where a half barb is 2.5 mps (5 Kts), a whole barb is 5 mps (10 Kts), and a triangular flag is 25 mps (50 Kts). These are additive on the shaft of the arrow. What should be noted is that for mid-latitude (approximately 30 N - 55N) the flow is fairly zonal (predominately east-west) in the winter very strong at 150 mb and lighter at 50 mb. In summer at mid-latitudes the flow is not only light and zonal, but there is a change in direction between 150 mb and 50 mb (sometimes occurring a little higher than 50 mb) where the lower flow (150 mb) is mostly westerly (winds blowing from the west) and mostly easterly at 50 mb. This change of direction can be used to conserve energy with fairly minor altitude adjustments. The subtropical and tropical regions

tend to be dominated by generally easterly winds at all levels up to the operational flight levels, stronger in the lower levels of the subtropical region, particularly in the winter. Portions of the tropics are influenced by the easterly jet stream (strong east winds centered about 25 km (82 000 ft) at 10N-15N in the summer season), and these winds often blow rather strongly down to HAPP operation levels.

The wind profile depicted in Figure A-4 is a representation of the maximum wind speeds expected for the windiest month above Cape Canaveral, Florida with a 95% probability-of-occurrence wind profile. That is the extreme curve on the right. For HAPP interests the wind speed at the 95% level at 20 Km would be 27 m/sec. The four other curves are synthetic profiles below 6, 12, 18 and 24 Kms based on 99% probability-of-occurrence wind build-up. These curves are primarily to help define wind shear at the 1% level beneath the selected level.

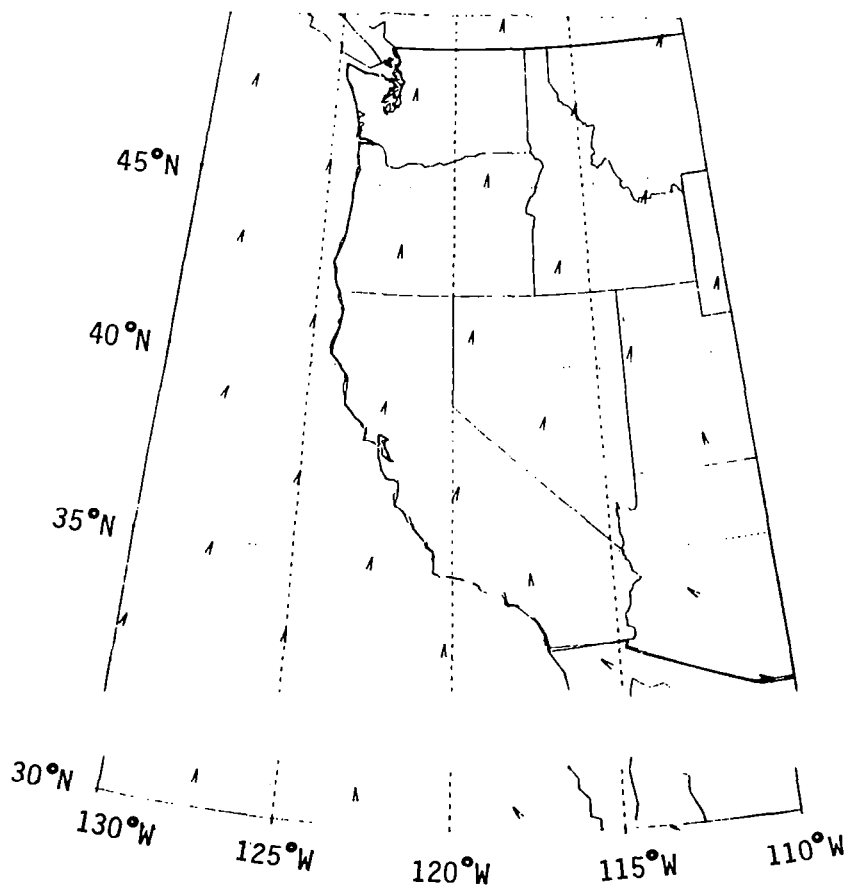

Figure A-1. Nearest Gridpoint Coverage to Primary Mission Area.

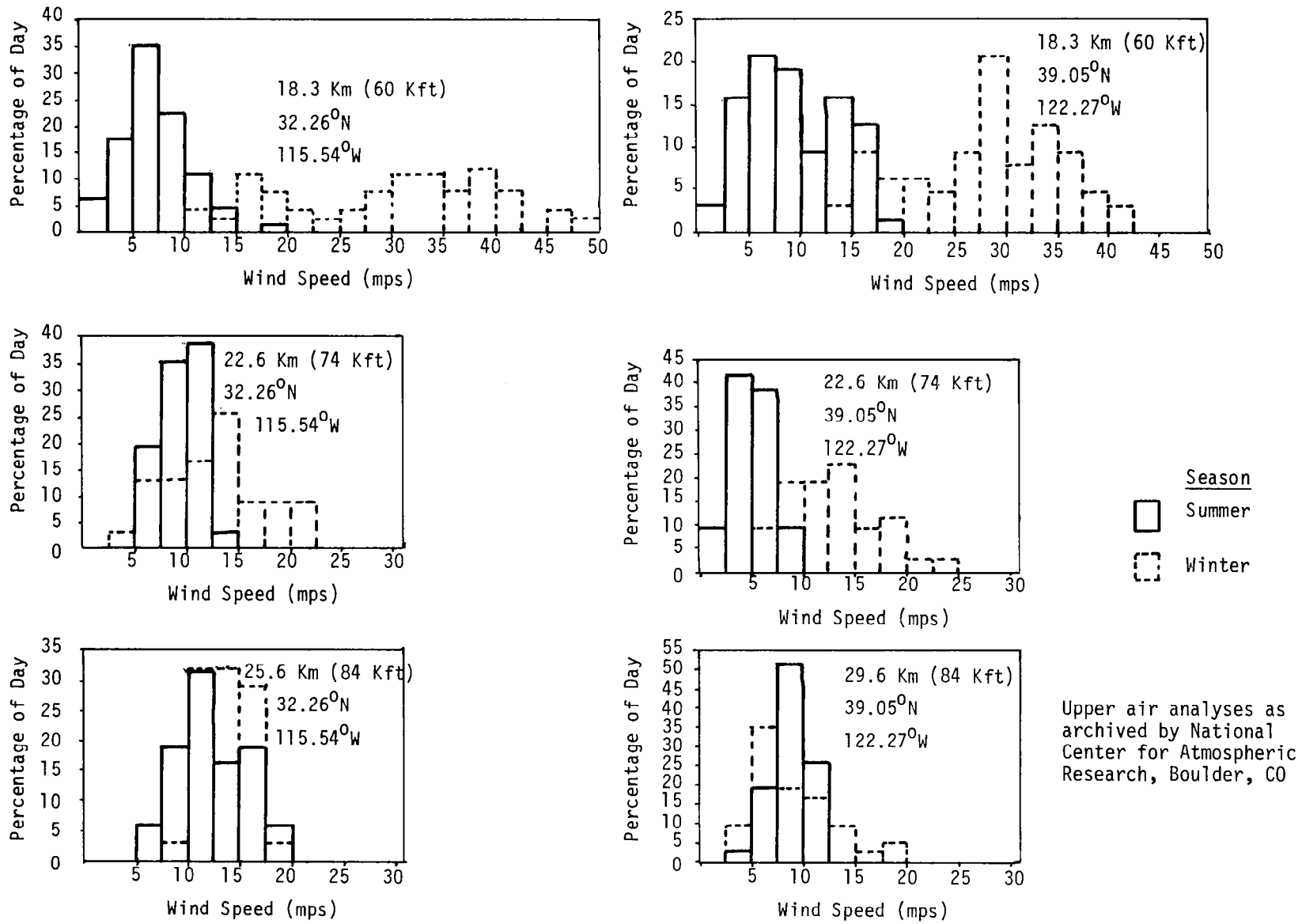

Upper air analyses as archived by National Center for Atmospheric Research, Boulder, CO

Figure A-2. Wind Histograms For The Southern (Left) and Northern (Right) Extremities of the San Joaquin Valley

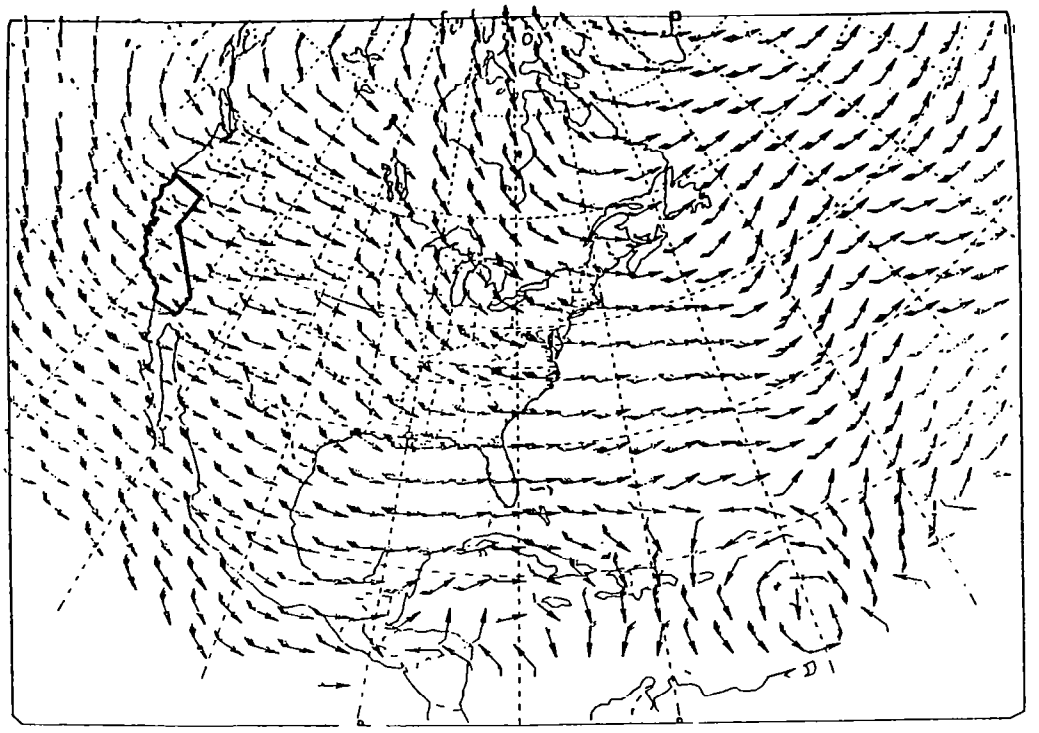

Winter

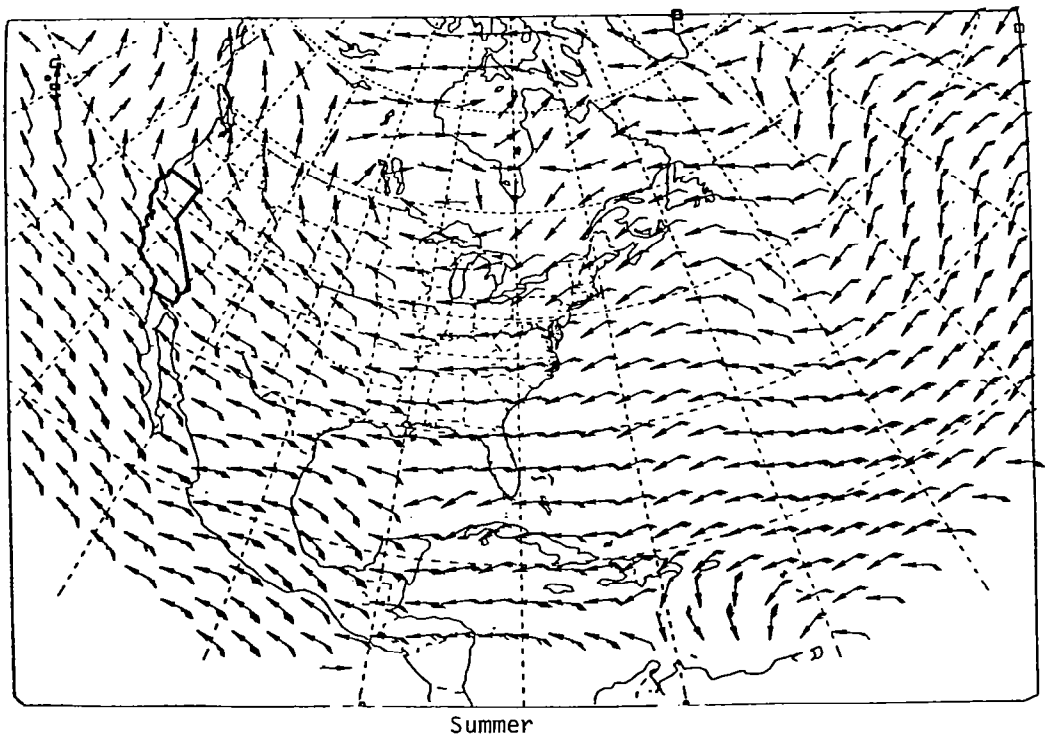

Summer

Figure A- 3. Wind Flow Charts for the Continental United States at 22.6 Km (74 Kft)

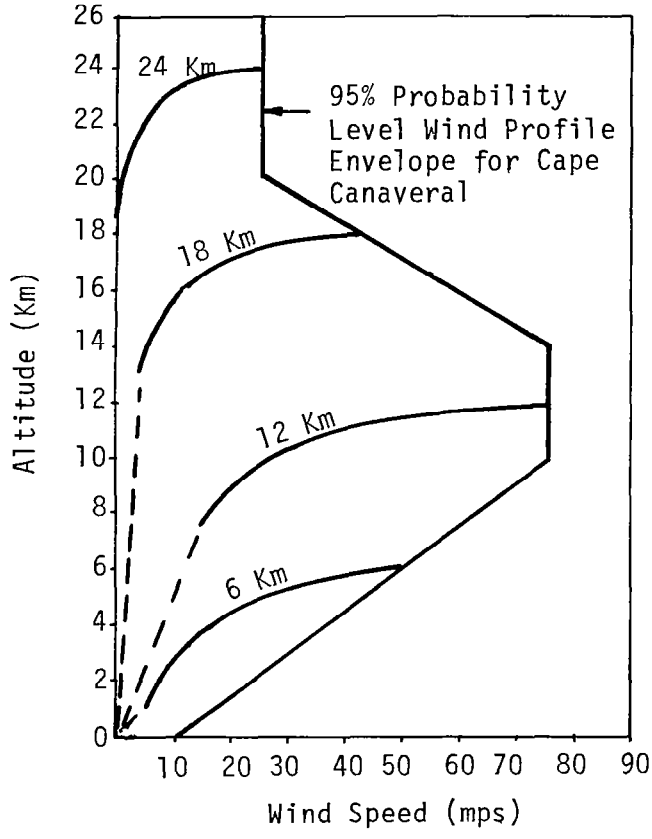

Figure A-4. Wind Profile for Cape Canaveral, Florida. Data from Ref 1.

APPENDIX B

FUEL CELL AND ELECTROLYZER PERFORMANCE CHARACTERISTICS

Symbols

NOTATION	DEFINITION	UNITS
A	Constant in Tafel equation	volts
A_c	Electrode area per cell	ft^2
A_i	Activity of substance i	unitless
C	Cell	
E	Thermodynamically reversible fuel cell	volts
G	Gibbs free energy	Joules/ gram-mole
i	Current density	amps/ft^2
i_{ea}	Anode exchange current density	amps/ft^2
i_{ec}	Cathode exchange current density	amps/ft^2
i_{la}	Limiting current density for anode	amps/ft^2
i_{lc}	Limiting current density for cathode	amps/ft^2
K_c	Cell electrolyte electrical conductivity	mho/ft
K_w	Constant of law of mass action	unitless
M	Molality	unitless
n	Number	unitless
P	Pressure	atmosphere
P'	Power density	W/ft^2

Symbols
(Continued)

NOTATION	DEFINITION	UNITS
P_i	Partial pressure of substance i	atmosphere
R	Universal gas constant	8.314 Joules/ gram-mole^{o}K
r	Product of electrode area and cell resistance	ohmft^2
R_c	Resistance per cell	ohms
^{o}K	Temperature	K
V_c	Voltage per cell	volts
X_p	Ratio of operating power density to peak power density	unitless
z	Number of electrons transferred	unitless
α	Transfer coefficient	unitless
γ_i	Activity coefficient of substance i	unitless
ΔV	Overpotential	unitless
Δx_c	Separation between anode and cathode	ft
η	Efficiency	unitless
Φ	Faraday constant	$9.6578^{x}10^{4}$ coulombs/ gram-mole

Subscripts

A	Activation (overpotential)
a	Anode
C	Concentration (when used as subscript to overpotential)

Subscripts
(Continued)

NOTATION	DEFINITION	UNITS
C	Cell (when used as subscript to voltage)	
c	Cathode	
EL	Electrolyzer	
FC	Fuel cell	
i	Substance index	
O	Ohmic (overpotential)	
o	Reference value	
T	Threshold (overpotential)	

FUEL CELL AND ELECTROLYZER PERFORMANCE CHARACTERISTICS

A fuel cell converts chemical energy stored in a set of reactants to electrical energy; an electrolyzer performs the reverse process of converting the products of the fuel cell reaction back into the original reactants. The ideal thermodynamically reversible fuel cell potential, E in volts, can be expressed in terms of the molar Gibbs free energy of the fuel cell chemical reaction, ΔG in Joules/gram-mole, as:

$$E = \frac{-\Delta G}{z \Phi} \qquad \text{(B-1)}$$

where z is the number of electrons transferred in the reaction and Φ is the Faraday constant equal to 9.6478×10^4 coulombs/gram-mole. The reaction with the highest energy release per unit mass is the hydrogen/oxygen reaction:

$$2H_2(g) + O_2(g) + 6H_2O(\ell) \longrightarrow 4H_3O^+(aq) + 4OH^-(aq)$$

The separate electrode reactions that occur simultaneously are:

$$2H_2 + 4H_2O \longrightarrow 4H_3O^+ + 4e^- \quad \text{(cathode)}$$

$$4e^- + O_2 + 2H_2O \longrightarrow 4OH^- \quad \text{(anode)}$$

For this reaction z=4. The Gibbs free energy of the reaction can be expressed as:

$$\Delta G = \Delta G_o + RT \ln\left(\frac{A^4_{H_3O^+} A^4_{OH^-}}{A^2_{H_2} A_{O_2} A^6_{H_2O}}\right) \qquad \text{(B-2)}$$

when this is divided by $-z\Phi$ where $z=4$ it becomes the Nernst Equation:

$$E = E_o - \frac{RT}{4\Phi} \ln \left(\frac{A^4_{H_3O^+} A^4_{OH^-}}{A^2_{H_2} A_{O_2} A^6_{H_2O}} \right) \qquad \text{(B-3)}$$

where A_i is the activity of substance i, R is the gas constant (8.314 $J/_{gmole-K}$), E_o is a reference potential 1.2339 volts and T is the temperature in Kelvins. The activity of substance i for gases can be expressed in terms of the partial pressure of substance i, P_i, a reference pressure P_o and an activity coefficient γ_i, as:

$$A_i = \frac{P_i}{P_o} \gamma_i \qquad \text{(B-4)}$$

For solid solutes the activity of substance i can be expressed in terms of the molality (amount of solute per unit mass of solvent), M_i; a standard molality, M_o; and an activity coefficient, γ_i, as:

$$A_i = \frac{M_i}{M_o} \gamma_i \qquad \text{(B-5)}$$

Making these substitutions the Nernst Equation becomes:

$$E = E_o - \frac{RT}{4\Phi} \ln \left[\left(\frac{M^4_{H_3O^+} M_{OH^-}}{P^2_{H_2} P_{O_2} A^6_{H_2O}} \right) \left(\frac{\gamma^4_{H_3O^+} \gamma_{OH^-}}{\gamma_{H_2} \gamma_{O_2}} \right) \right] \qquad \text{(B-6)}$$

Using the law of mass action,

$$A_{H_3O^+} A_{OH^-} = K_w A_{H_2O} \quad , \qquad \text{(B-7)}$$

where K_w is a constant for specified pressure and temperature, this simplifies to:

$$E = E_o - \frac{RT}{4\Phi} \ln\left(\frac{K_w^4 A_{H_2O}^2}{P_{H_2}^2 P_{O_2}}\right) \qquad \text{(B-8)}$$

The efficiency of a fuel cell and electrolyzer is the product of the coulombic efficiency and the voltage efficiency. In a fuel cell, the coulombic efficiency is the ratio of electronic charges transferred to load to the electronic charges transferred in the actual fuel cell reaction. In an electrolyzer the coulombic efficiency is the ratio of electronic charges resulting in the production of H_2 and O_2 to the electronic charges sent through the electrolyzer. Charges may be consumed in parasitic reactions or lost due to leakage currents. Fuel cells and electrolyzers are usually designed to control these losses to less than 2%. In a fuel cell the voltage efficiency is the ratio of the measured voltage of a cell, V_c, to the reversible or thermodynamic voltage, E, given by the Nernst Equation as a function of the pressure and temperature combination at which the reaction occurs. The difference between the reversible voltage, E and the operating voltage, V_c, is known as the over-potential. The over-potential is caused by one or more of the following polarizations: (1) activation (2) concentration and (3) ohmic.

The activation overpotential, ΔV_A, is caused by the physiochemical processes associated with the absorption of molecules or atoms on electrode surfaces. This overpotential is controlled by the rate determining reaction and the corresponding activation energy required before reaction occurs. In the H_2/O_2 reaction the rate determining reaction is that associated with the O_2 electrode. Platinum catalysts are used in electrode designs to minimize this over potential. The activation polarization can be expressed as the sum of that due to the anode (a)

$$\Delta V_{A_a} = -\frac{RT}{\alpha_a z\Phi} \ln\left(\frac{i}{i_{ea}}\right) \quad , \qquad \text{(B-9)}$$

and that due to the cathode (c)

$$\Delta V_{A_c} = -\frac{RT}{\alpha_c z\Phi} \ln\left(\frac{i}{i_{ec}}\right) \qquad \text{(B-10)}$$

where α_a and α_c are the transfer coefficients of the anode and cathode reactions, respectively, and i_{ea} and i_{ec} are the exchange current densities associated with the anode and cathode, respectively.

The concentration overpotential is caused by the depletion of ion concentrations in the vicinity of the electrodes. This usually occurs at high current densities. This overpotential depends on diffusion of particular ions and can be reduced by agitation or stirring actions. The concentration overpotentials of the anode and cathode can be expressed as

$$\Delta V_{C_a} = \frac{RT}{z\Phi} \ln \left(1 - \frac{i}{i_{la}}\right) \tag{B-11}$$

and

$$\Delta V_{C_c} = \frac{RT}{z\Phi} \ln \left(1 - \frac{i}{i_{lc}}\right) \tag{B-12}$$

respectively, where i_{la} and i_{lc} are the limiting current densities of anode and cathode, respectively.

The ohmic overpotential is the consequence of electrical resistances in the cell solution and electrodes. The ohmic overpotential, ΔV_o, can be expressed as

$$\Delta V_O = ri \tag{B-13}$$

where $r = A_C R_C \doteq \Delta X_C / K_C$, A_C is the electrode area, R_C is the resistance of a cell, ΔX_C is the separation between cathode and anode and K_C is the cell electrolyte electrical conductivity in mho/ft.

Since there is little reason to operate the cell in a condition (high current densities) which causes significant concentration polarization, the expressions for activation and ohmic overpotentials can be combined to give the cell operating voltage as

$$V_{FC} = E - \Delta V_A - \Delta V_O \tag{B-14}$$

or

$$V_{FC} = E - \left(\frac{\alpha_a + \alpha_c}{\alpha_a \alpha_c}\right)\left(\frac{RT}{z\Phi}\right) \ln i + \left(\frac{RT}{z\Phi}\right) \ln \left[\left(i_{ec}\right)^{\frac{1}{\alpha_c}} \left(i_{ea}\right)^{\frac{1}{\alpha_a}}\right] \tag{B-15}$$

$$- ri$$

This is a form of the Tafel equation which can be alternatively expressed as

$$V_{FC} = \left(V_o - A \ln i - ri\right)_{FC} \tag{B-16}$$

The voltage efficiency of the fuel cell can then be approximated as

$$\eta_{FC} = \frac{V_{FC}}{E} = \left(\frac{V_o}{E} - \frac{A}{E} \ln(i) - \frac{ri}{E}\right)_{FC} \tag{B-17}$$

where E is the ideal reversible potential at the pressure and temperature of fuel cell operation.

The electrolyzer is subject to the same polarizations as the fuel cell. There is, however, an additional phenomenon that contributes to the overpotential of an electrolyzer. This is manifested in electrolyzer operation by the fact that a cell voltage significantly greater than the open circuit voltage must be achieved before any current will flow, i.e., before any gas can be evolved from the electrodes. This "threshold" overpotential, ΔV_T, is equivalent to the requirement that electronically charged particles attain an energy in excess of a certain minimum before reactions can occur. The operating potential for an electrolyzer can be expressed as

$$V_{C_{EL}} = E + \Delta V_T + \frac{\alpha_a + \alpha_c}{\alpha_c \alpha_c} \frac{RT}{z\Phi} \ln i + \frac{RT}{z\Phi} \ln \left[(i_{ea})^{\frac{1}{\alpha_a}} (i_{ec})^{\frac{1}{\alpha_c}}\right] \tag{B-18}$$

$$+ ri$$

which has the form

$$V_{C_{EL}} = (V_o + A \ln i + ri)_{EL} \tag{B-19}$$

The corresponding efficiency is then

$$\frac{1}{\eta_{EL}} = \frac{V_{C_{EL}}}{E} = \left(\frac{V_o}{E} + \frac{A}{E} \ln i + ri\right)_{EL} \tag{B-20}$$

Using available cell data, the values of V_o, A and r can be determined as indicated in Figure B-1. Knowing the operating temperature and pressure a value for E can be calculated. These are then used in equations (B-17) and (B-20) to determine fuel cell or electrolyzer efficiencies as depicted in Figure B-2. Because the mass of a fuel cell and electrolyzer depend on the power density at which the unit is to operate, it is preferable to express the efficiencies in terms of the power densities. Using the relationships

$$P'_{C_{FC}} = (V_c\ i)_{FC} = \eta_{FC}\ Ei_{FC} \tag{B-21}$$

and

$$P'_{C_{EL}} = (V_c\ i)_{EL} = \frac{Ei_{EL}}{\eta_{EL}} \tag{B-22}$$

the expressions for the efficiencies become

$$\eta_{FC} = \left[\frac{V_o}{E} - \frac{A}{E} \ln\left(\frac{P'_C}{\eta E}\right) - \left(\frac{rP'_C}{E^2\eta}\right)\right]_{FC} \tag{B-23}$$

and

$$\frac{1}{\eta_{EL}} = \left[\frac{V_o}{E} + \frac{A}{E} \ln\left(\frac{\eta P'_C}{E}\right) - \frac{r}{E^2}\eta\ P'_C\right]_{EL} \tag{B-24}$$

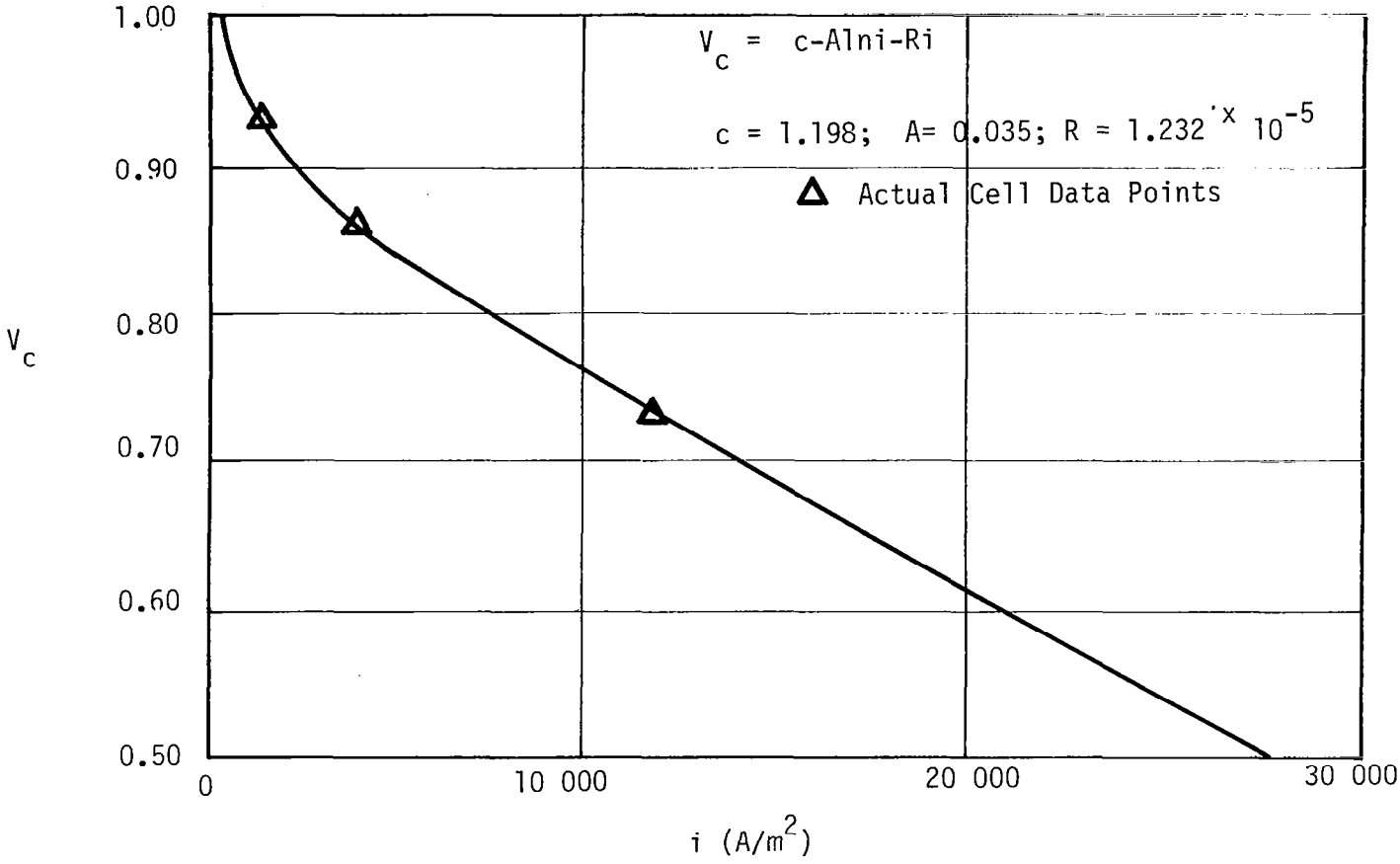

FIGURE B-1 FUEL CELL VOLTAGE AS A FUNCTION OF CURRENT DENSITY

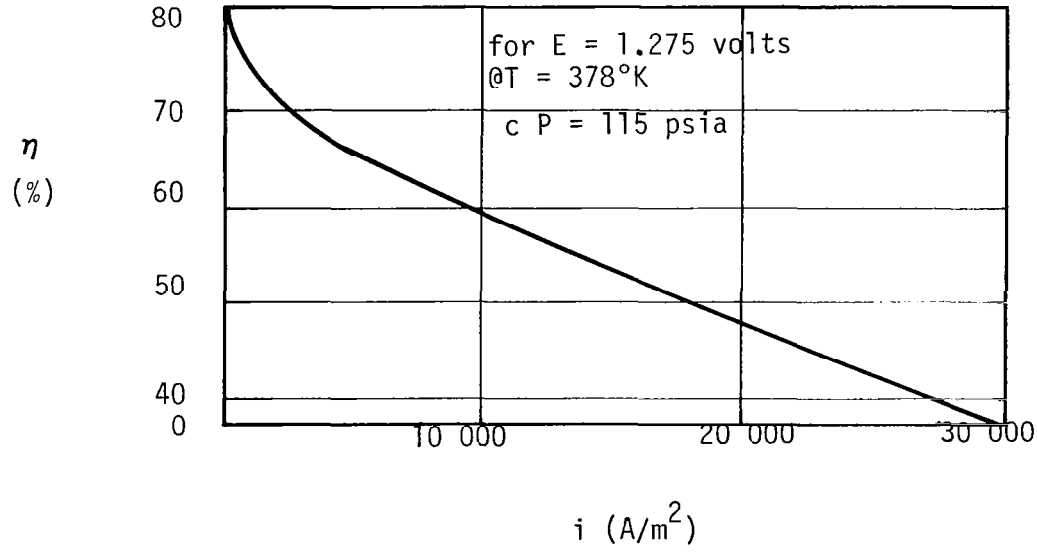

FIGURE B-2 FUEL CELL VOLTAGE EFFICIENCY AS A FUNCTION OF CURRENT DENSITY

Rather than dealing with these transcendental equations, it was deemed desirable to obtain an expression for η_{FC} and η_{EL} that were explicit functions of the power density.

For the fuel cell, this is done by rewriting the equation as

$$\left[\eta\right]_{FC} = \left[\frac{V_o}{E} + \frac{A}{E} \ln\left(\eta\right) - \frac{A}{E} \ln\left(\frac{P'_C}{E}\right) - \frac{r}{E\eta} P'_C\right]_{FC} \qquad \text{(B-25)}$$

and approximating $\ln\left(\frac{1}{\eta}\right)$ by $\frac{\eta}{2} - \frac{1}{2\eta}$

which is good for $\eta \geq 0.5$.

This allows the equation to be expressed as a quadratic in η as

$$\eta_{FC} = \left(1 + \frac{A}{2E}\right)_{FC} - \eta_{FC}\left[\frac{V_o}{E} - \frac{A}{E} \ln\left(\frac{P'_C}{E}\right)\right]_{FC} + \left(\frac{P'_C R}{E^2} - \frac{A}{2E}\right)_{FC} = 0 \qquad \text{(B-26)}$$

Using the quadratic formula

$$\eta_{FC} = \left[\frac{V_o - A \ln\left(\frac{P'_C}{E}\right)}{2E + A}\right]_{FC} \left\{1 - \left[1 - \frac{(2E + A)\left(\frac{2P'_C r}{E} - A\right)}{\left[V_o - A \ln\left(\frac{P'_C}{E}\right)\right]}\right]_{FC}\right\} \qquad \text{(B-27)}$$

Similarly, the equation for the electrolyzer becomes

$$\left[\frac{1}{\eta}\right]_{EL} = \left[\frac{V_o}{E} + \frac{A}{E} \ln \eta + \frac{A}{E} \ln \frac{P'_C}{E} + \frac{P'_C r\eta}{E^2}\right]_{EL} \qquad \text{(B-28)}$$

and using the same approximation can be expressed as a quadratic as

$$\eta_{EL}^2 = \left(\frac{P'_C r}{E^2} - \frac{A}{2E}\right)_{EL} + \eta_{EL}\left(\frac{V_o}{E} + \frac{A}{E} \ln \frac{P'_C}{E}\right)_{EL} + \left(\frac{A}{2E} - 1\right)_{EL} = 0 \qquad \text{(B-29)}$$

Using the quadratic formula

$$\eta_{EL} = \left[\frac{V_o + A \ln\left(\frac{P'_C}{E}\right)}{\frac{2P'_C r}{E} - A}\right]_{EL} \left\{\left[1 + \frac{(2E - A)\left(\frac{2P'_C}{E} - A\right)}{\left[V_o + A_{EL} \ln\left(\frac{P'_c}{E}\right)\right]}\right]_{EL}^{1/2} - 1\right\} \quad \text{(B-30)}$$

Because power to the electrolyzer varies as a function of insolation available, it is necessary to specify electrolyzer efficiency in terms of its value at a specific operating point. This point is chosen as the peak power point. If this is done then the efficiency can be expressed as a function of the ratio of operating power to peak power

$$X_{P_{EL}} \equiv \frac{P_{C_{EL}}}{P_{C_{EL}}} = \frac{P'_{C_{EL}}}{P'_{C_{EL}}} \quad \text{(B-31)}$$

The power density, $P'_{C_{EL}}$, in the electrolyzer efficiency equation can then then be expressed in terms of $X_{P_{EL}}$ as

$$P'_{C_{EL}} = P_{C_{EL}} X_{P_{EL}} \quad \text{(B-32)}$$

Similarly for the fuel cell

$$P'_{C_{FC}} = P_{C_{FC}} X_{P_{FC}} \quad \text{(B-33)}$$

Therefore, by specifying the cell constants (E, V_o, A, r), $P_{C_{FC}}$ and $P'_{C_{EL}}$, a functional relationship between the efficiency and operating power has been obtained for use in the power train sizing methodology.

APPENDIX C

REACTANT TANK SIZING

Symbols

NOTATION	DEFINITION	UNITS
A_1, A_2	Reaction constants	--
E	Energy	Joules
F	Safety factor	unitless
f	Ratio of mass of tank to mass of reactants	unitless
G	Gibbs free energy	Joules
M	Mass	Kg
$\hat{m}$	Molecular weights	Kgmole/mole
n	Number of moles	--
P	Pressure	Pascals(N/m^2)
R	Universal gas constant	8.314 Joules/ gram-mole^oK
T	Temperature	^oK
V	Volume	m^3
X	Chemical X that reacts with H_2	--
η	Efficiency	unitless
ρ	Density	kg/m^3
σ_t	Tensile strength of tank material	N/m^2

Subscripts

i	Species i
n	Number of atoms
t	Tank

REACTANT TANK SIZING

The volume and mass of tanks needed to contain a specified mass of gaseous reactants can be obtained by applying the principles of thermodynamics and stress analysis. From the perfect gas equation of state

$$V_i = \frac{n_i RT}{P} \qquad \text{(C-1)}$$

where V_i = volume of species i in m^3

n_i = number of moles of species i

R = gas constant (8.314 J/gmole^{o}k)

T = absolute temperature in Kelvins, and

P = pressure in Pascals (N/m^2)

For the reaction

$$a_1 H_2 + a_2 X_n \rightleftharpoons H_{2a_1} X_{na_2}$$

a specified energy requirement, ΔE_o; and a Gibbs free energy per mole of products, ΔG; the number of moles of each reactant needed to supply the energy ΔE_o is

$$\Delta n_{H_2} = a_1 \frac{\Delta E_o}{\Delta G} \quad \text{and} \quad \Delta n_{X_n} = a_2 \frac{\Delta E_o}{\Delta G} \qquad \text{(C-2)}$$

For an isothermal tank with initial pressure, P_1, and final pressure, P_2, use of the perfect gas equation of state gives the volume of each reactant tank as

$$V_{H_2} = \frac{a_1 \Delta E_o}{\Delta G} R \left[\frac{T}{P_1 - P_2} \right]_{H_2} \tag{C-3}$$

and

$$V_{X_n} = a_2 \frac{\Delta E_o R}{\Delta G} \left[\frac{T}{P_1 - P_2} \right]_X \tag{C-4}$$

If $\hat{m}_{H_2}$ and $\hat{m}_{X_n}$ are the molecular weights of the reactants, the mass of reactants consumed to give energy ΔE_o is

$$M_{H_2} = \hat{M}_{H_2} a_1 \frac{\Delta E_o}{\Delta G} \quad \text{and} \quad M_{X_n} = \hat{m}_{X_n} a_2 \frac{\Delta E_o}{\Delta G} \tag{C-5}$$

The mass of the tanks required to hold reactants

$$M_{TANKS_i} = \frac{3}{2} \frac{F \rho_t V_i P}{\sigma_t} 1 \tag{C-6}$$

where F = safety factor

ρ_t = density of tank material and

σ_t = tensile strength of tank material

This gives

$$M_{TANKS_{H_2}} = \frac{3}{2} F \left(\frac{P_t}{\sigma_t} \right) a_1 \frac{\Delta E_o}{\Delta G} R \left[\frac{P_1 T}{(P_1 - P_2)} \right]_{H_2} \tag{C-7}$$

$$M_{TANKS_{X_n}} = \frac{3}{2} F\left(\frac{\rho_t}{\sigma_t}\right) a_2 \frac{\Delta E_o}{\Delta G} R \left[\frac{P_1 T}{(P_1 - P_2)}\right]_{X_n} \tag{C-8}$$

The mass of reactants is given as

$$M_{H_2} = \hat{m}_{H_2} n_{1_{H_2}} = a_1 \hat{m}_{H_2} \frac{\Delta E_o}{\Delta G} \left(\frac{P_1}{P_1 - P_2}\right)_{H_2} \tag{C-9}$$

$$M_{X_n} = \hat{m}_{X_n} n_{1_{X_n}} = \hat{m}_{X_n} a_2 \frac{\Delta E_o}{\Delta G} \left(\frac{P_1}{P_1 - P_2}\right)_{X_n} \tag{C-10}$$

The ratio of mass of tanks to mass of reactants is then

$$f_{H_2} = \frac{3}{2} \frac{\rho_t}{\sigma_t} \frac{RT}{\hat{m}_{H_2}} \tag{C-11}$$

and

$$f_{X_n} = \frac{3}{2} \frac{\rho_t RT}{\sigma_t \hat{m}_{X_n}} \tag{C-12}$$

The total mass fraction of tanks to reactants is then

$$f = \frac{3}{2} F \left(\frac{\rho_t}{\sigma_t}\right) R \frac{\left\{ a_1 \left[\frac{P_1 T}{(P_1 - P_2)}\right]_{H_2} + a_2 \left[\frac{P_1 T}{(P_1 - P_2)}\right]_{X_n} \right\}}{\left\{ a_1 \hat{m}_{H_2} \left[\frac{P_1}{(P_1 - P_2)}\right]_{H_2} + a_2 \hat{m}_{X_n} \left[\frac{P_1}{(P_1 - P_2)}\right]_{X_n} \right\}} \tag{C-13}$$

For $P_2 << P_1$ and $T_{H_2} = T_{X_n}$ this reduces to

$$f = \frac{3}{2} F\left(\frac{\rho_t}{\sigma_t}\right) RT \quad \frac{(a_1 + a_2)}{(a_1 \hat{m}_{H_2} + a_2 \hat{m}_{X_n})} \tag{C-14}$$

For Kevlar

$$\frac{3}{2} R \left(\frac{\rho_t}{\sigma_t}\right) = \left(0.01669 \frac{gm}{gmole\ ^oK}\right) \tag{C-15}$$

As an example, the H_2/O_2 reaction gives $a_1 = 1$, $a_2 = 1/2$

$\hat{m}_{H_2} = 2$ and $\hat{m}_{O_2} = 32$, so that the fraction of reactant mass needed for tanks is

$$f = (1.39 \times 10^{-3}/K)\ F^*T \tag{C-16}$$

If a safety factor of 2 and a tank temperature of 273°K is used, the mass fraction, f, is equal to 0.76. If 15% attachments are added, this becomes 0.87. Therefore, if there is 3695.6 watt-hr. per kg of product (H_2O) at 273°K, there is 1986.9 watt-hr. per Kg of reactants and tanks or 0.50 kg of tanks and reactants are required per kw-hr of required energy in storage.

APPENDIX D

HEAT TRANSFER FOR ENERGY COLLECTOR SURFACES

Symbols

NOTATION	DEFINTION	UNITS
a	Unit vector normal to surface	unitless
C	Temperature coefficient for energy conversion efficiency	%/K
F	View factor	unitless
$f(T_1)$	Function of T_1	W/m^2
$g(T_2)$	Function of T_2	W/m^2
h_c	Convection film coefficient	W/m^2-K
I_s	Solar flux	W/m^2
P_f	Packing factor for surfaces containing energy collectors	unitless
Q	Heat flux per unit area	W/m^2
T	Temperature	°K
α	Absorptance	unitless
ϵ	Emittance	unitless
η	Energy conversion efficiency	unitless
γ	Angle between unit normal to surface and incident solar flux	degrees
σ	Stefan-Boltzman constant	$Whr/(°K)^4$

Subscripts

NOTATION	DEFINITION
A	Albedo
B	Back or inside of a surface
C	Convection
D	Direct solar
E	Emitted (from surface)
F	Front or outer side of a surface
FS	Free stream
I	Infrared (from the earth)
IR	Infrared
PVA	Photovoltaic conversion from albedo
PVS	Photovoltaic conversion from direct solar
S1 or 1	Side 1
S2 or 2	Side 2
ϕ	Reference value

HEAT TRANSFER FOR ENERGY COLLECTOR SURFACES

The following derivation is used to estimate the average temperatures of sun pointing (Side 1) and earth pointing (Side 2) of an energy collector and to determine the corresponding photocell efficiency. The assumptions used in this derivation are:

(1) Neglect the effects of surface curvature;

(2) Upper and lower surfaces are either joined conductively into what approximates a single surface such that $T_1 = T_2$ or are separated by air such that the only significant thermal coupling is radiative heat transfer;

(3) For radiative coupling, the view factor for inner surfaces is assumed equal to 1.0 and energy reflected back to originating surface is negligible.

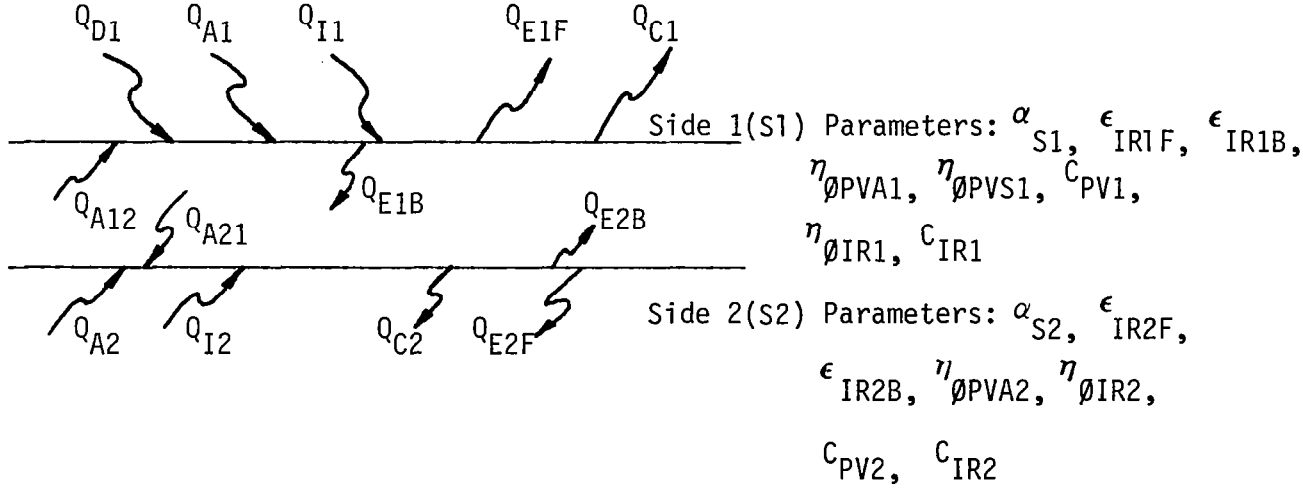

FIGURE D-1: SCHEMATIC OF VARIOUS HEAT FLUXES INTO AND OUT OF COLLECTOR SURFACES(S)

The terms used in figure D-1 are explained in the following paragraphs.

Q_{D1} is the portion of the direct incident flux that is absorbed thermally by S_1. The spectrum of the flux is approximately AMØ and the geometry of the sun collector orientation is taken into account. Also taken into account is the portion of the direct flux converted to electricity. If the solar absorptance is α_{S1}, the efficiency of electrical conversion is $\eta_{PVS1} = \eta_{\emptyset PVS1} + C_{PVT1}(T_1 - T_\emptyset)$, the unit vector normal to the surface is $\vec{a}$, the angle between $\vec{a}$ and the solar flux $\vec{I}_s$ is γ and P_{f1} is the packing factor then:

$$Q_{D1} = (\alpha_{S1} - \eta_{PVS1} P_{f1}) \vec{I}_S \cdot \vec{a} = (\alpha_{S1} - \eta_{PVS1} P_{f1}) I_S \cos\gamma \qquad \text{(D-1)}$$

Q_{A1} and Q_{A2} are the portions of the solar albedo that are absorbed thermally by S1 and S2, respectively. The spectrum of the flux is approximated by AM1. The view factor for each side is included as well as any conversion of the available flux to electricity. Because the spectrum is very similar to AMØ in wavelength range, the absorptance is the same as that for the direct flux (α_{S1} for side 1 and α_{S2} for side 2). The efficency of the electrical conversion process is η_{PVA1} and η_{PVA2} for S1 and S2, respectively. These efficiencies are assumed functions of temperature as is η_{PVS1} such that

$$Q_{A1} = (\alpha_{S1} - \eta_{PVA1} P_{f1}) I_A F_{1A} \qquad \text{(D-2)}$$

where F_{1A} is the albedo view factor for S1

Similarly for side 2

$$Q_{A2} = (\alpha_{S2} - \eta_{PVA2} P_{f2}) I_A F_{2A} \qquad \text{(D-3)}$$

Q_{I1} and Q_{I2} are the portions of the longwave infra-red that are absorbed thermally by S1 and S2, respectively. The spectrum of the flux is approximated by 300K black body. The effect of geometry is taken into account by the view factors F_{1I} and F_{2I} for S1 and S2, respectively.

The effect of conversion of flux to electrical energy is taken into account by the efficiency $\eta_{IR} = \eta_{\emptyset IR} + C_{IRT} (T - T_{\emptyset})$. Furthermore, because of the similarity of the incident and emitted spectra $\alpha_{IR_i} = \varepsilon_{IRi}$. Therefore,

$$Q_{I1} = (\epsilon_{IR1F} - \eta_{IR1} P_{f1}) I_I F_{I1} \quad \text{(D-4)}$$

and

$$Q_{I2} = (\epsilon_{IR2F} - \eta_{IR2} P_{f2}) I_I F_{I2} \quad \text{(D-5)}$$

where ϵ_{IR1F} and ϵ_{IR2F} are the emittances of the "front" sides of surfaces 1 and 2, respectively.

Q_{E1F}, Q_{E1B}, Q_{E2F} and Q_{E2B} are the emitted fluxes of the front and back sides of surfaces 1 and 2.

Therefore,

$$Q_{E1F} = \epsilon_{IR1F} \sigma T_1^4 \quad \text{(D-6)}$$

$$Q_{E1B} = \epsilon_{IR1B} \sigma T_1^4 \quad \text{(D-7)}$$

$$Q_{E2F} = \epsilon_{IR2F} \sigma T_2^4 \quad \text{(D-8)}$$

$$Q_{E2B} = \epsilon_{IR2B} \sigma T_2^4 \quad \text{(D-9)}$$

Q_{C1} and Q_{C2} are the net fluxes convected away from the "front" sides of both S1 and S2. These are determined from convective film coefficients, $h_{C1} = h_{C1}(T_1)$ and $h_{C2} = h_{C2}(T_2)$, and the free stream temperature T_{FS}. The film coefficients are assumed to be equivalent to that of a flat plate and are functions of the free stream conditions.

Therefore,

$$Q_{C1} = h_{C1} (T_1 - T_{FS}) \quad \text{(D-10)}$$

and

$$Q_{C2} = h_{C2} (T_2 - T_{FS}) \quad \text{(D-11)}$$

Q_{A12} and Q_{A21} are the fluxes emitted by S1 and absorbed by S2 and vice versa. This is non-zero for the case of a separate non-transparent surface 2. Using the emittances as before

$$Q_{A12} = \epsilon_{IR1B}\, \epsilon_{IR2B}\, \sigma T_1^4 \tag{D-12}$$

$$Q_{A21} = \epsilon_{IR1B}\, \epsilon_{IR2B}\, \sigma T_1^4 \tag{D-13}$$

Using these relationships for the various fluxes the steady-state heat balance equations for these surfaces are determined as follows

Surface 1 with transparent surface 2:

$$Q_{D1} + Q_{A1} + Q_{I1} + Q_{A2} + Q_{I2} = Q_{E1F} + Q_{E1B} + Q_{C1} \tag{D-14}$$

Surface 1 with opaque surface 2:

$$Q_{D1} + Q_{A1} + Q_{I1} + Q_{A21} = Q_{E1F} + Q_{E1B} + Q_{C1} \tag{D-15}$$

Surface 2 opaque:

$$Q_{A2} + Q_{I2} + Q_{A12} = Q_{E2F} + Q_{E2B} + Q_{C2} \tag{D-16}$$

For the transparent case, there is one temperature and it can be found by determining the zero of

$$f(T_1) = Q_{D1} + Q_{A1} + Q_{I1} + Q_{A2} + Q_{I2} - (Q_{E1F} + Q_{E1B} + Q_{C1}) \tag{D-17}$$

For the opaque under Surface, T_1 can be expressed in terms of T_2 through equation (D-16)

$$T_1 = [(Q_{E2F} + Q_{E2B} - Q_{A2} - Q_{IR2})/(\epsilon_1 \epsilon_2 \sigma)]^{1/4} \tag{D-18}$$

This expression for T_1 can then be used in equation (D-15) to find the value of T_2 that gives the zero of

$$g(T_2) = Q_{D1} + Q_{A1} + Q_{I1} + \epsilon_2\epsilon_1\sigma T_2^{\,4} - Q_{E1F} - Q_{E1B} - Q_{C1} \quad \text{(D-19)}$$

This value of T_2 is then used to determine temperature T_1 which in turn determines the operating efficiencies of the photocells.

APPENDIX E

A THEORETICAL DEFINITION OF EQUILIBRIUM ALTITUDE

Consider a solar HAPP RPV in steady state cruise conditions. Its systems are in equilibrium; thrust power at the propeller is exactly equal to drag. This power for propulsion is being generated inside its power train along with power to run its payload and auxilliary housekeeping and communications functions. These three categories of power consumption along with losses in each component of the power train sum over a day's time to exactly equal the amount of solar energy available at some constant altitude and being collected by the HAPP's solar cells. This is the concept of equilibrium altitude and it can be expressed as an algebraic equation which relates aerodynamic design parameters to power train design parameters.

The HAPP photovoltaic power trains described elsewhere in this report are all described schematically. None of the power train components operates at 100% efficiency so losses will occur at each point in the power train. Transmission losses along wires connecting components exist but will be ignored for simplicity in this discussion. Ambient pressure and temperature variations will affect the efficiency of several components, but their effects will be assumed to show up in changes in component efficiencies.

Thrust Power Available

Thrust power available over a 24 hour day comes from two different places in the power train. During nighttime, propulsive energy is extracted from what has been stored by the electrolyzer during the day. It passes from the electrolyzer to the fuel cell to the power conditioner to the motor and gearbox and is turned into torque to turn the propeller. Thrust power available will be assumed constant here over a 24 hour period for simplicity, but will always be just equal to thrust power required. In terms of energy, this nighttime equality can be expressed as

$$(E_{THRUST})_{NIGHT} = \frac{P_{REQ}\ t_{NIGHT}}{\eta_{ELEC}\ \eta_{FC}\ \eta_{COND}\eta_{MOTOR}\eta_{GEAR}\eta_{PROP}} \qquad (E\text{-}1)$$

During the daytime, thrust power is supplied by the photovoltaic cells and goes directly to the power conditioner, then to the motor, gear box, and propeller. It can be expressed as

$$(E_{THRUST})_{DAY} = \frac{P_{REQ}\ t_{DAY}}{\eta_{COND}\eta_{MOTOR}\eta_{GEAR}\eta_{PROP}} \qquad (E\text{-}2)$$

Power For Auxilliaries

Auxilliary power, as has been discussed in other sections of this report, includes power for maintaining attitude in three-dimensional space by running control actuators, on-board computers to monitor attitude and decide when to use controls, and communications links to transmit and receive status on position in four dimensional space. Also included would be power required for cooling, or heating if necessary, each component in the power train. It does not exclude the power required to run a payload or to heat or cool it. As should be expected, these are all functions which must run throughout a 24 hour day.

This auxilliary power comes from two places during a 24 hour day and can be expressed similarly to thrust power. Again, in terms of energy

$$(E_{AUX})_{NIGHT} = \frac{P_{AUX}\ t_{NIGHT}}{\eta_{ELEC}\ \eta_{FC}\eta_{COND}} \qquad \text{(E-3)}$$

and

$$(E_{AUX})_{DAY} = \frac{P_{AUX}\ t_{DAY}}{\eta_{COND}} \qquad \text{(E-4)}$$

The less than perfect efficiency of auxilliary power components is expressed in their power required.

Power for Payload

Although the missions used to size candidate solar HAPP RPV's in this report are all characterized by having payloads which run during daylight hours only, this will be modified in this derivation for simplicity. Payload power includes power to run mission sensors, to cool or warm them, and to overcome less than perfect efficiencies. The energy required to generate payload power comes from two different places over a 24 hour day and can be expressed as:

$$(E_{PAY})_{NIGHT} = \frac{P_{PAY}\ t_{NIGHT}}{\eta_{ELEC}\ \eta_{FC}\ \eta_{COND}} \qquad \text{(E-5)}$$

and

$$(E_{PAY})_{DAY} = \frac{P_{PAY}\ t_{DAY}}{\eta_{COND}} \qquad \text{(E-6)}$$

Energy Out of the Collector

Energy collected at the photovoltaic cells during periods of sunlight (days) is split into two streams. The larger stream goes into the electrolyzer to be stored as chemical energy for nighttime use. This energy into the electrolyzer is the summation of equations E-1, E-3, and E-5, or

$$(E_{ELEC})_{IN} = (E_{THRUST})_{NIGHT} + (E_{AUX})_{NIGHT} + (E_{PAY})_{NIGHT} \quad \text{(E-7)}$$

A smaller stream of energy collected during daylight hours goes directly to the power conditioner to be turned into daytime power, so total energy out of the collectors will be

$$(E_{COLL})_{OUT} = (E_{ELEC})_{IN} + (E_{THRUST})_{DAY} + (E_{AUX})_{DAY} + (E_{PAY})_{DAY} \quad \text{(E-8)}$$

$$(E_{COLL})_{OUT} = (E_{THRUST})_{NIGHT} + (E_{THRUST})_{DAY} + (E_{AUX})_{NIGHT} + (E_{AUX})_{DAY} + (E_{PAY})_{NIGHT} + (E_{PAY})_{DAY} \quad \text{(E-9)}$$

Expanding to incorporate equations E-1 through E-6:

$$(E_{COLL})_{OUT} = \frac{P_{REQ}\ t_{NIGHT}}{\eta_{ELEC}\eta_{FC}\eta_{COND}\eta_{MOTOR}\eta_{GEAR}\eta_{PROP}} + \frac{P_{REQ}\ t_{DAY}}{\eta_{COND}\eta_{MOTOR}\eta_{GEAR}\eta_{PROP}} + \frac{P_{AUX}\ t_{NIGHT}}{\eta_{ELEC}\eta_{FC}\eta_{COND}} + \frac{P_{AUX}\ t_{DAY}}{\eta_{COND}} + \frac{P_{PAY}\ t_{NIGHT}}{\eta_{ELEC}\eta_{FC}\eta_{COND}} + \frac{P_{PAY}\ t_{DAY}}{\eta_{COND}} \quad \text{(E-10)}$$

This expression can be regrouped to

$$(E_{COLL})_{OUT} = \frac{1}{\eta_{COND}}\left(t_{DAY} + \frac{t_{NIGHT}}{\eta_{ELEC}\eta_{FC}}\right)\left(\frac{P_{REQ}}{\eta_{MOTOR}\eta_{GEAR}\eta_{PROP}} + P_{AUX} + P_{PAY}\right) \quad \text{(E-11)}$$

Energy Into The Collector

Total energy into collectors during daylight hours is a complicated function of the three-dimensional orientation of collectors to the sun's rays. Its intensity is also a function of altitude, latitude, time of day, and time of year. We will for simplicity, though, express this complicated function as an integral of the solar flux over a day's time, or

$$(E_{COLL})_{IN} = \int_{t_{DAY}} Idt \; S_{COLL} \tag{E-12}$$

This can be related to collector output as

$$(E_{COLL})_{OUT} = \eta_{COLL} S_{COLL} \int_{t_{DAY}} Idt \tag{E-13}$$

Relationship of Powertrain Component Variables to Aerodynamic Variables

Note the presence of a thrust power required term in equation E-11 which was put in earlier as being equal to thrust power available. Equation E-11 can be solved for this term using E-13:

$$P_{REQ} = \left[\frac{\eta_{COND}\,\eta_{COLL}\,\eta_{COLL} \int_{t_{DAY}} Idt}{\left(t_{DAY} + \frac{t_{NIGHT}}{\eta_{ELEC}\,\eta_{FC}} \right)} - P_{AUX} - P_{PAY} \right]^2 \eta^2_{MOTOR}\,\eta^2_{GEAR}\,\eta^2_{PROP} \tag{E-14}$$

Thrust power required can also be written as

$$P_{REQ} = DV \tag{E-15}$$

$$P_{REQ} = \frac{\rho S_{REF} C_{DT}}{2} V^3 \tag{E-16}$$

Substituting

$$V = \sqrt{\frac{2}{\rho C_L} W/S_{REF}} \tag{E-17}$$

and squaring both sides yields

$$P_{REQ}^2 = \frac{\rho^2 S_{REF}^2 C_{D_T}^2}{4} \left(\frac{2}{\rho C_L} \frac{W}{S_{REF}} \right)^3 \quad \text{(E-18)}$$

$$P_{REQ}^2 = \frac{2 S_{REF}^2}{\rho} \left(\frac{C_{D_T}}{C_L^{3/2}} \right)^2 \left(\frac{W}{S_{REF}} \right)^3 \quad \text{(E-19)}$$

Substituting this into equation E-14 squared yields

$$\frac{2 S_{REF}^2}{\rho} \left(\frac{C_{D_T}}{C_L^{3/2}} \right)^2 \left(\frac{W}{S_{REF}} \right)^3 =$$

$$\left[\frac{\eta_{COND} \eta_{COLL} \eta_{COLL} \int_{t_{DAY}} Idt}{\left(t_{DAY} + \frac{t_{NIGHT}}{\eta_{ELEC} \eta_{FC}} \right)} - P_{AUX} - P_{PAY} \right]^2 \eta_{MOTOR}^2 \eta_{GEAR}^2 \eta_{PROP}^2 \quad \text{(E-20)}$$

Equilibrium Altitude Equation

Equation E-20 has a term related to altitude on the left side. This air density is an indicator of the altitude at which solar energy collected and distributed is just exactly equal to the sum of constant thrust energy required over a 24 hour day and internal energy needs. This is equilibrium altitude. Equation E-20 can be rearranged as follows to yield a final definitive description of the relationship between equilibrium altitude, power train parameters, and aerodynamic parameters. Solving Equation E-20 for ρ:

$$\rho = \frac{2\,S_{REF}^2 \left(\frac{C_{D_T}}{C_L^{3/2}}\right)^2 \left(\frac{W}{S_{REF}}\right)^3}{\left[\eta_{COND}\,\eta_{COLL}\,\eta_{COLL}\,\frac{\int_{t_{DAY}} Idt}{\left(t_{DAY} + \frac{t_{NIGHT}}{\eta_{ELEC}\,\eta_{FC}}\right)} - P_{AUX} - P_{PAY}\right]^2 \eta_{MOTOR}^2\,\eta_{GEAR}^2\,\eta_{PROP}^2} \qquad \text{(E-21)}$$

Now multiply through by the reciprocal of sea level density to nondimensionalize:

$$\sigma = \frac{\rho}{\rho_o} = \frac{\frac{2\,S_{REF}^2}{\rho_o} \left(\frac{C_{D_T}}{C_L^{3/2}}\right)^2 \left(\frac{W}{S_{REF}}\right)^3}{\left[\eta_{COND}\,\eta_{COLL}\,\eta_{COLL}\,\frac{\int_{t_{DAY}} Idt}{\left(t_{DAY} + \frac{t_{NIGHT}}{\eta_{ELEC}\,\eta_{FC}}\right)} - P_{AUX} - P_{PAY}\right]^2 \eta_{MOTOR}^2\,\eta_{GEAR}^2\,\eta_{PROP}^2} \qquad \text{(E-22)}$$

Recall that, at constant speed and altitude, drag and thrust are equal and lift and weight are equal, so

$$\frac{D}{L} = \frac{T}{W} = \frac{P_{AV}}{VW} = \frac{C_{D_T}}{C_L} \qquad \text{(E-23)}$$

Substituting

$$\sigma = \frac{\rho}{\rho_o} = \frac{\frac{2\,S_{REF}}{\rho_o \sqrt{C_L}} \left(\frac{C_{D_T}}{C_L^{3/2}}\right) \left(\frac{W}{S_{REF}}\right)^2 \frac{P_{AV}}{V_{CR}}}{\left[\eta_{COND}\,\eta_{COLL}\,\eta_{COLL}\,\frac{\int_{t_{DAY}} Idt}{\left(t_{DAY} + \frac{t_{NIGHT}}{\eta_{ELEC}\,\eta_{FC}}\right)} - P_{AUX} - P_{PAY}\right]^2 \eta_{MOTOR}^2\,\eta_{GEAR}^2\,\eta_{PROP}^2} \qquad \text{(E-24)}$$

$$\sigma = \frac{\frac{2\,S_{COLL}S_{REF}}{\rho_o\sqrt{C_L}}\left(\frac{C_{D_T}}{C_L^{3/2}}\right)\left(\frac{W}{S_{REF}}\right)^2\frac{P_{AV}}{S_{COLL}}\frac{1}{V_{CR}}}{\left[\frac{\eta_{COND}\,\eta_{COLL}S_{COLL}\int Idt}{\left(t_{DAY}+\frac{t_{NIGHT}}{\eta_{ELEC}\eta_{FC}}\right)} - P_{AUX} - P_{PAY}\right]^2\eta^2_{MOTOR}\eta^2_{GEAR}\eta^2_{PROP}} \qquad \text{(E-25)}$$

and define a ratio of collector area to wing reference area such that

$$f_{PACK} = \frac{S_{COLL}}{S_{REF}} \qquad \text{(E-26)}$$

and substitute equation E-26 into equation E-25 to get:

$$\sigma = \frac{\frac{2\,f_{PACK}\,S^2_{REF}}{\rho_o\sqrt{C_L}}\left(\frac{C_{D_T}}{C_L^{3/2}}\right)\left(\frac{W}{S_{REF}}\right)^2\left(\frac{P_{AV}}{S_{COLL}}\right)\frac{1}{V_{CR}}}{\left[\frac{\eta_{COND}\,\eta_{COLL}\,S_{COLL}\int Idt}{\left(t_{DAY}+\frac{t_{NIGHT}}{\eta_{ELEC}\eta_{FC}}\right)} - P_{AUX} - P_{PAY}\right]^2\eta^2_{MOTOR}\eta^2_{GEAR}\eta^2_{PROP}} \qquad \text{(E-27)}$$

Parametric Application of The Equilibrium Altitude Concept

The foregoing derivation has led to a single expression which relates vehicle aerodynamic design parameters to powertrain component efficiencies and to the ratio of powertrain power out to collector area. What remains is to relate these parameters to powertrain component mass-to-power ratios.

To put equation E-27 into a simpler but less general form where auxilliary and payload power are either self-contained or supplied elsewhere:

$$\sigma = \frac{\dfrac{2\, f_{PACK}\, S^2}{\rho_o \sqrt{C_L}} \left(\dfrac{C_{DT}}{C_L^{3/2}}\right) \left(\dfrac{W}{S_{REF}}\right)^2 \left(\dfrac{P_{AV}}{S_{COLL}}\right) \dfrac{1}{V_{CR}}}{\left[\dfrac{\eta_{PROP}\, \eta_{GEAR}\, \eta_{MOTOR} \eta_{COND} \eta_{COLL}\, \eta_{COLL}\, t_{DAY}^{\int Idt}}{\left(t_{DAY} + \dfrac{t_{NIGHT}}{\eta_{ELEC}\, \eta_{FC}}\right)^2} \right]^2} \quad \text{(E-28)}$$

$$\sigma = \frac{2\, f_{PACK}\, S^2_{REF} \left(\dfrac{C_{DT}}{C_L^{3/2}}\right) \left(\dfrac{W}{S_{REF}}\right) \left(\dfrac{P_{AV}}{S_{COLL}}\right) \left(t_{DAY} + \dfrac{t_{NIGHT}}{ELEC\ FC}\right)^2}{\rho_o \sqrt{C_L}\ V_{CR} \left(\eta_{PROP}\, \eta_{GEAR}\, \eta_{MOTOR}\, \eta_{COND}\, \eta_{COLL}\, S_{COLL} \dfrac{\int Idt}{t_{DAY}}\right)^2} \quad \text{(E-29)}$$

Equation E-29 and equation 13 in the text (power train methodology section) are related through the ratio of collector area to thrust power available and can be solved in conjunction with one another to define workable solar HAPP design points.

REFERENCES

1. Hasty, P. L.: A Description of the Atmospheric Turbulence Environment Derived From the Critical Atmospheric Turbulence (ALLCAT) Program. Tech. Report AFFDL-TR-77-4, April 1977.

2. U.S. Standard Atmosphere, 1976 NOAA, NASA and USAF, Washington, D.C., 1976, NOAA-S/T76-1562.

3. Anon: Solar Electromagnetic Radiation. NASA SP-8005, May 1971.

4. Ametek, Inc.: Solar Energy Handbook Theory and Applications. Radnor: Chilton Book Company, 1979.

5. Selby, J.E., et al.: "Atmospheric Transmittance/Radiance: Computer Code LOWTRAN 4". AFGL-TR-78-0053, 28 Feb 1978.

6. Clark, W.M.: High Altitude Daytime Sky Background Radiation Measurement Program. Wright Patterson AFB, Ohio, AFSC-AL-TDR-64-134-Pt 1., Jan 1964.

7. Dennison, A.J., "Illumination of a Space Vehicle Surface Due to Sunlight Reflected from Earth". American Rocket Society; Journal, 32, p. 635-637, Apr 1962.

8. Goetz, D. and Grosch, C.B., "Earth Emitted Infrared Radiation Incident Upon a Satellite". J. of Aerospace Science, p. 521-524, May 1962.

9. Anon: Earth Albedo and Emitted Radiation. NASA SP-8027, July 1971.

10. Fitz, C.E. et al.: Albedo and Planet Radiation Intercepted by an Earth Satellite. Alexandria, Virginia, AEDC-TDR-63-92, May 1963.

11. Curran, Patrick and Faulkner, Dennis: "Samarium - Cobalt Motor-Controller For Mini-RPV Propulsion". Proceedings of 17th Intersociety Energy Conversion Engineering Conference, Paper No. A29116, Aug 1982.

12. Teske, Duane and Faulkner, Dennis: "Electromechanical Flight Control Servo Actuator". Proceedings of the 18th Intersociety Energy Conversion Engineering Conference, Aug 1983.

13. Larabee, Eugene E. and French, Susan: Propeller Design and Analysis for Pedal Driven and Other Odd Aircraft. Technical Soaring, Dec 1981, Vol, 7, No. 2, p. 49-65.

14. Althaus, D.: Stuttgarter Profil Katalog I. Stuttgart University, 1972.

15. Nicolai, Leland M.: Fundamentals of Aircraft Design. University of Dayton, Dayton, OH, 1975.

16. Abbott, I.H., and von Doenhoff, A.E.: Theory of Airfoil Sections. NY, Dover, 1959.

17. Hoerner, Sighard F.: Fluid-Dynamic Drag. Hoerner Fluid Dynamics (Brick Town, NJ), c. 1965.

18. Liebeck, R.H.: "Design of Subsonic Airfoils for High Lift". Journal of Aircraft, Vol. 15, No. 9, Sept 1978, pp. 547-61.

19. Wortmann, F.X.: "Experimental Investigations on New Laminar Profiles for Gliders and Helicopters". Ministry of Aviation Translation TIL/T.4906, Mar 1969 (avail. ASTIA, Arlington, VA), (Z. Flugwiss, Vol, 5, No. 8, 1957, pp. 228-248).

20. Wortmann, F.X.: "Progress in the Design of Low Drag Airfoils". Boundary Layer and Flow Control, G. V. Lachmann, London, 1961, pp. 748-770.

21. Wortmann, F.X.: "A Critical Review of the Physical Aspects of Airfoil Design at Low Mach Numbers". Motorless Flight Research - 1972, J.L. Nash-Webber, ed, NASA CR-2315, Nov. 1973.

22. Miley, S.: "On the Design of Airfoils for Low Reynolds Numbers". AIAA Paper No. 74-1017, Sept 1974.

23. McMasters, J.H. and Henderson, M.L.: "Low Speed Single Element Airfoil Synthesis". NASA Conference Publication 2085 Part I, Science and Technology of Low Speed and Motorless Flight, Mar 1979.

24. MacCready, P.B., and Lissaman, P.B.S., et al.: Sun Powered Aircraft Design. AIAA 81-0916, May 1981.

25. Cowley, Martyn: Solar Challenger. Aero Modeller, June 1981, Vol, 46, issue 545, pp. 280-287.

26. Erickson, A.C., Austin, J.F., and Mouthrap, L.C: Electrochemical Cell Technology For Orbital Energy Storage. NASA CR-160878, June 1980.

27. Martin, R.E.: Advanced Technology Light Weight Fuel Cell Program. NASA CR-165417, Aug. 1981.

28. Martin, R.E.: Electrochemical Energy Storage for an Orbiting Space Station. NASA CR-165436, Dec. 1981.

29. Lockheed Missiles and Space Company: A Study of Multi-KW Solar Arrays for Earth Orbit Application. NASA CR-161453, Apr 1980.

30. Kuhn, Ira F., et al.: Regenerative Fuel Cell System Optimization. B-K Dynamics, Inc., 15 June 1981, sponsored by DARPA and monitored by Wright Patterson AFB under contract no. F33657-80-C-0343.

31. Rauschenback, H.S.: Solar Cell Array Design Handbook. Van Nostrand, New York, 1980.

1. Report No.	2. Government Accession No.	3. Recipient's Catalog No.
NASA CR-3699		

4. Title and Subtitle	5. Report Date
A PRELIMINARY STUDY OF SOLAR POWERED AIRCRAFT AND ASSOCIATED POWER TRAINS	December 1983
	6. Performing Organization Code
7. Author(s)	8. Performing Organization Report No.
David W. Hall, Charles D. Fortenbach, Emanual V. Dimiceli, Robert W. Parks	
	10. Work Unit No.
9. Performing Organization Name and Address	11. Contract or Grant No.
Lockheed Missiles and Space Company, Inc. 1111 Lockheed Way Sunnyvale, CA 94086	NAS1-16975
	13. Type of Report and Period Covered
12. Sponsoring Agency Name and Address	Contractor Report
National Aeronautics and Space Administration Washington, D. C. 20546	14. Sponsoring Agency Code

15. Supplementary Notes

Langley Technical Monitor: James W. Youngblood
Final Report

16. Abstract

A study was performed to assess the feasibility of regeneratively powered solar high altitude powered platform (HAPP) remotely piloted vehicles (RPVs) and to recommend those technologies which must be pursued to make long duration solar HAPPs feasible. This study defined a methodology which involved characterization and parametric analysis of roughly two dozen variables to determine vehicles capable of fulfilling the primary mission. One of these vehicles was then conceptually designed. Variations of each major design parameter were investigated along with state-of-the-art (SOTA) changes in power train component capabilities. Results are presented along with recommendations for future work. The mid-latitude mission studied would be attainable by a solar HAPP in the late 1980s or early 1990s if fuel cell, electrolyzer and photovoltaic technologies are pursued. Vehicles will be very large and have very lightweight structures in order to attain the combinations of altitude and duration required by the primary mission. Therefore, many structural questions must be addressed.

17. Key Words (Suggested by Author(s))		18. Distribution Statement
HAPP Solar RPV Regeneratively powered Photovoltaic collectors Fuel cell	Electrolyzer Low Reynolds number	Unclassified - unlimited Subject Category 07

19. Security Classif. (of this report)	20. Security Classif. (of this page)	21. No. of Pages	22. Price
Unclassified	Unclassified	208	A10

For sale by the National Technical Information Service, Springfield, Virginia 22161

NASA-Langley, 1983